CONTROL ALGORITHMS AND IMPLEMENTATION FOR VARIABLE SPEED STALL REGULATED WIND TURBINES

Thesis submitted for the degree of

Doctor of Philosophy

at the University of Leicester

by

Dimitrios Bourlis

Department of Engineering

University of Leicester

October 2010

ABSTRACT

In this research control algorithms and implementation for variable speed stall regulated wind turbines are presented. This type of wind turbine has a simpler and more robust construction and can have lower requirements for maintenance than the existing pitch regulated wind turbines. Due to these features these wind turbines can have reduced cost, which is a crucial parameter especially for large scale wind turbines. However, this type is not commercially available yet due to existing challenges in its control. In this research a complete control scheme for variable speed stall regulated wind turbines has been developed and implemented in a fully dynamic hardware-in-loop simulator for variable speed wind turbines. The simulator was developed as part of the project in order to validate the designed control algorithms. The developed control system uses novel adaptive methods in order to maximize the energy production of the wind turbines at below rated wind speeds as well as to control the power of the wind turbine at above rated wind speeds. In addition, several types of controllers including robust controllers have been used and tested, which resulted to novel control solutions for stall regulated wind turbines. The main advantage of the proposed control method is that it uses existing hardware without requiring additional sensors, so it more effectively exploits information coming from measurements available in existing wind turbine converters. Through software and hardware simulations the proposed control algorithms seem to be quite promising and give confidence for the future development of variable speed stall regulated wind turbines.

ACKNOWLEDGEMENTS

I would like to thank Prof. Dawei Gu and Dr Matt Turner for their help in robust control.

Also, I would like to thank Dr Sajjad Fekriasl for his help in Kalman filtering.

I would like to thank my supervisor Dr J.A.M Bleijs for his help as well as for his suggestions during the writing of the thesis.

In addition, I would like to thank Mr Luigi Alessandro for his support and help in the laboratory, Dr John Twiddle for helping me with the use of dSPACE ds1102 and also Mr Jan Schwarz from dSPACE Ltd for his extensive help with the use of dSPACE ds1103.

Further, I would like to thank Prof. Bill Leithead and Dr Stephen Dodd for their last remarks.

I would like to thank my colleagues and my friends for their help and advice.

Finally, I would like to thank EPSRC for providing the funding to pursue this research.

To my parents

Table of Contents

LIST OF ACRONYMS

AC: Alternating current
ANN: Artificial neural network
AKF: Adaptive Kalman filter
AR: Autoregressive
BTC: Bumpless transfer controller
BW: Bandwidth
CS: Constant speed
DAQ: Data acquisition
DC: Direct current
DFT: Discrete Fourier transform
DT: Discrete time
EKF: Extended Kalman filter
FOC: Field oriented controller
GS: Gain scheduling
HILS: Hardware-in-loop simulator
HSS: High speed shaft
IAE: Innovation adaptive estimator
IG: Induction generator
IIR: Infinite impulse response
IM: Induction machine
KF: Kalman filter
LHP: Left half plane
LPF: Low pass filter
LPV: Linear parameter varying
LSS: Low speed shaft
MA: Moving average
MIMO: Multiple Inputs multiple outputs
MMAE: Multiple model adaptive estimator
MPPT: Maximum power point tracking
MR: Model reference
NDE: Non-driving end
NR: Newton Raphson
PR: Pitch regulated
RAL: Rutherford Appleton laboratory
RHP: Right half plane
RTW: Real-time workshop
SMC: Sliding mode controller
SR: Stall regulated
SRd: Speed reduction
TR: Torque reduction
UKF: Unscented Kalman filter
VS: Variable speed
WT: Wind turbine

1. Introduction

1.1. The Wind Turbine

The Wind Turbine (WT) is a system that can be used to convert the kinetic energy of the wind to electrical energy.

The main components of a WT are the turbine rotor, usually three bladed, the drivetrain, the generator and possible power electronics. Figure 1.1 gives a simple schematic of a WT.

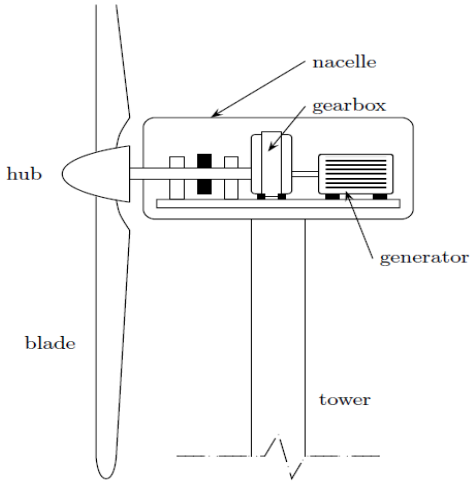

Figure 1.1. WT schematic [1].

The rotor blades can either be rigidly mounted on the rotor hub at a fixed "pitch angle" or through a variable pitch mechanism, for power limitation purposes. The interaction of the rotor blades with the oncoming wind results in the development of an aerodynamic torque which rotates the rotor. For the transmission of this torque from the rotor to the generator, either a direct coupling or a step-up gearbox may be used, depending on the type and the number of pole pairs of the generator (induction,

synchronous, synchronous with permanent magnets). In the case of a gearbox, the drivetrain also contains a Low Speed Shaft (LSS) and a High Speed Shaft (HSS), at the rotor and generator side respectively.

1.2. Aerodynamics

When the rotor of the WT is subjected to an oncoming flow of wind, an aerodynamic torque T_a is developed as a result of the interaction between the wind and the rotor blades. In this section, aerodynamic phenomena due to the interaction between the WT and the oncoming wind that affect T_a, such as the rotational sampling and the dynamic inflow, are briefly described, while mathematical models for these phenomena are provided in Chapter 2. More details on aerodynamics can be found in [1, 2].

1.2.1. Aerodynamic power and torque

An expression for the aerodynamic power of the rotor P_a has been derived in [1, 2, 3] using simplified aerodynamics, where the rotor has been considered as an actuator disk, subjected to uniform air flow, which converts the kinetic energy of the wind into mechanical energy. P_a is expressed by:

$$P_a = \frac{1}{2}\pi\rho R^2 C_p V^3, \qquad (1.1)$$

where ρ is the air density, R the radius of the rotor, V the effective wind speed seen by the rotor [1] and C_p the power coefficient of the rotor.

The effective wind speed *V*, is a result of a number of phenomena due to the interaction of the rotor and the oncoming wind. These phenomena are described in the following subsections.

C_p is defined as ratio of the power extracted from the wind to the power available in the wind [2, 3, 4] and it is a measure of the aerodynamic efficiency of the rotor, which indicates the ability of the rotor to extract power from the wind:

$$C_p = \frac{P_a}{P_{wind}} = \frac{P_a}{\frac{1}{2}\rho A V^3}, \qquad (1.2)$$

where *A* is the swept area by the rotor.

The tip speed ratio of the rotor is defined as the ratio of the blade tip speed to the wind speed:

$$\lambda = \omega R/V, \qquad (1.3)$$

where ω is the rotational speed of the rotor.

C_p is a nonlinear function of the tip-speed ratio λ and the pitch angle θ and it is particular for each rotor, with its shape depending on the rotor blade profile. C_p has a theoretical maximum of $C_{p_{max}}$=0.593, known as the Betz limit, which indicates that the maximum ability to extract power from the wind is less than 60% [1, 3]. In practice this value is lower, usually $C_{p_{max}}$=0.45. In general, for a WT it is desirable to operate at $C_{p_{max}}$ for every *V* and so to have maximum aerodynamic efficiency for every *V*, unless the rated power of the WT P_N is reached.

The aerodynamic torque T_a is given by the expression:

$$T_a = \frac{P_a}{\omega} = \frac{1}{2\omega}\pi\rho R^2 C_p V^3 \qquad (1.4a)$$

This can be also written as:

$$T_a = \frac{1}{2}\pi\rho R^3 C_q V^2, \qquad (1.4b)$$

where C_q is the torque coefficient of the rotor, defined as $C_q = C_p / \lambda$. Typical C_p and C_q curves of a rotor with blades at a fixed pitch angle θ are given in Figure 1.2.

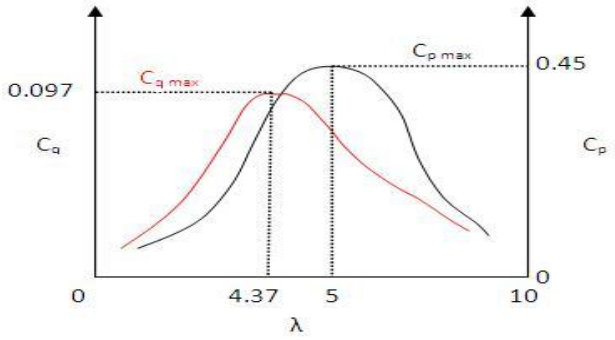

Figure 1.2. Typical C_p (black) and C_q (red) curves of a stall regulated WT.

In Figure 1.2 it can be observed that the maximum of the torque coefficient ($C_{q_{max}}$) is obtained at a lower tip speed ratio than the maximum power point ($C_{p_{max}}$), which is the case in general. The value of λ that corresponds to $C_{p_{max}}$ is the optimum tip speed ratio, λ_o:

$$\lambda_o = \frac{\omega_o R}{V}, \qquad (1.5)$$

where ω_o is the optimum rotational speed of the rotor for a given V.

A description of effects due to the interaction of the wind flow with the WT rotor follows.

1.2.2. Spatial filtering

Due to the large size of the rotor, the wind turbulence [1] contributes to the produced aerodynamic torque in an average manner, since local wind turbulence effects are smoothed out by the rotor [3]. This is known as spatial filtering of the rotor.

1.2.3. Rotational Sampling

During operation, the rotor of an actual WT faces a non-uniform wind flow due to:

a) The wind shear, which is the increase of the wind speed with height [1, 2, 3].

b) Non-perpendicular wind flow to the rotor, during fast changes of the wind direction, which are impossible for the yaw mechanism to follow.

c) The lack of spatial correlation, due to wind turbulence.

Due to the above and also due to other effects such as the tower shadow or structural asymmetries of the rotor blades [1, 2, 3], a sampling effect takes place as the rotor blades pass through the various points of the wind profile [1, 2, 3]. This sampling effect, known as rotational sampling, causes aerodynamic torque pulsations, which result in increased energy at integer harmonics of the blade passing frequency at the power spectrum of T_a. For a three bladed rotor, the 1st and the 3rd harmonic of ω and multiples are the most dominant, while for a fully symmetrical rotor the 1st harmonic is absent.

When these harmonics are not eliminated, they appear on the spectrum of the produced power, impacting its quality. Considering that there is little damping on a Variable

Speed (VS) WT [5], these harmonics have to be removed by the control system of the generator, but without extensive control action, in order to not stress the drivetrain.

1.2.4. Dynamic Inflow

So far it has been assumed that there are no dynamics in the production of T_a, which is not true, as it has been established that when changes of V, θ or ω occur, T_a does not immediately take its steady state value given by Eqn. (1.4), but only after a certain time. This phenomenon is known as the dynamic inflow and it is a consequence of the time required for the wake, rotating behind the rotor, to adjust to the new airflow conditions [3]. During this time, the forces developed on the blades and consequently T_a, are different than what is expected under steady state conditions [6].

1.3. Types of Wind turbines

Wind turbines can be categorized in the following four types, depending on the electrical power conversion technology and the power limitation method that are used:

1) Constant Speed Stall Regulated WT (CS SR WT).
2) Constant Speed Pitch Regulated WT (CS PR WT).
3) Variable Speed Stall Regulated WT (**VS SR WT**).
4) Variable Speed Pitch Regulated WT (VS PR WT).

Of the above types, the first, second and the fourth have been widely used, while the third one, VS SR WT, is not yet commercially available, due to existing challenges in

its control. In the following sections, the key features of the above types of WT are briefly described.

1.3.1.Constant Speed Wind turbines

A CS WT uses a cage Induction Generator (IG), as a generator, with a direct electrical connection to the electricity grid. The basic arrangement can be seen in Fig 1.3. This type of WT operates at a fixed speed imposed by the frequency of the grid and the number of pole pairs of the generator and it achieves optimum power production only at one wind speed.

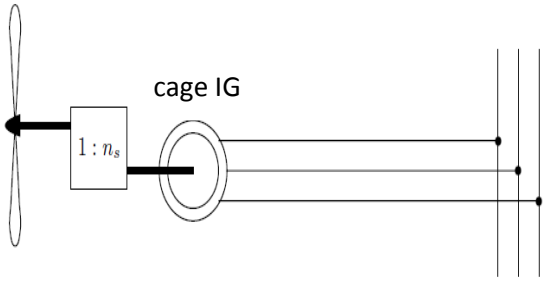

Figure 1.3. Constant speed WT with cage IG [1].

1.3.2. Variable Speed Wind turbines

A VS WT can achieve optimum power production over a wide range of wind speeds. This is achieved through speed control of the rotor by controlling the reaction torque of the generator using a variable speed drive.

Most VS WTs use different types of generator, such as Doubly Fed wound rotor IG (DFIG) (Figure 1.4a), cage IG (Figure 1.4b) or synchronous generator.

WTs with a DFIG are preferred due to the lower rating and cost of the used power converter, since only a percentage of the power passes through it (usually up to 30%) [1]. However, the DFIG has the disadvantage of increased control complexity. Therefore, the use of cage IG or synchronous generators with full power converters gradually have become more popular, because the cost of the power electronics has fallen over recent years.

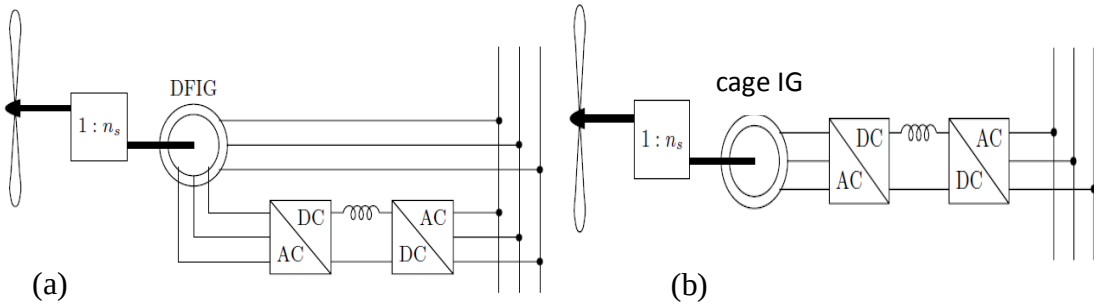

Figure 1.4. Variable speed wind turbine with (a) DFIG and (b) cage IG. [1]

The electrical system of a VS WT then consists of a generator-side converter and a grid-side converter, both connected back-to-back via a DC link. The first converter, which can also work as a variable speed drive for the generator, acts as a rectifier, converting the variable frequency/variable amplitude AC voltage of the generator to DC voltage of variable level, while the second acts as an inverter, converting the DC voltage into AC of a frequency and amplitude, matching that of the grid.

1.3.3. Power limitation-pitch and stall regulated wind turbines

The rating of the generator and/or the power electronics impose an upper limit for the power of the WT, the rated power P_N. Considering that in a VS WT, the produced power increases with the cube of the wind speed, a power limitation method is needed in high wind speeds to ensure safe operation. In the following, the wind speed

corresponding to $P=P_N$ is defined as the rated wind speed of the WT, V_N, while wind speeds $V< V_N$ and $V> V_N$ are referred to as below and above rated respectively.

Power limitation is practically achieved by reducing the aerodynamic efficiency of the rotor and this is realized via pitch or stall regulation. In order to get an insight on how these methods work, a simple schematic of a blade element is given in Figure 1.5, where θ is the angle between the plane of rotation and the blade chord (pitch angle), where the chord is the line connecting the two ends of the blade. If the undisturbed wind velocity towards the blade is $\vec{V}_w$ and the blade tip speed is $\vec{V}_b$, then the wind velocity seen by the rotating blade is $\vec{W}=\vec{V}_w - \vec{V}_b$, which hits the blade at an angle *a* relative to its chord. This is the "angle of attack". Due to the impinging wind $\vec{W}$, two forces are developed on the blade element, one perpendicular and one parallel to it. These are the Lift force, *L* and the Drag force *D*, respectively.

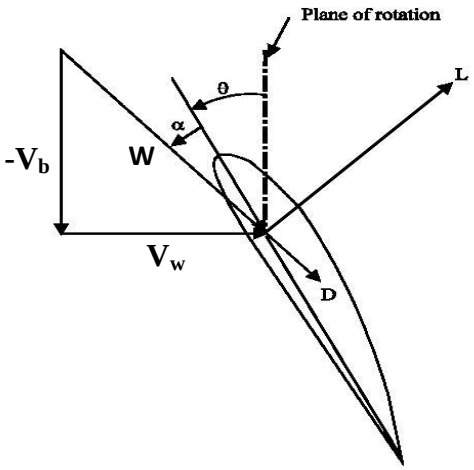

Figure 1.5. Velocities and forces, acting on a rotor blade. [7]

1.3.3.1. Stall regulation

In a WT when the wind speed $\vec{V}_w$ increases relative to the blade tip speed $\vec{V}_b$, the angle α increases too, which results in an increase of L and consequently an increase of T_a. However, if the wind further increases and α exceeds a certain value, the air flow detaches from the blade and the lift force drops, which results in drops of T_a and P_a. This can be seen in Figure 1.6, where typical plots of the lift, C_L and drag C_D coefficients with α are shown. It can be observed that after the angle of attack exceeds α=13°, C_L drops, and C_D starts rising.

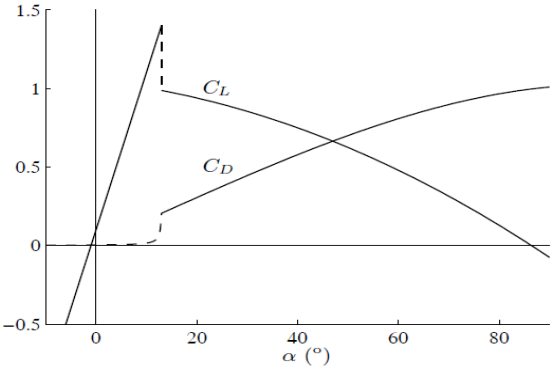

Figure 1.6. C_L and C_D coefficients of a WT rotor blade. [1]

Stall regulation refers to the controlled intentional enforcement of the rotor blades to stall and it can be achieved at constant speed, constant torque or constant power [8, 9, 10]. Here, only the third approach is of interest, since the objective is to keep P=P_N for every V> V_N, as shown in Figure 1.7 and this can be achieved by reducing the speed of the rotor via control of the reaction torque of the generator. However, the dynamics that are involved in this control loop are highly nonlinear and non-minimum phase [1] and pose challenges on the control system design. The control of VS SR WTs is still an open research issue and thus these WTs are not yet commercially available.

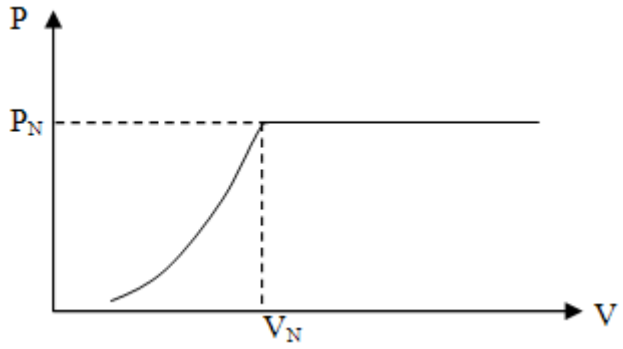

Figure 1.7. Desired power versus wind speed relation for a VS SR WT.

1.3.3.2.Pitch regulation

Pitch regulation refers to power limitation by feathering the blades (increasing θ), which also results to reduction of L. This method is widely used in modern wind turbines. It is mentioned that power limitation is also possible by reducing θ, which is known as active stall.

1.4. Scope of the research

The control of the VS SR WT equipped with cage IG is the scope of the research. The interest in this type of WT is because of its simple and more robust construction compared to the PR WTs, due to the absence of the pitch mechanism, which can considerably reduce the cost, since in large scale WTs this should be able to effectively handle quite heavy blades. In particular for offshore WTs the absence of a pitch mechanism would result in reduced maintenance time and costs. For the same reason, the cage IG is preferred, due to its simple and robust construction, which renders the system ideal for applications, where the maintenance is a major consideration.

The goal of the research is to overcome the existing challenges in the control of VS SR WT and to contribute that way towards their commercial production.

In the following section, existing control methods for VS WTs that can be applied to VS SR WTs are reviewed.

1.5.Control of variable speed stall regulated wind turbines

1.5.1.Control for below rated operation

The main control objective for a VS WT for below rated operation is maximum power production. This control objective can be shown graphically in a *T*-ω plane, as the one of Figure 1.8, where the T_a characteristics of the WT are given as functions of ω, for several values of *V* and the locus of the maximum power points is shown for every *V*. This locus is a quadratic curve described by Eq. (1.5).

$$T_a = K\omega^2, \qquad (1.5)$$

where

$$K = \frac{1}{2\lambda_o^3}\rho\pi R^5 C_{p_{max}} \qquad (1.6)$$

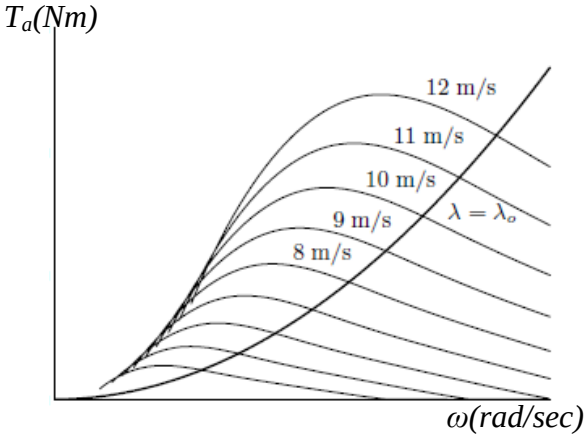

Figure 1.8. T_a characteristics and maximum power point locus [1].

Eq. (1.5) gives the desired value of T_a for every V, in order for the WT to achieve operation with maximum power production ($C_p = C_{p_{max}}$). In fact, in Eq. (1.5) it is assumed that ω has its optimum value, which can be obtained from Eqn. (1.4) and this is:

$$\omega_o = \frac{\lambda_o V}{R}, \qquad (1.7)$$

Consequently, optimum control of the WT can be achieved by speed tracking of the value of Eq. (1.7) by the rotor speed, ω [1, 10]. However, in order to obtain ω_o, knowledge of the effective wind speed V is required. However, a "point wind speed measurement" of an anemometer cannot describe the whole non-uniform wind flow that interacts with the WT rotor and therefore the effective wind speed is not measurable [10]. In [10] the possibility of estimating V through WT measurements is mentioned. However, in that case problems with more than one V solutions appear, due to the nonlinear V-T_a relation [10]. This can be observed in Figure 1.8, where it can be seen that the T_a characteristics for different wind speeds, intersect each other at the leftmost part of the graph, so for the same value of T_a and ω, at least two different choices for V exist.

Due to the above challenges, control methods based on V were abandoned.

1.5.1.1.Conventional control (Indirect control)

The control of the generator of VS WTs used in commercial WTs in below rated conditions is currently performed by setting its torque equal to the value given in Eqn. (1.5) [1, 2, 11, 12]. Hence, the control law for the generator torque is given as:

$$T_g = K\omega^2 \ , \qquad (1.8a)$$

Compensation for the drivetrain losses can be also included:

$$T_g = K\omega^2 - \gamma\omega \ , \qquad (1.8b)$$

where γ is the estimated friction loss coefficient, ω the rotor speed and K is given by Eqn (1.6).

The control of Eqns. (1.8) is often mentioned as Indirect control, since it does not take into account the dynamics of the WT, due to the large rotor inertia and therefore it has the disadvantage that it can lead to considerable deviations of the operating point from $C_{p_{max}}$, during fast wind speed changes [1, 11]. In [11] it is established that this control law performs better, when the C_p curve is broad, as it is the case in VS PR WTs, so excursions of the operating point do not cause considerable power loss. Similar conclusions can be also found in [12].

It is finally mentioned that in general, measurement of the rotor speed ω is not available, therefore, the control of Eqn. (1.8) is realized through the generator speed measurement ω_g, which is nominally equal to ω scaled up with the gearbox ratio, N, in case this is used. Of course, the factor K of Eqn. (1.8) has to take into consideration the presence of a gearbox.

Alternative indirect control methods in below rated operation have been proposed in [10, 13-15]. These are based on torque tracking of $K\omega^2$, from the estimated $\hat{T}_a$ or from the measured drivetrain torque, T_D, or a combination of them. These approaches attempt to increase the aerodynamic efficiency obtained by Eqn. (1.8), but as it has been shown in [9], their effectiveness is limited by the presence of large torque transients in the drivetrain, so these methods are not further considered here.

In general, torque tracking methods are not of interest here, due to the different control objectives for below and above rated operation, which require complicated switching solutions, in order to avoid torque transients, when the operation of the WT moves from one region to the other [10, 16, 17].

To conclude, none of the above indirect control methods have been considered in this work, since according to [10] they lead to reduced aerodynamic efficiency when used in a system with peaky C_p curve, as it is the case with VS SR WTs, as was also mentioned in [18].

For the above reasons, direct control strategies based on speed tracking are preferred.

1.5.1.2.More sophisticated control methods (Direct control)

Direct control methods are based in closed loop speed control of the generator and have been of particular interest in the literature, due to the tight $C_{p_{max}}$ tracking that theoretically can be achieved. Such control methods have been proposed for both SR and PR WTs utilizing various types of generators (cage IG, DFIG and synchronous machine).

Specifically, in [1, 19, 20] a Linear Parameter Varying (LPV) controller is proposed, while in [21] a Linear Quadratic Gaussian (LQG) controller for ω_o tracking is presented, see Eqn. (1.7). However, all assume that ω_o can be obtained from wind measurements, which is unacceptable as mentioned earlier. Also, [1] presents a detailed methodology for designing an LPV controller and the option of obtaining ω_o through an algorithm consisting of a Kalman Filter (KF) for T_a estimation and a Newton-Raphson (NR) method for subsequent V computation through Eqn. (1.4). This approach, of estimating

V through T_a, can be also found in [22], where a detailed description of the problem of dual solution for V together with suggestions to overcome this in VS PR WTs, is given. However, limitations regarding the use of a KF for T_a estimation, as well as challenges regarding the applicability of the V estimation algorithm in VS SR WTs are not addressed.

It is noted, that the LPV controller mentioned in [1] is quite a novel scheme in the area of the WT control and therefore is further investigated in a later chapter. Regarding the LQG controller, it has been theoretically studied in numerous publications, [23-26], in combination with simplified drivetrain models. However, this type of controller has not guaranteed robustness, as stated in [27] and therefore is not further discussed here.

In a similar way, in [23-26] LQG and a number of different Proportional-Integral (PI) schemes are proposed to be used either as torque or speed trackers. However, in the case of speed tracking, it is assumed that ω_o is given by:

$$\omega_o = \sqrt{\frac{\hat{T}_a}{K}}, \qquad (1.9)$$

where $\hat{T}_a$ is a T_a estimate and K is given by Eqn. (1.6).

In principle, Eqn. (1.9), which is actually obtained after rearranging Eqn. (1.5), holds only for steady state conditions, so it cannot be used for high performance control.

In [28], a method based on a PI controller and on a $\hat{V}$ estimate obtained by an Artificial Neural Network (ANN) with inputs the aerodynamic power, P_a and the rotor rotational speed, ω is proposed. However, a vast amount of data is required in order to train the ANN and furthermore there is no guarantee that all the possible relations between ω, P and V can be accurately reproduced by the ANN. In addition, P_a is estimated, using an "approximate derivative" using a lumped simplified model of the drivetrain, so

considerable inaccuracies on $\hat{V}$ estimation are expected when this scheme is applied to an actual system with a complex drivetrain. In [29] an improved approach is proposed, including a more sophisticated ANN and a more detailed drivetrain model. However, it is again assumed that P_a can be accurately obtained through speed derivatives and as the complexity of the drivetrain increases, the number of the derivatives to be calculated on line increases too, so the effectiveness of the approach in an actual system is limited by the presence of measurement noise.

In [30], a Proportional-Integral-Derivative (PID), an LQG and an adaptive Model Predictive Controller (MPC) are proposed and compared, while the reference for the controllers is based on a $\hat{V}$ estimate produced by an Extended Kalman Filter (EKF), where V is augmented into the state vector using the first order Autoregressive (AR) process:

$$\dot{V} = n, \qquad (1.10)$$

where n is a white noise sequence.

However, in general, such a WT dynamic model is not observable, because the nonlinear relation between the effective wind speed V and the aerodynamic power dictates that the same amount of energy can be produced at more than one value of V. This means that there is more than one possible state vector that represents the same distribution of the mechanical energy in the WT, so such a system is not observable and consequently its states cannot be estimated by an observer. It is mentioned that observability of the system would be ensured in case the aerodynamic power or torque characteristics (Figure 1.8) of the WT are broad enough such that they do not intersect each other. However, in [30], details about the operation of the estimation scheme are not given.

In [31], an adaptive PID controller using a "Mother Wavelet Basis Function Network" is used, to control the WT. However, the proposed solution is of high complexity and it also assumes that V is provided.

In [32] an adaptive backstepping controller able to adapt to uncertainties in the WT parameters is proposed. However, the speed reference for the controller is not based on the wind conditions, so the control scheme is not optimal.

In [33] the use of an H_∞ robust controller is proposed. However, the study is limited to a simplified WT model and the performance of the controller is only accessed through a step change in the wind speed. Further, in [34] multiobjective H_2/H_∞ control design [1, 27] is proposed, in order to both maximize energy capture and to minimize shaft torque loads. However, in order for these two objectives to be satisfied, the WT rotor speed is assumed to be available, as well as the effective wind speed, V. Obviously, this method cannot be applied in an actual WT in the presented form, because only the generator speed is available and also V is not measurable [10].

More complete control schemes including both ω_o estimation via KF and NR and speed controller design are proposed in [35], where nonlinear control methods, such as dynamic state feedback linearization are proposed. However, the proposed nonlinear method requires on-line calculation of derivatives, which is impractical. In addition, application of the KF in a WT includes challenges due to the nonstationary nature of the wind, which poses limitations to its performance and methods to overcome these challenges are not proposed or implemented.

In [36] a continuous time sliding mode controller is proposed, which is claimed to be chatter-free, but assumes again knowledge of V. Also, the controller has been tested only through software simulations using a simplified WT model. In practice, the

performance of the controller will deteriorate due to the limited sample rate of the hardware to be implemented and due to additional modes of the WT drivetrain, so attempts to enhance the performance of the controller will eventually introduce chattering, as this is shown based on hardware simulations later.

Finally, Maximum Power Point Tracking (MPPT) has been proposed as an alternative control method, which can possibly maintain optimum operation of the WT even under change of parameters such as the shape of C_p curve [37]. However, this algorithm requires considerable computational power, since it performs a DFT on line. Furthermore, it is based on V measurements, needed to estimate on-line the tip speed ratio λ and also C_p, so its effective application in an actual system is doubtful.

All of the proposed direct control methods, presented so far, for below rated operation of VS WTs, were characterized by limitation in theoretical observations, increased complexity or simplifying assumptions that renders them inappropriate for actual applications. In addition, not one of the above mentioned publications refers to the achieved aerodynamic efficiency of the proposed methods or possible benefits when applied to VS SR WTs.

1.5.2.Control for above rated operation

The main control objective for above rated wind speed operation, is to perform stall regulation at constant power, as mentioned in Section 1.3.3.1. How this can be achieved, is shown in Figure 1.9, where the locus of the operating point for a VS SR WT over the whole operating region is shown in a T_a-ω plane [1] and where ω_A is the rotational speed that the control starts operating, ω_N the rated rotational speed, V_{ω_N} the

effective wind speed corresponding to ω_N for maximum power operation, V_N the rated wind speed, P_N the rated power and T_N the rated torque of the generator.

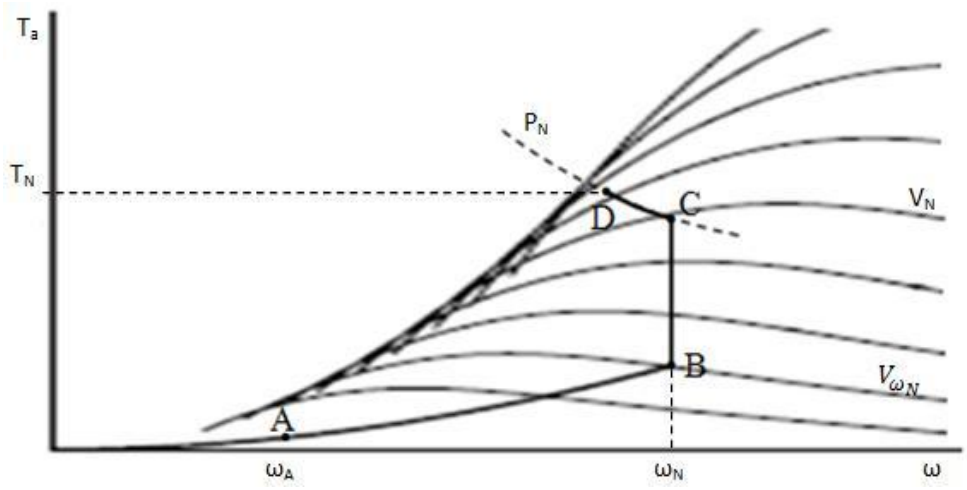

Figure 1.9. Control strategy of a stall VS SR WT [1].

Part AB is the maximum power locus, which was shown in Figure 1.8 and part BC represents constant speed operation, after the WT reaches its rotational speed limit at point B.

After this, when the power reaches its rated value at the point C, the operating point should move on the curve CD, which is part of the hyperbolic curve of constant power, P_N, given by:

$$P_N = \omega T_a \qquad (1.11)$$

When the rated torque of the generator T_N is reached at point D, the mechanical brake of the WT should be activated, in order to provide additional braking torque to stop the WT.

Alternatively, it is also possible to extend variable speed operation (and therefore maximum power production) until P_N is reached, without operating in the constant

speed part BC [1]. However, such a strategy would result in large torque transients at the intersection of the two curves, posing additional challenges to the control design. Therefore, the existence of the part BC is considered essential, while its length can be minimized.

In [9, 10], techniques based on optimum torque tracking by the estimated aerodynamic torque $\hat{T}_a$ for part CD, are proposed. However, the design of such a controller is quite challenging, since the control must be performed through the generator torque, so it can induce large torque loads on the drivetrain, as also mentioned in [10]. In [10] and [13] several other limitations of these techniques, resulting from the unstable and non-minimum phase dynamics of the WT in the stall region, are discussed, while in [38] a control scheme with increased robustness but reduced performance is presented. In addition, it is assumed that the aerodynamic power is available to the controller, which is not trivial. Furthermore, in [39] a scheme with an outer power controller and an inner speed controller is proposed, with the simplified assumption that $\hat{P}_a$ can be obtained by a simple observer and that the power controller can be easily designed, which is not the case, due to the nonlinear dynamics involved. In [40] a similar scheme is proposed, with a generator power feedback, P_g, instead of $\hat{P}_a$ in combination with an integral power controller. This approach is quite simplistic and cannot be realized in an actual WT, since dynamic differences between P_g and $\hat{P}_a$ as well as WT nonlinearities have not been considered.

In the more recent literature, [1], a more promising approach for realizing the control strategy of Figure 1.9, is proposed, via speed control of the generator, for the whole operating region, while the transitions from AB to BC and CD parts of the locus can be achieved by altering the speed reference of the controller. In addition, desirable load

alleviation can be achieved for the whole operating region by appropriately relaxing the bandwidth requirement of the controller. In [1] emphasis is put on the control design (LPV) rather than in the application of the scheme to an actual system, so several simplifying assumptions are made (e.g. simple drivetrain model, availability of *V*, speed reference based on *V*).

The literature review on the stall regulation schemes reveals issues in all the proposed methods, which are either based on simplifications of the dynamics or in dealing with only part of the problems, or both. Nowhere a complete control scheme is proposed that is realizable for the entire operating region in a VS SR WT and this is the issue to be addressed in this research.

1.6.Proposed control strategy for a variable speed stall regulated wind turbine

The actual T_a-ω plot for the simulated WT including the operating point locus (black), is shown in Figure 1.10.

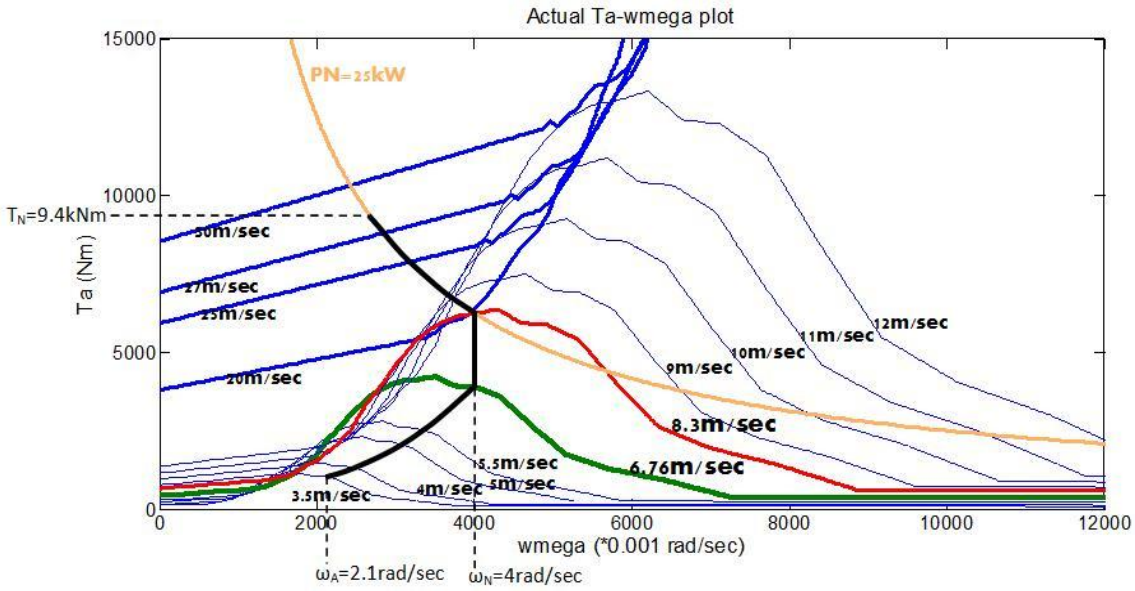

Figure 1.10. Actual T_a-ω plot of the simulated WT.

As can be seen, ω_A=2.1 and ω_N=4rad/sec. Also, P_N=25kW and T_N=9.4kNm (T_N/39.16=240Nm at the HSS, where N=39.16) and V_{ω_N}=6.76m/sec (green coloured T_a-ω characteristic) and V_N=8.3m/sec (red characteristic). Finally, $V_{cut\text{-}in}$=3.5m/sec (for ω=ω_A) and $V_{cut\text{-}out}$=28m/sec (for T_a=T_N). The locus of Figure 1.10 satisfies the maximum energy extraction and efficient power limitation objectives for below and above rated wind speeds respectively, for the simulated WT.

The control strategy proposed here is based on the locus of Figure 1.10, using speed control. A description of the requirements and issues that need to be addressed by the control system follows in the next paragraphs.

Specifically, the control system should be able to stabilize the nonlinear WT system, due to the aerodynamics, in the whole operating region. In addition, it should eliminate the cyclical torque loads of the drivetrain, caused by the effective wind speed *V* and the excitement of drivetrain oscillations, due to the dominant blade resonance mode.

In this study the drivetrain has been modeled with three masses and two stiffnesses, as shown in Chapter 2 and the blade resonance mode is represented by the first resonance mode of the drivetrain. Efficient damping of this mode by the controller is required, in order to eliminate the wear of the blades during operation.

The modes of the drive system can be excited by the effective wind speed, which includes high frequency harmonics of the rotational frequency of the rotor, as discussed in Section 1.2. Consequently, modeling of these phenomena is essential, in order to effectively assess the performance of the control system.

In this study, the effects of the rotational sampling have been modeled using appropriate filters, as seen in Chapter 2, in order to model effects due to structural asymmetries of the rotor, tower shadow, wind shear, etc.

Finally, high frequency components in *V*, due to the tower fore-aft motion need also to be considered, since an effective control system should eliminate these oscillations too. At this stage, this phenomenon was not considered, as tower dynamic models for the simulated WT were unknown.

Regarding the operation of the system, the reference of the controller is provided through an estimate of T_a and/or consequent numerical computation of *V*, while the $\hat{T}_a$ estimate is provided from Kalman Filters (KF) adaptable to non-stationary wind conditions and arbitrary measurement noise level.

Regarding the speed controllers, several choices are proposed, such as gain scheduled PI, gain scheduled H_∞, H_∞ LPV and sliding mode controllers.

Issues and limitations regarding the practical implementation of the controllers, such as discretization, actuator saturation, elimination of noise and robustness have also been taken into account throughout the development.

In addition, issues related with the acquisition of the speed reference, such as multiple *V* solutions have been successfully addressed.

Furthermore, effective and easy to implement stall regulation methods are proposed, in order to overcome problems related with the nonlinear and non-minimum phase dynamics at that region.

1.7.Methodology

The methodology that has been followed is described in the following paragraphs:

A detailed model of a VS SR WT is first developed in Simulink. This model includes the aerodynamics, the drivetrain and the electrical generator and drive dynamics. The parameters of the model chosen are based on an existing CS SR WT.

Then, control systems based on the above model are designed and implemented first in the continuous and then in the discrete time domain using MATLAB-code (M-code) in combination with Simulink blocks.

The control systems are simulated in Simulink and their performance is tested for various conditions of turbulence, dynamic inflow and rotational sampling, using appropriate wind input series. These wind series come either from site data obtained from the Rutherford Appleton Laboratory (RAL) where the simulated WT is situated or through modeling using filtered white noise or based on approaches proposed in [41].

After the controllers are shown to perform satisfactory, they are implemented in a Hardware-In-Loop Simulator for VS WT (HILS) for verification. The development of the HILS was another part of the project and the goal of this developing was to represent as close as possible the dynamics of an actual WT, in order to be able to effectively validate the designed control algorithms for VS SR WTs.

The control algorithms are tested in the HILS using wind series as described above or using externally provided signals.

Finally, the performance of the control schemes is accessed through the hardware simulation results.

1.8.Thesis structure

The structure of the thesis is as follows:

In Chapter 2, the modeling of a VS SR WT is presented, followed by the description of particular SR WT, which has been used throughout the thesis.

In Chapter 3, the development of HILS for VS SR WTs is described.

In Chapter 4, an introduction to the proposed control algorithm is given and the operation of Adaptive Kalman Filters (AKF) for aerodynamic torque estimation is described.

In Chapter 5, the estimation of the effective wind speed and of the optimum reference for the generator speed, depending on the operating conditions, is presented.

In Chapter 6, the design and application of the speed controllers is described and hardware simulation results of the proposed complete control scheme for a VS SR WT are given.

Finally, in Chapter 7, general conclusions, recommendation for future work and the original contribution of the thesis are presented.

It is mentioned that further detail regarding certain sections of the above chapters can be found through the references and the appendices that follow.

2. Wind Turbine Modeling

2.1. Introduction

In this chapter dynamic models of a VS SR WT are presented. These models are used for the development of the HILS and the control algorithms that are presented in the following chapters. Also, later in this chapter a CS SR WT is presented, data of which have been used for the subsequent control design and testing.

In general, a VS SR WT with a cage IG can be represented by the scheme of Figure 2.1, where its basic parts: rotor, drivetrain, IG and power electronic converters are shown.

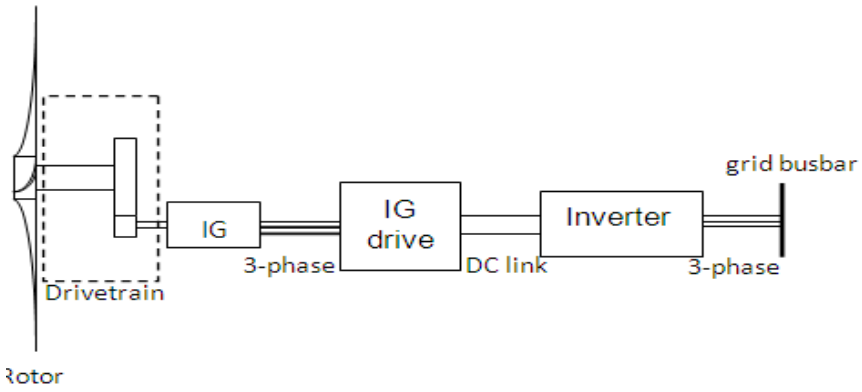

Figure 2.1. Schematic representation of a VS SR WT.

In the following sections, the dynamic models of the WT rotor, the drivetrain, the IG and the IG drive as well as their Matlab/Simulink implementation are presented. It is mentioned that the dynamics of the grid side inverter of Figure 2.1 are not discussed, since they do not directly affect the control of the IG.

2.2. Rotor dynamics

A model of the rotor dynamics should include all the aerodynamic effects, taking place during the aerodynamic torque production, as discussed in Section 1.2. Therefore, in addition to the expression for T_a as given by Eqn. (1.4a) or (1.4b) it should include the effects of rotational sampling and the dynamic inflow. It is mentioned that the spatial filtering (Section 1.2.2) has not been included in this model, since filtering the wind turbulence effects was not of interest throughout the control algorithms development.

2.2.1. Aerodynamic torque

The structures of Eqns. (1.4a & b) converted in Simulink models are shown in Figure 2.2 (a) and (b) respectively.

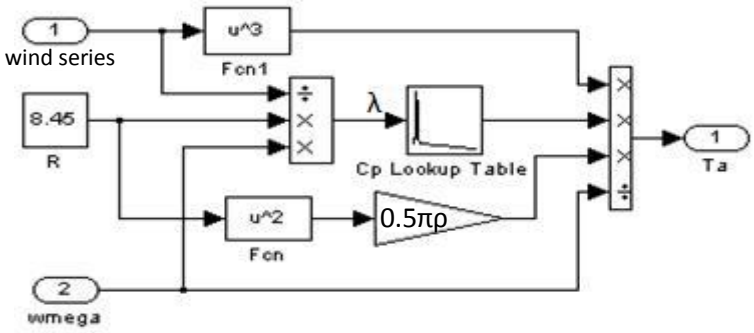

Figure 2.2a. Simulink implementation of (1.4a).

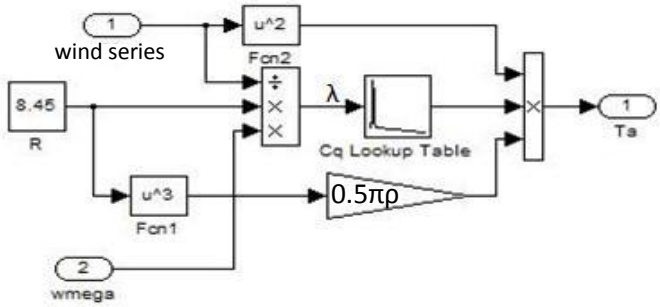

Figure 2.2b. Simulink implementation of (1.4b).

As can be seen, the basic models of Figure 2.2 have two inputs, *wind series* and ω and one output, T_a. The C_p and C_q curves have been included using look-up tables, which take λ as an input. The value R=8.45 (m) is based on a WT model, which will be described at a later section.

2.2.2. Rotational sampling

The rotational sampling effects are modeled according to [43], where filters of the form of Eqn. (2.1) are proposed, described in the Laplace (s) domain. Similar filters can be also found in [1]. These filters are applied to the effective wind speed V, before this is fed into the model of Figure 2.2 and they actually amplify a small frequency area around a harmonic component of interest (in particular ω due to rotor asymmetry and 3ω, where ω is the rotor rotational speed), while in the rest of the spectrum they have unity gain.

$$H = \frac{\frac{h^2+d^2}{h^2}(s+h)^2}{(s+(d+jh))(s+(d-jh))} \ , \qquad (2.1)$$

In Eqn. (2.1), the harmonic component of interest is set via the parameter $h=\omega_* N$, where N is the number of blades of the rotor. There is also a damping factor d which is used to adjust the height of the spectral peak at the harmonic h. Here two filters have been used with $h_1 = \omega$ and $h_2 = 3\omega$, respectively, while different values of $0.1<d<1$ have been tried.

2.2.3. Dynamic Inflow

To model the dynamic inflow, a lead-lag filter has been proposed in [3, 6]. This filter is applied to the output of the model of Figure 2.2 and it is given by:

$$H = \frac{as+1}{bs+1}\ , \qquad (2.2)$$

where a>b. In practice, the coefficients a and b are not constants, but according to [43], these are functions of V, ω and θ. So, (2.2) should be expressed as in Eqn. (2.3).

$$H = \frac{a(V,\omega,\theta)s+1}{b(V,\omega,\theta)s+1}\ . \qquad (2.3)$$

However, the functions $a(V,\omega,\theta)$ and $b(V,\omega,\theta)$ have not been established in the literature, so a complete mathematical description of these dynamics for the whole operating region of the WT is not possible. To overcome this limitation, several values of the coefficients have been tried, to simulate a variety of inflow dynamics, as will be seen in later chapter.

2.2.4. Complete aerodynamic model

The complete Simulink model that describes the production of T_a, is obtained after including the models of Eqns. (2.1-2) into the basic model of Figure 2.2. Eqn. (2.2) is easily implemented using a "Transfer Function block". Since ω is time-varying, Eqn. (2.1) is time-varying and it is implemented using an "Embedded Matlab Function" which has been programmed using M-code. The complete model is shown in Figure 2.3, based on the basic model of Figure 2.2 (b). In Figure 2.3 it can be seen that the lead-lag coefficients of Eqn. (2.2) have initially been set to α=11.25 and β=7.25, found in [3, 6]. The "Embedded Matlab Function" block "rot_s" contains two rotational sampling filters according to Eqn. (2.1), one for the 1st and one for the 3rd harmonic of ω.

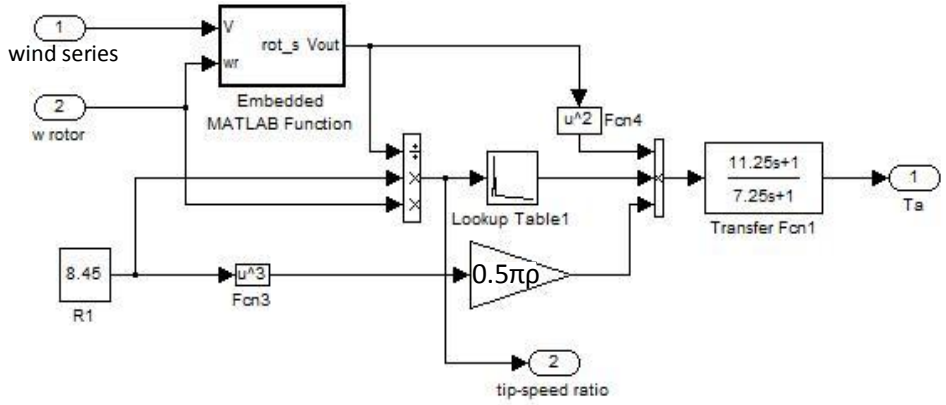

Figure 2.3. Simulink model of WT aerodynamics.

2.3. Drivetrain modeling

The drivetrain of the WT can be modeled as system with three masses and two stiffnesses, as shown in Figure 2.4, where I_1, I_2, I_g are the moments of inertia of the rotor, the generator and the gearbox respectively and K_1 and K_2 the stiffnesses of the LSS and the HSS respectively [44, 45]. This model has two inputs, T_a and T_g. It can be represented by the following dynamic equations:

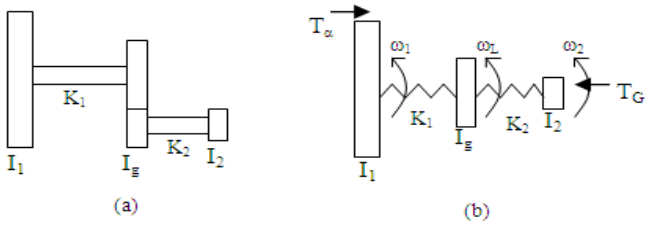

Figure 2.4. WT drivetrain: (a) schematic, (b) dynamic model.

$$I_1\dot{\omega}_1 = T_a - \gamma_1\omega_1 - K_1\theta_1 \,, \qquad (2.4)$$

$$I_2\dot{\omega}_2 = K_2\theta_2 - \gamma_2\omega_2 - T_g, \qquad (2.5)$$

$$I_g\dot{\omega}_L = K_1\theta_1 - NK_2\theta_2, \qquad (2.6)$$

$$\dot{\theta}_1 = \omega_1 - \omega_L, \qquad (2.7)$$

$$\dot{\theta}_2 = N\omega_L - \omega_2, \qquad (2.8)$$

where $\omega_1$is the rotational frequency of the LSS, ω_2 the rotational frequency of the HSS, ω_L the rotational frequency of the low speed gear (coupled to the LSS), $\gamma_1$and γ_2 are the friction loss coefficients for the rotor and the generator respectively, I_1, I_2 and I_g the inertias of the rotor, generator and low speed gear respectively, N the gear ratio, K_1 and K_2 the stiffness coefficients of the LSS and the HSS respectively, while T_g is the torque of the generator and T_a is the aerodynamic torque of the rotor.

Figure 2.5 shows the implementation of Eqns. (2.4-8) using Simulink blocks.

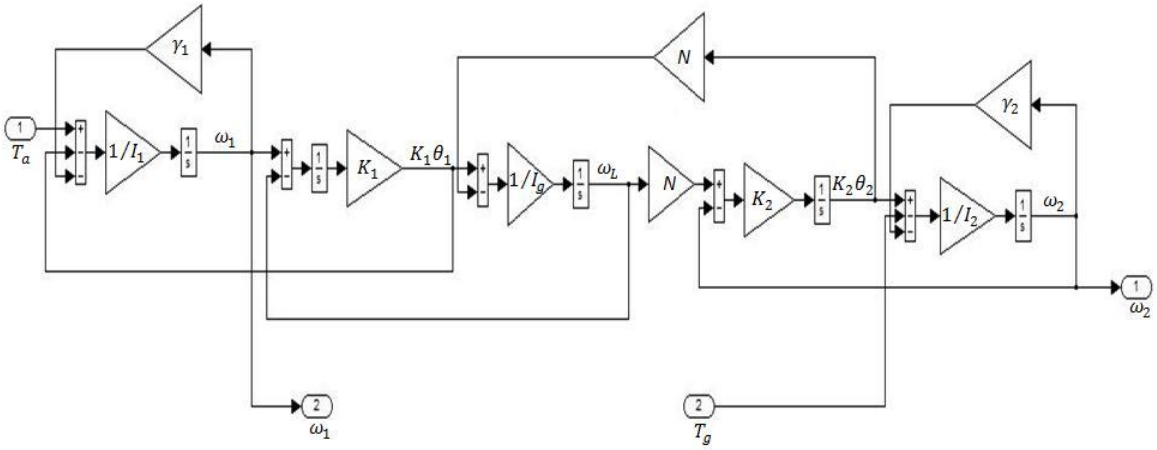

Figure 2.5. Simulink implementation of Eqns. (2.4-8).

By combining the model of Figure 2.5 with the one of Figure 2.3, a complete Simulink implementation of the Rotor + Drivetrain is obtained.

2.4. Induction generator modelling

The IG has been modeled using Eqn. (2.15), which describes the dynamics of the IG torque T_g [3, 46]:

$$\tau \dot{T}_g + T_g = D_e(\omega_g - \omega_z), \qquad (2.15)$$

where τ is determined by the resistance and the leakage inductance of the rotor winding and D_e is the slope of the IG characteristic at its linear part (for small values of the slip) [1, 3, 46]. ω_z is given by:

$$\omega_z = 2\pi f/p, \qquad (2.16)$$

where p is the number of pole pairs of the IG and f is the frequency of the stator currents. A typical $T(\omega)$ characteristic of the IG, is shown in Figure 2.6 (a).

Although Eqn. (2.15) has been derived for a grid connected IG, it can be also used for an IG operating at variable speed, providing that D_e remains constant during the variable speed operation. Figure 2.6 (b) shows the $T(\omega)$ characteristics of an IG for variable speed operation with constant D_e.

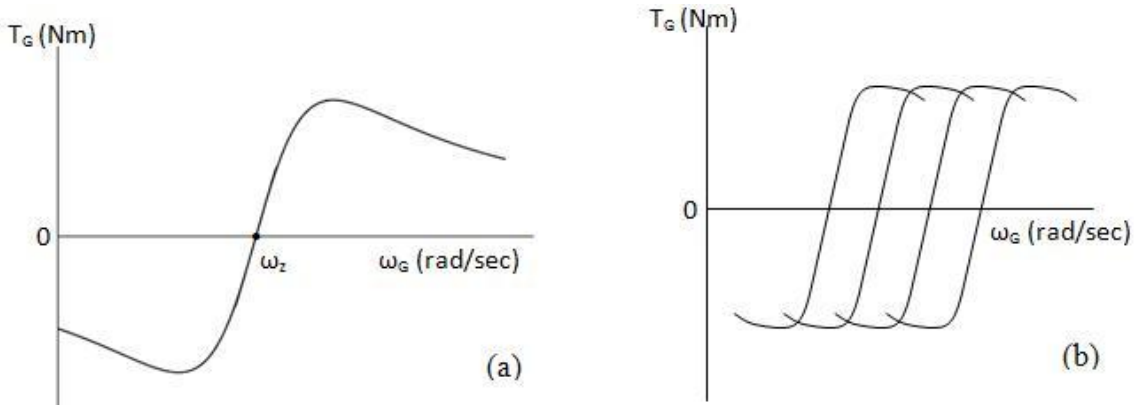

Figure 2.6. (a) IG characteristic, (b) variable speed operation.

The variable speed operation described by the characteristics of Figure 2.6 (b) is realized using Field Oriented Controlled (FOC) IG drives. This type of IG drive

maintains the slope of the IG characteristic as well as the maximum available torque for any value of the synchronous speed ω_z, where ω_z is now provided by the IG drive.

The Simulink implementation of Eqn. (2.15) is shown in Figure 2.7.

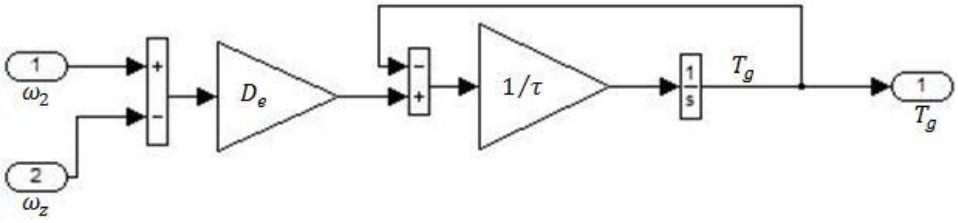

Figure 2.7. Simulink implementation of IG dynamics.

2.5. Induction generator drive modeling

The function of the FOC IG drive is to control the IG as a separately excited DC machine. In a DC machine the field flux and the armature flux are orthogonal in space so torque control can be obtained by controlling the armature current without any change in the field current, thus achieving fast torque control. However, in an IG the magnetizing and torque-forming current components are coupled in the stator current. Separate control of these currents requires an appropriate controller, which includes decoupling techniques. This type of controller is called a Vector or Field Oriented Controller and is implemented on DSPs in industrial AC machine drives.

Its operating principle is as follows: A rotating reference frame is created using the incremental position of the rotor. Then, certain quantities such as currents and fluxes of the machine, are decomposed onto this reference frame into quadrature and direct axis components, which can now be controlled separately, achieving fast torque control as in

a DC motor. In Figure 2.8 an implementation of rotor flux-oriented control is shown [47].

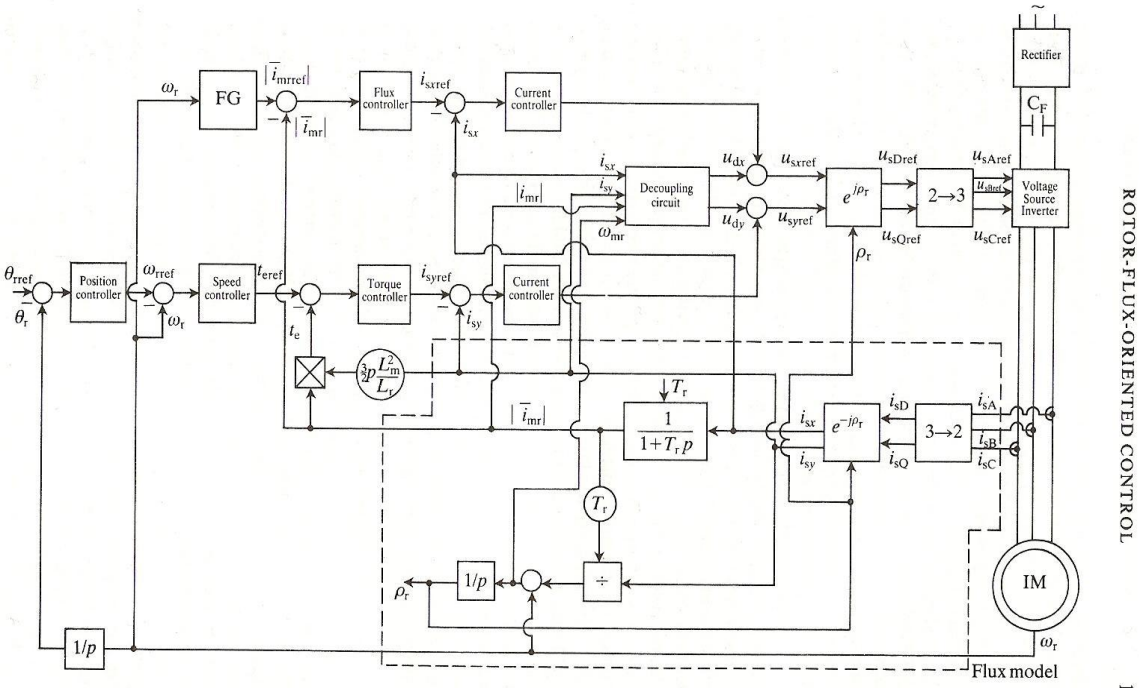

Figure 2.8. Flux-oriented vector controller [47].

As can be seen, the input to the control algorithm is a reference speed, which is compared with the speed measurement from the rotor of the machine. The speed controller produces the torque reference and the torque controller in turn produces the reference for the quadrature-axis stator current in the rotating frame fixed to the rotor flux space phasor. The vector control algorithm then produces the references for the voltages for the three phases of the machine. These references drive a voltage source PWM inverter, which applies the demanded voltages to the machine. Several variations and implementations of a FOC algorithm can be found in the literature and have been implemented inside industrial drives; e.g. a torque controller may not exist, or different type of current controllers are used (PI or hysteresis controllers). However, all these types work under the same basic principle.

Assuming that the estimates for the IG torque and currents are accurate, which is the case in high performance industrial drives, here it is proposed that the whole vector control algorithm can be modeled using a PI controller of adequate bandwidth. This PI controller expressed in the s-domain is given by:

$$\omega_z = \frac{K_p s + K_I}{s}(T_{g_{ref}} - T_g). \qquad (2.17)$$

In state space form Eqn. (2.17) becomes:

$$\dot{x} = T_{g_{ref}} - T_G, \qquad (2.18)$$

$$\omega_z = K_I x + K_p(T_{g_{ref}} - T_G), \qquad (2.19)$$

where K_p and K_I are the proportional and integral gains respectively and $T_{g_{ref}}$ is the reference for the IG torque, which is externally provided, as it will be seen in a later section. The model of Eqns. (2.18-19) can be used in conjunction with the IG model of Eqn. (2.15), which provides T_g. The PI gains of the model were selected as K_p=0.24 and K_I=32 (rad/sec/Nm), which results in a bandwidth of 40Hz. It is mentioned that actual drives can have much greater bandwidth. However, here this is set intentionally to a relatively low value, in order to establish stricter criteria for the robustness of the IG control algorithms. The Simulink model of Eqn. (2.17) is shown in Figure 2.9.

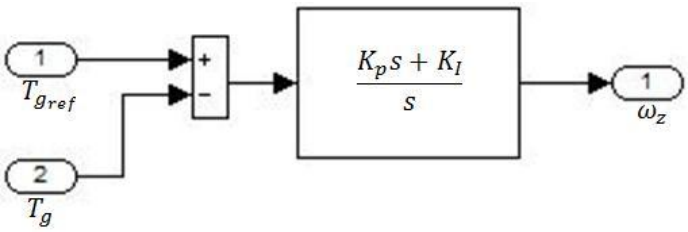

Figure 2.9. Simulink implementation of the IG drive model.

2.6. Overall model of the wind turbine

The complete Simulink model of the VS SR WT, including the rotor, the drivetrain, the IG and the IG drive, is obtained after combining the aforementioned models. Figure 2.10 shows this model, where all the individual models are represented as subsystems.

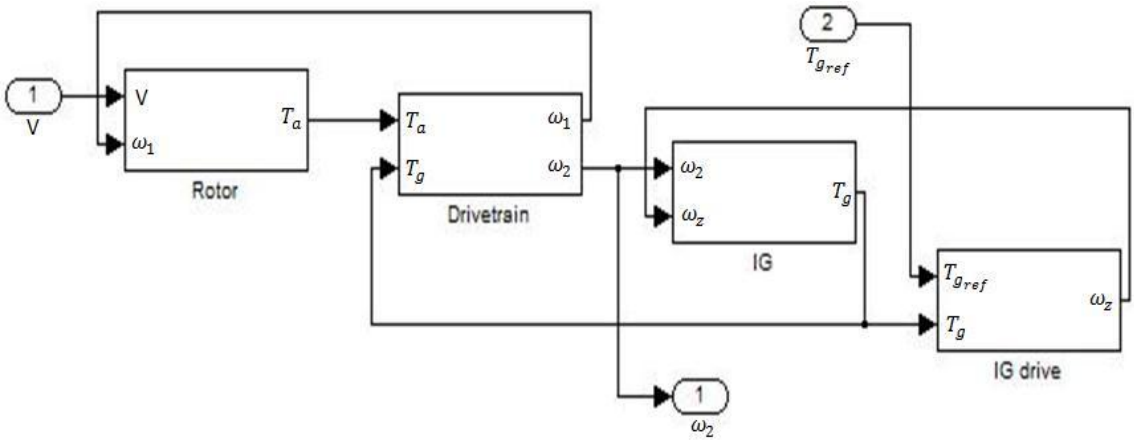

Figure 2.10. Simulink implementation of the complete model of the WT.

As can be seen from Figure 2.10, the model has only one output, ω_2, which represents the IG rotational speed, as it is the case in actual WTs. In addition, the model has only one controllable input, the reference for the IG torque $T_{g_{ref}}$, while its remaining input, the wind speed *V*, acts as a disturbance to the speed control loop.

2.6.1. Nonlinear model of the wind turbine dynamics

The dynamic equations governing the model of Figure 2.10 are given by Eqns. (2.20-26).

$$I_1\dot{\omega}_1 = \frac{1}{2}\rho\pi R^3 C_q(\omega_1, V)V^2 - \gamma_1\omega_1 - K_1\theta_1, \qquad (2.20)$$

$$I_2\dot{\omega}_2 = K_2\theta_2 - \gamma_2\omega_2 - T_G, \qquad (2.21)$$

$$I_g\dot{\omega}_L = K_1\theta_1 - NK_2\theta_2, \qquad (2.22)$$

$$\dot{\theta}_1 = \omega_1 - \omega_L, \quad (2.23)$$

$$\dot{\theta}_2 = N\omega_L - \omega_2, \quad (2.24)$$

$$\dot{T}_G = \frac{D_e K_p - 1}{\tau} T_G + \frac{D_e}{\tau}\omega_2 - \frac{D_e K_I}{\tau}\psi - \frac{D_e K_p}{\tau} T_{g_{ref}}, \quad (2.25)$$

$$\dot{\psi} = T_{g_{ref}} - T_G \quad (2.26)$$

The above model has two inputs, namely V and $T_{g_{ref}}$. As can be seen, Eqns. (2.20-24) are identical to Eqns. (2.4-8), where T_a has been substituted with Eqn. (1.4b). Eqns. (2.25-26) result after Eqn. (2.15) is combined with Eqns. (2.18-19). In the model dynamics due to dynamic inflow, as described by Eqn. (2.2), have been omitted for simplicity, since it has been shown in [48] that they are do not affect the control design.

A nonlinear term can be observed due to T_a in the right hand side of Eqn. (2.20). This nonlinear term establishes a nonlinear feedback from ω to T_a and due to this feedback, the WT is not unconditionally stable. The dynamics are stable for below rated and in mild stall operation (negative feedback due to the negative slope of the C_q curve), but unstable for deep stall operation (operation on the left hand side of the C_q curve, where its slope is positive) [1, 23].

For the design of WT controllers using linear control methods, linearized representation of the above model is required. This is developed in the next section.

2.6.2. Linearized dynamic model

The linearized dynamic model of the WT is obtained after the Jacobians of Eqns. (2.20-26) are computed (Appendix A.1). Thus, the coefficient C_q in Eqn. (2.20) has been

analytically expressed through a function of ω_1 and V. Here, the 2nd order polynomial of Eqn. (2.27) has been used to approximate C_q [1]:

$$C_q = C_{q_{max}} - K_q(\frac{\omega R}{V} - \lambda_{q_{max}})^2 \quad (2.27)$$

Although higher order polynomials can give a better fit, they would increase the complexity of the resulting equations and are not therefore preferred.

The resulting linearized model is given by the following state equations:

$$I_1\dot{\omega}_1 = A_{11}\omega_1 + B_{11}V - K_1\theta_1 - 2\gamma_1\omega_1, \quad (2.28)$$

$$I_2\dot{\omega}_2 = K_2\theta_2 - \gamma_2\omega_2 - T_G, \quad (2.29)$$

$$I_g\dot{\omega}_L = K_1\theta_1 - NK_2\theta_2, \quad (2.30)$$

$$\dot{\theta}_1 = \omega_1 - \omega_L, \quad (2.31)$$

$$\dot{\theta}_2 = N\omega_L - \omega_2, \quad (2.32)$$

$$\dot{T}_G = \frac{D_eK_p - 1}{\tau}T_G + \frac{D_e}{\tau}\omega_2 - \frac{D_eK_I}{\tau}\psi - \frac{D_eK_p}{\tau}T_{G_{ref}}, \quad (2.33)$$

$$\dot{\psi} = T_{G_{ref}} - T_G, \quad (2.34)$$

where

$$A_{11} = \left(-\pi R^5 K_q\right)\omega_1 + \pi R^4 K_q \lambda_{q_{max}} V, \quad (2.35)$$

$$B_{11} = \pi R^4 K_q \lambda_{q_{max}}\omega_1 + \pi R^3\left(C_{q_{max}} - K_q{\lambda_{q_{max}}}^2\right)V \quad (2.36)$$

The difference between the models of Eqns. (2.28-36) and Eqns. (2.20-26) is that in the second, $T_a = \frac{1}{2}\rho\pi R^3 C_Q(\omega_1, V)V^2$ has been replaced by its linearized expression:

$$T_a = \frac{\partial T_a}{\partial \omega_1}\omega_1 + \frac{\partial T_a}{\partial V}V + \gamma_1\omega_1 = (A_{11} + \gamma_1)\omega_1 + B_{11}V \quad (2.37)$$

As can be seen from Eqns. (2.35-37), the operating point of the linearized model depends on ω_1 and V, while ω_1 is also a state of the model. In order to proceed to a linear analysis of the WT dynamics, it is assumed that ω_1 and V are kept constant in Eqns. (2.35-36), in order to determine a constant operating point. It is mentioned that this analysis fails to accurately describe the dynamic behavior of the WT around the chosen operating point, because of their dependency on ω_1, but it is considered a useful tool in order to get a general insight. Details can be found in [1].

The general Simulink representation of Figure 2.10 can be also used for the representation of Eqns. (2.28-36), with the only difference that the block "Rotor" should now contain the linearized expression of Eqn. (2.37).

2.7. Simulated wind turbine

In order to develop a HILS, as well as control algorithms for a VS SR WT, data from a real WT of this type are needed. Since this type of WT is not yet commercially available, the data used in this research are that of a CS SR WT, a 45kW Windharvester WT that has been installed at the Rutherford Appleton Laboratory (RAL), in Oxfordshire. The data of this turbine has been taken from [3].

2.7.1. Description and parameters of the Windharvester wind turbine

This WT has a 3-bladed rotor and its drivetrain consists of a LSS, a step-up gearbox and a HSS. In fact, the gear arrangement consists of a fixed-ratio gearbox, followed by a belt drive. This was originally intended to accommodate different rotor speeds during the low wind and high wind seasons. The drivetrain can be seen in Figure 2.11.

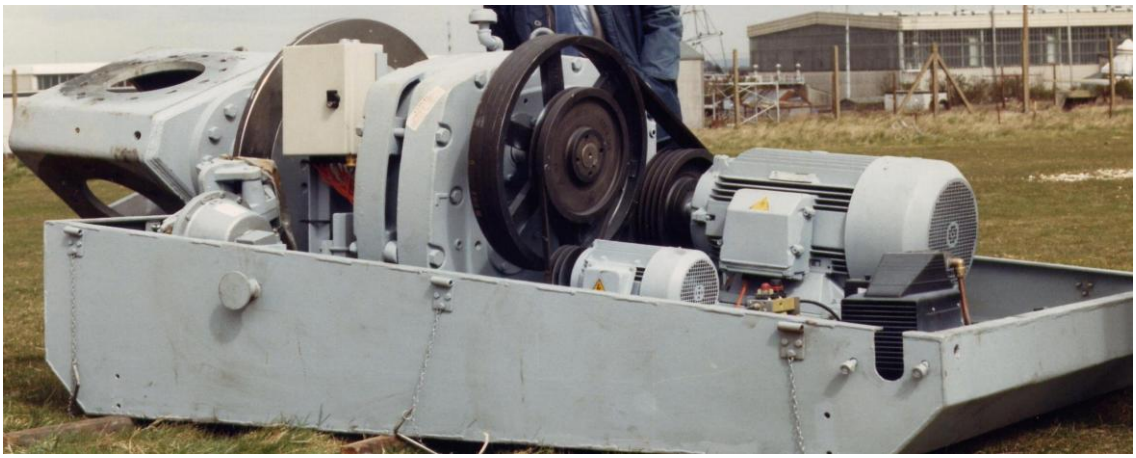

Figure 2.11. Drivetrain of the Windharvester WT.

The data for this WT are given in Table 2.1.

Rotor inertia, I_1	14145 Kgm^2
Gearbox inertia, I_g	34.2 Kgm^2
Generator inertia, I_2	0.3897 Kgm^2
LSS stiffness, K_1	$3.36 \cdot 10^6$ Nm/rad
HSS stifness, K_2	$2.13 \cdot 10^3$ Nm/rad
Rotor radius, R	8.45 m
Gearbox ratio, N	1:39.16
LSS rated rotational frequency, ω_1	4.01 rad/sec
Rated power of the generator, P_N	45 kW

Table 2.1. Wind turbine data.

Due to the presence of the compliant belt drive system, the belt drive system with the HSS form an equivalent HSS with a relatively low stiffness, as can be observed from Table 2.1.

The C_p and C_q curves of the rotor of the WT are shown in Figure 2.12 (a) and (b) respectively (Appendix A.2). In addition, the data have been slightly modified in order

to obtain the steeper C_p curve, shown in Figure 2.12 (c), with the corresponding C_q curve shown in Figure 2.12(d). A steeper C_p curve requires less speed reduction during stall regulation at constant power and therefore it can be preferred for a VS SR WT, although there are restrictions in the control bandwidth [13]. In addition, such a C_p curve requires more accurate control in below rated operation. Thus, the modified curves are also used to assess the performance of the proposed control methods, as it is shown in a later chapter.

The maximum power coefficient $\mathbf{C_{pmax}=0.45}$ is obtained for a tip speed ratio $\boldsymbol{\lambda_{Cpmax}=4.02}$, while **t**he maximum torque coefficient is $\mathbf{C_{qmax}=0.098}$ for a tip speed ratio $\boldsymbol{\lambda_{Cqmax}=4.37}$.

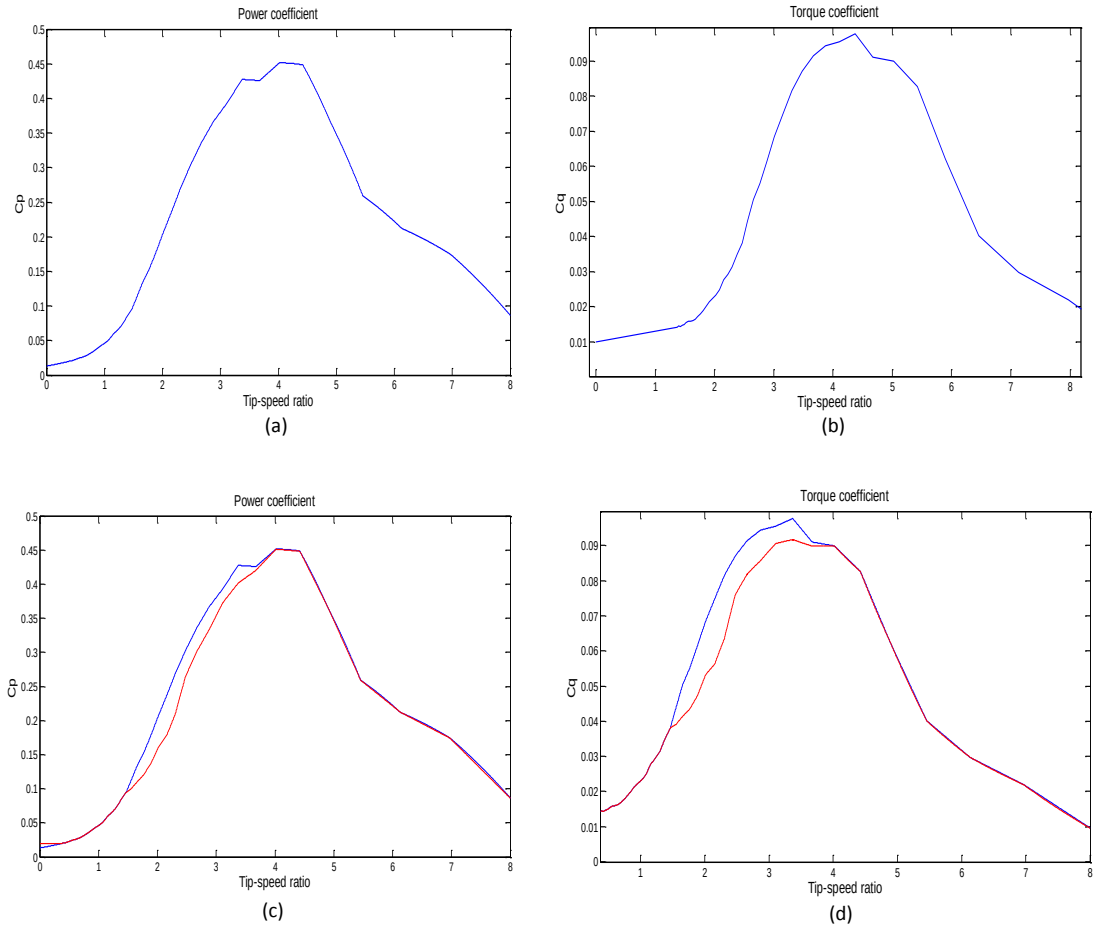

Figure 2.12. (a) Power and (b) torque coefficient curve of the Windharvester WT (original). (c) Power and (d) torque coefficient curve (red) (steeper).

The estimated friction loss factors for the rotor and the generator are taken from [3] and are given in Table 2.2.

Rotor friction loss constant, γ_1	68.06
IG friction loss constant, γ_2	0.041

Table 2.2. Friction loss coefficients

The generator of the WT is a 4-pole 415V 50Hz cage machine of 45kW. Table 2.3 lists the other parameters of the IG.

Inertia of the generator, I_2	0.3897 kgm^2
slope of the slip curve, D_e	72.0 Nm/rad/sec
Rotor time constant, τ	36.5msec
number of pole pairs, p	2

Table 2.3. Parameters of the IG for the Windharvester WT.

2.7.2. Dynamic analysis of the wind turbine

In this section a linearized dynamic model of the WT is examined. The C_q-λ curve of Figure 2.12(b) has been approximated by the polynomial of Eqn. (2.27) with the parameters of Table 2.4.

$C_{q_{max}}$	0.097
K_q	0.0143
$\lambda_{q_{max}}$	4.373

Table 2.4. Polynomial parameters for C_q approximation.

The actual curve and its approximation are shown in Figure 2.13.

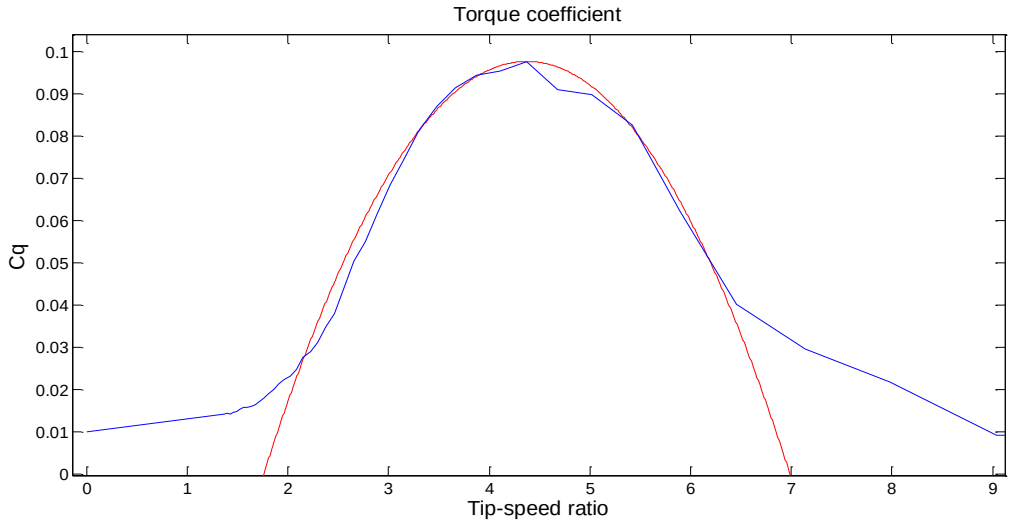

Figure 2.13. Actual C_q curve (blue) and its approximation (red) using Eqn. (2.27).

Now that the WT dynamics are described by analytical expressions, the transfer functions from the inputs to the outputs of the linearized model can be examined. Only the dynamic Eqns. (2.28-32) are considered which include the most dominant modes of the WT model. This reduced dynamic model has two inputs, V and T_g and one output, ω_2 and therefore the associated transfer functions are $G_{V\omega_2}$ and $G_{T_g\omega_2}$, respectively. The Bode plots of $G_{V\omega_2}$ and $G_{T_g\omega_2}$ are shown in Figures 2.14 and 2.15, respectively for two operating points, namely one for below rated operation (ω_1,V)=(4rad/sec, 6.76m/sec) and one for above rated operation (deep stall), (4 rad/sec, 8.76m/sec).

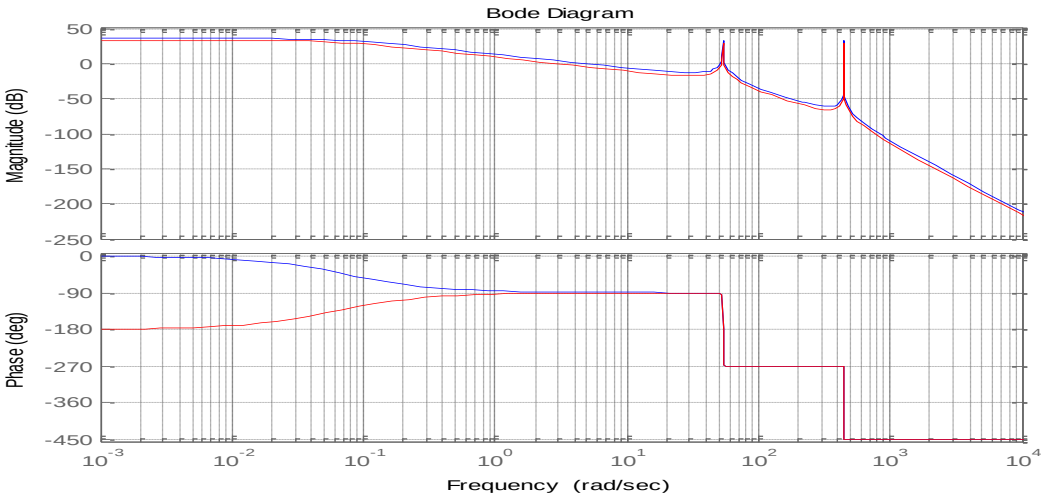

Figure 2.14. Bode plots of $G_{V\omega_2}$ for below rated (blue) and deep stall operation (red).

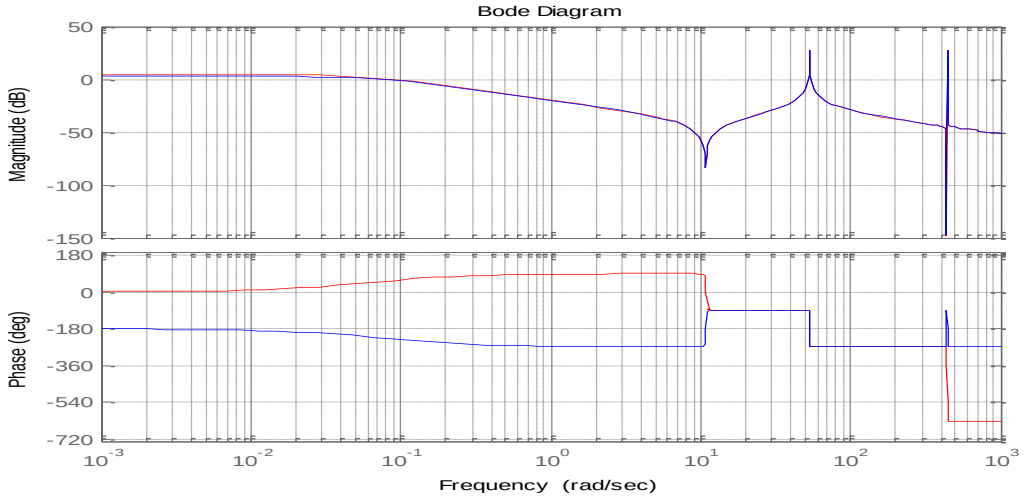

Figure 2.15. Bode plots of $G_{T_g\omega_2}$ for below rated (blue) and deep stall operation (red).

As can be seen from the above plots, a phase change of 180° occurs, for frequencies less than 0.1rad/sec as the operating point of the WT moves from below rated to stall operation, for both transfer functions. This observation is not of particular interest regarding $G_{V\omega_2}$, which in any case it acts as a disturbance to the control loop. However, it is of particular importance for $G_{T_g\omega_2}$, where closed loop control is applied. Table 2.5 shows the poles and zeros of $G_{T_g\omega_2}$ for below rated operation (left column) and deep stall operation (right column).

Below rated		**Deep stall**
Poles		
$\mathbf{p_{1,2}}$	-7.6246e-004 ±4.4340e+002i	-7.2036e-004 ±4.4340e+002i
$\mathbf{p_{3,4}}$	-5.1283e-002 ±5.3415e+001i	-4.8306e-002 ±5.3415e+001i
$\mathbf{p_5}$	-7.4453e-002	6.0920e-002
Zeros		
$\mathbf{z_{1,2}}$	-2.2775e-005 ±4.4031e+002i	2.1141e-005 ±4.4031e+002i
$\mathbf{z_{3,4}}$	-3.6645e-002 ±1.0810e+001i	3.4016e-002 ±1.0810e+001i

Table 2.5. Poles and zeros of $G_{T_g\omega_2}$ for below rated (left) and above rated (right) operation.

As can be seen in Table 2.5, in below rated operation, all the poles and zeros are situated in the Left Half Complex Plane (LHP), so the system is stable, as mentioned in section 2.5.1. However, when the system operates in deep stall, one pole ($\mathbf{p_5}$) and all the zeros of the system migrate to the Right Half Plane (RHP), so $G_{T_g\omega_2}$ is unstable and non-minimum phase and therefore more difficult to control. The rest of the poles remain almost unaffected by the change in operating conditions and this was also confirmed through a modal analysis, as seen in the next section.

Due to the RHP pole of Table 2.5, the lower control bandwidth (BW) requirement increases. Also, due to the RHP zeros of Table 2.5, the BW is constrained to be BW<10.8rad/sec.

The modes of the IG and IG drive that were neglected at this analysis appear at the LHP at frequencies equal or higher than 169.64rad/sec and also do not depend on the changes of the operating point, so they do not considerably affect the dynamic behavior of the WT inside the control bandwidth and therefore are not included in the analysis.

2.7.3. Examination of mode sensitivity to system parameters

2.7.3.1. Preliminaries

The following notation is assumed for a dynamic system:

$$\dot{x} = Ax + Bu, \qquad (2.38)$$

where x is the state vector, $\dot{x}$ its time derivative, A the system matrix, B the input matrix and u the input vector.

By examining the eigenvalues of the system matrix of a dynamic system useful conclusions can be drawn for the relation between its modes and its states. In addition, by examining the "generalized participation" of its modes, the sensitivity of them to changes in the elements of the system matrix can be revealed.

For a dynamic system with system matrix AϵR^{nxn} with *n* distinct eigenvalues λ_i, *i*=1...*n* the right and left eigenvector v_i and w_i are given by Eqns. (2.39) and (2.40) respectively [50].

$$Av_i = \lambda_i v_i, \qquad (2.39)$$

$$w_i A = \lambda_i w_i, \qquad (2.40)$$

where $v_i \epsilon R^{nx1}$ and $w_i \epsilon R^{1xn}$.

The right eigenvector shows the influence that a particular mode has on all the states of the system, while the left eigenvector shows the influence that any state has to a particular mode.

According to [51] the generalized participation p_{ihj} of a mode h is defined by the multiplication of the *i*-th component of the right eigenvector and the *j*-th component of the left eigenvector as shown in Eqn. (2.41).

$$p_{ihj} = v_{ih} w_{hj} \qquad (2.41)$$

The generalized participation is a measure of the sensitivity of the particular mode to changes of an element of the matrix A: [51]

$$p_{ihj} = \lambda'_h \text{ for } a_{ji} \qquad (2.42)$$

where $\lambda'_h = \frac{d\lambda_h}{da_{ji}}$.

2.7.3.2. Application to wind turbine model

The WT model considered here is shown in Eqns. (2.43-47):

$$I_1\dot{\omega}_1 = A_{11}\omega_1 + B_{11}V - K_1\theta_1, \qquad (2.43)$$

$$I_2\dot{\omega}_2 = K_2\theta_2 - \gamma_2\omega_2 - T_g, \qquad (2.44)$$

$$I_g\dot{\omega}_L = K_1\theta_1 - NK_2\theta_2, \qquad (2.45)$$

$$\dot{\theta}_1 = \omega_1 - \omega_L, \qquad (2.46)$$

$$\dot{\theta}_2 = N\omega_L - \omega_2, \qquad (2.47)$$

where A_{11} and B_{11} are given in Eqns. (2.35) and (2.36) respectively.

The system matrix, *A* for the above equations is shown in Eqn. (2.48), where it can be seen that change of the operating conditions only affect the element A[1,1], see Eqn. (2.35).

$$A=\begin{bmatrix} A_{11} & 0 & -K_1/I_1 & 0 & 0 \\ 0 & -G_2/I_2 & 0 & K_2/I_2 & 0 \\ 1 & 0 & 0 & 0 & -1 \\ 0 & -1 & 0 & 0 & N \\ 0 & 0 & K_1/I & -NK_2/I & 0 \end{bmatrix} \qquad (2.48)$$

The right and left eigenvectors of *A* can obtained using the following MATLAB commands:

[V,D]=eig(A), (2.49)

[W,D]=eig(A.'), (2.50)

which will return a right eigenvector matrix *V*, a left eigenvector matrix *W* and a matrix *D* with the eigenvalues of *A* at its diagonal. Then, the generalized participation matrices

p_{ihj} can be obtained through Eqn. (2.41) for every mode *h* of Eqn. (2.48). These participation matrices follow, where only elements that correspond to non-zero and parameterized elements of *A* are displayed, while the rest have been masked with zeros. Also, only the magnitudes of the participations are displayed, since the phase does not add useful information in the case of sensitivity examination.

The participation matrices P_{i1j} P_{i3j} and P_{i5j} for the modes $\boldsymbol{p_{1,2}}$, $\boldsymbol{p_{3,4}}$ and $\boldsymbol{p_5}$ respectively, are shown below.

$$P_{i1j}=\begin{bmatrix} 1.8106\text{e}-006 & 0 & 0 & 0 & 0 \\ 0 & 4.2809e-005 & 0 & 0 & 0 \\ 3.3847e-006 & 0 & 0 & 0 & 6.7650e-006 \\ 0 & 3.4728e-006 & 0 & 0 & 2.7217e-004 \\ 0 & 0 & 0 & \mathbf{1.6951e-002} & 0 \end{bmatrix}, \quad (2.51)$$

$$P_{i3j}=\begin{bmatrix} 2.0708e-005 & 0 & 0 & 0 & 0 \\ 0 & \mathbf{4.6506e-004} & 0 & 0 & 0 \\ 4.6633e-006 & 0 & 0 & 0 & 1.2417e-007 \\ 0 & 4.5449e-006 & 0 & 0 & 4.8686e-006 \\ 0 & 0 & 0 & 3.0322e-004 & 0 \end{bmatrix}, \quad (2.52)$$

$$P_{i5j}=\begin{bmatrix} \mathbf{2.5520e-002} & 0 & 0 & 0 & 0 \\ 0 & 1.0766e-003 & 0 & 0 & 0 \\ 1.2026e-007 & 0 & 0 & 0 & 2.9034e-010 \\ 0 & 6.0580e-009 & 0 & 0 & 1.3576e-008 \\ 0 & 0 & 0 & 8.4554e-007 & 0 \end{bmatrix}, \quad (2.53)$$

As can be seen, the elements $P_{i1j}[1,1]$ and $P_{i3j}[1,1]$ are very small, which explains why the poles $\boldsymbol{p_{1,2}}$ and $\boldsymbol{p_{3,4}}$ remained almost unchanged in Table 2.5 (For these poles the elements $P_{i1j}[5,4]$ and $P_{i3j}[2,2]$ are the largest respectively, which indicate sensitivity to other parameters of the system). On the other hand, $P_{i5j}[1,1]$ is considerably higher, which explains the big change of the pole $\boldsymbol{p_5}$ with the change in the operating conditions.

2.8. Conclusions

At this chapter, dynamic models and Simulink implementation of a VS SR WT were presented. In addition, the characteristics and the dynamics of a CS SR WT were briefly described, since this WT is used in later chapters for HILS and controllers design. Furthermore, a modal analysis of the WT dynamic model provided a more comprehensive way to understand the relation between the modes and the actual parameters of the system. The next chapter presents the development of the HILS for VS SR WTs.

3. Hardware-in-loop simulator

3.1. Introduction

In this chapter the development and implementation of a HILS for VS SR WTs is presented. The HILS is used for the final testing of the developed control methods, after these methods have been successfully tested using software WT models. Although these models are indicative of the performance of the control methods, they do not capture the nonlinear characteristics and therefore the complete dynamic behaviour of actual IGs and variable speed drives, used in an actual WT. Simulations using HILS can overcome this limitation and better characterize the performance of any control system, since these are now tested under conditions that are closer to those in an actual VS SR WT.

3.2. Previous implementations

HILS for CS and VS WTs have been described in several publications, such as [3, 21, 52-57].

In particular, [3] describes a DC HILS using a PC with a very early version of Windows operating system and MATLAB, which did not enable accurate modeling of the wind turbine aerodynamics and dynamics and using a test-rig consisting of a DC motor coupled to an IG through a belt drive system. Although this arrangement enabled the easy accommodation of generators of different sizes, it differentiated considerably the

dynamics of the HILS from that of the actual simulated wind turbine, due to the presence of the belt drive. Discrepancies from the actual WT dynamics were observed, but these were not identified and resolved and were attributed to noise as well as rotational sampling mismodeling. Specifically, the contribution of the compliant belt drive system, the DC motor drive and the absence of closed loop speed control of the IG, had not been considered as potential causes of the difference in the dynamic behaviour of the HILS from the actual simulated WT. In addition, a motor inertia compensation method was used. This method was based on model inversion, which could only compensate for the slower acceleration of the motor, but not for its slower deceleration, since the motor drive was set to operate at the first quadrant only, so negative torque demands were not recognized by the drive. Therefore, this method was ineffective.

Regarding the HILS described in [21, 52-57], in most of them non-commercial power converters and IG drives are used, while in others, insufficient details about the used models and operation of the HILS are given.

3.3. Current hardware-in-loop simulator development

3.3.1. Hardware-in-loop simulator with DC motor drive and geared belt drive

Here, the implementation of a fully dynamic HILS for VS SR WTs is presented. Initially, the hardware available for this development was the test rig with the belt drive [3] and a thyristorized Mentor II of Control Techniques DC motor drive. For the WT aerodynamics and drive-train dynamics modeling, a PC running Windows NT and equipped with MATLAB/Simulink and a dSPACE ds1102 simulation platform was made available from the Control Laboratory of the Engineering Department of the

University of Leicester. The IG was connected to the grid through a Variac and the DC motor was torque-controlled via torque demands from the WT model to the DC drive and the WT simulation loop was closed through a speed measurement form the DC motor to the PC, as mentioned in [3]. The HILS was driven by simulated wind speed series produced via filtering of band-limited white noise.

Initial challenges that had to be overcome were in brief the appropriate setting of the DC drive as well as the compensation of nonlinearities and offsets of the dSPACE terminals. In addition, soft starting of the simulator was necessary, in order to avoid large torque transients and consequent trips of the DC drive during the starting. Thus, a starting routine was developed, which smoothly accelerated the IG to its rated speed, before this was turned on with the Variac.

The above CS HILS worked successfully and this development set the basis for the development of more accurate HILS. Specifically, the used version of MATLAB/Simulink provided limited modeling facilities, since complicated functions such as time-varying filters, necessary for rotational sampling effects (Chapter 2) or controllers, needed to be modeled using functions written in C language. Such a development would be quite time consuming due to the debugging process and therefore a more recent version of MATLAB/Simulink was required. In addition, the maximum allowed sampling rate of the WT model in order this to be real-time implementable in dSPACE ds1102 was 10msec. This value did not allow real-time implementation of WT models more complicated than the ones used in [3], where the dynamics of the gearbox of the WT were neglected. Therefore, a more powerful simulation platform was required.

Due to the above reasons the CS WT was redeveloped using the same test rig but with a PC running a current version of MATLAB/Simulink and equipped with a dSPACE ds1103 simulation board that allows much higher sampling rates and provides additional facilities. The development was based on more detailed dynamic models, which include the inertia of the gearbox. In addition, an effective hardware compensation method based on reference model speed tracking, inspired by [58-59], was applied, since it was identified that the primary cause of the simulation discrepancies found in [3], was the existence of the hardware parts of the HILS. All the details for the implementation of the CS HILS can be found in Appendix A.4.

After this, the HILS was upgraded for VS operation, by connecting the IG to the grid through power converters. At this development, the DC motor was speed controlled. The simulation loop was closed through the torque of the IG, which was estimated from the IG drive and sent back to the PC. The torque feedback was preferred, because the speed feedback used in the DC HILS caused instability. Although this instability was eliminated by the grid connected IG in the case of the DC HILS, the variable speed IG drive could not provide adequate damping in the case of VS HILS.

In order to assess the performance of the HILS, WT simulations were performed. The simulated WT worked in the regions AB and BC of Figure 1.9, using speed control as proposed in Section 1.6, using a PI controller. The wind input was provided via an external signal. During simulations at the part BC and for winds higher than 7m/sec, instability occurred. This instability was attributed to the compliant belt and in order to get an insight, an approximate model of the HILS was developed in Simulink, since the exact parameters of the system, such as the belt stiffness, were not known. This analysis is provided in Appendix A.5. The conclusions are that the HILS hardware severely alters the dynamics of the simulated WT by dramatically reducing the

frequency of the RHP zeros of the WT. According to [27], it is possible to alter the zeros of a specific input – output path of a Multiple Inputs Multiple Outputs (MIMO) system by applying appropriate control at another input of the system. The HILS hardware can be considered as a MIMO system with inputs the torque demand to the DC drive as well as the torque demand to the IG drive and outputs the speed of the DC motor and the IG. Therefore, compensation via speed reference tracking for the IG was attempted, as this was successfully implemented for speed tracking of the DC motor in the case of the CS HILS. This was realized using a PI compensator, which now provided the torque demand to the DC drive. The approximate theoretical analysis (Appendix A.5) showed that by increasing the compensator gains the RHP zeros can be moved to the expected by the theoretical model positions. However, at the same time the compensator causes other LHP poles of $G_{T_{g_{ref}}\omega g}$ to move into the RHP. This observation was verified through hardware simulations, where instability was observed. The HILS instability was eliminated by reducing the compensator gains, but then poor speed tracking was observed at the IG, especially during intense torque control action from the speed controller of the IG.

Due to the above reasons, the HILS was considered satisfactory for general WT modeling for power system studies, but inappropriate for testing of sophisticated control methods for VS SR WTs.

3.3.2. Hardware-in-loop simulator with directly coupled induction machines

For the purpose of this research, another test rig was used, with a direct drive coupling between the prime mover and the IG. This test rig had been initially considered more appropriate, due to the direct drive coupling of the machines, which can therefore more

effectively simulate the stiff drive-train of a WT and was used as soon as it was made available for the project. The setup consists of two cage Induction Machines (IM) rated at 3kW connected back-to-back via a stiff coupling, as can be seen in Figure 3.1.

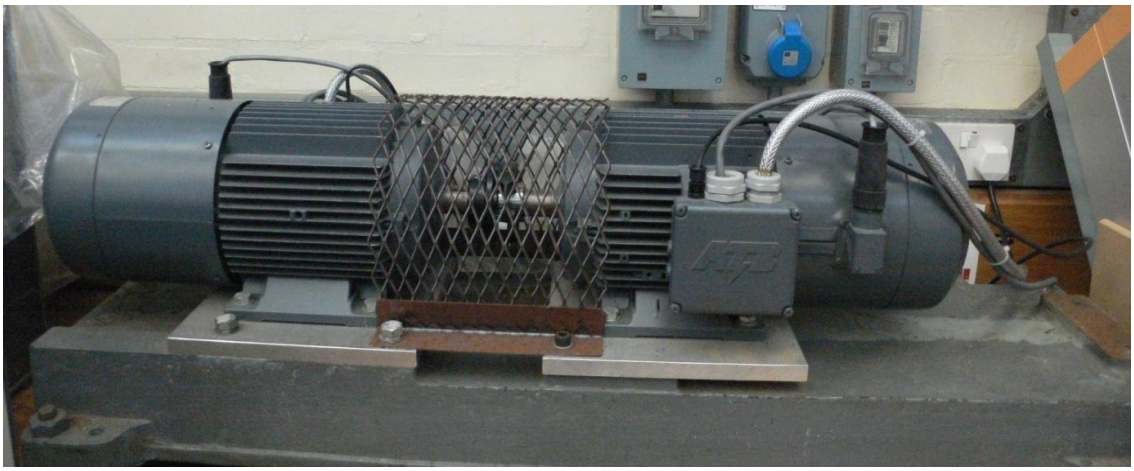

Figure 3.1. IG setup with directly coupled IMs.

This setup also includes two vector-controlled variable speed drives (Cegelec GD3000E) with a faster dynamic response than the Mentor II DC drive.

During operation of the HILS, the IG drive acts as a rectifier and sends the power produced by the IG to a DC link. From there, the power is used to energize IM drive, which therefore only absorbs the loss power from the grid. Figure 3.2 provides a schematic diagram of the electrical connection of the drives.

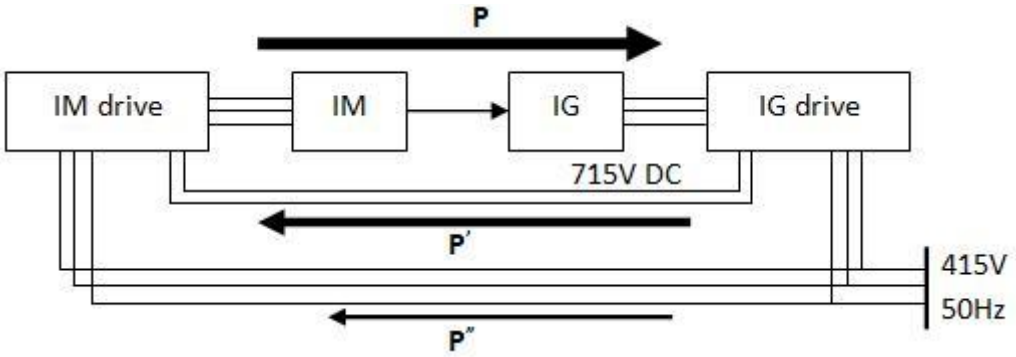

Figure 3.2. Electrical connections between the IM and IG drive.

As can be seen, power P is transferred from IM drive to IG drive through the IM and IG. Also, power $P^{'}$ is transferred from IG to IM drive through the DC link of 715V. During steady wind conditions, $P^{'} = P\text{-}ls$, where ls includes the mechanical and electrical losses of the machines and drives. Therefore, only a small amount of power $P^{''}$ is transferred from the electricity grid to IM drive. IG drive absorbs almost zero power from the grid.

Alternatively, the power can be sent back to the grid via an ALSPA MV3000E inverter, in order to simulate the electrical system of a VS WT. The inverter can be seen in Figure 3.3, placed inside a cubicle, with all the associated control circuits. At the bottom, an LCL filter can be seen, which was designed to suppress the high current harmonics due to the switching function of the MV3000E. Design details of the control circuits and the filter can be found in the Appendices A.6-7.

Figure 3.3. MV3000E (left), GD3000E (right).

The input to the HILS is a wind time series which can be obtained by the following ways:

a) Wind site-data obtained from RAL.

b) Wind time series produced using approaches based on the sampling of the Van der Hoven spectrum and the Von Karman wind turbulence model, as described in B.21 [41].
c) Voltage signal applied externally to one of the ADCs of dSPACE (i.e. for step-change response).

The full description and operation of the HILS (referred to as AC HILS) are presented in the next section.

3.4. Description and operation of the AC hardware-in-loop simulator

The AC HILS and a block diagram of its basic arrangement are shown in Figure 3.4(a) and (b) respectively, where it can be seen that it consists of the following parts:

1) PC (running MATLAB/Simulink)
2) dSPACE ds1103 (DSP + DAQ)
3) IM drive (Cegelec GD3000E)
4) IM (Rated at 3kW)
5) IG (Rated at 3kW)
6) IG drive (Cegelec GD3000E)

Figure 3.4(a). Wind turbine hardware-in-loop simulator.

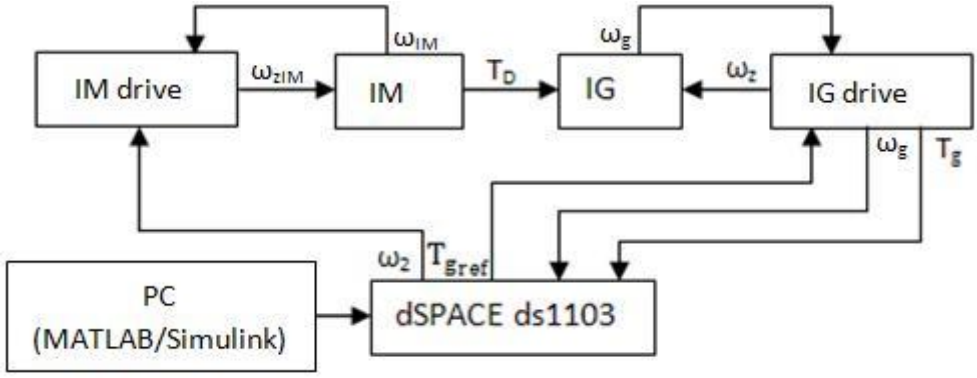

Figure 3.4(b). Block diagram of the HILS.

As can be seen from Figure 3.4(b) the speed of the IM and IG are provided to the IM and IG drives respectively from incremental encoders fitted to the NDE of the machines.

MATLAB/Simulink is used to develop the model of the simulated WT, as described in Chapter 2. This model includes the rotor and drive-train dynamics of the WT. The WT model is then converted into an executable C program, using the Real Time Workshop

(RTW) of MATLAB and it is automatically loaded on the dSPACE board, where it can run in real time.

dSPACE provides powerful data acquisition (DAQ), monitoring, managing and controlling of the HILS facilities in real time through the software environment ControlDesk. Figure 3.5 shows the data acquisition and control layout in ControlDesk, during a simulation of a VS SR WT. As can be seen, several displays and plotters can be added for real time monitoring and data acquisition, as well as knobs for altering parameters of the system during the simulation.

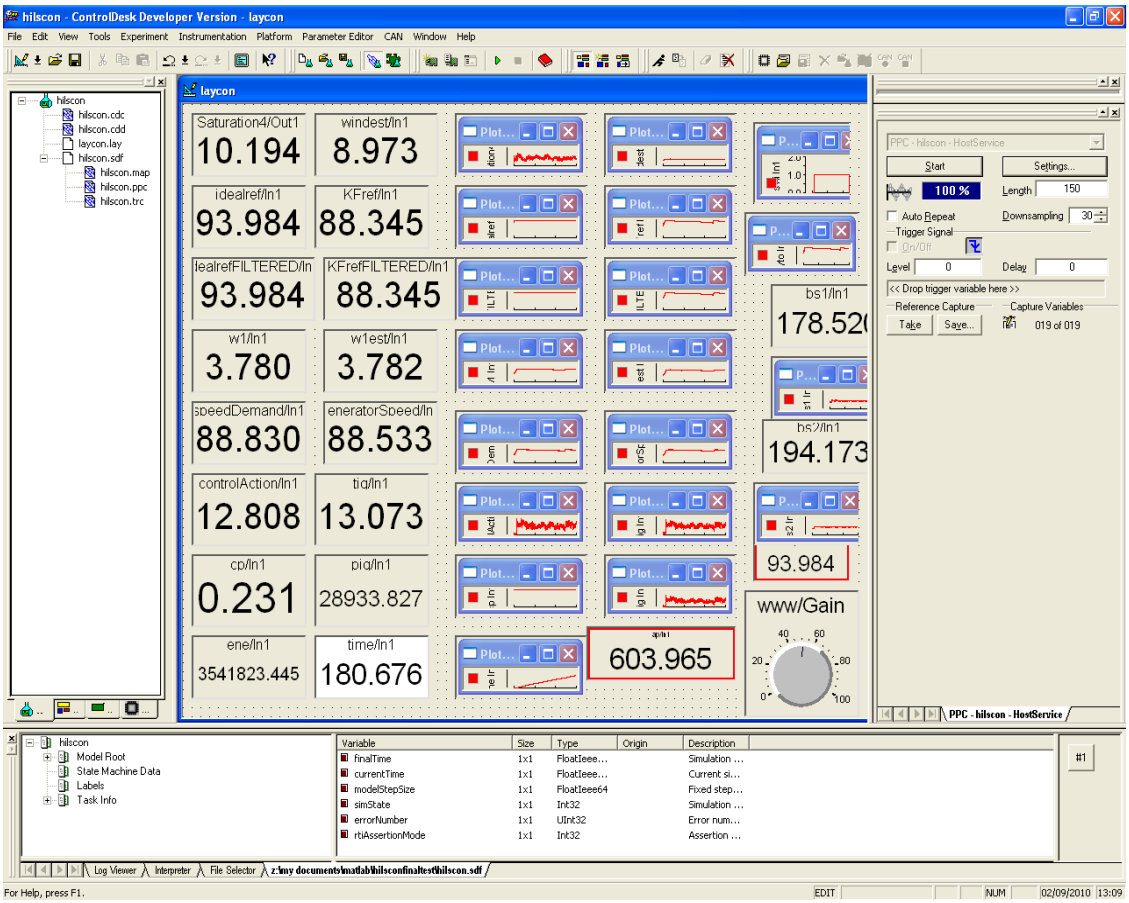

Figure 3.5. Experiment layout in ControlDesk, during a simulation of a VS SR WT in HILS.

3.4.1. Wind turbine simulation

Running on dSPACE, the model controls the speed of the IM, ω_{IM}, by continuously updating speed demands, ω_2, to the IM drive, which in turn drives the IM with stator currents of variable frequency ω_{zIM}.

The IM acts as the prime mover for the IG, which acts as the IG of the simulated WT. IG is controlled by the IG drive, with currents of variable frequency ω_z. The torque of IG, T_g, is estimated by the IG drive and is fed back to dSPACE, to close the simulation loop with the real time WT model.

3.4.2. Wind turbine control system simulation

Further to the described WT simulation loop, Figure 3.4(b) also shows a second simulation loop, through dSPACE, the command signal $T_{g_{ref}}$, which is the reference for the torque of the IG from the IG drive as well as the speed measurement ω_g. This part simulates the control system of the IG of the VS SR WT. The control system is implemented in real time in dSPACE and receives the speed measurement of the IG and continuously sends torque demands to the IG drive, as it is the case in an actual WT. It is mentioned that the control system can be of any choice. Sophisticated control systems such as described in later sections, use the IG torque estimate T_g too.

3.4.3. Real time models

Figure 3.6 shows the real time models that are used for the HILS and their interconnections with the hardware parts, in order to form the WT and control system simulation loops. As can be seen, both simulation loops have been developed in the same Simulink file and run simultaneously but independent of each other, in dSPACE.

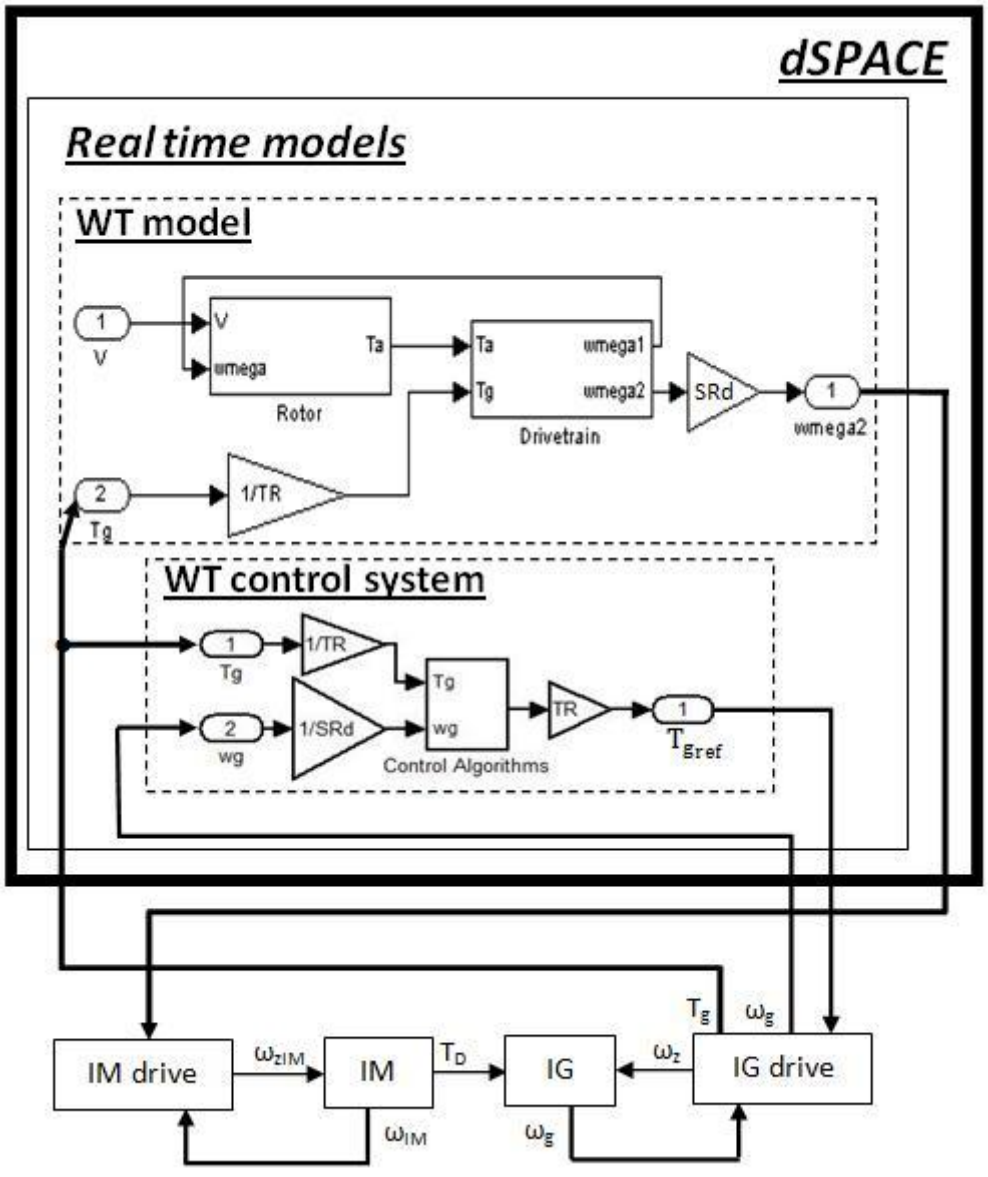

Figure 3.6. Real time models of HILS and interconnections with the hardware.

The "Rotor" and "Drivetrain" models of the WT model are given in Figures 3.7 and 3.8 respectively, while the control algorithms are described in the next chapters. Details for the WT models can be found in Chapter 2.

Furthermore, in Figure 3.6 it can be seen that $T_{g_{ref}}$ is first scaled down by a Torque Reduction (TR) factor, TR<1, in order to accommodate the low rated IG. T_g, in turn, is scaled up to the initial level with a "1/TR" factor, to comply with the requirements of Simulink models of the WT and WT control system. Also, the speed demand to the IM drive, can be scaled up/down using a factor SRd (Speed Reduction). The IG speed, ω_g then is scaled down/up with a "1/SRd" factor, to comply with the requirements of the Simulink model of the WT control system.

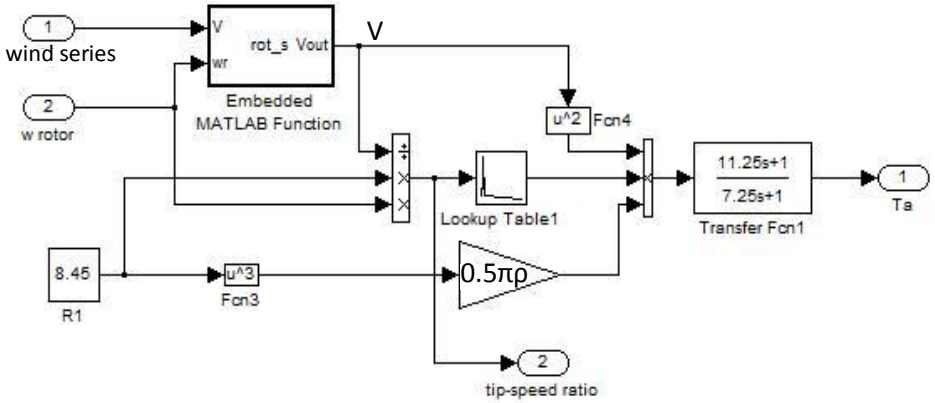

Figure 3.7. Rotor dynamics.

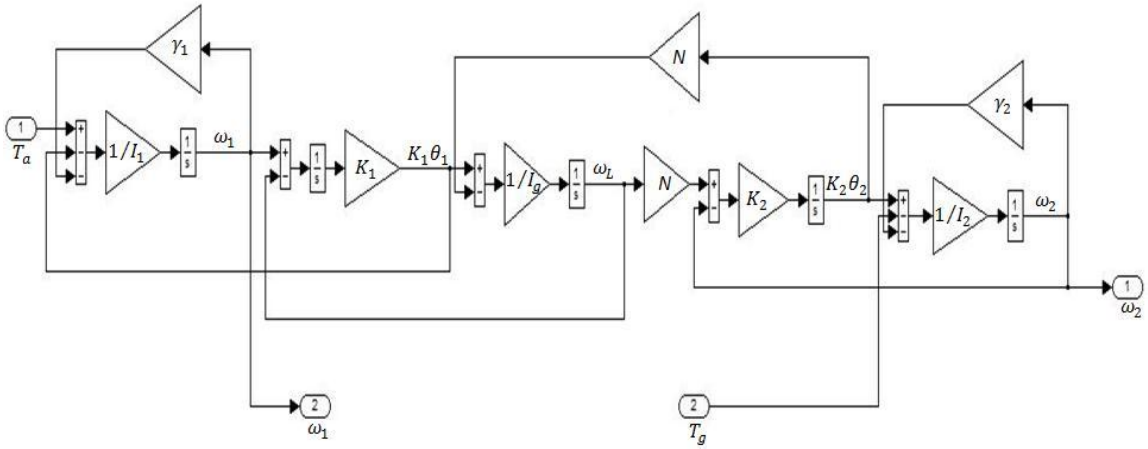

Figure 3.8. Drivetrain dynamics.

3.5. Dynamics of the hardware in the loop simulator

For a successful implementation of the HILS, the transfer function $G_{T_{g_{ref}}\omega g}$ from $T_{g_{ref}}$ to ω_g that the WT control system sees in the HILS, should be the same as the one that would be seen in the actual WT (for more detail on this transfer function see Chapter 2). Therefore, the $G_{T_{g_{ref}}\omega g}$ of the HILS, obtained experimentally using a signal analyzer (Appendix A.8) is compared with the theoretical one obtained by the linearized WT dynamic model of Eqns. (2.28-34). The transfer functions are evaluated for an arbitrary operating point of the WT: (ω_1,V) = (4rad/sec, 6.76m/sec). For this operating point λ=5, which is the optimum tip-speed ratio for the simulated WT. It is noted that the conclusions regarding the dynamic behavior of the HILS for that operating point can be generalized for any operating point in below and above rated operating region.

Figure 3.9 shows the experimental measurement of $G_{T_{g_{ref}}\omega g}$, for frequencies 250mHz (1.57rad/sec) to 100Hz (628.3rad/sec) in closed loop measurement.

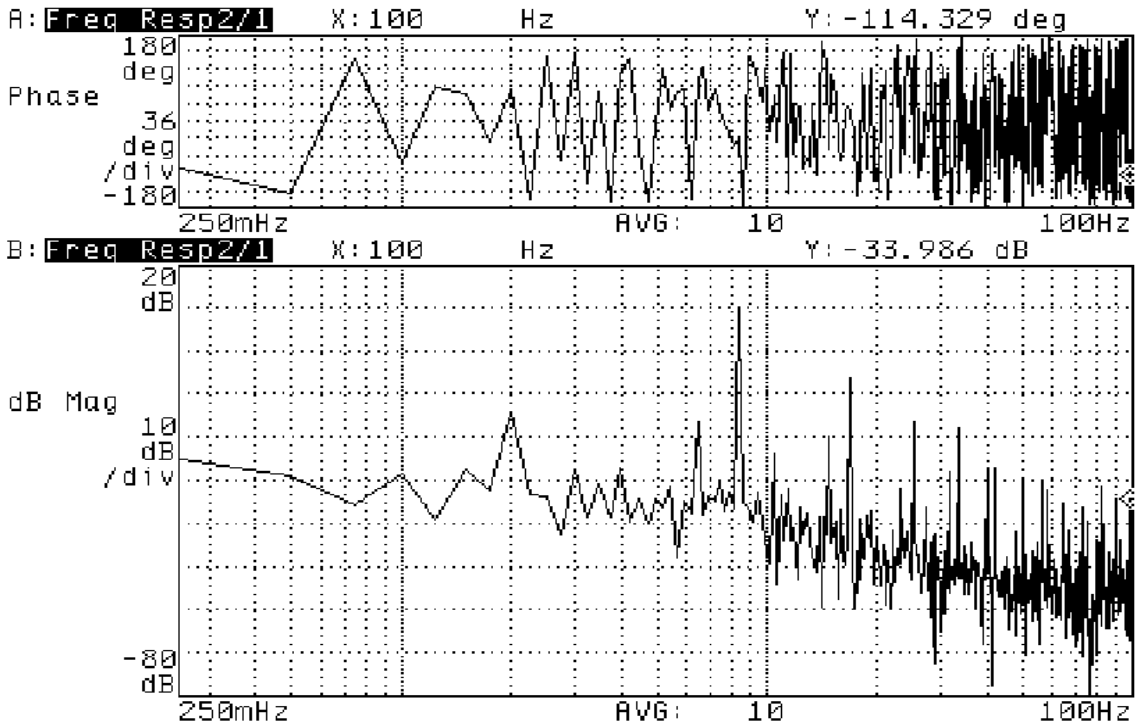

Figure 3.9. Experimental $G_{T_{g_{ref}}\omega g}$ of the HILS.

The Bode plot of the theoretical $G_{T_{g_{ref}}\omega g}$ is shown in Figure 3.10. The frequency region in rad/sec between the vertical bold lines in Figure 3.10 corresponds to the frequency window (Hz) of Figure 3.9.

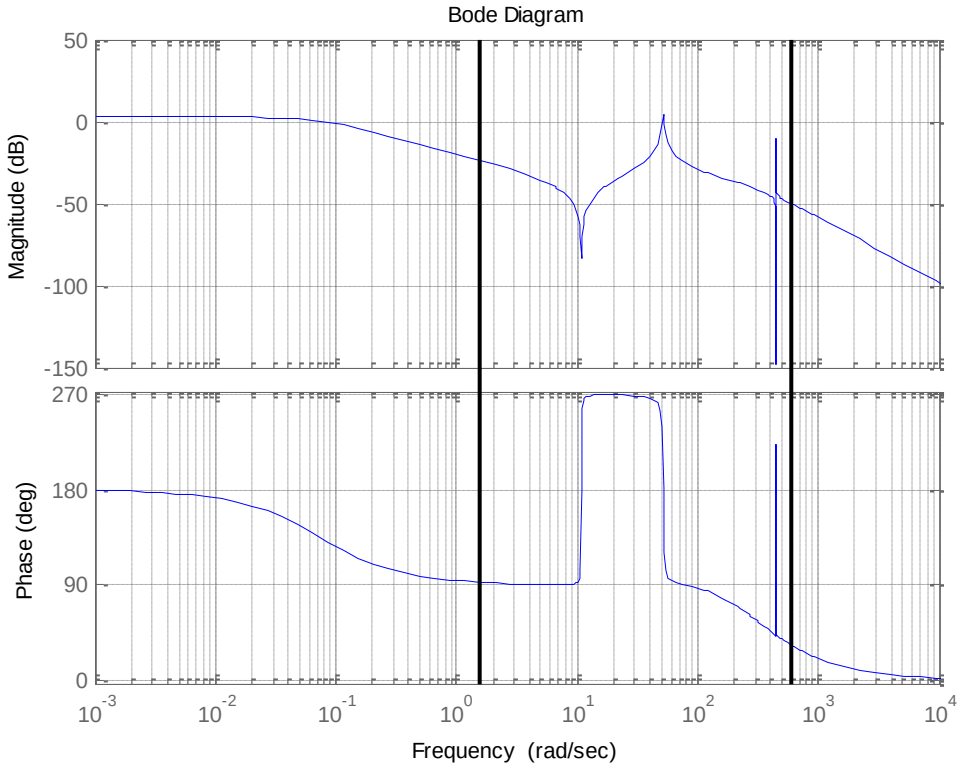

Figure 3.10. Theoretical $G_{T_{g_{ref}}\omega g}$ of the WT model.

By comparing Figures 3.9 and 3.10 it can be observed that the experimental graph retains the main features of $G_{T_{g_{ref}}\omega g}$ (level of -20dbs at 250mHz, peak at around 8Hz). However, as Figure 3.9 was from a closed loop measurement, no real significance can be attributed to it. The attenuation of -60dbs at 100Hz indicates that the experimental graph is quite close to the theoretical one, which for the same frequency exhibits an attenuation of -50Hz. It is mentioned that in Figure 3.9, the 2nd and 3rd harmonics of the component of 8Hz can be also observed, which possibly are result of the nonlinearities of the WT rotor (these are not represented in the linearized theoretical model of Figure 3.10, see Section 2.5.2) or of the nonlinearities of the hardware.

Regarding the phase plots, it seems that there are considerable differences from the theoretical plot. These differences are inevitable and are due to the presence of the IM and IM drive, which in any case introduce additional dynamics to the simulated drivetrain. Although these discrepancies between the models did not cause instability, as it was the case with the HILS with belt drive coupling, they are expected to affect the performance of the control algorithms to be tested. Thus, understanding of their effect is necessary and this is described in the next chapters.

3.6. Conclusion

In this chapter the development of HILS for VS SR WTs was presented. The aim of the development was to represent as close as possible the dynamics of any simulated VS SR WT for control testing purposes. Two test rigs were analyzed, in order to examine their suitability for the HILS and the dynamic analysis and compensation techniques that were presented are novel in the area of HILS design for VS SR WTs.

In general, it is quite a challenging task to develop a HILS that absolutely represents the simulated VS SR WT dynamics. Specifically, the HILS hardware adds extra poles on the simulated dynamic system. Thus, ideally the HILS should be designed such that these poles are first of all stable and also not in dominant frequencies, i.e. within the control bandwidth of the simulated WT.

Although the final design that was presented in this chapter seemed to exhibit some differences from the ideal dynamics of the simulated wind turbine, in general it satisfies its objectives for the purpose of this research. In the following chapters, where hardware simulation results from the developed control systems are presented, the influence of the HILS hardware will be identified and further discussed.

4. Adaptive aerodynamic torque estimation

4.1. Introduction

As mentioned in Section 1.6, the proposed control method is based on the speed control of the IG of the WT with the speed reference for the controller to be based on the estimated effective wind speed, $\hat{V}$ and aerodynamic torque, $\hat{T}_a$. Specifically, $\hat{T}_a$ is used to obtain the aerodynamic power $\hat{P}_a = \hat{T}_a\hat{\omega}$, where $\hat{\omega}$ is the rotor speed estimated by the Adaptive Kalman Filter (AKF).

The structure of the proposed control scheme is shown in Figure 4.1 inside the dashed frame, consisting from an AKF, a NR routine, a speed reference ω_{ref} determination routine and a speed controller.

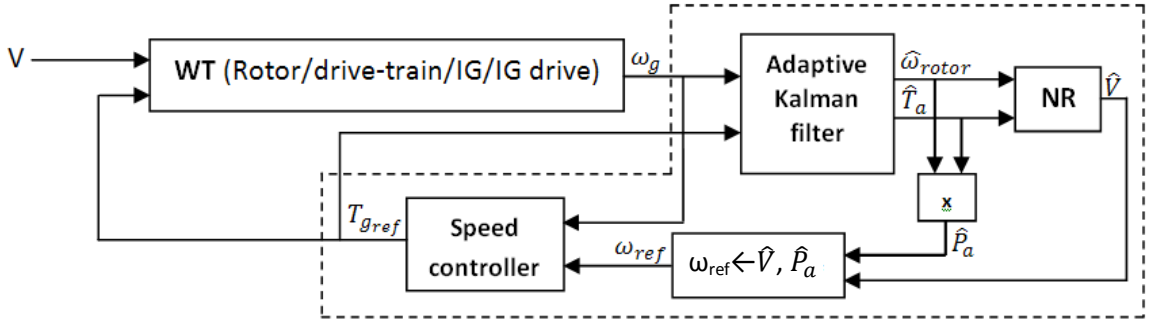

Figure 4.1. Proposed control scheme for a VS SR WT.

The advantage of using the AKF instead of a KF is that the first can provide $\hat{T}_a$ estimates of high accuracy for arbitrary wind conditions and/or measurement noise, so the problem of initial selection of the noise covariance matrices in the KF algorithm is eliminated, as it will be seen in the following sections. In addition, the $\hat{P}_a$ estimate is used in order to determine ω_{ref} in deep stall operation, via power regulation algorithms

that enable power control to any desirable level P_L, with $P_{\omega_N}<P_L<P_N$, where P_{ω_N} is the maximum power when operating at ω_N (obtained when $V=V_{\omega_N}$). Such a control scheme has not previously been proposed or implemented in hardware in HILS.

The selected values of the parameters of Figure 1.9 are listed in Table 4.1.

ω_N (ω_N*N at the HSS)	4rad/sec (4*39.16rad/sec)
V_{ω_N}	6.76m/sec
P_N	25kW
V_N	9.3m/sec
T_N	160Nm

Table 4.1. Operating point locus parameters (see Figure 1.9).

In the following sections, the proposed AKFs are described, while V and ω_{ref} estimation as well as power regulation methods, are described in Chapter 5.

4.2. Kalman filtering

The discrete KF is a recursive discrete time algorithm, which provides state estimates of linear dynamic systems subjected to random perturbations, such as disturbances. The KF is the optimum linear recursive state estimator, because it provides state estimates with the minimum possible error variance [60]. The operation of the KF is described in the following paragraphs.

Eqns. (4.1-2) comprise a discrete time dynamic system:

$$x_{k+1} = \Phi x_k + \Gamma u_k + w_k, \quad (4.1)$$

$$z_{k+1} = H x_{k+1} + n_{k+1}, \quad (4.2)$$

where $k=t/T_s$, with t the continuous time scale and T_s(sec) the sampling time of the system. In Eqns. (4.1-2) $x \epsilon R^n$ is the state vector, $u \epsilon R^m$ the input vector, $z \epsilon R^r$ is the measurement vector, $w \epsilon R^n$ a white noise sequence, which models a fictitious process noise reflecting the modeling uncertainties in Eqn. (4.1) and $n \epsilon R^r$ is the measurement noise, a white noise sequence representing the noise due to the sensor and quantization of the data acquisition system. These noise sequences are assumed to be independent of each other, which is reasonably valid for a WT, and have normal probability distributions [61]:

$$p(w) \sim N(0, Q), \tag{4.3}$$

$$p(n) \sim N(0, R), \tag{4.4}$$

where $Q \epsilon R^{n \times n}$ and R $\epsilon R^{r \times r}$ are unknown and possibly changeable over time.

The KF receives as inputs the input vector, u of the dynamic system and the noisy measurement vector, z of some of its states and produces an estimate for all of the states of Eqn. (4.1).

The algorithm is structured in a prediction & update scheme according to the following equations:

Predict:

$$\hat{x}_{k+1|k} = \Phi \, \hat{x}_{k|k} + \Gamma u_k, \tag{4.5}$$

$$\hat{P}_{k+1|k} = \Phi \, \hat{P}_{k|k} \Phi^T + Q_k, \tag{4.6}$$

Update:

$$\hat{x}_{k+1|k+1} = \Phi \, \hat{x}_{k+1|k} + K_{k+1}(z_{k+1} - H \, \hat{x}_{k+1|k}), \tag{4.7}$$

$$\hat{P}_{k+1|k+1} = \Phi(I - K_{k+1} H) \, \hat{P}_{k+1|k}, \tag{4.8}$$

$$K_{k+1} = \hat{P}_{k+1|k} H^T (H \hat{P}_{k+1|k} H^T + R)^{-1}, \qquad (4.9)$$

where $\hat{x}_{k+1|k}$, $\hat{P}_{k+1|k}$ and $\hat{x}_{k+1|k+1}$, $\hat{P}_{k+1|k+1}$ are the a-priori and a-posteriori state vector and state estimation error covariance respectively, while K_{k+1} is the Kalman gain, which is updated in every cycle.

During the operation of the algorithm, the Kalman gain soon converges to a steady state value, which can therefore be calculated offline [60]. However, when the KF is enhanced with adaptive routines, online adjustment of K_{k+1} is required.

At the prediction step, the estimated value $\hat{x}_{k|k}$, which is the mean of the true state vector at time *k*, is dynamically projected forward at time *k+1* to produce $\hat{x}_{k+1|k}$.

At the update step, the mean $\hat{x}_{k+1|k}$ is corrected subject to the measurement z_{k+1} to give the a-posteriori mean $\hat{x}_{k+1|k+1}$.

The same mechanism holds for the propagation of the covariance $\widehat{P}$ of the true state x around its mean $\hat{x}$.

As can be seen from Eqns. (4.5-9) the KF in principle contains a copy of the applied dynamic system, the state vector of which, $\hat{x}_k$ is corrected at every update step by the correcting term $K_{k+1}(z_{k+1} - H \hat{x}_{k+1|k})$ of Eqn. (4.7). The expression inside the parenthesis is called the Innovation sequence of the KF:

$$r_k = z_{k+1} - H \hat{x}_{k+1|k}, \qquad (4.10)$$

which is equal to the estimation error at every time step. When the KF state estimate is optimum, r_k is a white noise sequence [60].

4.3. Stability of a closed loop control system with a Kalman filter

Stability of a closed control system incorporating KFs in feedback is guaranteed by the "Separation theorem," expressed for the case of LQG controllers, which states that the closed loop is stable provided that the controller and the KF are stable [27]. It is mentioned here, that the Separation theorem also applies to the proposed control scheme, since the KF and the controller are connected in a similar arrangement to that of an LQG controller (Details about LQG can be found in [27]). In addition, in [61] it is stated that the KF is stable, when the used dynamic model is stable, which is the case for the present application. Furthermore, for AKFs, the adaptive algorithms should guarantee stable operation of the AKF, which was also the case, as this was observed through several hardware simulations. Therefore, the stability of the whole control scheme is guaranteed.

4.4. Aerodynamic torque estimation using Kalman filtering.

In order to estimate T_a using a Kalman filter, this has to be augmented into the state vector of the WT dynamic model [22, 35]. This can be performed using the random walk process model [22, 35, 62]:

$$\dot{T}_a = m, \tag{4.11}$$

and in discrete form:

$$T_{a_{k+1}} = T_{a_k} + w_k, \tag{4.12}$$

where m is a white noise sequence with intensity S_0 and w_k is a band limited white noise process with intensity:

$$Q_w = S_0 * T_s \tag{4.13}$$

The dynamic model used in the KF is that of Eqns. (2.4-8). Therefore, the KF receives as inputs the generator torque, T_g, which can be obtained by the IG drive and the generator speed measurement, ω_g. It is also mentioned that T_g can be replaced by $T_{g_{ref}}$, since due to the fast dynamic response of the IG drive, no difference is observed between $T_{g_{ref}}$ and T_g within the WT control bandwidth (BW<10rad/sec) and this may be useful in practice, because the signal $T_{g_{ref}}$ is not corrupted by additional measurement noise (it only contains measurement noise due to ω_g, which in any case is filtered by the speed controller). In addition, $T_{g_{ref}}$ is clean of harmonics of the switching frequency of the IG drive, which can impact the quality of $\hat{T}_a$. More details on the augmented dynamic model can be found in Appendix A.9.

In the following, when referring to Q, the variance Q_w is always implied, while when referring to the full process noise covariance matrix Q of Eqn. (4.6), this will be clarified.

4.5. Software testing of Kalman filters

Before being applied in the HILS, the designed KFs were tested in Simulink using the model of Figure 4.2 in closed loop, through the NR and the speed controller or with alternative torque control inputs to the WT through the switches 1 and 2.

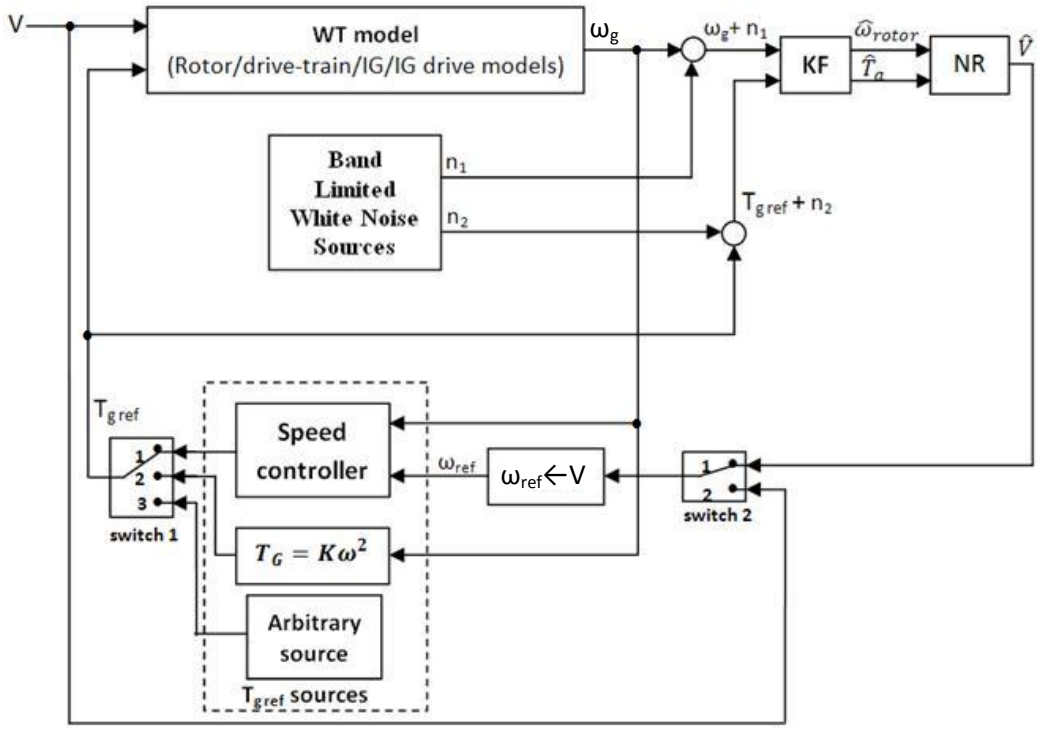

Figure 4.2. Model for KF testing.

The WT model used has been described in Chapter 2 (Section 2.6), while the other blocks are described in the following sections. As wind speed inputs, wind site data obtained from RAL, as shown in Figure 4.3(a) or simulated wind using filtered white noise, as shown in Figure 4.3 (b), were used. Also, in the model of Figure 4.2 white noise sources have been included, in order to simulate the presence of measurement noise at the links between the WT model and the control system.

In order to evaluate the performance of the KFs a comparison between the actual state values of the WT model and the estimated ones was performed, while emphasis was put on the $\hat{T}_a$ estimate, because the estimation of the rest of the states was always very accurate, since no uncertainty is involved (the vector ξ of Eqn. (A.9.5) has only one no zero element, corresponding to T_a).

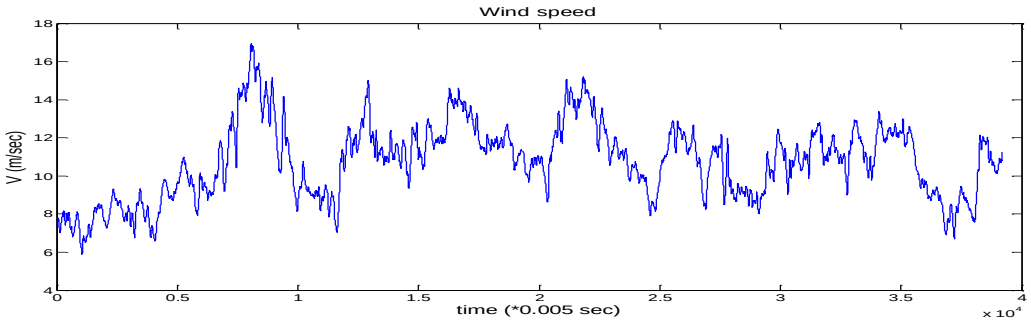

Figure 4.3. (a) Wind speed site data series from RAL (Duration of 196sec).

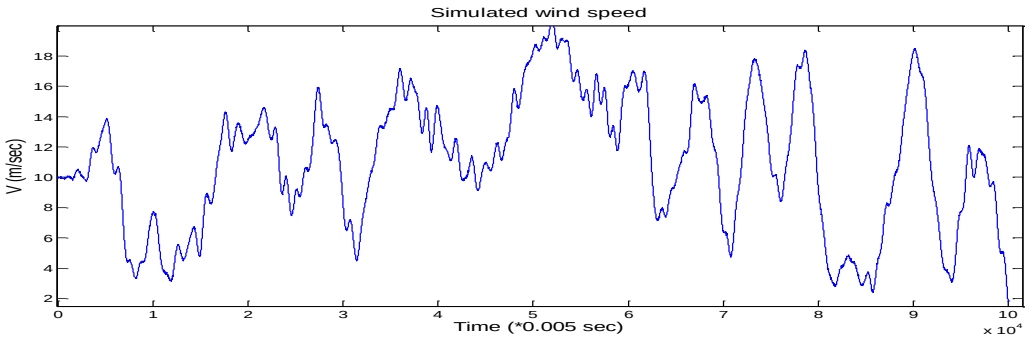

Figure 4.3. (b) Simulated wind series (Duration of 500sec).

Figure 4.4 shows T_a and $\hat{T}_a$ obtained by a KF with Q=100(Nm)^2 and R=0.01(rad/sec)^2, where Q is the process noise variance of Eqn. (4.13) and R the measurement noise variance, seen in Eqn. (4.9).

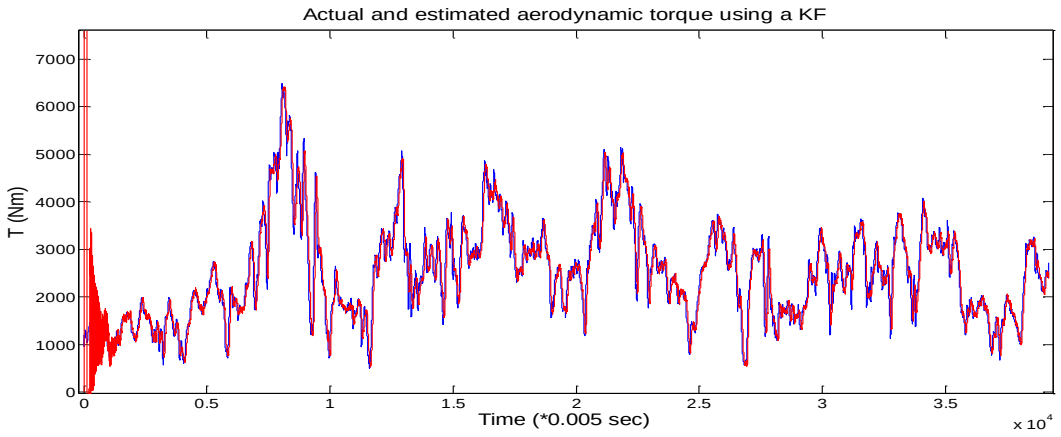

Figure 4.4. T_a (blue) and $\hat{T}_a$ (red) using a KF.

As can be seen, a KF can produce a very accurate $\hat{T}_a$ estimate, providing that Q and R are known. The transient in $\hat{T}_a$ observed at the first seconds of the simulation is

expected and it is due to the time required for the Kalman gain to settle to its optimum value. Through simulations it was shown that this transient dies out very quickly and that the settling time is almost invariant with the starting conditions of the KF i.e. initial choices of $\hat{x}_{k|k}$ and $\hat{P}_{k|k}$ in Eqns. (4.5-6)). In [60], methods for selecting appropriate initial conditions that ensure fast convergence can be found, but here this was not considered essential for the WT application.

4.6. Hardware testing of Kalman filters

4.6.1. Introduction

The demonstration of the KF performance in the HILS is now described. The discrete time KF algorithm has been implemented in Simulink using an "Embedded Matlab function" block, which has been programmed using M-code and runs in real time on dSPACE, as part of the "WT control system" in Figure 3.6. The sampling time of the KF is T_s=5msec and the following settings have been used: Q=100(Nm)^2 and R=0.001(rad/sec)^2. For the simulation, an external random voltage signal was used as effective wind speed V. Also, it should be mentioned that at this stage the KF was not used for closed loop speed control of the WT (The actual V was used for this purpose).

Figure 4.5 (a) shows the wind signal V and (b) the actual and estimated T_a.

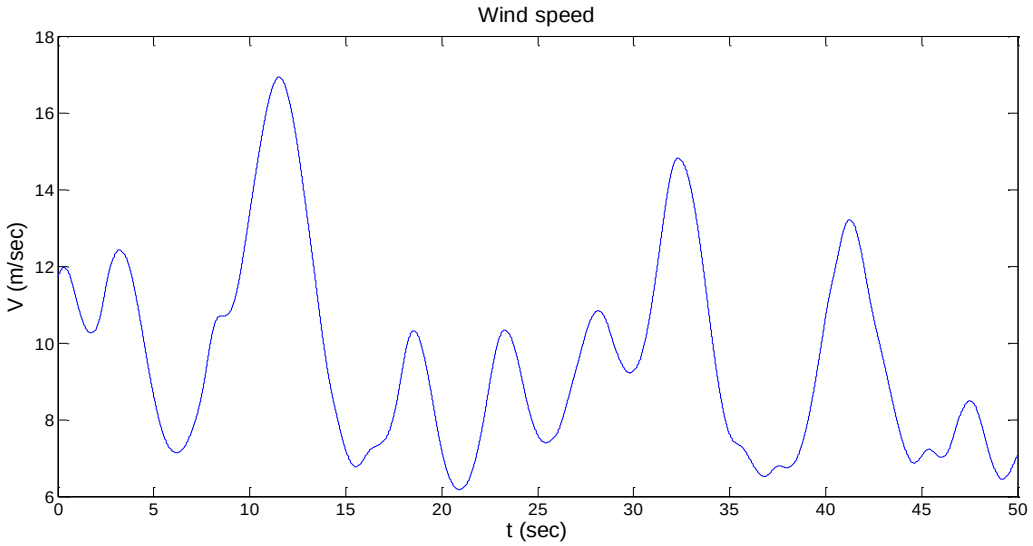

Figure 4.5 (a). Wind speed

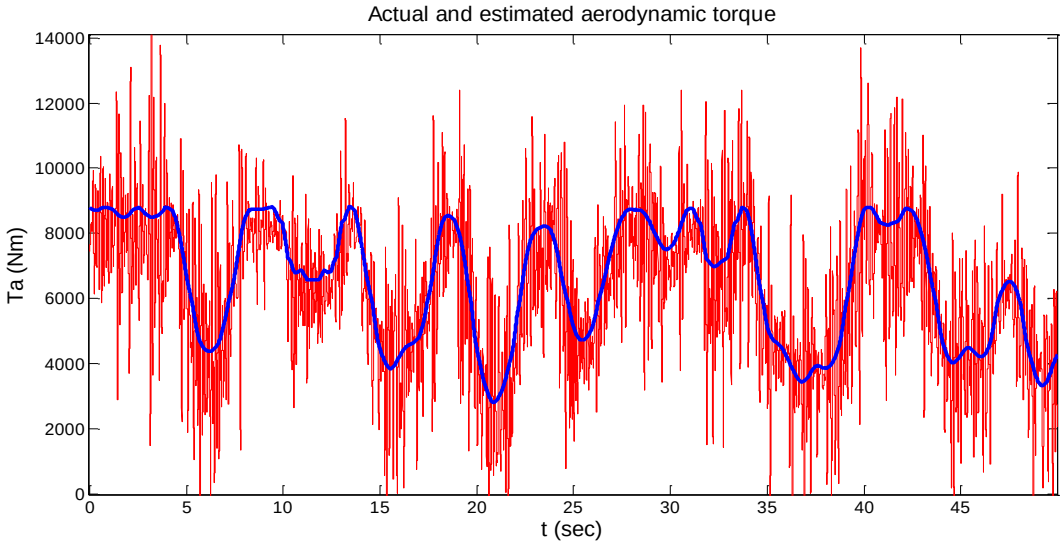

Figure 4.5 (b). T_a (blue) and $\hat{T}_a$ (red).

As can be seen, $\hat{T}_a$ is very noisy and this was due to the arbitrary choice of R, since the ω_g measurement contained considerable amount of noise and also due to the noise in $T_{g_{ref}}$ ($T_{g_{ref}}$ contains ω_g measurement noise, as this is propagated through the speed controller).

4.6.2. Measurement noise elimination through filtering

It is mentioned that in general, noise in the input vector u (see Eqns. (4.5)) cannot be eliminated by the KF and therefore it has to be eliminated using Low Pass Filters (LPF). Figure 4.6 shows another simulation, where an improved $\hat{T}_a$ estimate was obtained, after $T_{g_{ref}}$ was filtered (a discrete Moving Average (MA) filter of length L=100samples was used). However, a small time delay is introduced, due to the MA filter. In general minimum delay can be achieved with the use of dedicated IIR filters.

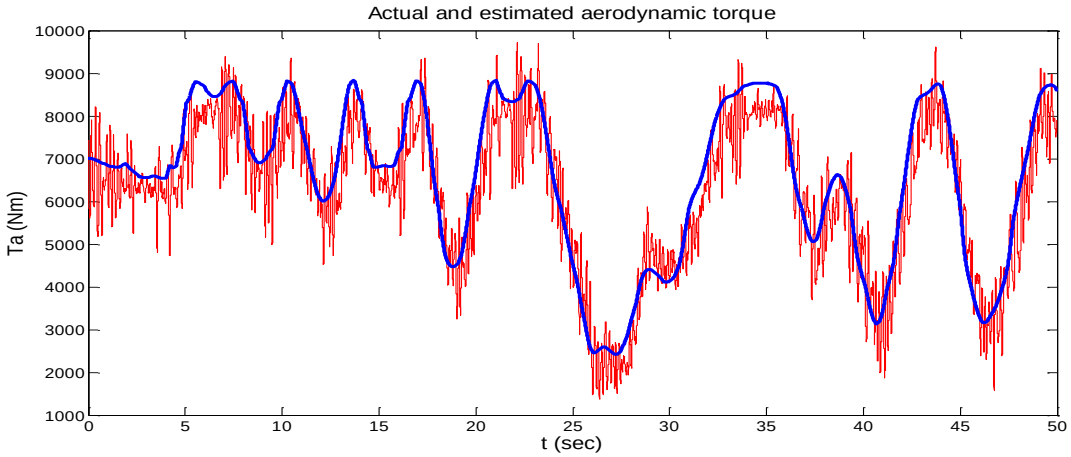

Figure 4.6. T_a (blue) and $\hat{T}_a$ (red) with filtered $T_{g_{ref}}$.

The remaining amount of noise in Figure 4.6 was effectively eliminated using the same MA filter at the ω_g input. Figure 4.7 shows the result of another simulation using this MA filter.

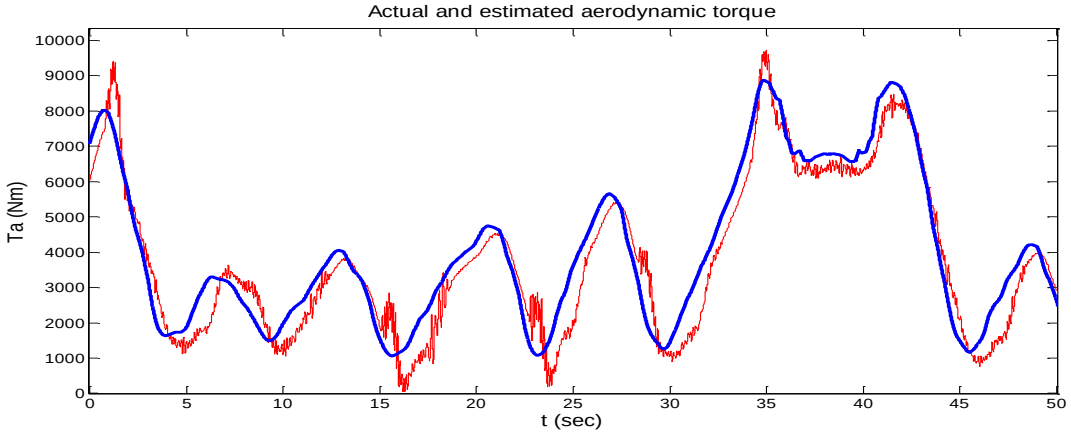

Figure 4.7. T_a (blue) and $\hat{T}_a$ (red) with filtered $T_{g_{ref}}$ and ω_g.

4.6.3. Speed measurement noise elimination through adaptation

The general problem of a state measurement z_k corrupted with uncorrelated noise of unknown or even time varying intensity R has been discussed in the literature [60, 63-65], where adaptive R estimation methods are proposed, in order to maintain optimum operation of the KF. Here, two R adaptive methods, found in [60] and [63, 64], have been implemented. Figure 4.8 (a) shows the obtained $\hat{T}_a$ using these routines (the MA noise filter in ω_g has been removed) and Figure 4.8 (b) shows the estimated R over time. Further details of the used methods can be found in Appendix A.11.

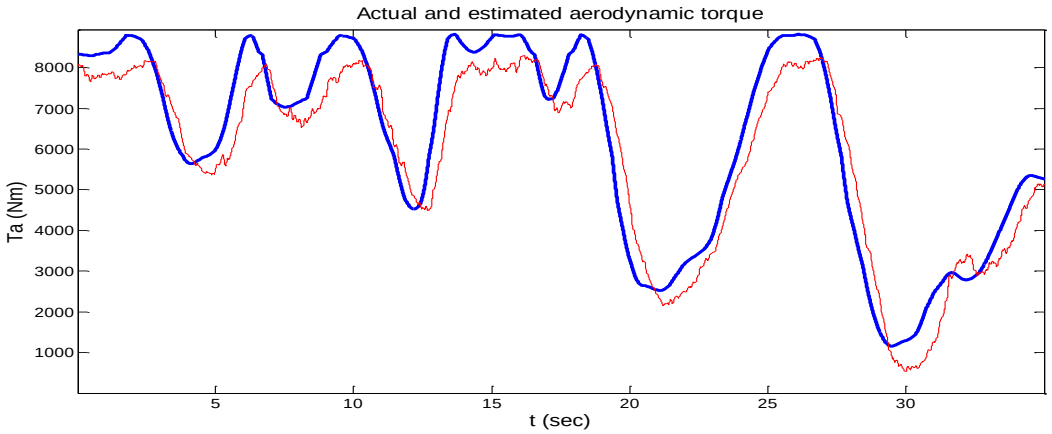

Figure 4.8(a). T_a (blue) and $\hat{T}_a$ (red) with filtered $T_{g_{ref}}$ and adaptation in noise intensity for ω_g.

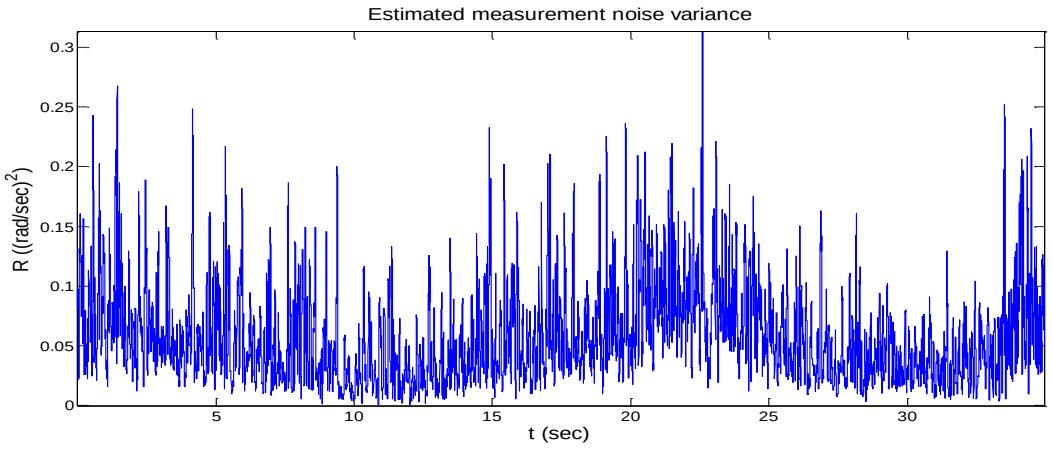

Figure 4.8 (b). $\hat{R}$ estimate.

As can be seen from Figure 4.8 (a) the R adaptation more effectively cancels the measurement noise. The $\hat{R}$ estimate shown in Figure 4.8 (b) is in average consistent

with the actual *R*, computed offline from ω_g samples, while the observed variation is due to mismatch between the KF dynamic model and the actual dynamic model including the HILS dynamics. Such a mismatch can happen when unknown dominant modes of the system are not included in the dynamic model of the KF and this seems to be the case with the HILS, as this was observed from the differences in the phase plots of Figures 3.9 and 3.10. This modelling mismatch is also the cause of a constant difference between T_a and $\hat{T}_a$, which can be observed in Figure 4.8(a).

Finally, the KF algorithm was seen not to be affected by the different time delays between its inputs, $T_{g_{ref}}$ and ω_g, since the first is passed through an LPF.

4.7. Considerations about unknown or changeable process noise variance

So far *Q* has been assumed known. However, in practice this is unknown and due to the changeable wind statistics, it may vary considerably when considered in short time, due to the wind turbulence [44]. The effects of a fixed choice of *Q* are described here.

Figures 4.9 (a) and (b) show T_a and $\hat{T}_a$ obtained using the software model of Figure 4.2, when the conventional below rated quadratic control was applied ("switch1"=1 and "switch2"=2), for *Q* = 10, 100 and 1000 $(\text{Nm})^2$ and with fixed *R* =0.01 $(\text{rad/sec})^2$ and n_2=0.

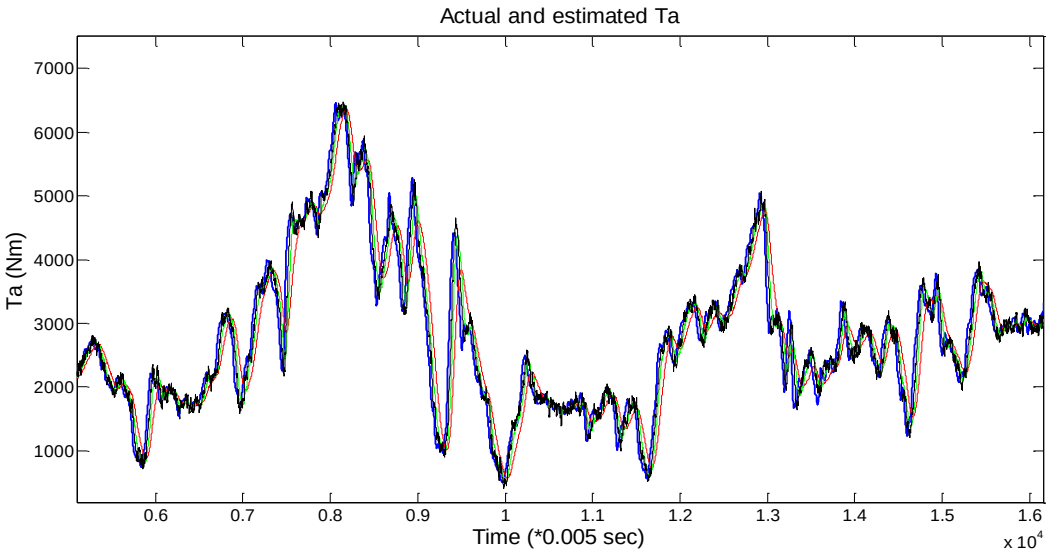

Figure 4.9. (a) T_a (blue) and $\hat{T}_a$ for Q=10 (red), 100 (green) and 1000 (black).

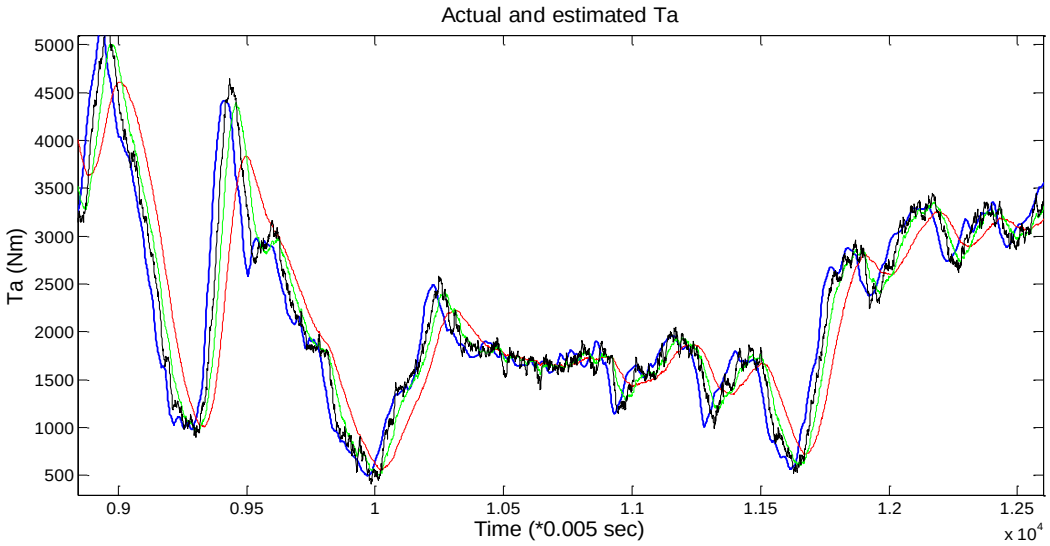

Figure 4.9. (b) Close-up view of Figure 4.9(a).

As can be seen, by gradually increasing Q, the model of Eqn. (4.12) assumes faster changes in T_a and therefore the time delay of the estimated waveform reduces. However, this causes the waveform to become noisier, when T_a does not exhibit appreciable changes.

In general, a fixed value for Q can be determined through simulations. However, there is no guarantee that the estimate will be valid under arbitrary wind conditions and therefore for a WT with wide variable speed operation and consequently wide torque

variations, more than one value of Q may be required. This can be seen by Figure 4.10 (a) and (b), where a fixed value of Q results to a very good $\hat{T}_a$ estimate for high wind speeds, but to a quite unacceptable one, when the wind speed is halved. For these results the wind series of Figure 4.3 (a) has been used and applied to a WT with a rotor of diameter 91.3m. Data of this WT was found in [66] and is shown in Table 4.2, on the next page. Since the characteristics of the shafts are not given, a simplified dynamic model of this WT was used, with a single dynamic equation, of the rotor dynamics.

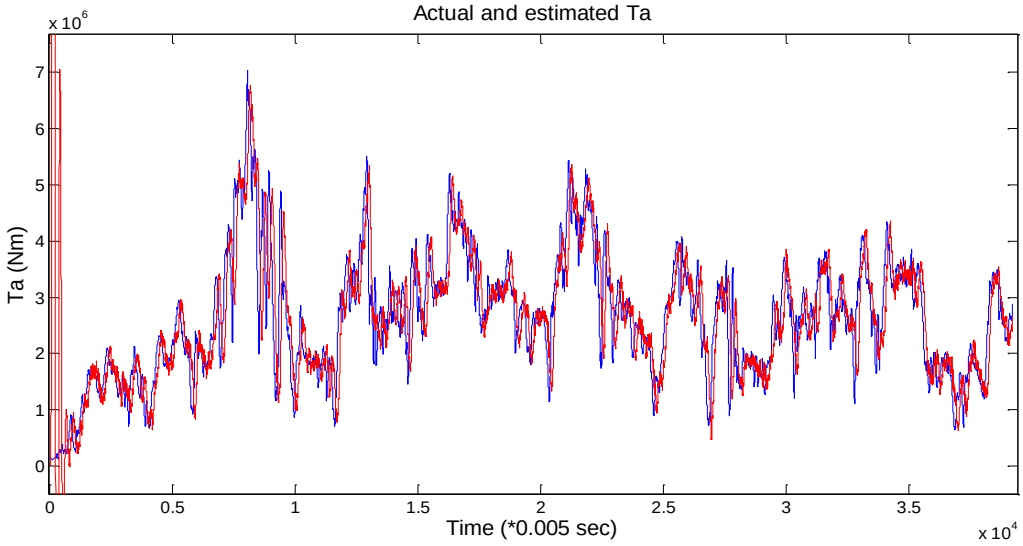

Figure 4.10 (a). T_a (blue) and $\hat{T}_a$ (red) for high wind speeds.

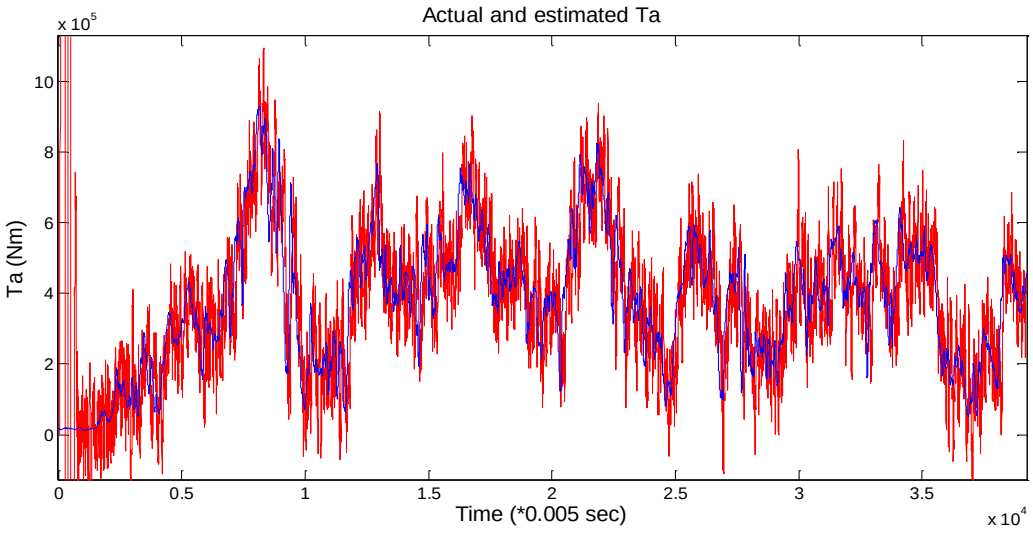

Figure 4.10 (b). T_a (blue) and $\hat{T}_a$ (red) for low wind speeds.

3MW Wind turbine characteristics	
Rotor diameter	91.3m
Rotor moment of inertia	12.6×10^6 Kgm^2
Generator moment of inertia	239 Kgm^2
Rated wind speed	13m/sec

Table 4.2. Large scale WT data.

Although the $\hat{T}_a$ estimate can be improved using LPFs, it was considered worthwhile to investigate alternative methods using AKFs, which do not introduce extra time delay as the LPFs. As it will be seen next, these methods can either provide a number of different fixed choices for *Q* and a dedicated algorithm selects the appropriate one each time, or they continuously adapt to the changeable *Q* during the operation of the filter.

4.8. Adaptive Kalman filtering

AKF can be used to obtain accurate state estimates of dynamic systems when certain parameters are unknown or time varying. In this section the application of AKF in WTs for T_a estimation under changing process noise variance *Q* is described.

In the literature [67-75], two major methods of AKF have been found: (a) Multiple Model Adaptive Estimation methods (MMAE) and (b) Innovation Adaptive Estimation methods (IAE), where the first method is based on the use of a bank of KFs each one tuned to a certain parameter value, while the second is based on the continuous online tuning of a single KF depending on the properties of its innovations sequence, given in Eqn. (4.10). [67-75]

In the following sections the application and advantages of each method for T_a estimation are described.

4.8.1. Multiple Model Adaptive Estimation

4.8.1.1. Introduction [67-75]

The MMAE consists of a bank of KFs, running in parallel and each one designed for a specific value of the unknown model parameter θ. In the case of the WT application, $\theta \equiv Q$ and it is assumed that it is possible to determine Q_{min} and Q_{max} such that $Q_{min} < Q < Q_{max}$.

For the design of a MMAE system, a set of N distinct choices of θ is created, $\Theta = \{\theta_1, \theta_2, \dots, \theta_N\}$ and then N KFs, KF_i, i=1…N, are designed, such that KF_i gives an optimum estimate when $\theta = \theta_i$ and an acceptable estimate within a region $(\theta_{i_{min}}, \theta_{i_{max}}) = \{\theta_i \epsilon \mathbb{R} | \theta_{i_{min}} < \theta_i < \theta_{i_{max}}\}$. By increasing N, the estimation accuracy is improved since the regions $(\theta_{i_{min}}, \theta_{i_{max}})$ become smaller for each θ_i. However, the computation load increases too.

The algorithm determines which of the N KFs gives the best estimate at any time by using a hypothesis testing unit, often called Posterior Probability Evaluator (PPE).

PPE continuously evaluates the posterior probabilities $P_k(\theta_i) = P(\theta = \theta_i | z_k)$ of the hypothesis θ=θ_i given the current measurement z_k at every time step. The probabilities $P_k(\theta_i)$ are calculated recursively using the Bayes' rule with the following formula:

$$P(\theta_i)_k = \frac{p(z_k|\theta_i)P(\theta_i)_{k-1}}{\sum_{i=1}^{N}[p(z_k|\theta_i)P(\theta_i)_{k-1}]}, \qquad (4.14)$$

where the probability density function $p(z_k|\theta_i)$ is:

$$p(z_k|\hat{x}(\theta_i)_k) = \frac{1}{(2\pi)^{n/2}|S_{i_k}|^{1/2}} e^{-(\frac{1}{2})r_{i_k}^T S_{i_k}^{-1} r_{i_k}}, \qquad (4.15)$$

and the innovation sequence of every KF$_i$, r_{i_k} is:

$$r_{i_k} = z_k - C\hat{x}_{i_{k|k-1}}. \qquad (4.16)$$

$\hat{x}_{i_{k|k-1}}$ is the predicted state vector for every KF_i. Also, the predicted innovation covariance matrix $S_{i_k} \epsilon R^{nxn}$ for every KF_i is:

$$S_{i_k} = C P_{i_k}^{-} C^T + R_{i_k} \qquad (4.17)$$

where $P_{i_k}^{-} \equiv P_{i_{k|k-1}}$ and R_{i_k} is the measurement noise variance, which has been also assumed time-varying. (in practice this is the same for every KF, since the same measurement z_k is used by all the KF_i; therefore $R_{i_k} \equiv R_k$)

Finally, the state estimate at any time instant k is given by the weighted sum of all the estimates of the KFs with the appropriate $P(\theta_i)_k$:

$$\hat{x}_{k|k} = \sum_{i=1}^{N} [P(\theta_i)_k \, \hat{x}(\theta_i)_k] \qquad (4.18)$$

During the operation of the system, the probabilities $P(\theta_i)_k$ change values continuously depending on the innovation sequences of the KFs. During optimum operation of a KF, Eqn. (4.16) is a white noise sequence and its autocorrelation computed by its time samples is equal to the statistical one S_{i_k} as predicted by the KF, so Eqn. (4.15) results to a high probability (the exponential term becomes high), while during suboptimum operation of the KF, due to mismatch with the actual model, the mean value of Eqn. (4.16) deviates from zero (i.e. is not white noise any more), which results in a low probability in Eqn. (4.15), which assumes zero mean white noise. As can be seen by Eqn. (4.14) and (4.18), an estimate $\hat{x}(\theta_i)_k$ with a history of high $P(\theta_i)_k$ contributes more to the final estimate $\hat{x}_{k|k}$. During starting of the algorithm, the prior probabilities in Eqn. (4.14) are initialized as:

$$P(\theta_i)_0 = 1/N. \qquad (4.19)$$

The effectiveness of the MMAE algorithm has been demonstrated in [67-75], where more details about it can be found. Here, the MMAE has been successfully applied for

the aerodynamic torque estimation of a WT. In Figure 4.11 the implementation of the MMAE algorithm for the WT application is shown.

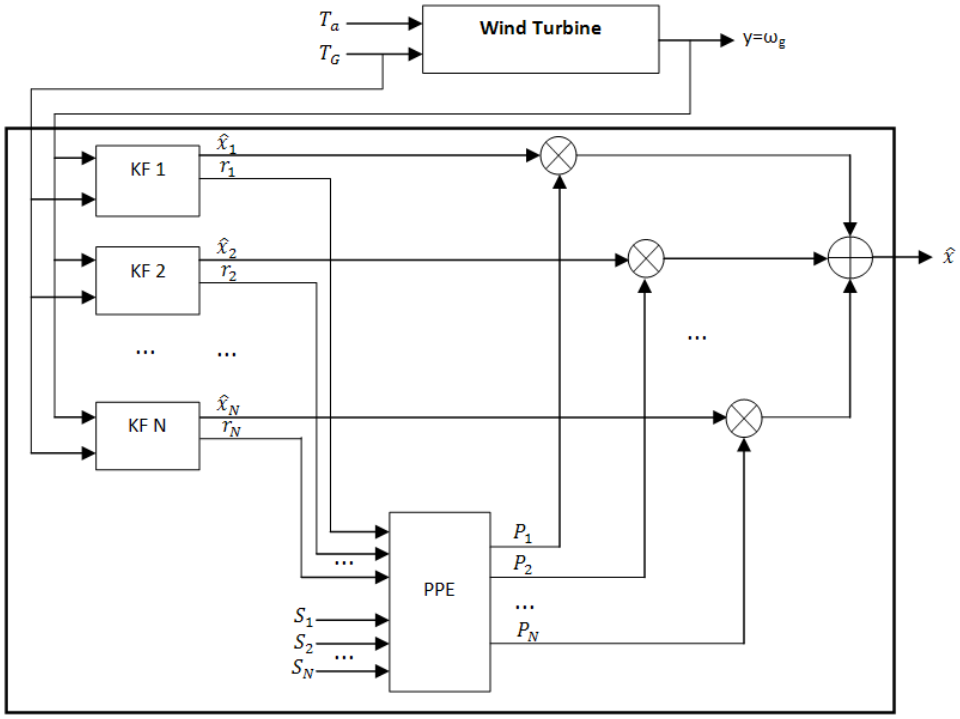

Figure 4.11. MMAE algorithm applied in a WT.

4.8.1.2.Software demonstration of MMAE performance for a 3MW wind turbine

Figures 4.12 (a) and (b) show T_a and $\hat{T}_a$ for the 3MW WT (see Table 4.2) obtained by the MMAE algorithm for low and high wind speeds respectively (compare with Figures 4.10). The MMAE consists of 5 KFs, designed for Q=9*10^6, 5*10^7, 10^8, 5*10^8 and 10^9 $(Nm)^2$.

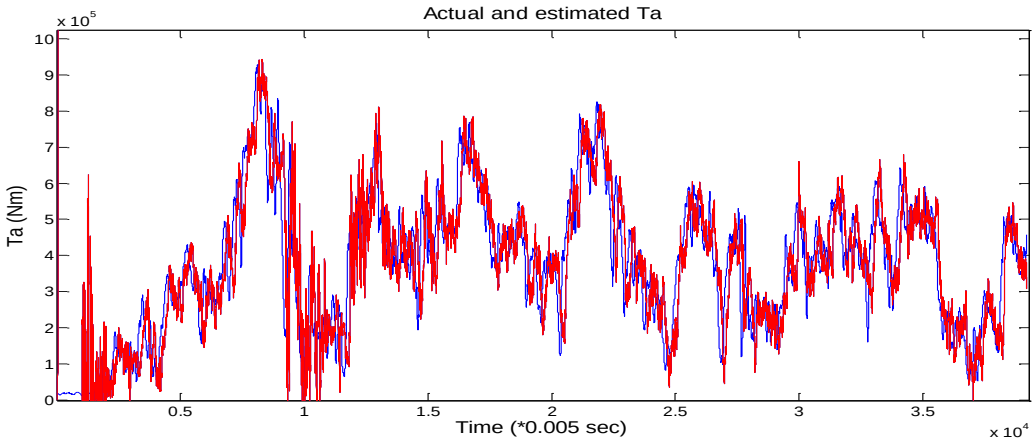

Figure 4.12(a). T_a (blue) and $\hat{T}_a$ (red) for low wind speeds using the MMAE algorithm.

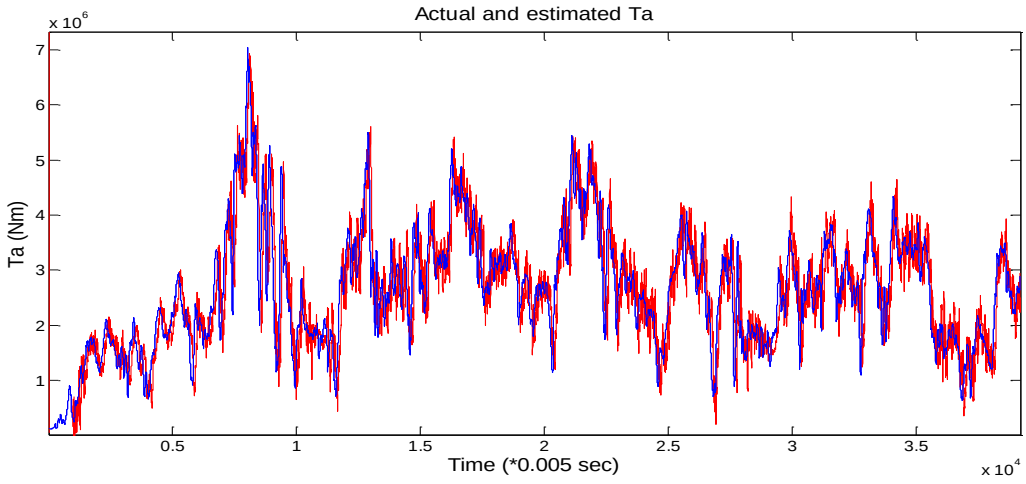

Figure 4.12(b). T_a (blue) and $\hat{T}_a$ (red) for high wind speeds using the MMAE algorithm.

Comparing Figures 4.12(a) with 4.10(b) a considerable improvement in $\hat{T}_a$ can be observed, when using the MMAE. Also, the $\hat{T}_a$ waveform of Figure 4.12 (b) in general exhibits a smaller time delay than the one of Figure 4.10 (b), as a result of the use of a KF with a higher Q=10^9(Nm)^2.

Figures 4.13 (a) and (b) show the probabilities $P(\theta_i)_k$ of Eqn. (4.14) for every KF for the two simulations above, respectively, where it can be seen that the MMAE switches between the different KFs depending on the statistics of the $\hat{T}_a$ estimate.

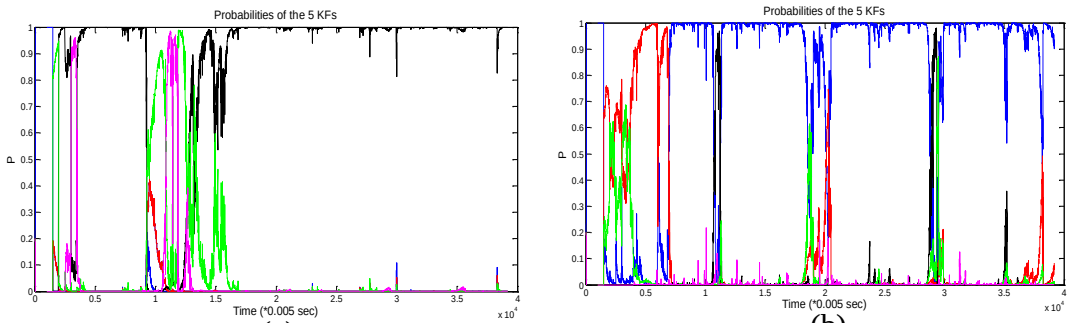

(a) (b)

Figure 4.13. Probabilities of the KF during the simulation for (a) low and (b) high wind speed respectively. (KF_1 - Q= $9*10^6$ (magenta), KF_2 - Q= $5*10^7$ (black), KF_3 - Q= 10^8 (red), KF_4 - Q= $5*10^8$ (green) and KF_5 - Q= 10^9 (blue).)

4.8.1.3. Important remark

In order for the MMAE algorithm to converge, ergodicity of Eqn. (4.16) of each KF on S_{i_k} is a prerequisite [61, 68]. Specifically, ergodicity refers to the consistency between the statistical autocovariance, S_{i_k} of the random variables r_{i_k} and the autocovariance $S_k^{'}$ computed from their time samples by:

$$S_k^{'} = \frac{1}{N-1}\sum_{j=k-N}^{k}\left(r_j - \overline{r}\right)\left(r_j - \overline{r}\right)^T, \qquad (4.20)$$

where

$$\overline{r} = \frac{1}{N}\sum_{j=k-N}^{k} r_j \ , \qquad (4.21)$$

and N is the number of samples considered (in Eqns. (4.20-21) the index i is dropped for simplicity).

Consistency between S_{i_k} and $S_{i_k}^{'}$ is important, since in Eqn. (4.15) S_{i_k} is used, but $P(\theta_i)_k$ are updated based on the time history of r_{i_k}. Also, consistency between S_{i_k} and $S_{i_k}^{'}$ ensures that each KFs works in steady state so their estimates can be used and furthermore suboptimum operation of the KFs can be effectively detected as described above.

During start-up of the algorithm, the violation of the above assumptions while the KFs settle causes r_{i_k} to take huge values and therefore $P(\theta_i)_k$ to take extremely low values, which resulted in the MMAE algorithm to crash due to overflow.

In order to avoid this undesirable behaviour in an actual system, a low threshold for $P(\theta_i)_k$ has been set (set to 10^{-5}). Alternative solutions that effectively worked are:

1) Continuous resetting of $P(\theta_i)_k = 1/N$ until the KFs have been settled.

2) Addition of white noise at the measurement z_k during start-up, in order to increase S_k through R (Eqn. (4.17)) and make it more consistent with the actual $S_k^{'}$ (Eqn. (4.20)).

3) Replacement of S_{i_k} in Eqn. (4.15) by $S_{i_k}^{'}$ during start-up.

4.8.1.4.Hardware simulation results of Multiple Model Adaptive Estimator

The MMAE has been tested in the HILS for the following two cases:

A) The 3MW WT (Table 4.2). This has been simulated only for variable speed maximum power point operation using the conventional control of Eqn. (1.8). The MMAE consists of 3KFs tuned at Q=10^{10} (KF_1), 10^{11} (KF_2) and 10^{13} $(Nm)^2$ (KF_3).

B) The Windharvester WT (Table 2.1). (3KFs tuned at Q=10 (KF_1), 10^2 (KF_2) and 10^3 $(Nm)^2$ (KF_3).)

All the filters use MA noise filtering in both inputs (R adaptive KFs were also used and exhibited similar performance).

Figures 4.14 (A) (i-iii) show the obtained $\hat{T}_a$ estimates for (A) and the corresponding probabilities $P(\theta_i)_k$ over time.

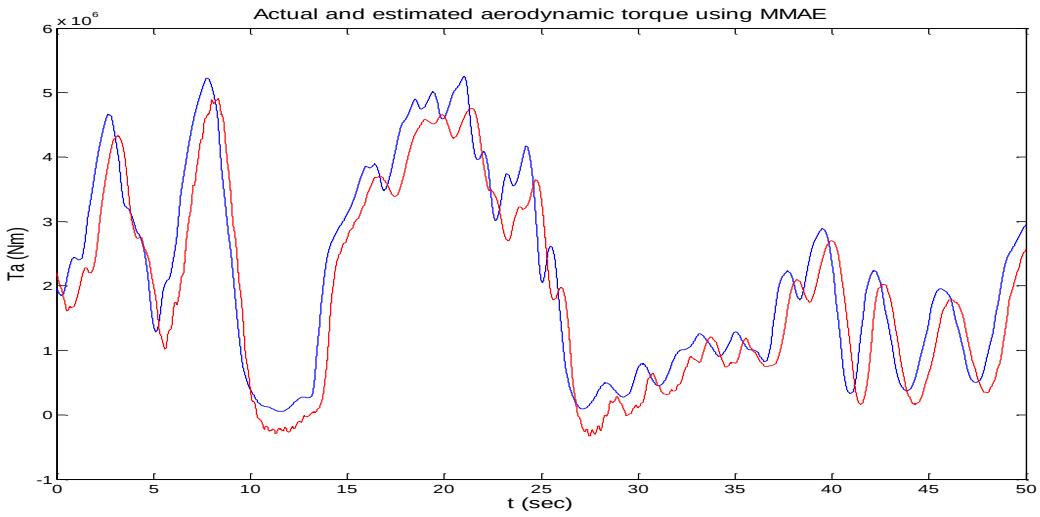

Figure 4.14(A)(i). T_a (blue) and $\hat{T}_a$ (red) using the MMAE algorithm for a 3MW WT.

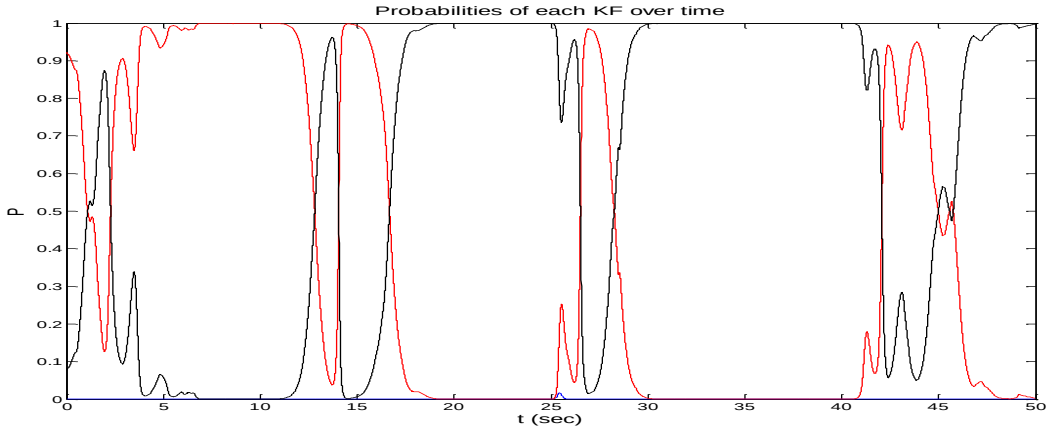

Figure 4.14(A)(ii). $P(\theta_i)_k$ for every KF_i, i=1,…,3. KF_1 (black), KF_2 (red), KF_3 (blue).

As can be seen from the Figures 4.14(A)(i-ii), the MMAE algorithm effectively switches between the KF_1 (slow model) and the KF_2 (faster model) depending on the variations of T_a . Specifically, KF_3 contains the fastest model and was always correctly ignored by the MMAE, since for the current T_a conditions it resulted in an oscillatory estimate. Figure 4.14 (A) (iii) shows a close view of the $\hat{T}_{a_i}$ estimate of each KF_i, i=1…3 and the final $\hat{T}_a$ of the MMAE, for the seconds 8-15. In the figure it can be seen that during the fast drop in the 9th second, $\hat{T}_a$ is attached to $\hat{T}_{a_2}$, while after the 12th second it converges to $\hat{T}_{a_1}$, as a result of the history of slow variations during the 10-12

seconds. Finally, at the 14th second, MMAE switches back to $\hat{T}_{a_2}$, which better approximates the fast rise of T_a.

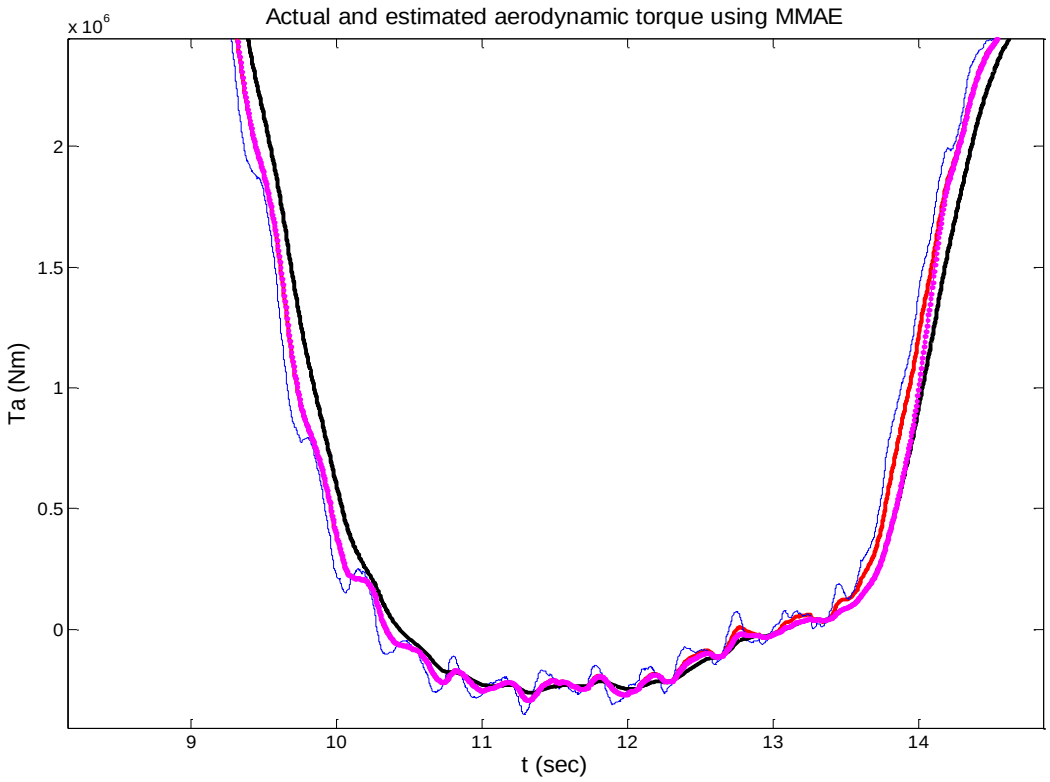

Figure 4.14(A)(iii). $\hat{T}_{a_1}$ (black), $\hat{T}_{a_2}$ (red), $\hat{T}_{a_3}$ (blue) and $\hat{T}_a$ (magenta).

Figures 4.14 (B)(i-ii), show the obtained $\hat{T}_a$ estimates for (B) and the corresponding probabilities $P(\theta_i)_k$ over time, respectively.

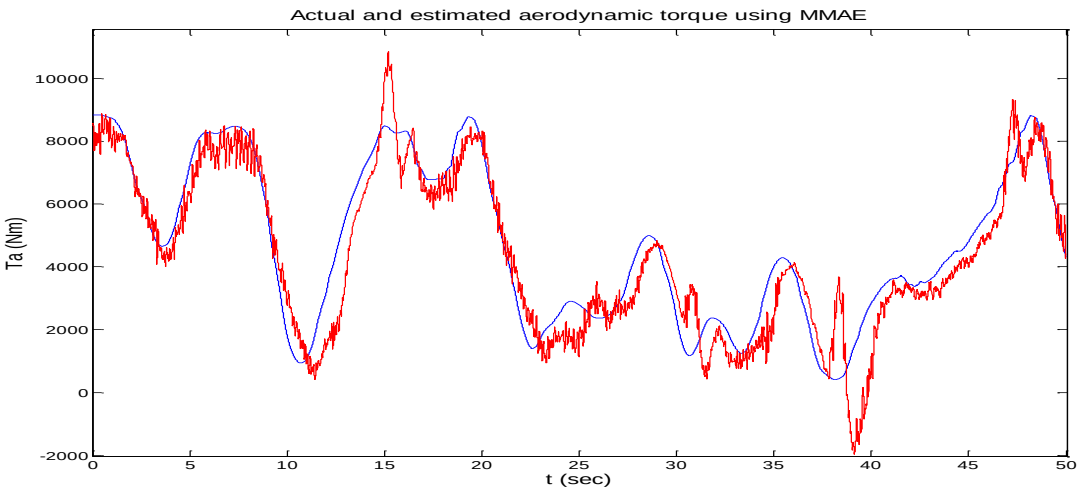

Figure 4.14(B)(i). T_a (blue) and $\hat{T}_a$ (red) using the MMAE algorithm for the Windharvester WT.

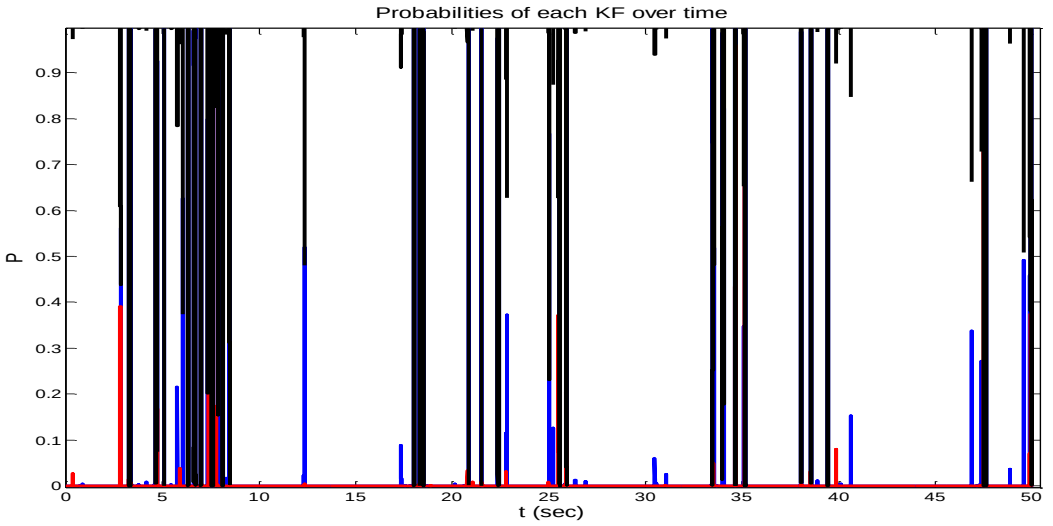

Figure 4.14(B)(ii). $P(\theta_i)_k$ for every KF_i, i=1…3. KF_1 (red), KF_2 (blue), KF_3 (black).

The observation in Figures 4.14 (B)(i-ii) shows a rather poor performance of the MMAE when applied to the Windharvester WT model, since the $\hat{T}_a$ estimate of the KF with the largest Q (KF_3) is always incorrectly selected. However, the MMAE should not be underestimated, since this poor performance is a consequence only of the effect of the HILS hardware at the WT model, which is not expected by the KFs, as mentioned in Section 4.6.3. A more detailed explanation can be found in Appendix A.13.

4.8.1.5. Conclusions on the Multiple Model Adaptive Estimator

MMAE algorithms in general provide flexibility in the initial selection of the process noise variance and also effective adaptation to changes of it, which is an important parameter in order to obtain an accurate $\hat{T}_a$ estimate. In addition, adaptation to arbitrary dynamic range of parameter changes is possible, by using an appropriate number of KFs.

It must also be mentioned, that in order for the algorithm to work successfully, all the dominant modes of the applied system must be included in the dynamic models of the KF bank (Appendix A.13).

4.8.2.Innovation Adaptation Estimation

4.8.2.1. Introduction

Innovation Adaptation Estimation methods (IAE), unlike the MMAE methods, use a single KF, which adapts to the changes of the process noise covariance matrix *Q* in real time, based on the statistics of the innovation sequence of the KF.

The *Q* adaptation method described here is novel and has been developed after a modification was made to an existing algorithm found in [64].

It is noted that a *Q* adaptation algorithm found in [63, 71] also performed well (A.12). However, its performance was severely degraded when the AKF was enhanced with simultaneous *R* adaptation (limitations due to simultaneous *R* and *Q* adaptation are also mentioned in [63]).

4.8.2.2. Adaptation routine in changeable process noise covariance

The proposed algorithm is based on the combination of the *Q* adaptation criterion found in [64] with the use of a PI controller in order to update *Q* at every time step.

Specifically, in [64], *Q* is recursively adapted using the formula:

$$Q_k = Q_{k-1}\sqrt{a}, \quad (4.22)$$

where $a = \frac{trace\{C\tilde{P}^{-}C^T\}}{trace\{CP^{-}C^T\}}$ and:

$$CP^{-}C^T = S_0 - R, \quad (4.23)$$

$$C\tilde{P}^{-}C^T = S_0{}' - R. \quad (4.24)$$

S_0 is the innovations covariance matrix, shown in Eqn. (4.25) (and Eqn. (4.16)) and $S_0{}'$ is the innovations autocorrelation computed using time samples of r_k, shown in Eqn. (4.26).

$$S_0 = CP^{-}C^T + R, \quad (4.25)$$

$$S_0{}' = \frac{1}{N}\sum_{i=K+1-N}^{k+1}(r_k r_k^T). \quad (4.26)$$

When the KF is optimum, the innovations are zero mean white noise so $S_0{}'=S_0$, while during suboptimum operation, the divergence of the outcome of Eqn. (4.26) from Eqn. (4.24), expressed in terms of their ratio *a*, is used to correct *Q*. The "trace" in general is used in order to take into account the residuals in a cumulative way, when more than one measurement is available.

The above algorithm was applied to the KF for T_a estimation, but without success, since quite frequently it introduced unacceptable oscillations in $\hat{T}_a$, although different recursive adaptation rules than the one of Eqn. (4.22) were tried.

The algorithm proposed here is based on continuous updating of Q in a non-recursive manner using a discrete time PI regulator with input the error $e = trace\{CP^{-}C^{T}\} - trace\{C\tilde{P}^{-}C^{T}\}$, shown in Eqn. (4.27) (in the z-domain):

$$Q_k = (K_p + \frac{K_I T_s}{1-z^{-1}})e_k, \qquad (4.27)$$

where K_p and K_I are the proportional and integral gains, respectively. These gains can be easily determined by testing the performance of the algorithm for the lowest and highest expected Q values. Typical used values for the Windharvester WT are: K_p=5000 and K_I=50 (Nm)^2.

This algorithm was tested with several wind input signals and for different levels of turbulence and in all the cases it provided an oscillation-free $\hat{T}_a$ estimate with small time delay. Through several closed loop simulations with the scheme of Figure 4.1 in HILS, the algorithm was seen to be stable.

Finally, this Q adaptation algorithm was also applied in combination with simultaneous R adaptation (see Appendix A.10) and no unacceptable interaction between the two routines was observed, apart from some instant variations in $\hat{R}$. In Appendices A.14-15 a comparison of the proposed algorithm with existing ones can be seen.

4.8.2.3. Software and hardware simulation results

A) Software (Simulink) results

Figure 4.15 (a) and (b) show T_a and $\hat{T}_a$ for the 3MW WT, for high and low wind speeds, respectively (In comparison with Figures 4.10 and 4.12) using the proposed Q adaptation algorithm.

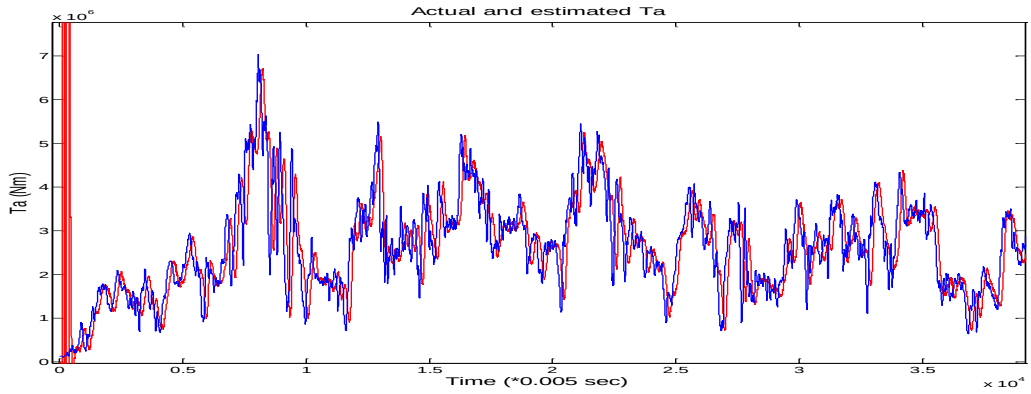

Figure 4.15 (a). T_a (blue) and $\hat{T}_a$ (red) for the 3MW WT, for high wind speeds using proposed Q adaptation algorithm.

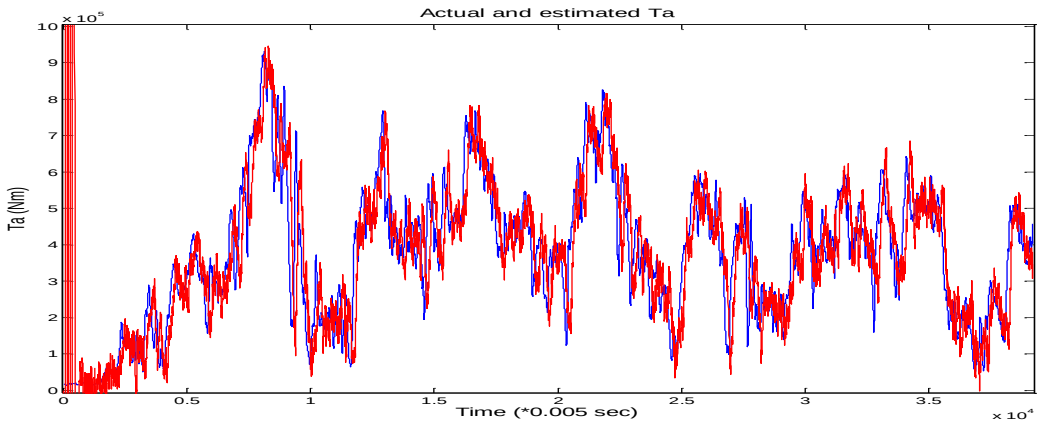

Figure 4.15 (b). T_a (blue) and $\hat{T}_a$ (red) for the 3MW WT, for low wind speeds using proposed Q adaptation algorithm.

By comparing Figures 4.15 and 4.10 the advantage of the proposed adaptive algorithm compared to the nonadaptive KFs can be observed. Specifically, the proposed filter achieved similar time delay in high wind speed, but much improved performance in low wind speeds. Compared to the MMAE (Figures 4.12), it provides a good tradeoff

between estimation accuracy and computation load (the MMAE can theoretically achieve better performance for a wider range of operating conditions, but with higher computational load).

B) Results using the Hardware In the Loop Simulator

Figure 4.16, shows the obtained $\hat{T}_a$ estimate using the proposed AKF with MA input denoising filters for the 3MW WT simulated in HILS, where it can be seen that it closely follows T_a.

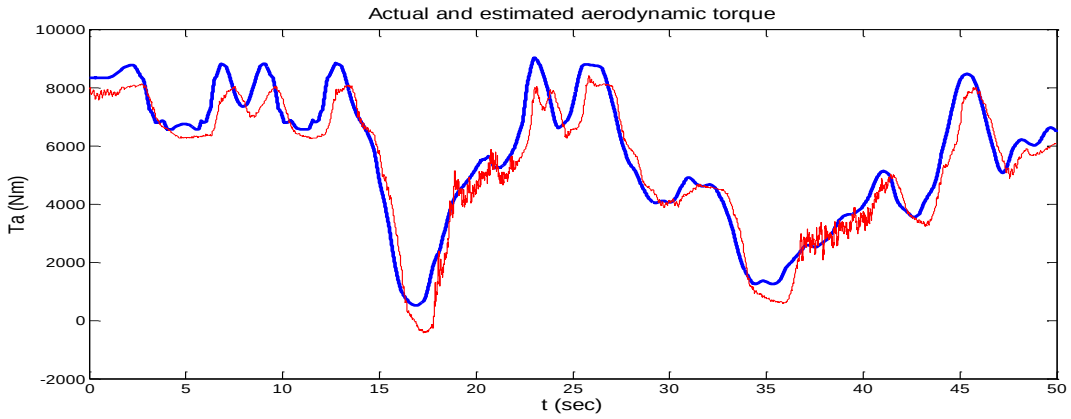

Figure 4.16. T_a (blue) and $\hat{T}_a$ (red) for the 3MW WT, for high wind speeds using proposed Q adaptation algorithm.

Figure 4.17(a) shows the result of an R and Q adaptive AKF for the Windharvester WT (the MA filter in ω_g has been removed) and (b) the $\hat{R}$ estimate (The $\hat{R}$ estimation routine updates the new $\hat{R}$ every 0.1 sec).

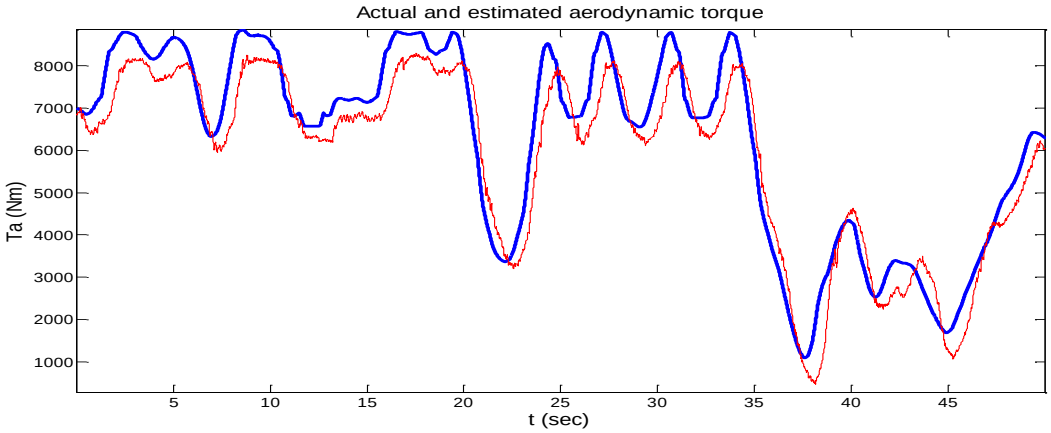

Figure 4.17(a). T_a (blue) and $\hat{T}_a$ (red) for the Windharvester WT, for high wind speeds using proposed Q adaptation algorithm in combination with R adaptation.

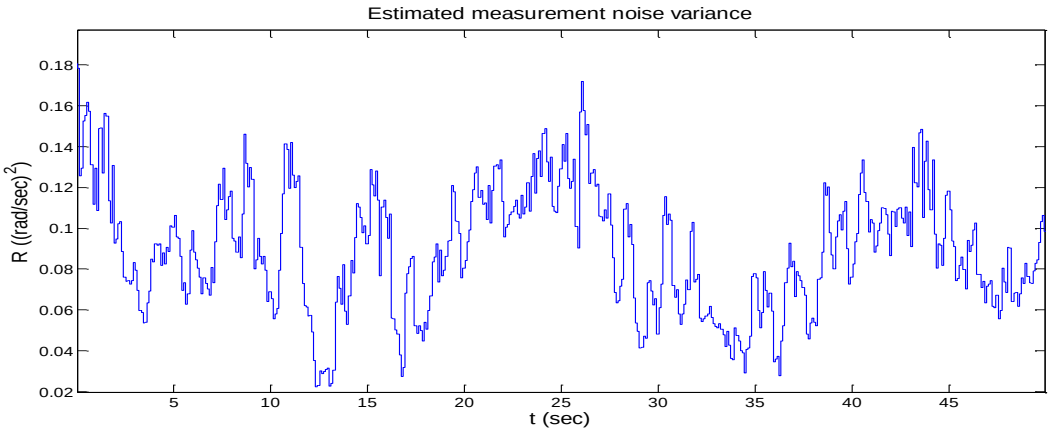

Figure 4.17(b). $\hat{R}$ estimate.

Figure 4.17(a) shows a very accurate $\hat{T}_a$ estimate and also Figure 4.17(b) shows that $\hat{R}$ stays at 0.1(rad/sec)^2 on average, slightly higher than what is observed in Figure 4.8 (b) for a nonadaptive in Q KF, due to the interaction with the Q adaptation. However, this interaction does not cause any unacceptable errors in the obtained $\hat{T}_a$ estimate.

Finally, Figure 4.18, shows the $\hat{T}_a$ estimates for the Windharvester WT, obtained by the IAE AKF and the MMAE (the second is also shown in Figure 4.14 (B)(i)). As can be seen, the IAE in this case outperforms the MMAE estimate, since the Q adaptation is not affected by the modeling uncertainty, as was the case for the MMAE (see Section 4.8.1.3).

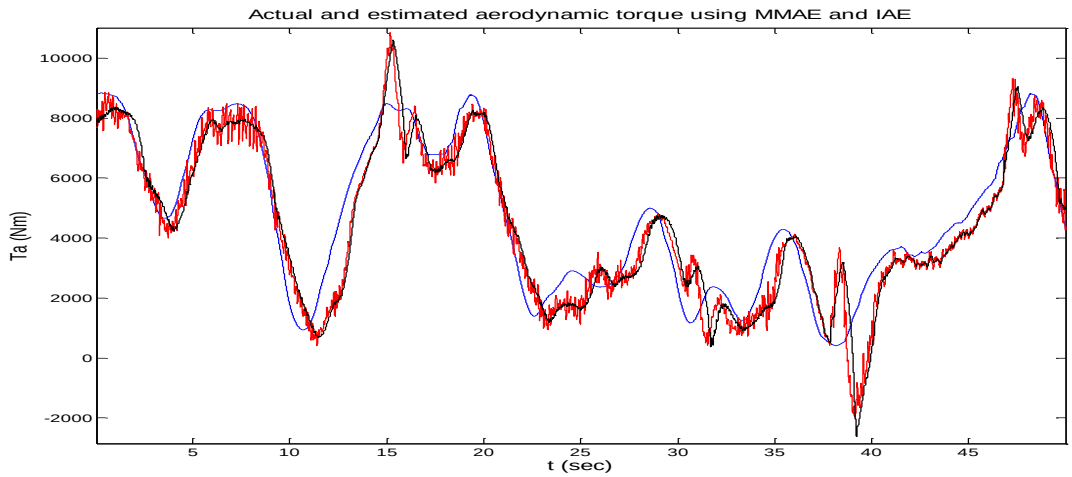

Figure 4.18. T_a (blue) and $\hat{T}_a$ from MMAE (red) and from IAE AKF (black) for the Windharvester WT.

4.8.2.4. Conclusions on the proposed innovation adaptive estimation method

In the previous section, the application of a novel IAE algorithm for accurate T_a estimation in WTs under unknown or time varying Q was presented.

The proposed IAE algorithm provided a very accurate $\hat{T}_a$ estimate, through continuous Q adaptation. In general, this algorithm produces a $\hat{T}_a$ estimate with a smaller time delay and reduced oscillations than can be achieved with a single KF, while the only requirement is the selection of the PI gains, which can be easily performed through simulations. In addition, the IAE provides a good solution when the computational load of a MMAE is a limiting factor.

4.9. Unscented Kalman filter

4.9.1. Introduction

The Unscented Kalman Filter (UKF) is a KF applied to nonlinear systems and it is based on the Unscented Transform (UT). More details about UKF and UT can be found in [76-78]. As mentioned in [61], nonlinear filtering may exhibit better performance in

certain applications and therefore it was considered worthwhile to investigate in order to be used for T_a estimation. Specifically, a KF including the UT at the prediction step (see Eqns. (4.5-4.6)) has been implemented and applied to WT models using the HILS (more details on this algorithm can be found in Appendix A.16).

4.9.2. Simulation results of UKF

In order to evaluate the performance of the UKF in this application, it was also tested through simulations using Simulink as well as the HILS.

Figure 4.19 (a) shows Simulink results of T_a and $\hat{T}_a$ obtained by the proposed UKF and (b) by a linear KF, both applied to the Windharvester WT model, where it can be seen that the UKF exhibits a smaller transient during the starting than the KF. In both filters R=0.01(rad/sec)^2 and Q=100(Nm)^2.

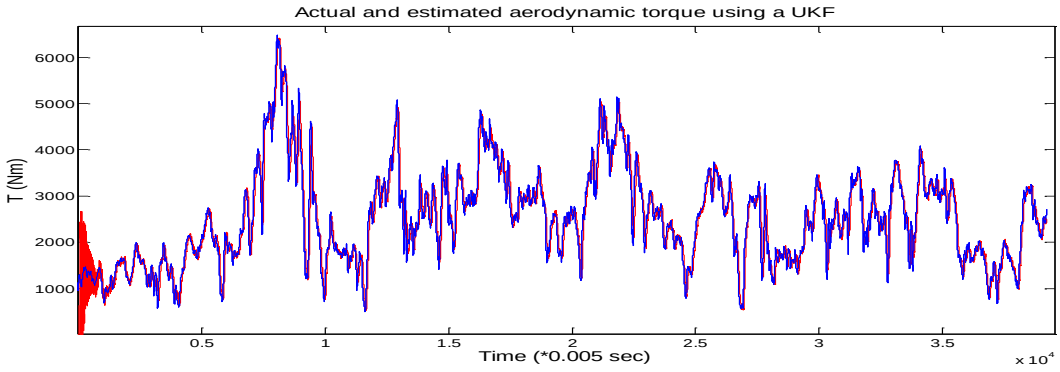

Figure 4.19 (a). T_a (blue) and $\hat{T}_a$ (red) using a UKF.

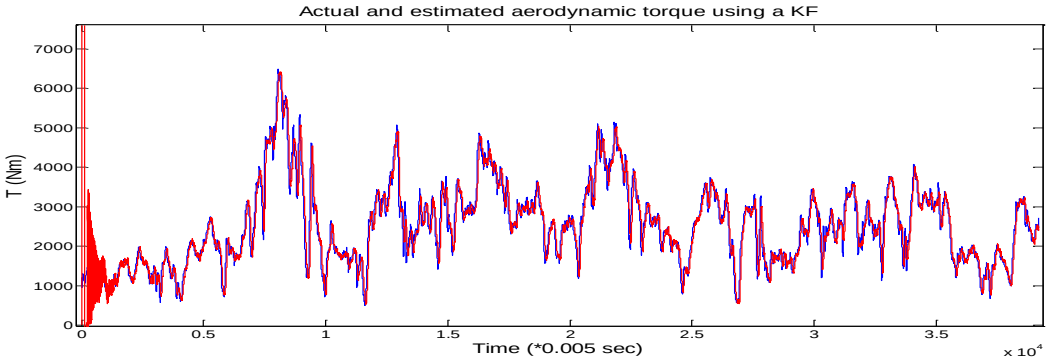

Figure 4.19 (b). T_a (blue) and $\hat{T}_a$ (red) using a KF.

Regarding the quality of the estimate, this was found to be the same as for the KFs so further experimental results do not add any new information.

It is noted that the MMAE and IAE Q adaptation algorithms as well as R adaptation algorithms can also be applied effectively to the UKF too.

4.10. Conclusions

In this chapter effective methods for aerodynamic torque estimation of a WT using adaptive KFs or UKFs were presented. Specifically, all the presented methods were implemented in the HILS and provided torque estimates of high accuracy. Also, the design, analysis as well as novel methods to overcome practical limitations were presented for a MMAE, in order to be applicable to a WT. Furthermore, a novel IAE method was presented, which exhibited remarkable estimation accuracy.

As it was shown, all the proposed adaptive estimation methods can provide accurate estimates under varying wind conditions as well as varying measurement noise level. In the next chapter, methods to produce the optimum speed reference for the WT IG, based on the obtained $\hat{T}_a$ estimates, are presented.

5. Effective wind speed estimation-Speed reference

5.1. Introduction

As mentioned in Chapter 1 (Section 1.5) and in the introduction of Chapter 4, an estimate of the effective wind speed $\hat{V}$ is used for the determination of the IG speed reference. This can be extracted by numerically solving Eqn. (1.4) using the Newton-Raphson (NR) method [22, 35]. Eqn. (1.4) is repeated in Eqn. (5.1).

$$T_a = \frac{1}{2}\rho\pi R^3 C_Q V^2 = \frac{1}{\omega} C_p \frac{1}{2}\pi\rho V^3 R^2 \qquad (5.1)$$

In order for the NR to be applied, the C_p-λ characteristic of the rotor is analytically expressed using a polynomial. Figure 5.1 shows the C_p curve (original curve of Figure 3.12) of the Windharvester WT rotor (Section 2.6) and its approximation by a 5th order polynomial, used for the NR.

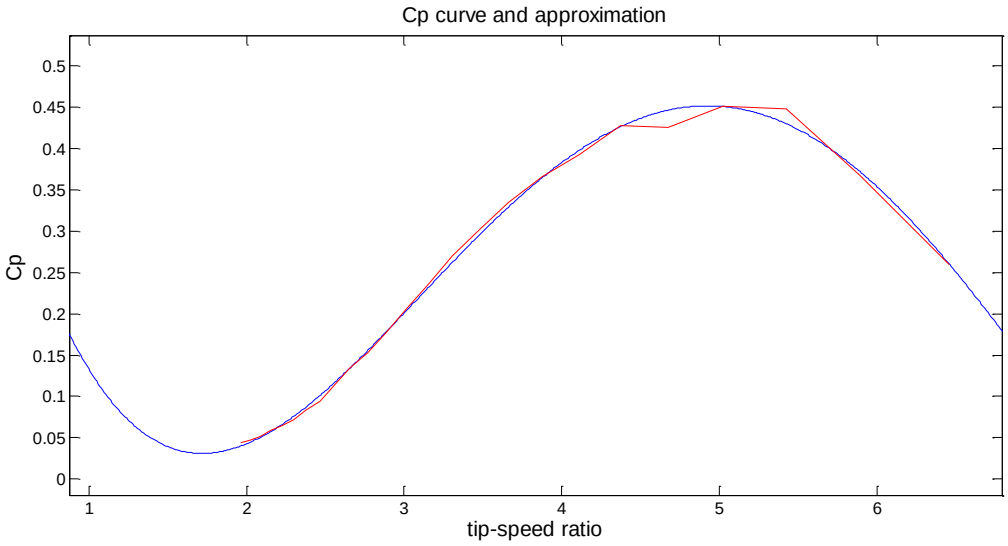

Figure 5.1. Actual C_p curve (red) and approximation using a 5th order polynomial (blue).

As can be seen, the approximated curve fits quite successfully the actual one.

Based on this, the NR seeks for V solution corresponding to $1.5<\lambda<6.5$, since the approximation is valid within this tip speed ratio range. If for any reason no solution exists at a certain time step, NR returns a high value for V, which ensures that no control is applied.

As mentioned in Section 1.5.1 a single value of T_a and of ω_{rotor} can lead to more than one V solutions for Eqn. (5.1) due to the intersections between the T_a characteristics of the rotor in different wind speeds. Figure 5.2 shows these points of intersections as dots in the T_a-ω_{rotor} graph for the Windharvester WT (see Section 2.7)

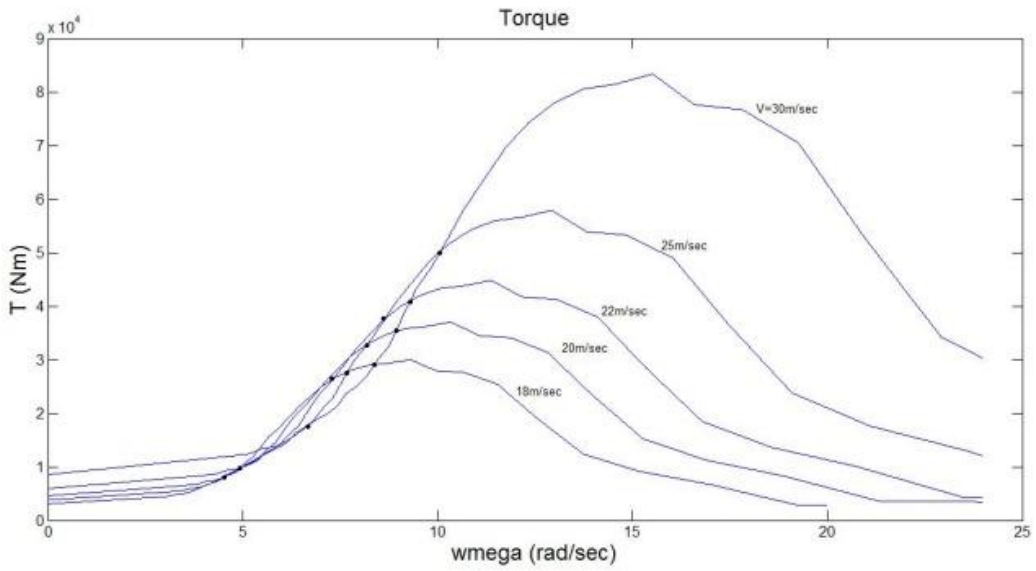

Figure 5.2. T_a characteristics of different wind speeds and points of intersection.

Specifically, if the rotor exhibits very low torque for very low tip-speed ratios, then the T_a characteristics for very high wind speeds may intersect with those corresponding to below rated wind speeds as can be seen in Figure 5.3 (a) and this can be the case for rotors with a steep C_q-λ curve. Also, ambiguity in V estimation can occur in the stall region too, since the T_a characteristics for above rated wind speeds may intersect each other, as seen in Figures 5.2 and 5.3(b) for an example point E(ω_M, $T_{\alpha M}$).

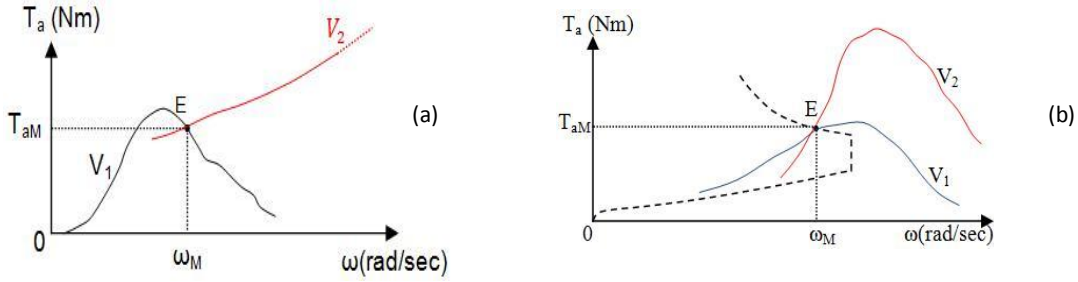

Figure 5.3. (a) Operating point for below rated and (b) above rated conditions.

Figure 5.4 (a) shows T_a versus V for a fixed value of ω_{rotor}, for a SR WT. As can be seen, T_a after exhibiting a peak drops and then starts rising again towards higher wind speeds [1]. Figure 5.4 (a) also displays three possible V solutions V_1, V_2 and V_3 corresponding to T_a=T_{aM}, given the fixed ω_{rotor}. Figure 5.4 (b) shows the plot of the function T_{aM}-T_a, where T_a is given by Eqn. (5.1).

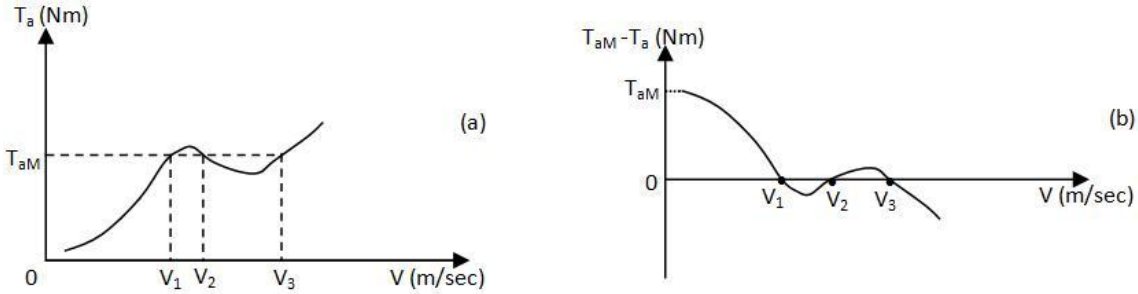

Figure 5.4. (a) T_a versus V and (b) T_{aM}-T_a versus V for fixed ω.

5.2. Speed reference at below rated conditions

In this section the speed reference for below rated wind speeds is described, while the speed reference for above rated wind speeds is described in the next section. Figure 5.5 is the same as Figure 1.9, where the desirable operating point locus for the VS SR WT is shown. Also, Figure 5.6 shows a graph similar to that of Figure 5.4 for ω_{rotor}=ω_N, where T_{ω_N} and P_N/ω_N are the aerodynamic torque levels corresponding to the points B and C of Figure 5.5 respectively.

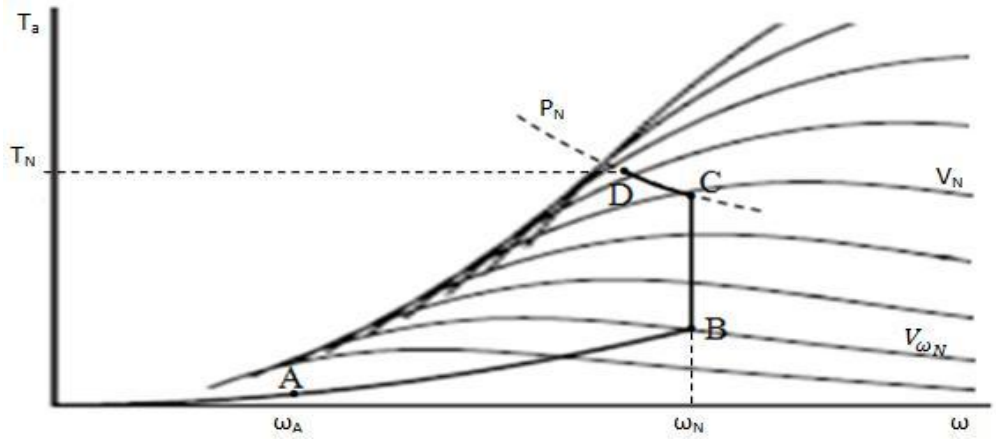

Figure 5.5. Control strategy of a stall VS SR WT [1].

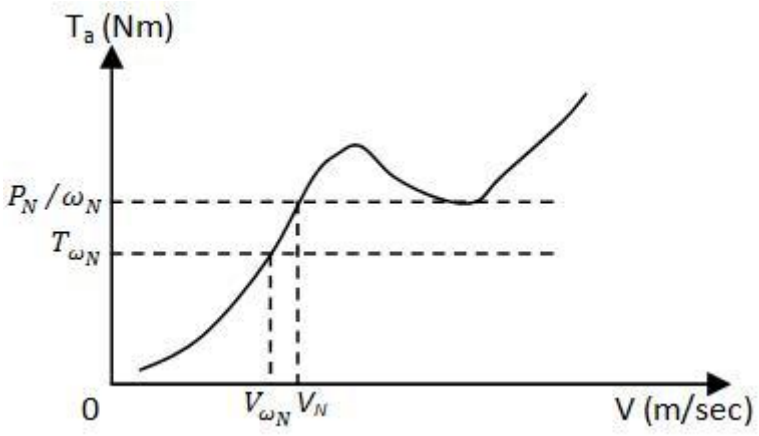

Figure 5.6. T_a versus V for $\omega=\omega_N$.

For the part AB of Figure 5.5, the optimum speed reference is: $\omega_{ref} = \frac{\lambda_0 V_1}{R}$, where V_1 is the lowest V solution seen in Figure 5.4. Also, for the part BC the speed reference is: $\omega_{ref} = \omega_N$. In addition, from Figure 5.6 it can be seen that for $\omega=\omega_N$ when $V_1>V_{\omega_N}$, the aerodynamic torque is always $T_a>T_{\omega_N}$. Therefore, V_1 can be effectively used in order to switch between the parts AB and BC. So, ω_{ref} for the part ABC can be expressed as:

$$\omega_{ref} = \begin{cases} \frac{\lambda_0 V_1}{R}, & V_1 < V_{\omega_N} \\ \omega_N, & V_1 > V_{\omega_N} \end{cases}, \qquad (5.2a)$$

This can be equivalently written as:

$$\omega_{ref} = \begin{cases} \frac{\lambda_0 V_1}{R}, & \omega_{ref} < \omega_N \\ \omega_N, & \omega_{ref} > \omega_N \end{cases} \qquad (5.2b)$$

Regarding V_1, it can be easily obtained with a NR if this is initialized at an appropriate point, as seen in Figure 5.7(a). Simulations showed that the starting point should not be situated at a quite high λ, because then the tangent line at the initialization point may intersect the V axis at a point that can cause further divergence of the NR algorithm, as seen in Figure 5.5(b). This limitation is caused by the particular shape of the $T_a(V)$ characteristic. It was found that the convergence of the NR is guaranteed if this is initialized at the point C, where the $T_a(V)$ characteristic changes curvature. The point C is located by the change in the sign of the second derivative of $T_a(V)$, which can be also numerically computed.

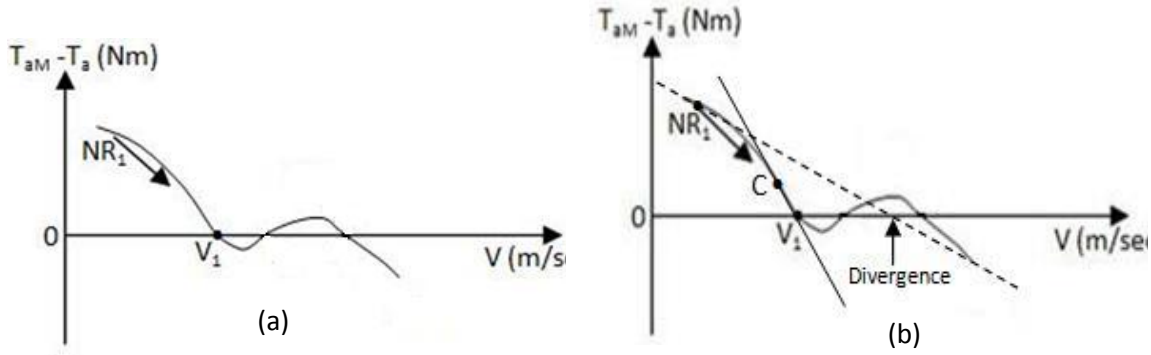

Figure 5.7. (a) NR routines used for V solution extraction of Eqn. (5.1) and (b) location of the initialization point C forNR_1.

Figure 5.8(a) shows a T_a - V plot similar to the one of Figure 5.6 for ω=4rad/sec for the Windharvester WT. Figure 5.8(b) shows the corresponding T_a - V plot and (c) shows the actual V and its estimate, $\hat{V}$ obtained in Simulink using the NR routine for the model of the Windharvester WT (using the arrangement of Figure 4.2).

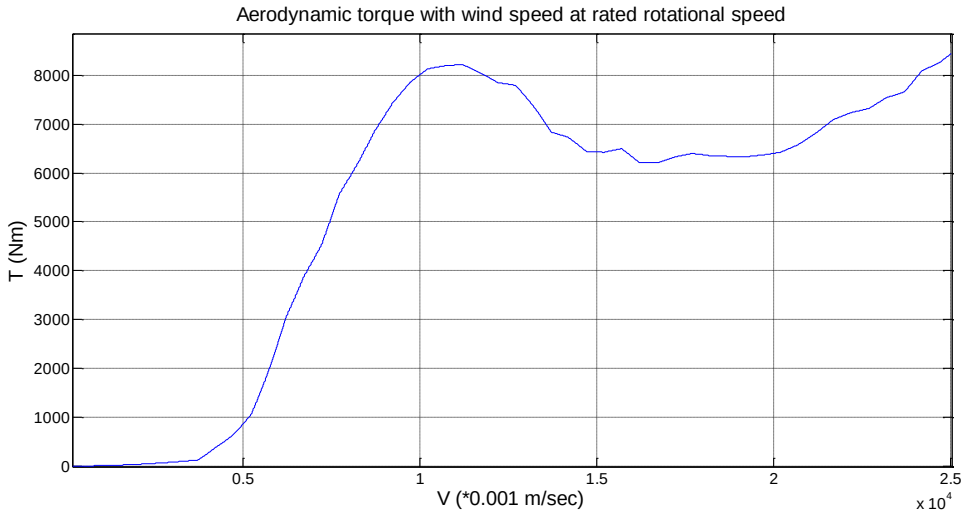

Figure 5.8(a). T_a versus V at ω_{rotor}=4rad/sec for the Windharvester rotor.

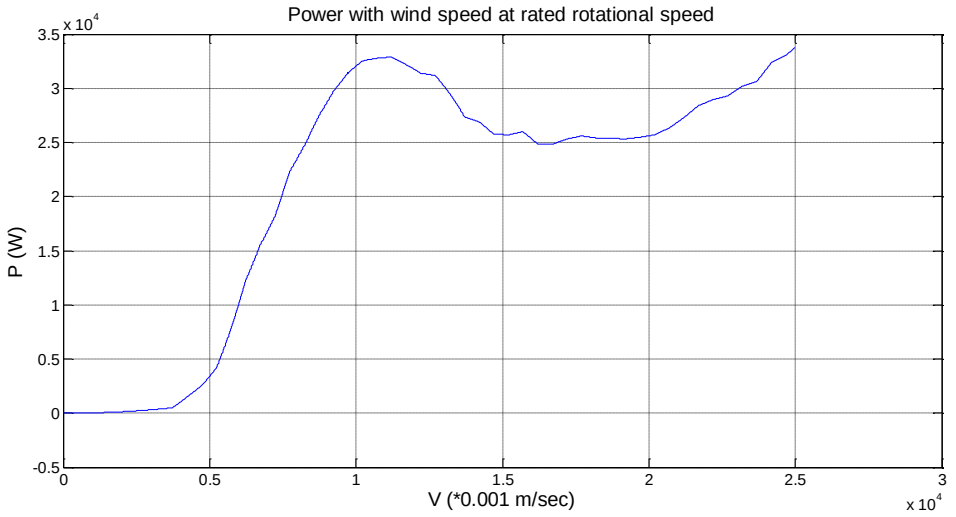

Figure 5.8(b). P_a versus V at ω_{rotor}=4rad/sec for the Windharvester rotor.

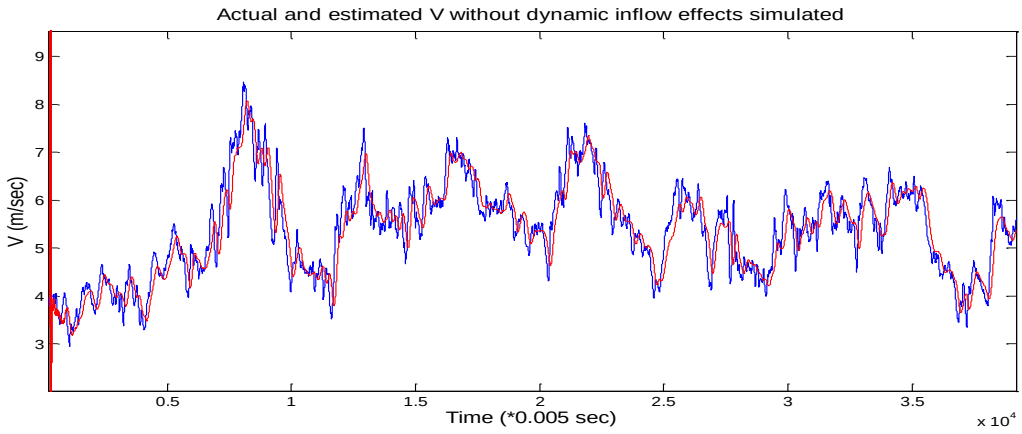

Figure 5.8(c). Actual V (blue) and estimated $\hat{V}$ (red) using NR.

As can be seen, the $\hat{V}$ estimate is very accurate as a result of the perfect fit of Figure 5.1. In addition, $\hat{V}$ is realistic, since V is always V<11m/sec, which is the value corresponding to the peak of the graphs of Figures 5.8 (a & b). According to Figures 5.4(a) and 5.8(a), when 11<V<23m/sec, V will be estimated as 7<V_1<11m/sec. This can be seen in Figure 5.9, which has been obtained with a simulation of the Windharvester WT in the HILS.

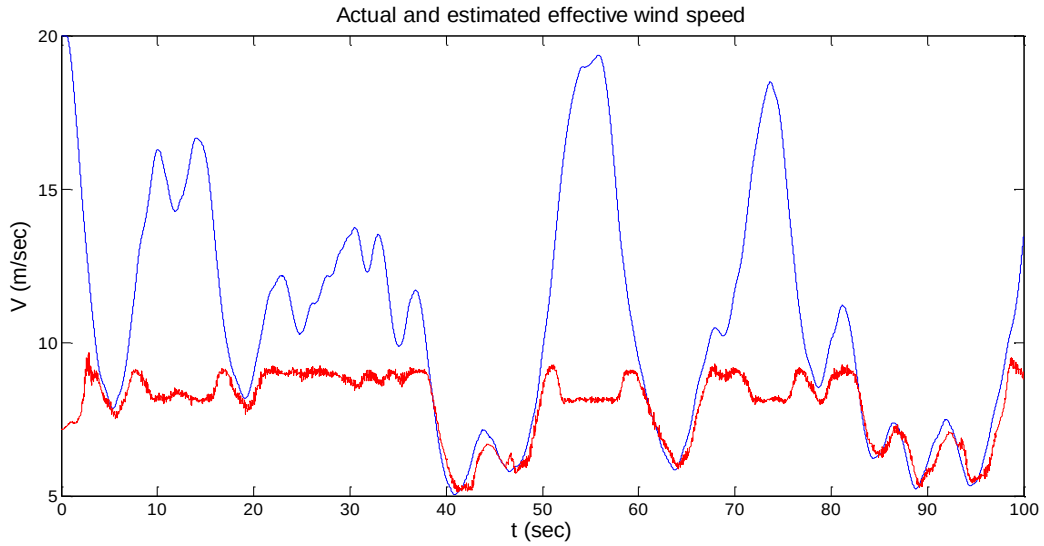

Figure 5.9. Actual V (blue) and estimated $\hat{V}$ (red) in HILS.

As can be seen, V reaches 20m/sec, but $\hat{V}$ cannot exceed 10m/sec, while for V<10m/sec $\hat{V}$ is very accurate (the value of 11m/sec expected by Figures 5.8 (a & b) is not reached due to the slight T_a underestimation that can be observed in the T_a - $\hat{T}_a$ plots of Chapter 4). In addition, when the actual V>10m/sec, $\hat{V}$>7m/sec always, according to Figures 5.8(a & b). Therefore operation with ω_{ref}=ω_N is guaranteed.

5.3. Speed reference in deep stall – Power limitation

Figure 5.10 shows P_a curves of the Windharvester WT for various wind speeds. Also, the rated power level, P_N is displayed. The black vertical line corresponds to the rated speed ω_R.

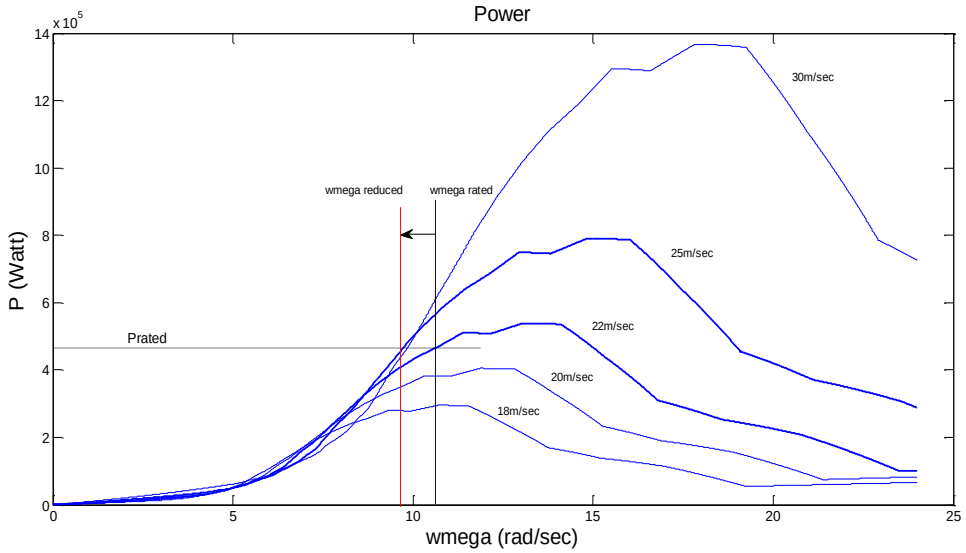

Figure 5.10. Power regulation using speed regulation in the stall region.

As can be seen, the rated power P_N is reached for V=22m/sec. If the wind increases to V=25m/sec, then the rotor speed needs to decrease to the point indicated by the intersection of the P_a curve of 25m/sec and the horizontal dotted line of $P=P_N$. The red line indicates the new rotational speed.

The methods for power control using stall regulation that have been developed here are:

A) Method based on the estimated wind speed -1. Hardware simulations showed that power limitation can be achieved. However, the effectiveness of the method is limited by the inability to correctly estimate V in the stall region. Also, power regulation to arbitrary power levels is not easy to implement. More details about this method can be found in Appendix A.17.

B) Method based on the estimated wind speed -2. This method uses an algorithm that continuously returns all the possible V solutions corresponding to the current P_a or T_a level. Then for each of them, the corresponding speed reduction, required to reach the desired power level, is calculated and the smallest one is used to form the new speed reference. This approach results in very effective power regulation, as can be seen by the software simulation results in Appendix A.18 and therefore motivates further work towards its use in an actual VS SR WT. However, because all the reference calculations are based on a static look up table of the C_p-λ curve of the rotor, the robustness of the approach in power/torque coefficient changes still needs to be assessed.

C) Methods based on the estimated aerodynamic power. Two methods that do not use knowledge of the aerodynamic characteristics of the rotor have been developed and tested using the HILS. These methods are considered more robust, because they do not assume knowledge of the aerodynamic characteristics of the rotor and therefore are more promising for application in an actual WTs. These methods are described in the next section.

5.4. Stall regulation at constant power

5.4.1.First method of power regulation

In this method, $\hat{P}_a$ is first low pass filtered, in order to smooth out power fluctuations due to high frequency wind turbulence. Then, the error $e = \hat{P}_a - P_N$ between $\hat{P}_a$ and the desired power level P_N is continuously checked and the speed reference is reduced or increased at fixed small amounts every T seconds, depending on the sign of e. Specifically, if $e(T) > 0$ the speed is reduced, while if e≤0, the speed is increased. A

key feature of the algorithm is the use of a larger fixed step for speed reduction than for speed increase, which aims to achieve a slower recovery of the original constant speed after a power increase. The flow diagram of Figure 5.11 describes the proposed algorithm.

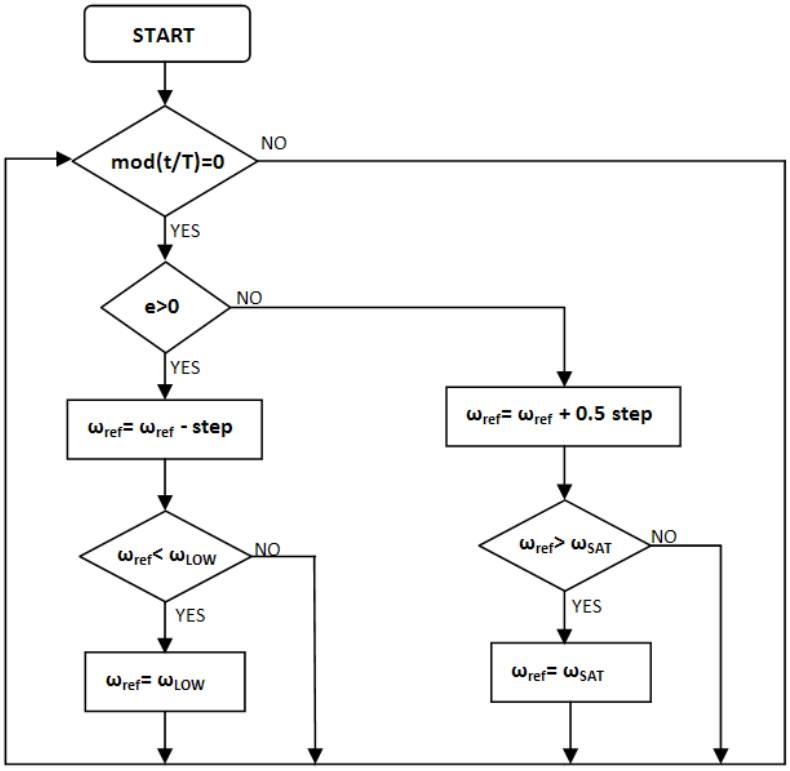

Figure 5.11. Power limitation method-1.

From Figure 5.11, it can be seen that ω_{ref} is constrained to vary in a range between ω_{LOW} and ω_{SAT}, where the first corresponds to the minimum allowed IG speed to prevent $T_{IG}>T_N$ and the second corresponds to ω_R. Finally, it is noted that the algorithm is activated only when $V>V_{\omega_R}$.

In the present application the power was filtered using an MA filter of length L=15secs. The time period T was chosen 4secs, while the step is equal to 0.01*ω_R.

5.4.2.Second method of power regulation

This method was developed as an improvement of the previous algorithm, which checks the power error only at specified time steps and therefore undetected hidden power oscillations may occur. The algorithm presented here overcomes this limitation by checking the error at every time step. The operation of this algorithm has been inspired by the procedure that would be possibly followed if manual power control was attempted and it is summarized at the following steps:

1) The error $e = \hat{P}_a - P_N$ is checked at every sample step T_s (T_s=5msec). Then, if the error remains > 0 for time T_e=*m1**T_s, where *m1* is a chosen number of samples, the speed reference is reduced by a fixed amount.

2) If after the reference reduction, the error is > 0, the algorithm continues reducing the reference in smaller steps, at every T_s until $e \leq 0$. As soon as this happens, the control is set back to step (1).

A routine for increasing the speed reference in case $e < 0$ runs in parallel to steps (1) and (2). The operation of the algorithm can be better described with the flow chart of Figure 5.12. (It is noted that this is an example implementation and more computationally efficient realizations may be possible.)

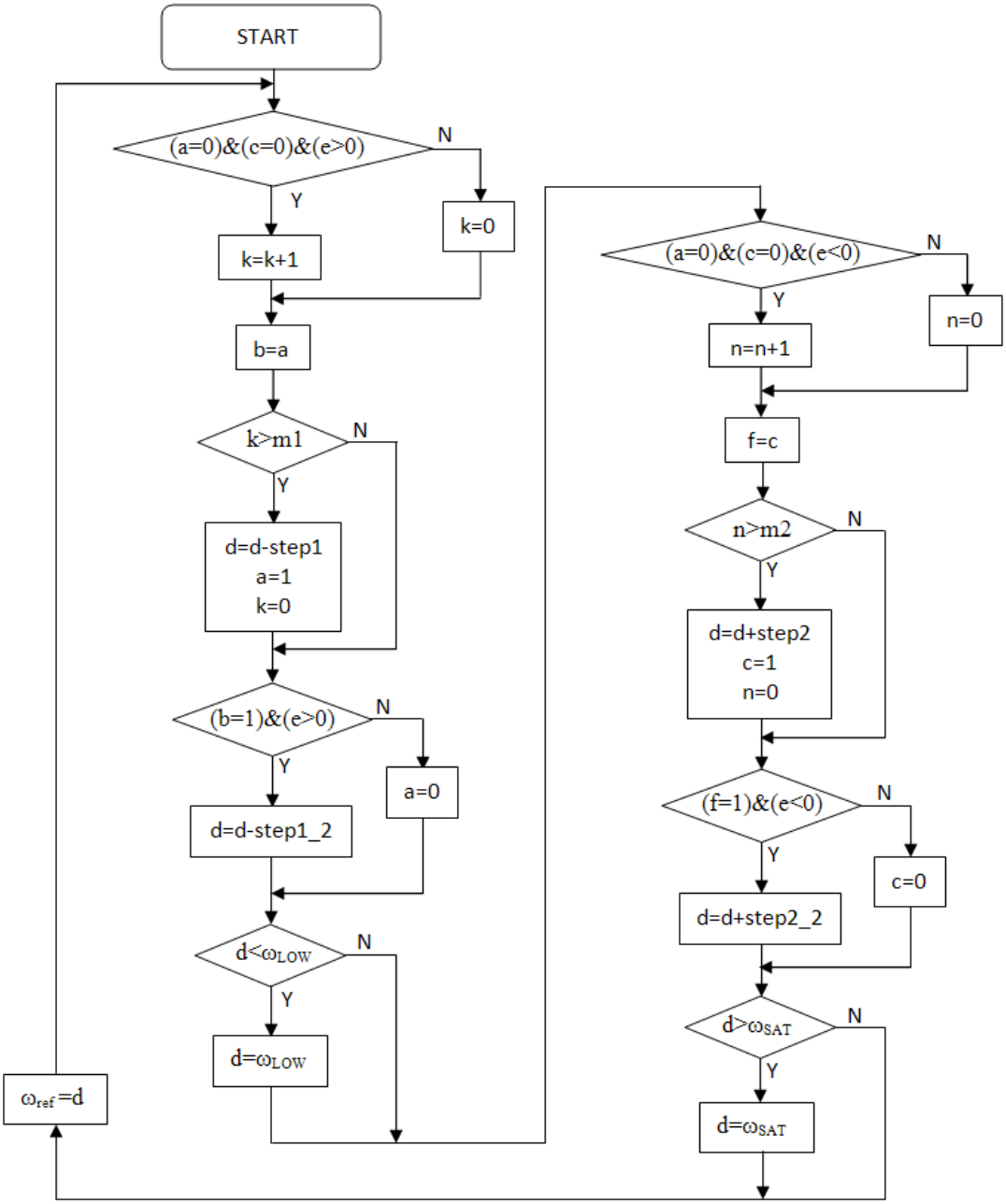

Figure 5.12. Power limitation routine-2.

As can be seen, the flow of the algorithm is controlled by the sign of the error *e* and the value of the binary variables *a,b,c,f,* which ensure no consequent change of the ω_{ref} within the same sample step T_s, by appropriate bypassing sections of the code. "step1" and "step1_2" comprise the speed reduction steps, where step1> step1_2, according to step (1).

Regarding the second branch of the algorithm, in a similar way "step2" and "step2_2" are the speed increase steps, where step2> step2_2.

It is mentioned that in order to achieve a slow recovery to the original $\omega_{ref,}$ it has been chosen step1> step1_2> step2> step2_2 and for the same reason, the number of sample steps for the second branch is set to *m2>m1*. Typical chosen values: step1=0.03*ω_R, step1_2=0.02*ω_R, step2=0.01*ω_R, step2_2=0.001*ω_R (rad/sec), *m1*=3 and *m2= m1*4* (sec).

5.4.3. Simulation results of power regulation-Improvement of the algorithm

Here, simulation results of the two power regulation algorithms are shown with emphasis to the second one. Hardware simulation results are shown in the next chapter, where the overall performance of the proposed control method for the VS SR WT is accessed.

Figure 5.13 shows the performance of the two algorithms at a fixed P_N=30kW compared to constant speed operation. From this figure it can be seen that the Power limitation routine-2 performs better than the routine-1.

Figure 5.14 shows (a) the performance of routine-2 during a step decrease in the demanded power P_N from 30 to 24kW and (b) the associated ω_{ref} and ω_g. All the simulations last 196sec (39200samples).

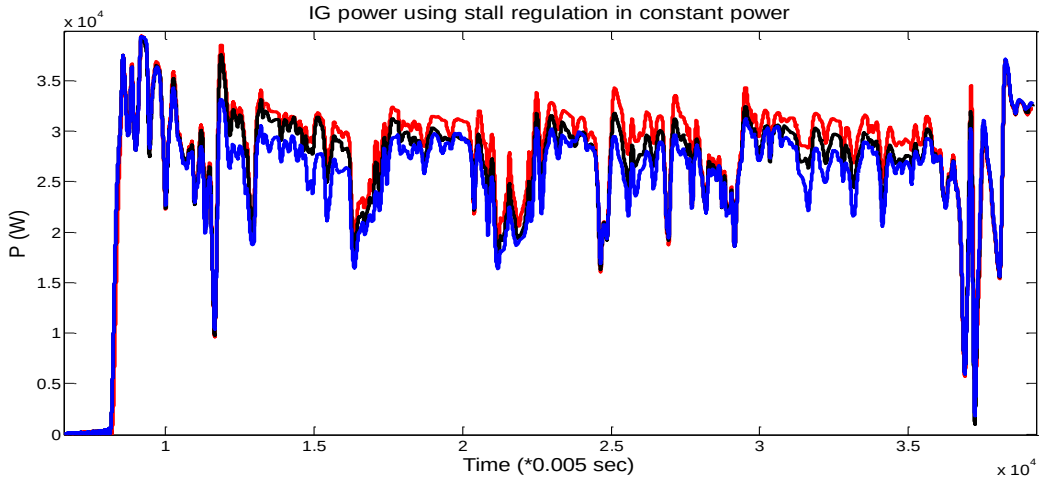

Figure 5.13. Power limitation using (a) routine-1 (black), routine-2 (blue) and constant speed stall regulation (red).

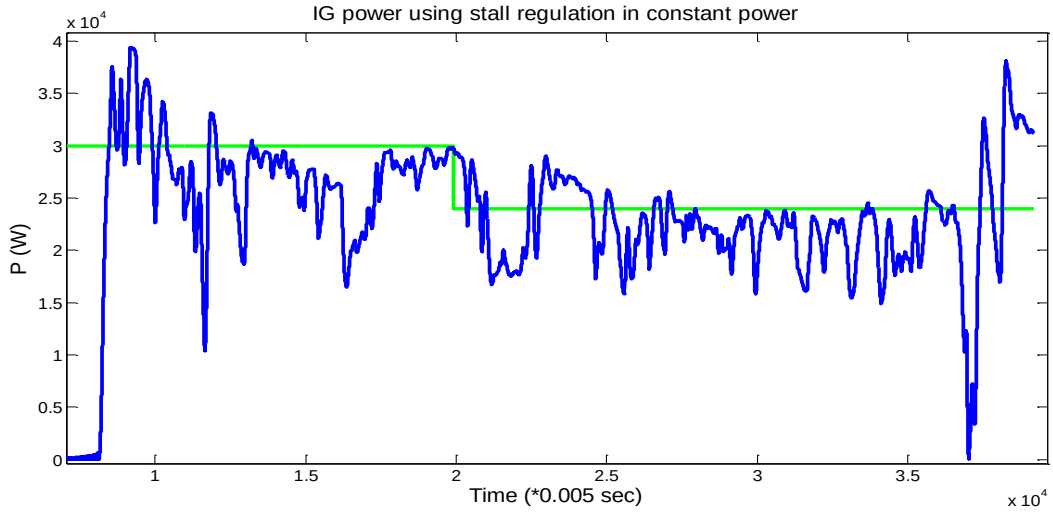

Figure 5.14 (a). Power regulation using routine-2 (blue) following a power reference (green).

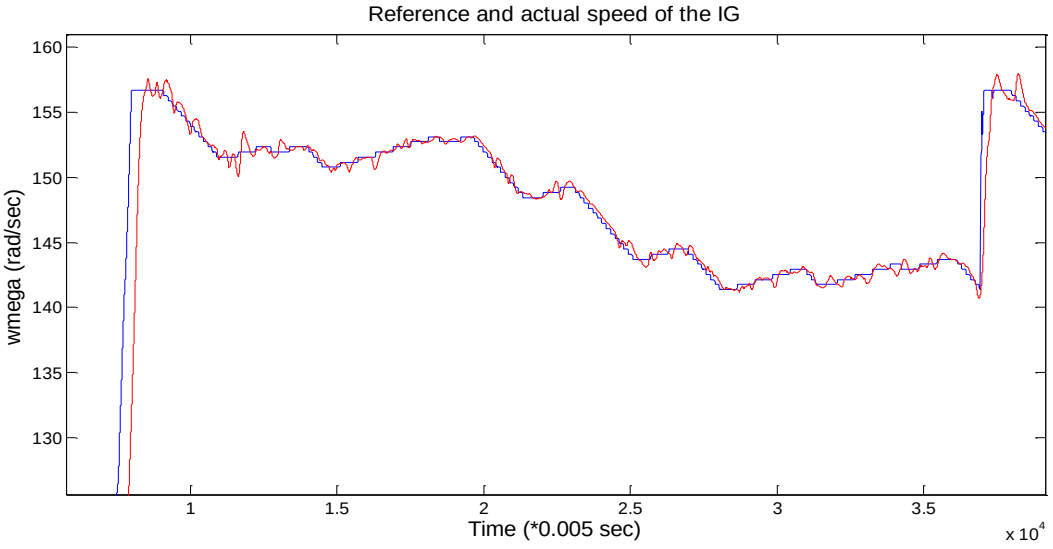

Figure 5.14 (b). ω_{ref} (blue) and ω_g (red) during power regulation.

As can be seen, the power regulation scheme successfully limits the power at its reference, by continuously adapting ω_{ref}, where a prerequisite is the accurate tracking of ω_{ref} by ω_g.

Figures 5.15(a) and (b) show the results of HILS implementation and demonstrate the effectiveness of the stall regulation scheme at a power level of 25kW. Similar behaviour to that in Figures 5.14 (a) and (b) can be observed (the used speed controller is a gain scheduled PI controller, described in Chapter 6).

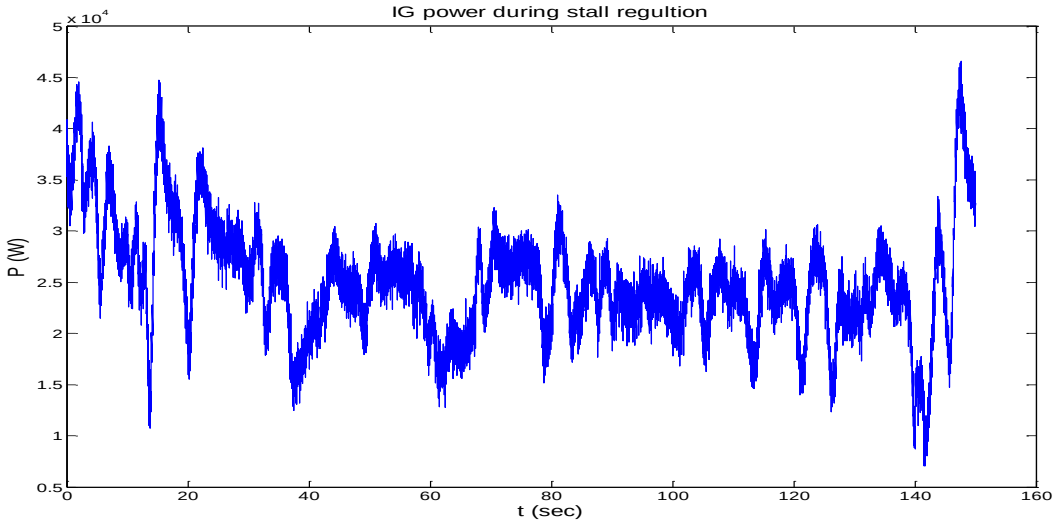

Figure 5.15 (a). Power regulation in HILS. P_N=25kW.

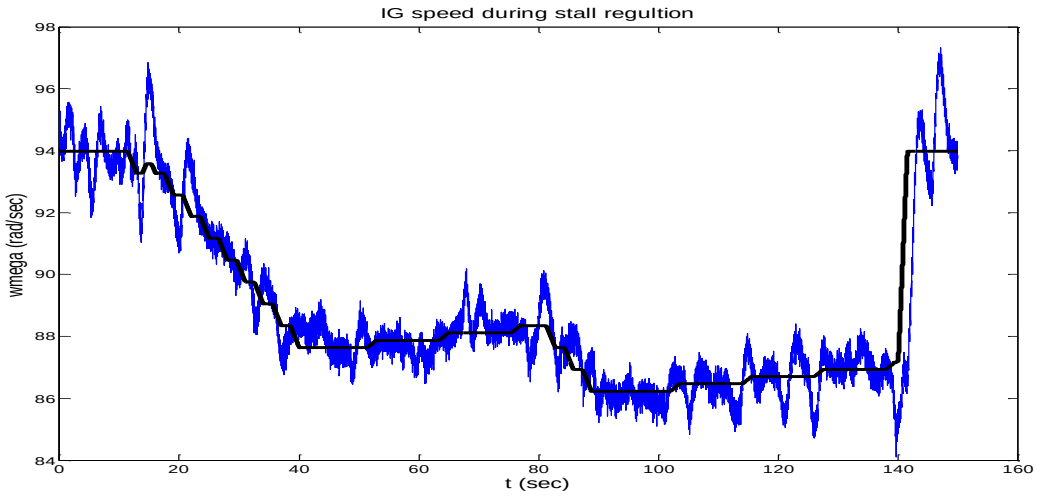

Figure 5.15 (b). Power regulation in HILS. P_N=25kW.

From Figures 5.13-15 it can be also seen that at time 3.73*10^4samples (for Figures 5.13-14) and at 140sec (for Figure 5.15), the power drops to a very low level and it immediately rises again to a high level, as a result of sudden wind speed lulls to below rated values and subsequent gusts (see black series in Figure 5.16).

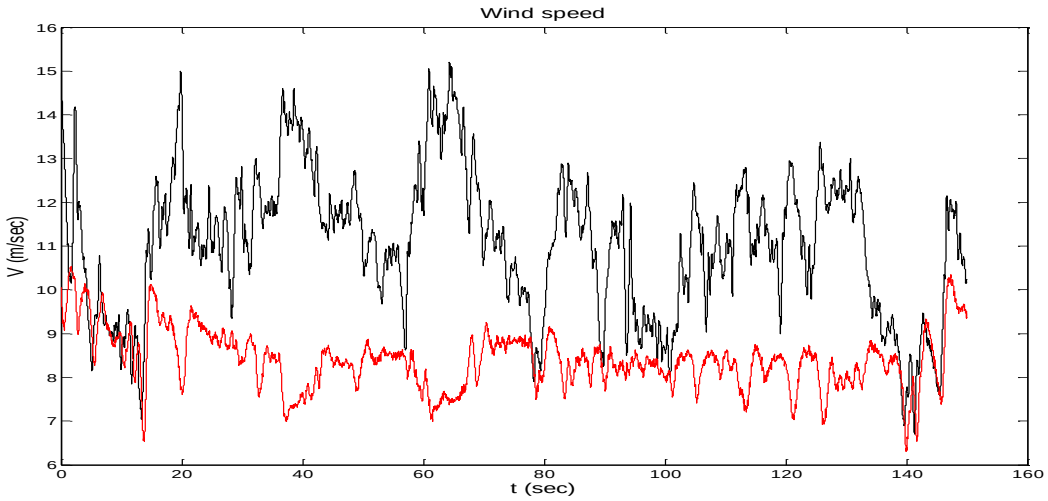

Figure 5.16. V (black) and $\hat{V}$ (red) in HILS.

The response of the algorithm during these wind speed excursions is better explained with the help of Figure 5.17.

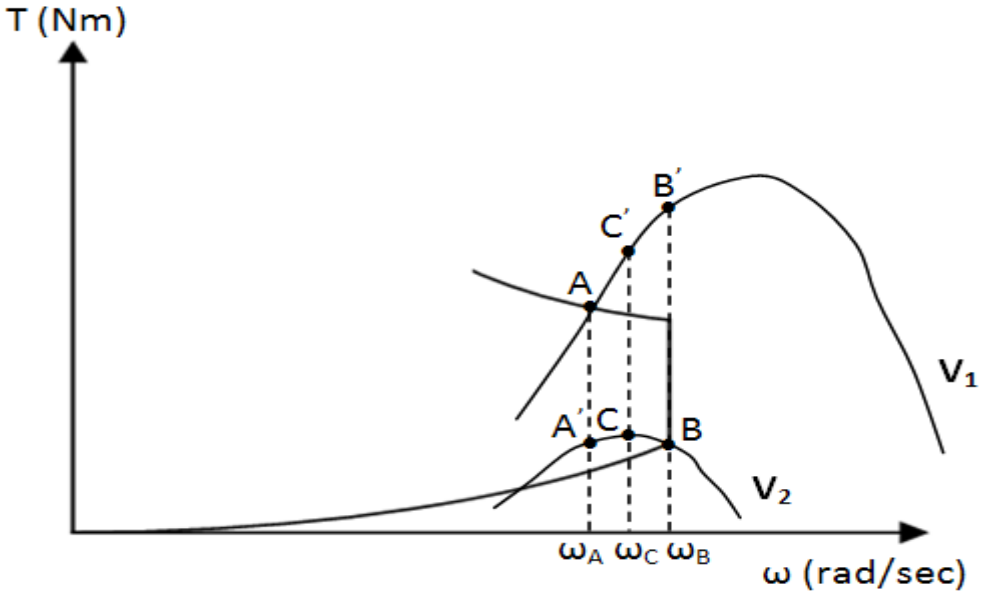

Figure 5.17. Operation of stall regulation during wind speed excursions from above to below rated values.

Assume that $V=V_1$ and the operating point is A. Then, if the wind suddenly drops to V_2, the speed reference jumps from ω_A to ω_B. The required acceleration causes the drop in output power seen in Figures 5.13-15. Then, if the wind increases again to V_1, the operating point moves to B', which leads to a peak in the output power.

In order to prevent this undesirable behaviour due to wind turbulence, the algorithm of Figure 5.12 has been enhanced with a mechanism that reduces the rate of change of the speed reference for a specified time period, when the wind speed drops. That way, when the wind drops from V_1 to V_2, the speed reference slowly increases, causing the operating point to move first from A to A' and then to slowly slide on the V_2 T_a-ω characteristic towards B. That way an abrupt power drop due to absence of torque is avoided. Also, if very soon, at point C the wind increases again to V_2, then the operating point moves to C', which is situated at a lower torque level than B'. That way, power excursions due to fast wind changes during the stall regulation are eliminated. Here, the time period during which the speed reference is controlled has been selected between 2.5 to 5 seconds, while a longer time period can achieve even better performance in terms of power/speed excursions. Figures 5.18(a-b) demonstrate the effectiveness of the algorithm via Simulink results, while hardware results and further details are provided in Chapter 6.

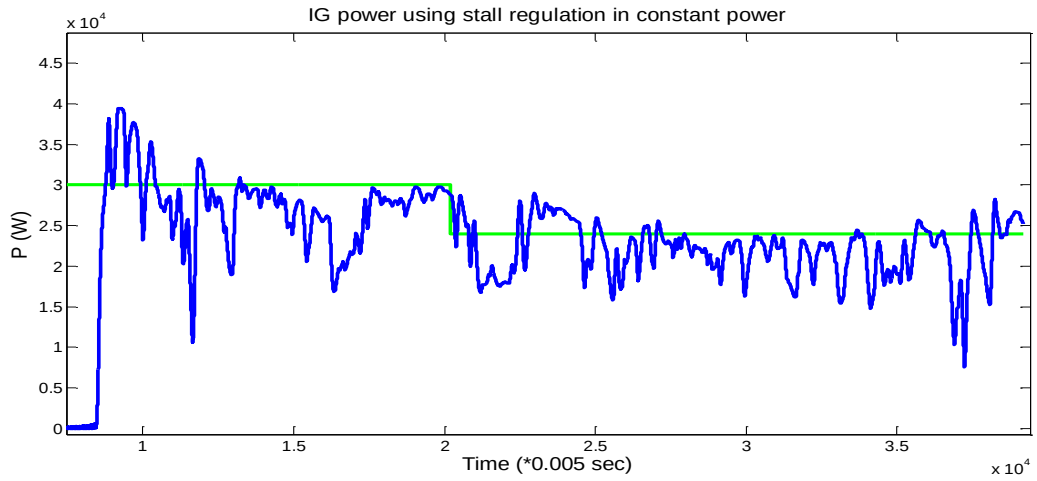

Figure 5.18 (a). Power regulation using routine-2 (blue) following a power reference (green) using mechanism for power excursions elimination.

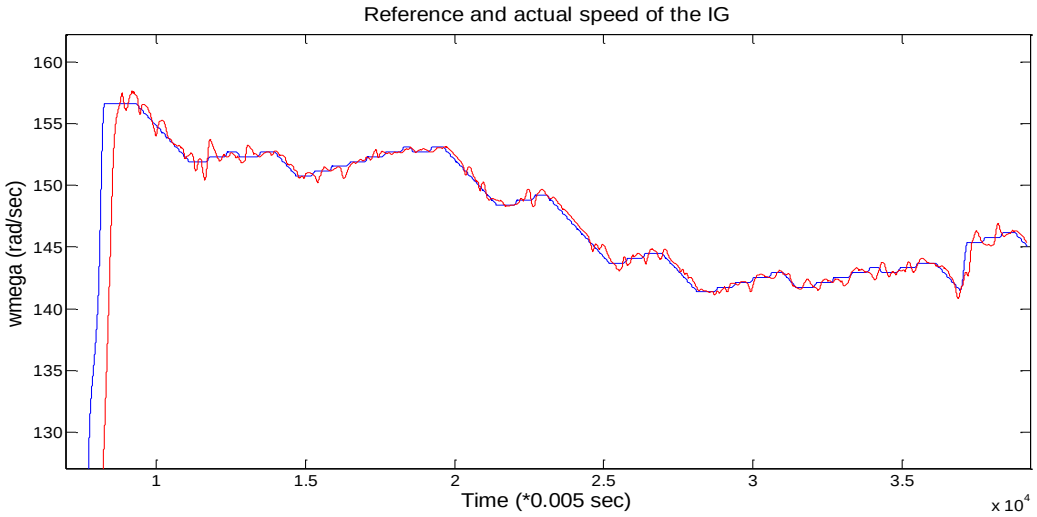

Figure 5.18 (b). ω_{ref} (blue) and ω_g (red) during power regulation.

5.5. Effect of the aerodynamic inflow on the effective wind speed estimation

So far it has been assumed that the $\hat{T}_a$ estimate obtained by the KFs is equal to the actual T_a of the rotor. However, as mentioned in Chapter 1 and 2, the value of T_a given by Eqn. (5.1) is altered due to the dynamic inflow. Therefore, in order to estimate the actual T_a of the rotor, the model of the dynamic inflow should be included in the KFs, or alternatively the $\hat{T}_a$ estimate of the KF should be passed through the inverted model of the dynamic inflow. Unfortunately, as mentioned in Chapter 2, this model is not exactly

known and therefore the V estimation is affected. Here, the impact of the dynamic inflow on $\hat{V}$ is examined.

Figure 5.19 shows T_a, evaluated using the Windharvester WT model, obtained at the output of the filter of Eqn. (2.2) with a=11.25 and b=7.25 (see Section 2.1.4) and without the use of this filter.

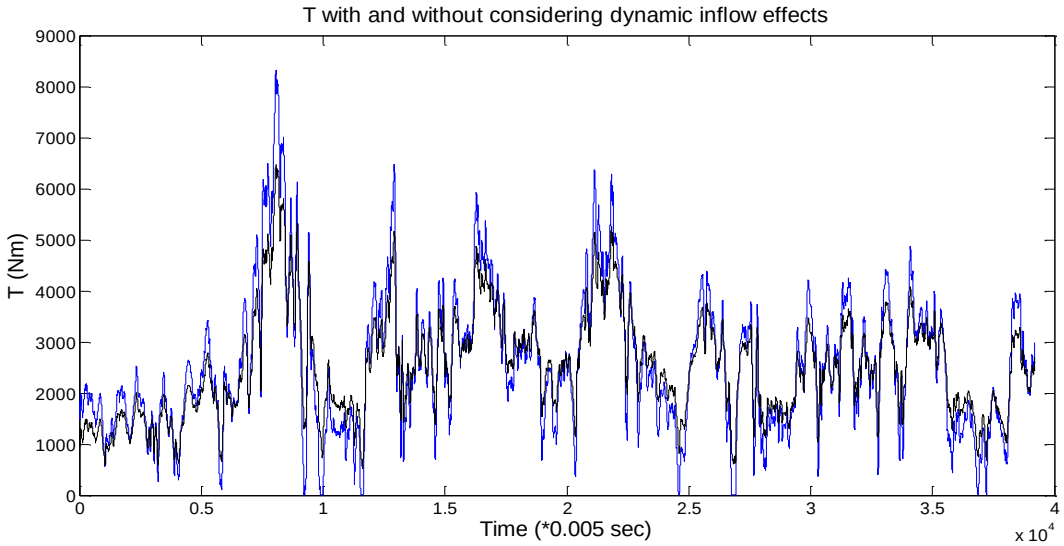

Figure 5.19. T_a with (blue) and without (black) dynamic inflow modelled. (lead lag of 11.25 and 7.25, respectively).

As can be seen, the dynamic inflow causes T_a to exhibit more extreme variations, as mentioned in [6] and this phenomenon becomes more intense as the ratio between the lead and lag coefficient of Eqn. (2.2) becomes larger.

The impact that this has in $\hat{V}$ is similar and can be seen in Figure 5.20, where the actual and the estimated effective wind speed are displayed.

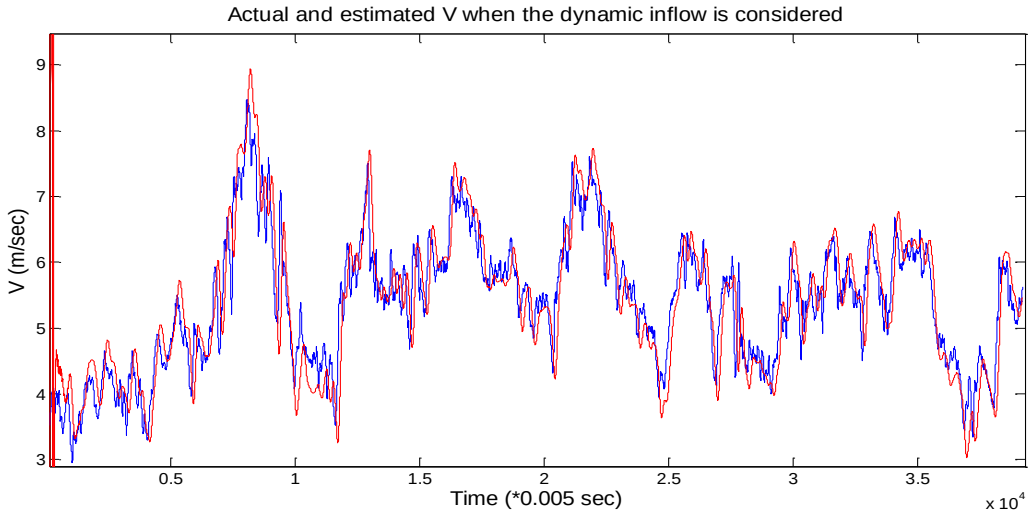

Figure 5.20. Actual (blue) and estimated (red) effective wind speed when dynamic inflow has been simulated. (lead lag of 11.25 and 7.25, respectively.)

As can be seen, $\hat{V}$ also exhibits larger excursions than what is expected by the actual V.

Figure 5.21 shows $\hat{V}$ when the lead lag coefficients have been chosen as a=11.25 and b=2.25, while Figure 5.22 shows the torque of the IG when the proposed closed loop speed control is applied (see Figure 4.1). Finally, Figure 5.23 shows the variation of C_p with time.

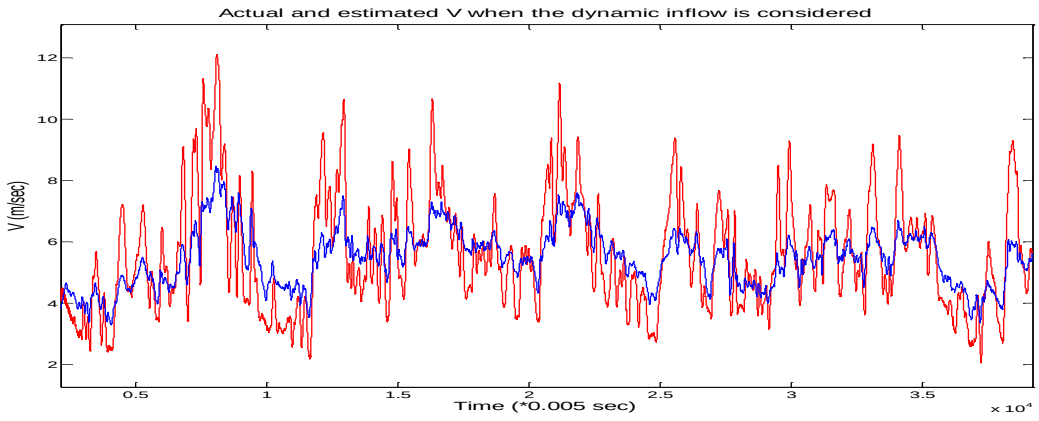

Figure 5.21. V (blue) and $\hat{V}$ (red) when dynamic inflow has been simulated. (lead lag 11.25 and 2.25, respectively.)

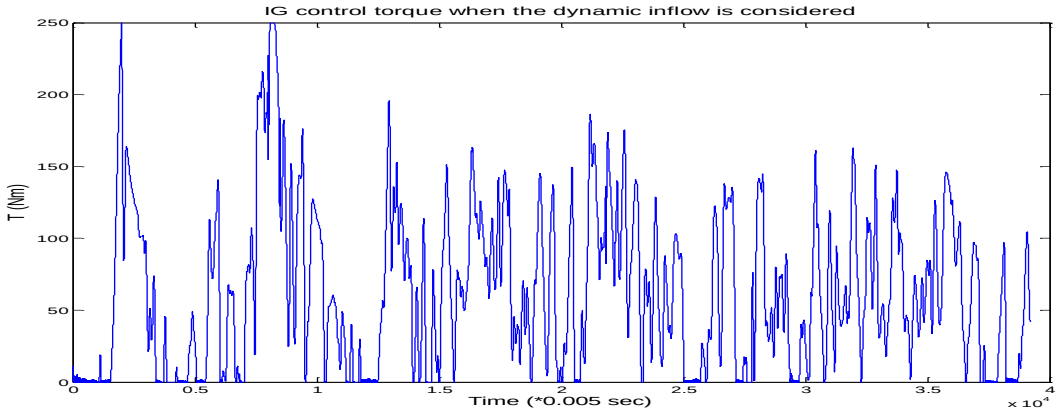

Figure 5.22. IG control torque when dynamic inflow has been simulated. (lead lag 11.25 and 2.25, respectively.)

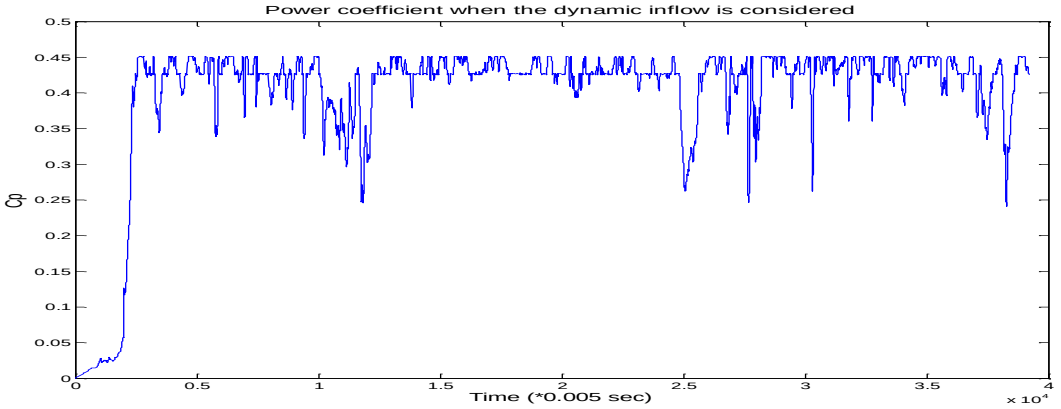

Figure 5.23. C_p when dynamic inflow has been simulated. (lead lag 11.25 and 2.25, respectively.)

As can be seen from the above figures, extreme dynamic inflow phenomena result in unacceptable IG torque control pulsations, but the control system still achieves a high C_p without considerable variations. Therefore, in order to smoothen the control torque, appropriate controller design is required or further filtering of the speed reference of the controller. Alternatively, an average static inflow model can be incorporated in the V estimation algorithm (if this can be identified), such that it provides a good compromise over the range of the intensity of the inflow effects during the operation of the WT.

5.6. Conclusions

In this chapter, effective methods to estimate the effective wind speed and to produce the optimum speed reference for the WT rotor were presented. Specifically, a thorough analysis of wind speed numerical extraction through the $T_a(V)$ characteristic using the Newton-Raphson method was presented. In addition, novel methods to overcome possible divergence of the algorithm as well as to overcome the problem of multiple solutions for V were effectively implemented and tested using the HILS. Further, in order to achieve stall regulation at constant power, a number of different novel methods were presented. The proposed methods achieved smooth power control without causing power peaks due to the nonlinear and non-minimum phase dynamics of the WT, as it was shown through software and HILS simulation results. Finally, the effect of the dynamic inflow in the performance of the wind estimation algorithm and the control system in overall was examined.

6. Speed controllers

6.1. Introduction

In this chapter the design for speed controllers for the IG of the WT is presented. The controller should satisfy conflicting specifications, such as accurate speed reference tracking and effective disturbance rejection due to high frequency components of the aerodynamic torque, but at the same time should not induce high cyclical torque loads to the drivetrain, via excessive control action. In addition, the controller should limit the torque of the IG to generating operation up to its rated torque, T_N (the last requirement can be relaxed provided T_N is not exceeded for an extensive time period).

In this chapter, the design of different types of speed controllers, such as Proportional-Integral (PI), H_∞, Linear Parameter Varying (LPV) H_∞ and Sliding Mode Controller (SMC) for the VS SR WT is presented and the performance of the controllers is assessed through software (Simulink) and hardware (HILS) simulations, while emphasis is put on the HILS results.

In HILS, the performance of each type of controller is compared with the conventional control of Eqns. (1.8) applied to the Windharvester model for below rated operation using the original and the steeper C_q/C_p curves for the rotor (see Figure 2.12(c-d)). Further, the controllers are tested for above rated operation and the advantages and disadvantages of each method are presented. Finally, HILS results for stall regulation at constant power using the power regulation algorithm of Section 5.4.2 are presented, as well as mixed operation at below and above rated conditions.

6.2. Control design considerations

In order to present the challenges in the control design, the transfer functions $G_{V\omega_2}$ and $G_{T_g\omega_2}$ of the linearized WT dynamic model are examined. A description of this model and an introduction to its dynamics for the simulated WT can be found in Sections 2.5.2 and 2.6.2, respectively, where it was shown that for deep stall operation, two conjugate zero pairs ($\mathbf{z_{1,2}}$ and $\mathbf{z_{3,4}}$) and a real pole ($\mathbf{p_5}$) of $G_{T_g\omega_2}$ move to the RHP.

Figure 6.1 shows a pole-zero plot of $G_{T_g\omega_2}$ in the complex plane, for several operating conditions. Namely, the speed of the rotor is set to its rated value, ω_1=4rad/sec, while the wind speed, V is set to 6.76m/sec (maximum aerodynamic efficiency), 10m/sec and 21m/sec, respectively. In the figure it can be seen, that as the wind speed increases and the system is gradually forced into deep stall, the real pole ($\mathbf{p_5}$), which was initially situated into the LHP moves rapidly into the RHP. The same happens for the zeros ($\mathbf{z_{3,4}}$), but in a slower rate. It is mentioned that the zeros ($\mathbf{z_{1,2}}$) that are situated near the imaginary axis at the top and bottom of Figure 6.1, also move into the RHP, but in a much slower rate. In addition, these zeros are of quite high frequency, 440rad/sec, so they do not impose any actual limitation to the control design, therefore are not further considered.

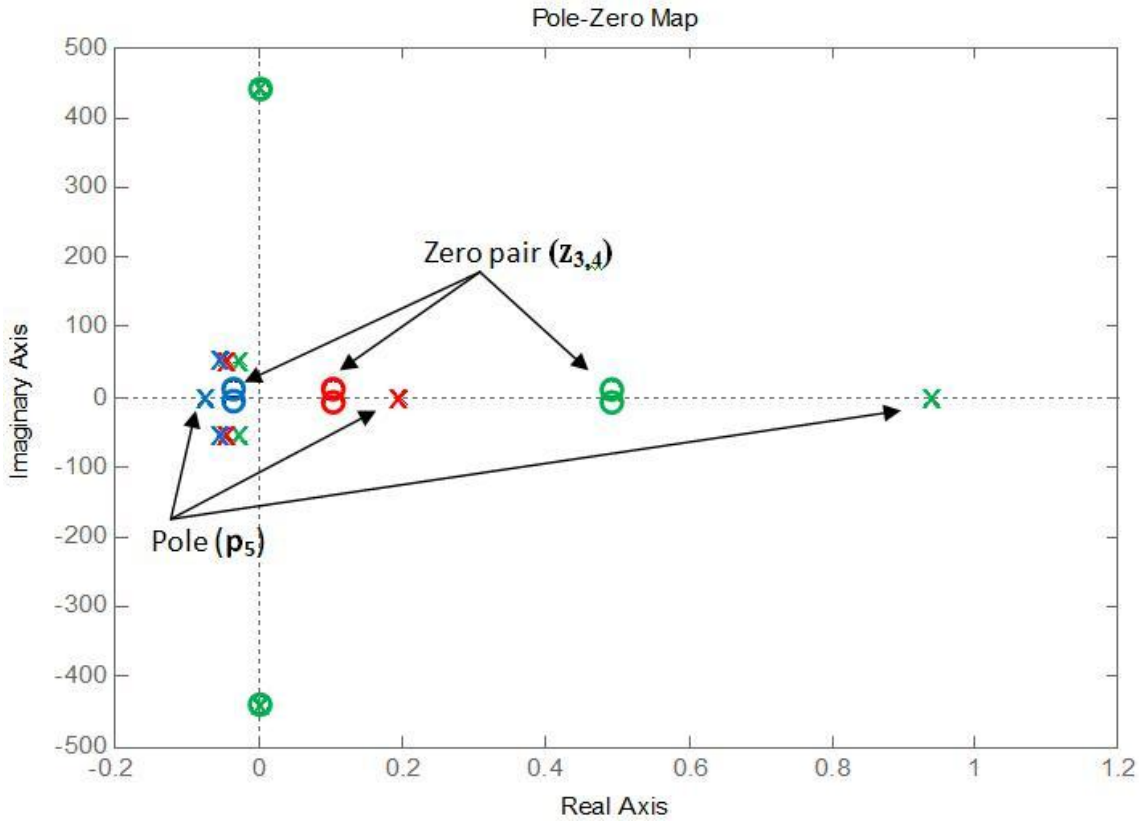

Figure 6.1. Pole and zero locations of $G_{T_g\omega_2}$ for operating conditions: ω_1=4rad/sec and V=6.76m/sec (blue), 10m/sec (red) and 21m/sec (green).

The actual limitation in the control design comes from the zeros ($\mathbf{z_{3,4}}$). Specifically, these are of quite low frequency, 10.8rad/sec, which remains constant as the zeros move to the right and have negative damping that gradually increases as the system is forced deeper into stall. In addition, the rapid movement of the pole ($\mathbf{p_5}$) to the right gradually increases the lower bandwidth requirement for the closed speed control loop, as the system is in deep stall. Table 6.1 gives details of the zeros ($\mathbf{z_{3,4}}$) and the pole ($\mathbf{p_5}$) for the three above mentioned operating conditions.

***V*(m/sec)**	**Pole (p_5)**	**Zeros ($z_{3,4}$)**
6.76	-0.0745	-0.0366±10.8i
10	0.196	0.105±10.8i
21	0.941	0.493±10.8i

Table 6.1. Pole ($\mathbf{p_5}$) and zeros ($\mathbf{z_{3,4}}$) locations with the operating conditions (rotor speed, ω_1=4rad/sec).

As can be observed, the low limit for the control loop bandwidth, imposed by the RHP pole ($\mathbf{p_5}$) increases to 0.941rad/sec at V=21m/sec and this can become quite higher as the wind speed increases to the cut-off limit of 25m/sec. Further, when the rotor speed is reduced for power limitation purposes, this causes a further shift of the pole to the right, since the system is forced deeper into stall. This can be seen in Figure 6.2, where the pole-zero positions are shown for the wind speed V=15m/sec, but for two different rotor speeds, ω_1=4 and 3.5rad/sec, respectively.

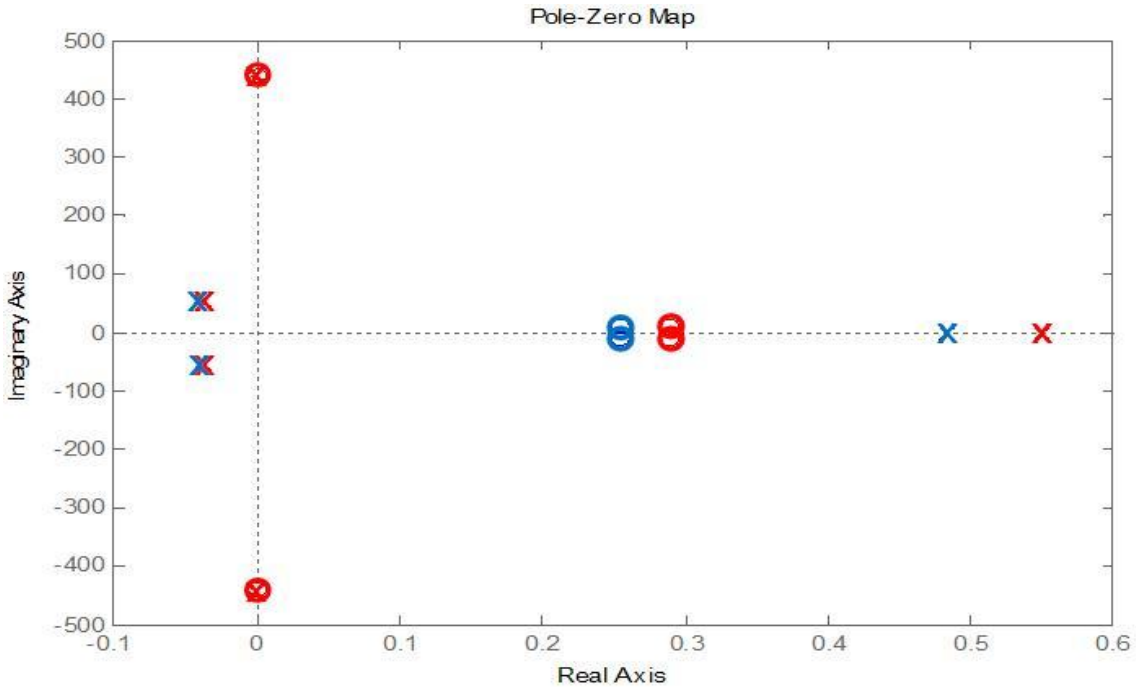

Figure 6.2. Movement of the RHP pole and zeros to the right due to rotor speed reduction: ω_1=4rad/sec (blue) and ω_1=3.5rad/sec (red).

The change in the position of the zeros and pole, respectively, is:

$z_{3,4}$: 0.254±10.8 → 0.289±10.8

p_5 : 0.483 → 0.549

As can be seen, the real part of the RHP zeros does in general not vary significantly, which can allow an upper limit for the control bandwidth of 10.8rad/sec [27]. However, the gradually increasing lower limit for the bandwidth, due to the RHP pole movement, can become quite restricting in high wind speeds.

Furthermore, the movement of the pole ($\mathbf{p_5}$) from the LHP to the RHP as the operating point of the WT passes through the top of the C_q curve, causes dramatic changes to the low frequency gain of $G_{T_g\omega_2}$. Specifically, when for high values of λ, $\mathbf{p_5}$ is situated deep inside the LHP, it contributes to a low DC gain. When $\mathbf{p_5}$ passes through zero, for λ=4.37 ($\lambda_{C_{qmax}}$, see Section 2.6), it maximizes the DC gain. Then, as it moves away from zero to the right, the gain is always reducing. Figure 6.3 shows the DC gain of $G_{T_g\omega_2}$ for several values of the effective wind speed, V and for fixed rotational speed, ω=4rad/sec. The plot clearly reflects the above observations.

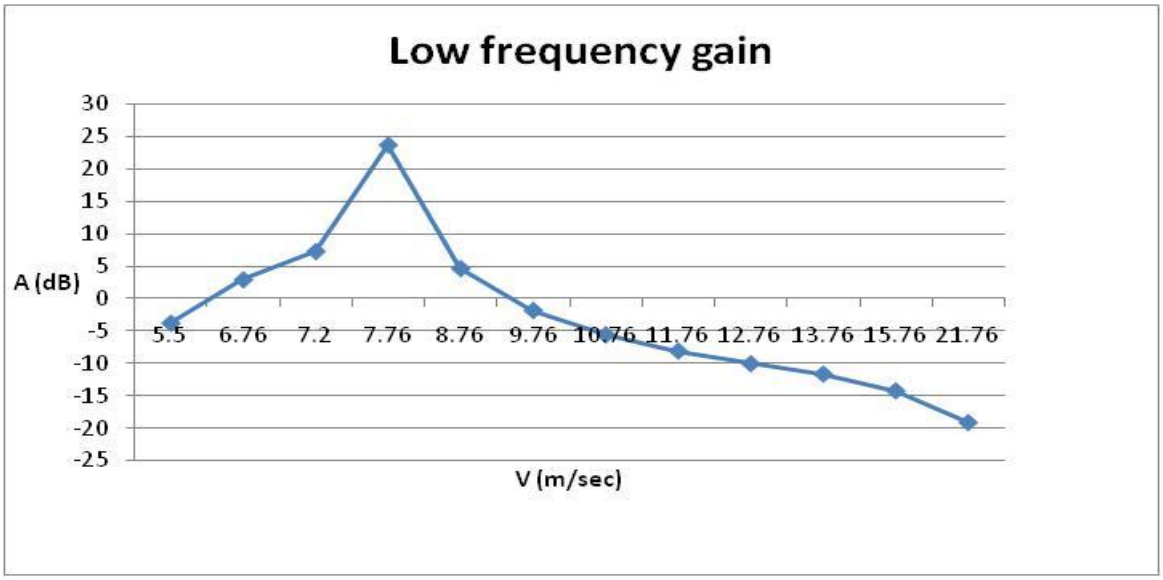

Figure 6.3. Low frequency gain of $G_{T_g\omega_2}$ versus V for fixed ω=4rad/sec.

A similar behaviour is observed for any choice of ω, while as ω decreases, slightly higher gains are observed.

Figure 6.4 shows the low frequency gain for the transfer function $G_{V\omega_2}$. As can be seen, the gain exhibits its maximum value at V=7.76m/sec, which corresponds to a tip speed ratio very close to $\lambda_{C_{qmax}}$.

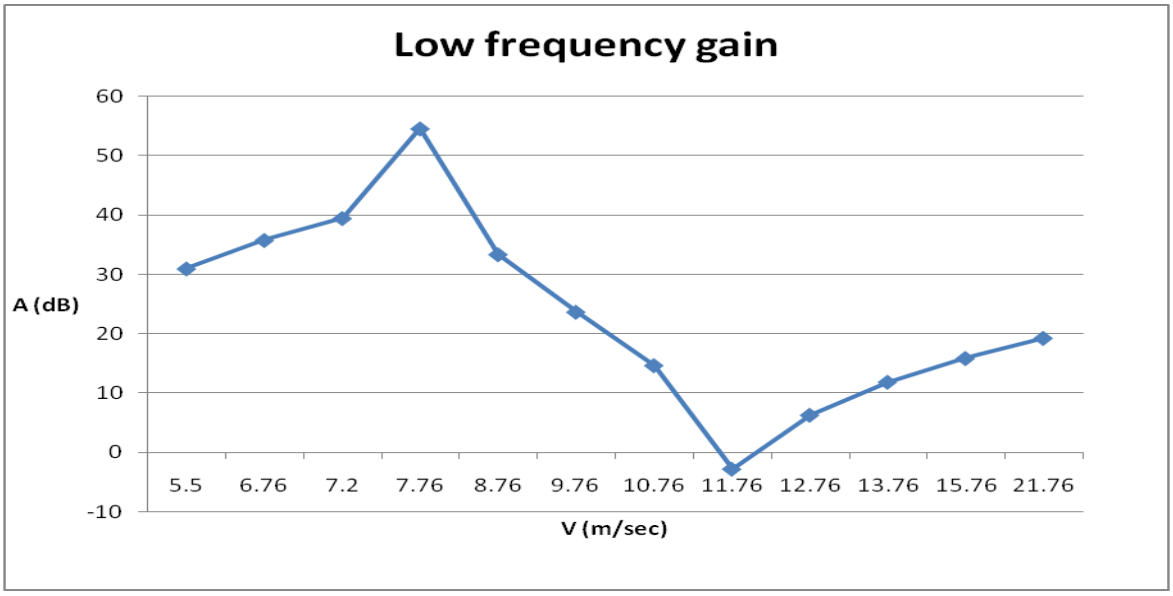

Figure 6.4. Low frequency gain of $G_{V\omega_2}$ versus V for fixed ω=4rad/sec.

From Figures 6.3 and 6.4 it can be concluded, that in general, during operation in deep stall, the controller gain requirement increases, in order to be able to compensate the gain loss of $G_{T_g\omega_2}$ at high wind speeds as well as the gradual increase of the influence of V to the WT rotational speed, as seen to happen for wind speeds above 11.76m/sec (Figure 6.4).

The above analysis has been performed specifically for the Windharvester WT (Section 2.6), since this is used for design and implementation of the controllers. However, similar properties can be observed in general for all VS SR WTs, while the particular

dynamic characteristics of each WT depend on the design of the rotor (width of the peak of the C_p curve [79]) and the drivetrain.

6.3. Wind series

The wind series that is mainly used for the simulations has been obtained from RAL and is shown in Figure 6.5. This wind series is scaled up or down appropriately by a factor k in order to simulate different wind conditions.

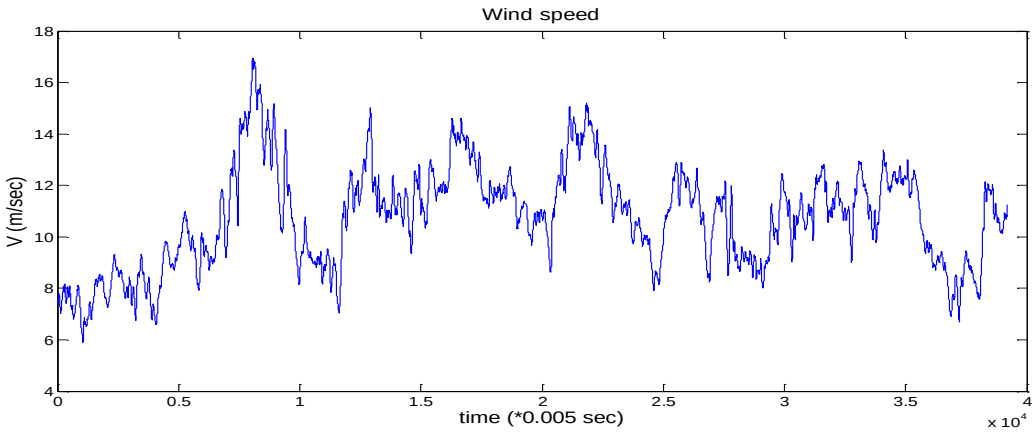

Figure 6.5. Wind speed site data series from RAL.

During the simulations the wind series passes through the rotational sampling filters for the 1st and 3rd harmonic of ω (see Section 2.1.2). Figures 6.6 (a) and (b) show ensemble wind series obtained for below and above rated operation respectively and Figures 6.6 (c) and (d) show their power spectrum, respectively, together with the power spectrum of the original series of Figure 6.5. The damping ratio for both 1st and 3rd harmonic filter (see Section 2.1.2.) was set to d=0.1, in order to evaluate the controllers in extreme disturbance variations.

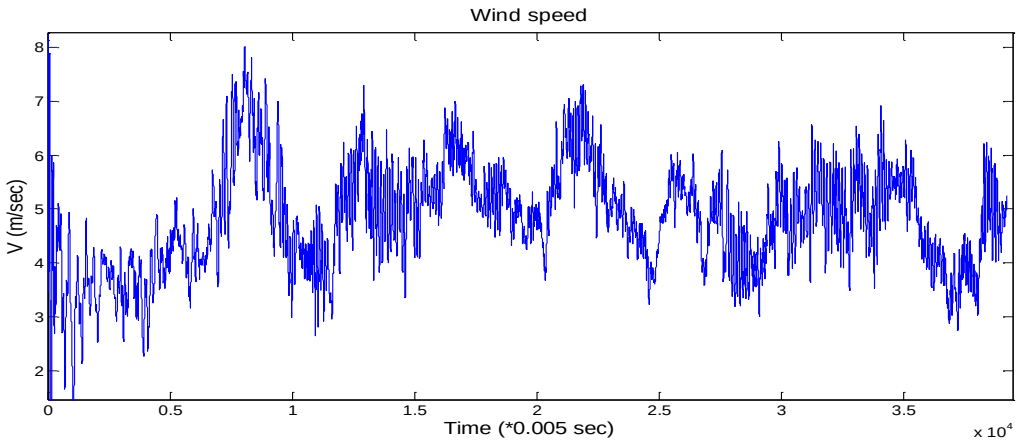

Figure 6.6 (a). Scaled down (k=0.3) effective wind speed series including rotational sampling effect for variable speed below rated operation.

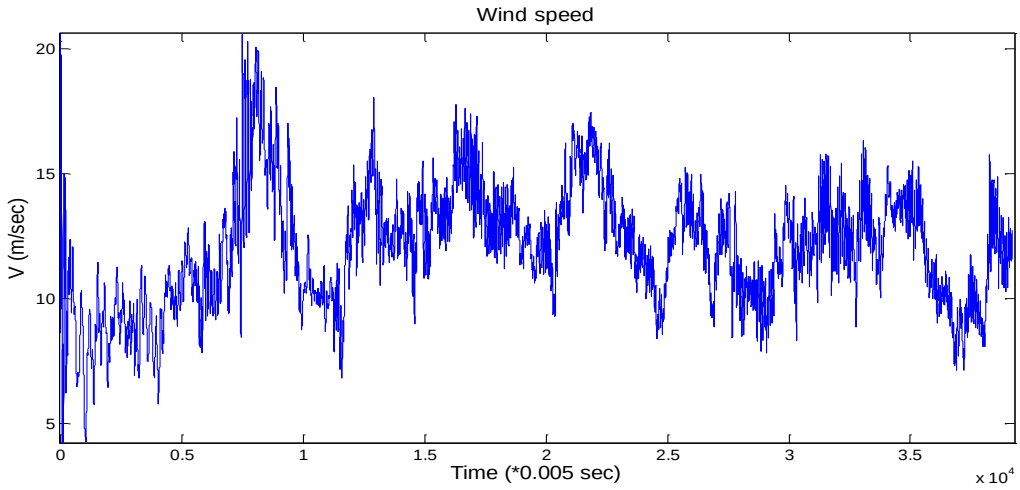

Figure 6.6 (b). Effective wind speed series with rotational sampling effect during above rated operation (the rotor speed was at 4rad/sec on average), (k=1).

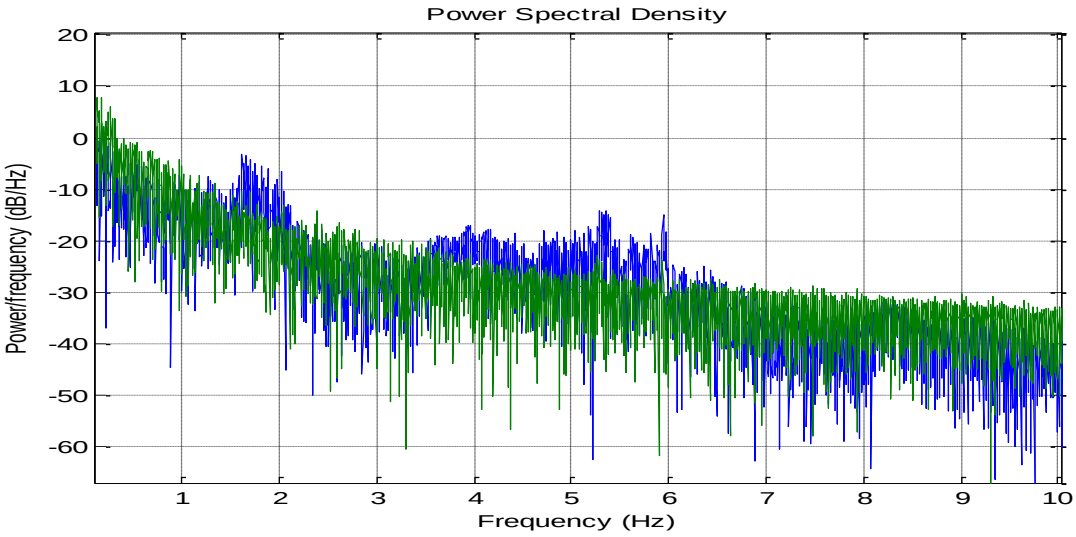

Figure 6.6 (c). Power spectrum of series of Figure 6.6 (a) (blue) and of series of Figure 6.5 (green).

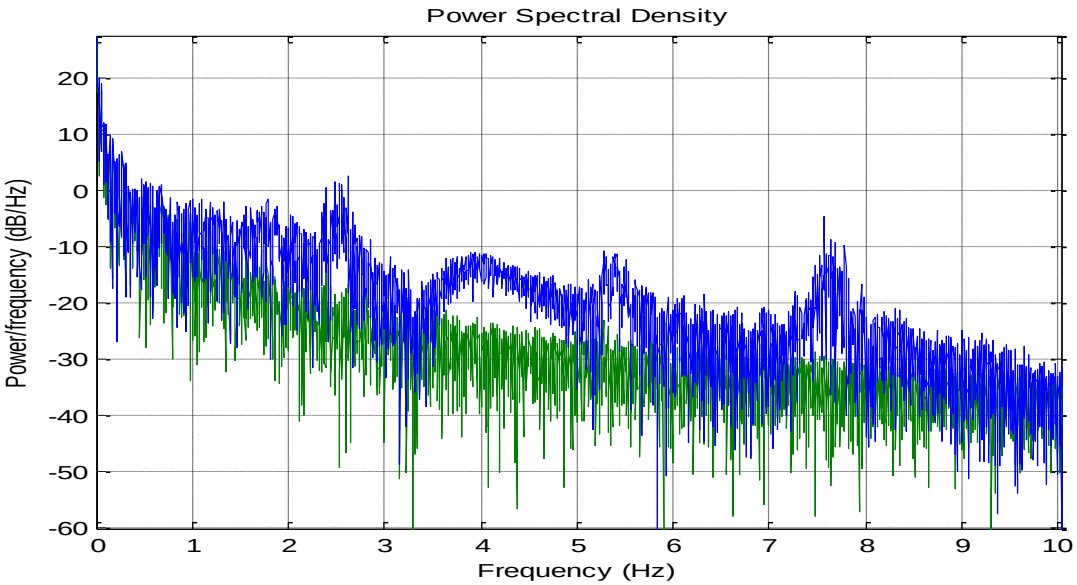

Figure 6.6 (d). Power spectrum of series of Figure 6.6 (b) (blue) and of series of Figure 6.5 (green).

As can be seen from the above figures, the wind series used for the simulations contains increased energy at higher frequencies. Also, the spectrum of Figure 6.6 (b) contains more power at higher frequencies, due to the higher rotational speed of the rotor.

6.4. Proportional-Integral controllers

6.4.1. Single Proportional-Integral controllers

6.4.1.1. Introduction

Initially, the possibility of using a single PI controller for the whole operating region of the WT was investigated. According to the previous section, this controller should be of sufficient bandwidth, in order to ensure stable operation under deep stall conditions, but at the same time should satisfy the contradicting requirement for lower controller gains and smooth control action in below rated operation. In addition, an alternative controller arrangement where the proportional term is applied only to the feedback

signal, (known as I-P controller [80, 81]) was tested, with the same PI gains. According to [80, 81] the I-P controller exhibits a reduced proportional kick and smoother control action under abrupt changes of the reference, as it is the case for below rated operation. The I-P controller is shown in Figure 6.7 inside the dashed frame. Figure 6.8 (a) and (b) show the Simulink implementation of the discrete PI and I-P controllers respectively, including a common anti-windup circuit. This circuit continuously measures the control signal before and after the saturation block and when their difference is positive, it zeros the output of the integrator through the switch. Similar approaches can be found in [81]. In Figures 6.8(a) and (b), P is the proportional gain, while the integral gain is included in the "Discrete-Time Integrator" block as a factor "K".

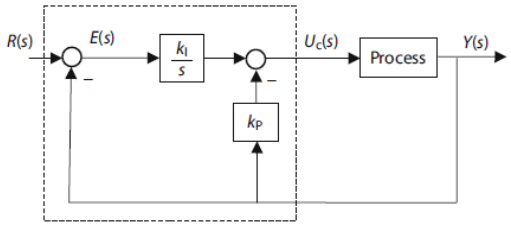

Figure 6.7. I-P controller [80].

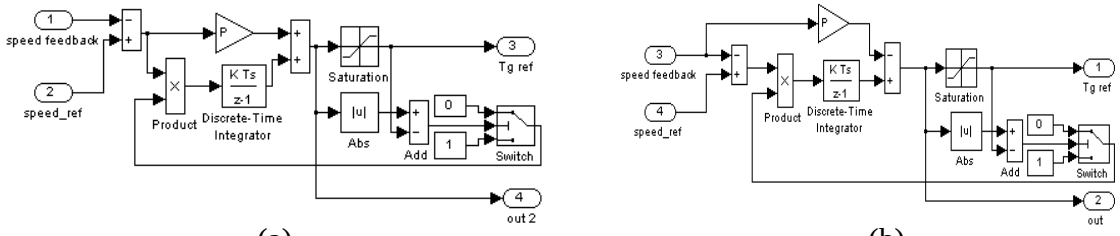

(a) (b)

Figure 6.8. Simulink implementation of (a) PI and (b) I-P controller.

In the above schemes all the input signals are assumed discretized. The sampling time of the controllers has been set to T_s=5msec, which results in a sampling frequency f_s=200Hz, which is 3 times higher than the fastest mode of the WT model (440rad/sec, see Section 2.6), and is therefore considered sufficiently high [82]. As can be seen, a

digitized output "2" provides the control output before the saturation. Its use will be seen in the next section.

6.4.1.2. Simulation results

Suitable gains for both controllers that satisfied the mentioned objectives are ***P***=20 and ***I***=10 Nm/rad/sec. Through Matlab modeling, it was established that these gains achieved stable operation of the WT for tip-speed ratios down to λ=1.12. Figure 6.9 shows the Bode plots of the closed loop transfer function from ω_{ref} to ω_2, $G_{\omega_{ref}\omega_2}$ of the WT with the continuous time I-P speed controller for two operating points, namely:

1) $\boldsymbol{\omega_1}$**=4rad/sec** and ***V*****=6.76m/sec** and

2) $\boldsymbol{\omega_1}$**=4rad/sec** and ***V*****=30m/sec**,

where ω_1 is the rotor speed according to the WT dynamic models of Chapter 2.

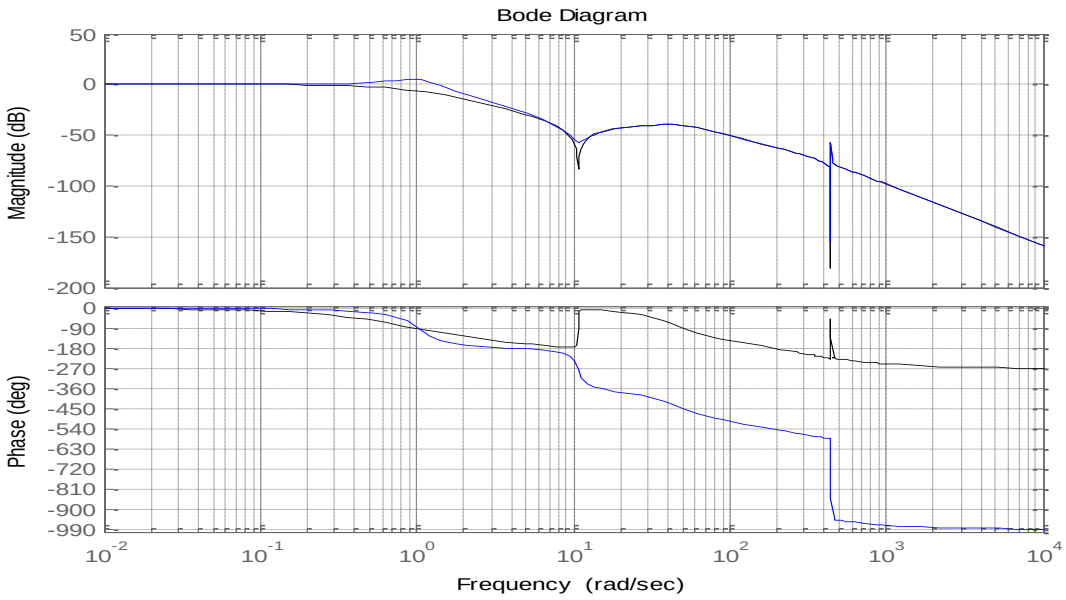

Figure 6.9. Bode plots of $G_{\omega_{ref}\omega_2}$ for operating conditions (1) (black) and (2) (blue).

As can be seen, the bandwidth of $G_{\omega_{ref}\omega_2}$ is 0.6rad/sec (-3dB) for operating conditions (1) while it is increased to 1.5rad/sec (-3dB) for operating conditions (2), where the system becomes more oscillatory as this is indicated by the peak of the magnitude Bode plot at 1rad/sec. It is mentioned that the above Bode plot analysis is also valid for the discrete time controller, for frequencies $\omega < \frac{2\pi f_s}{2} = 628.31$rad/sec.

A) Simulink simulation results

Figure 6.10 (a) shows the control action of a PI and an I-P controller for below rated operation and (b) shows the achieved C_p representing the aerodynamic efficiency for the two controllers. Also, Figure 6.10 (c) shows the control action for above rated winds and (d) the speed response of the WT. The simulations last 196 sec (39200 simulation steps of 5msec).

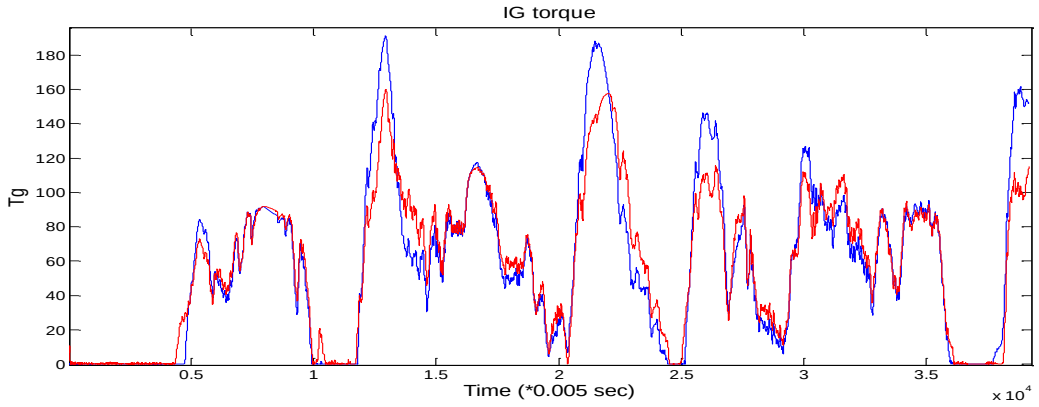

Figure 6.10(a). Control action of PI (blue) and I-P (red) controller.

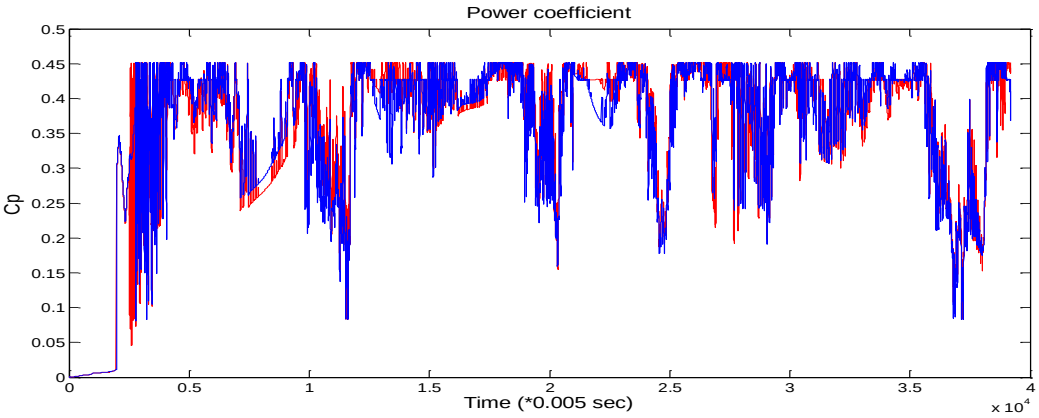

Figure 6.10(b). Corresponding C_p over time for below rated operation.

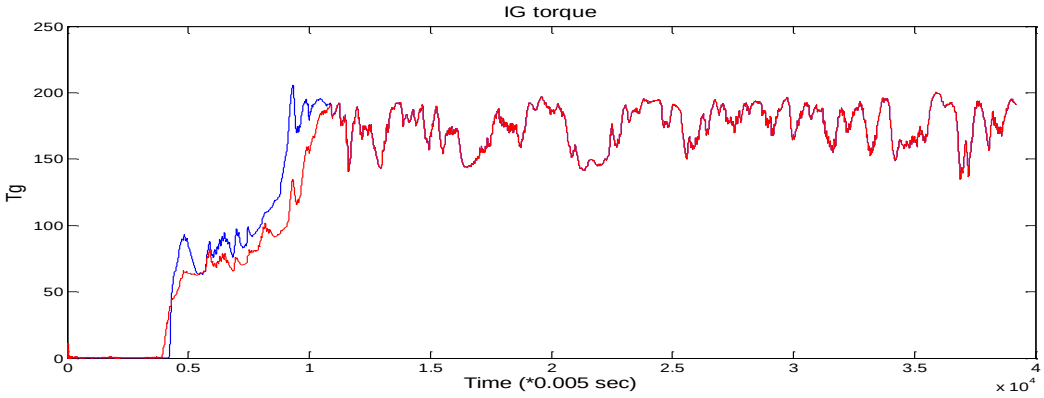

Figure 6.10(c). Control action for above rated operation.

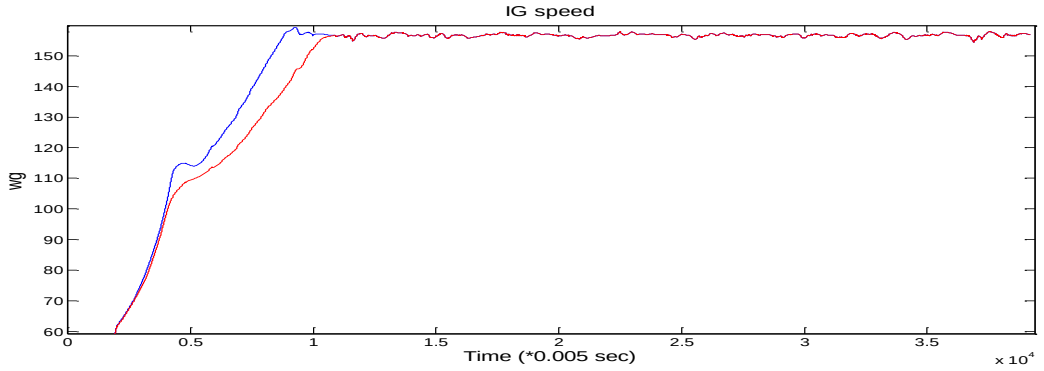

Figure 6.10(d). IG speed response.

From Figures 6.10 (a) and (b) it can be observed that the I-P controller reduces the pulsations of the control action and at the same time achieves aerodynamic efficiency comparable to the PI controller. Further, from Figures (c) and (d) it can be seen that the I-P controller achieves a smoother transition when the rated speed of the WT is reached (157rad/sec at the generator side).

B) Simulation results using the hardware in the loop simulator

Here, HILS results for the Windharvester WT for below rated operation are presented using the proposed control scheme for the IG (see Figure 4.1) with the I-P controller. The selected PI gains are 10 and 20 Nm/rad/sec, respectively. The speed reference for the controller is produced by the arrangement described in the introduction of Chapter

4, with an IAE AKF (Section 4.8.2) and a NR routine. The time series for the wind speed, IG speed reference, IG speed, torque, C_p, IG power and accumulated energy are shown in Figures 6.11(a-g) below.

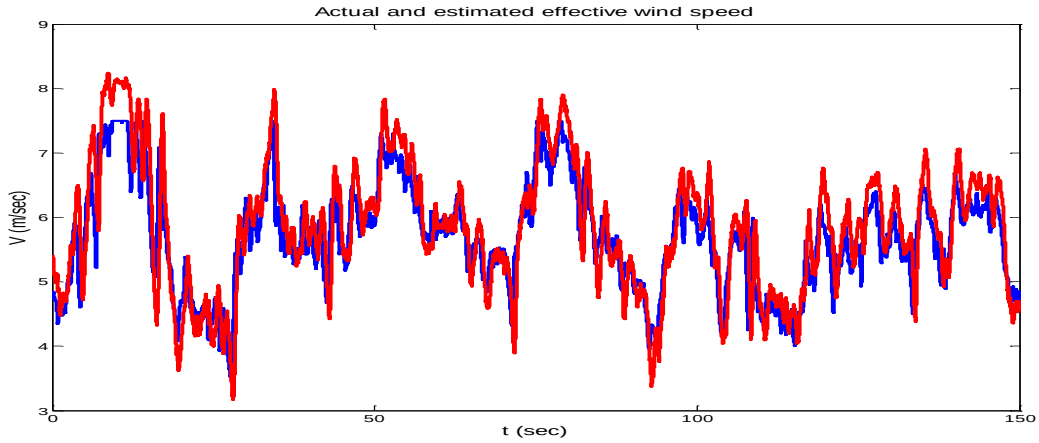

Figure 6.11 (a). Actual (blue) and estimated (red) wind speed.

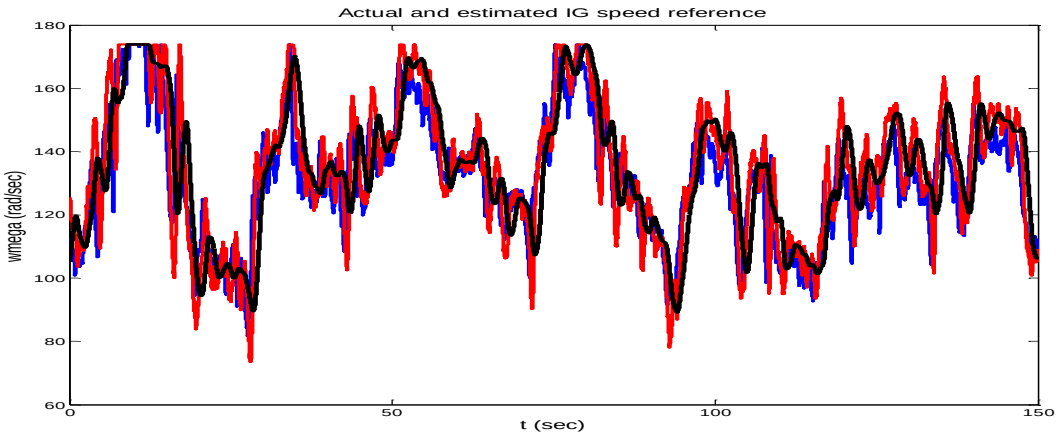

Figure 6.11 (b). Ideal (blue), estimated (red) and low pass filtered estimated IG speed reference (black).

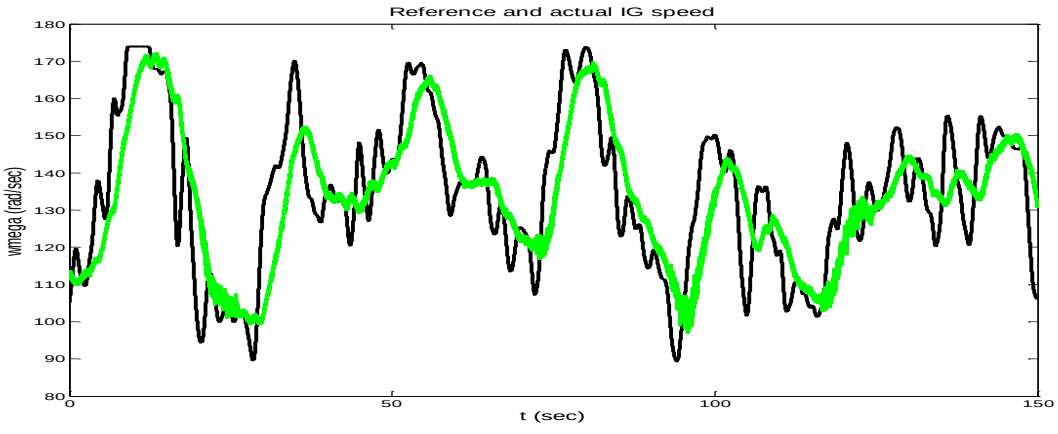

Figure 6.11 (c). Reference (LPF) (black) and actual (green) IG speed.

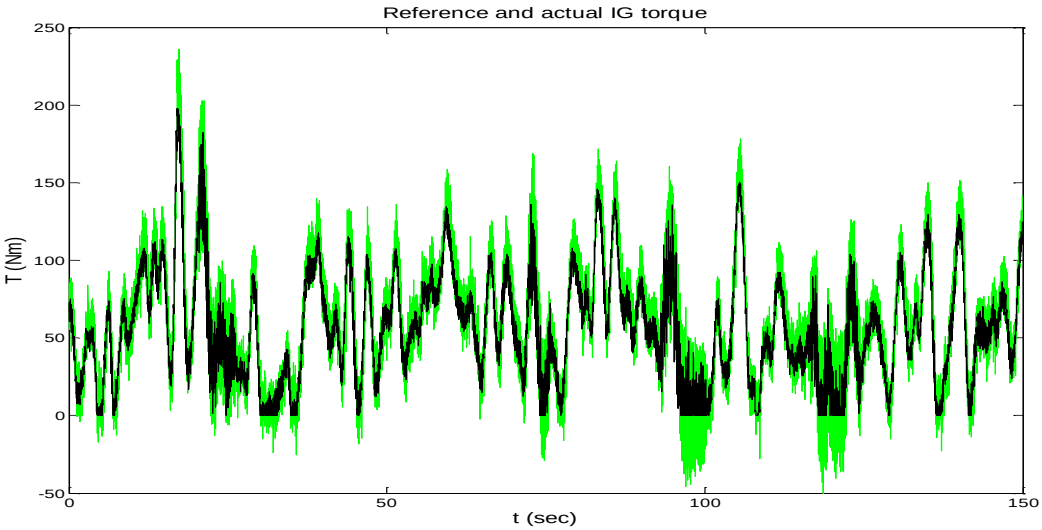

Figure 6.11 (d). Torque demand ($T_{g_{ref}}$) (black) and actual IG torque (T_g) (green).

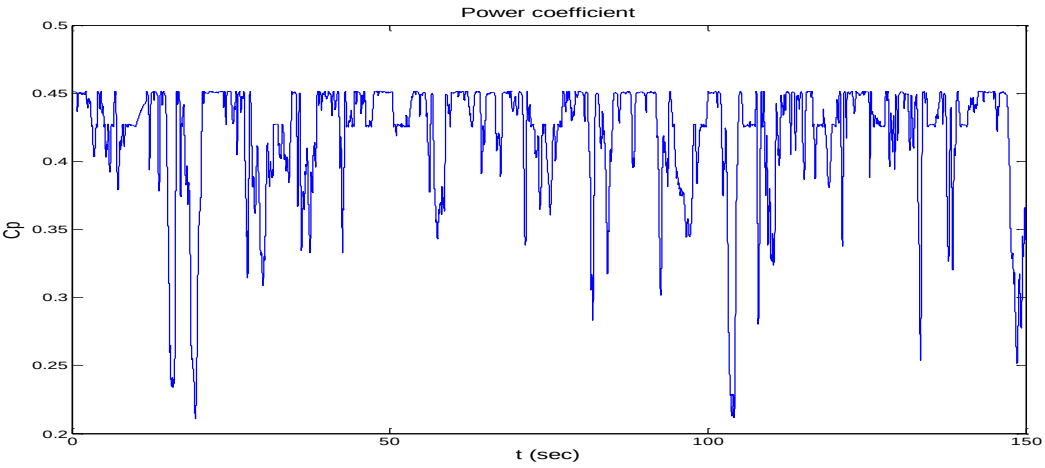

Figure 6.11 (e). Power coefficient in time.

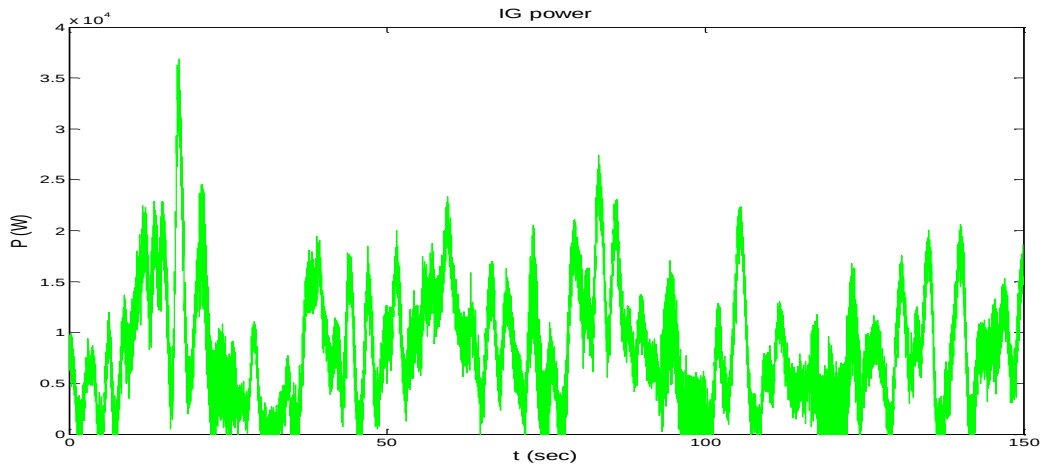

Figure 6.11 (f). IG power in time.

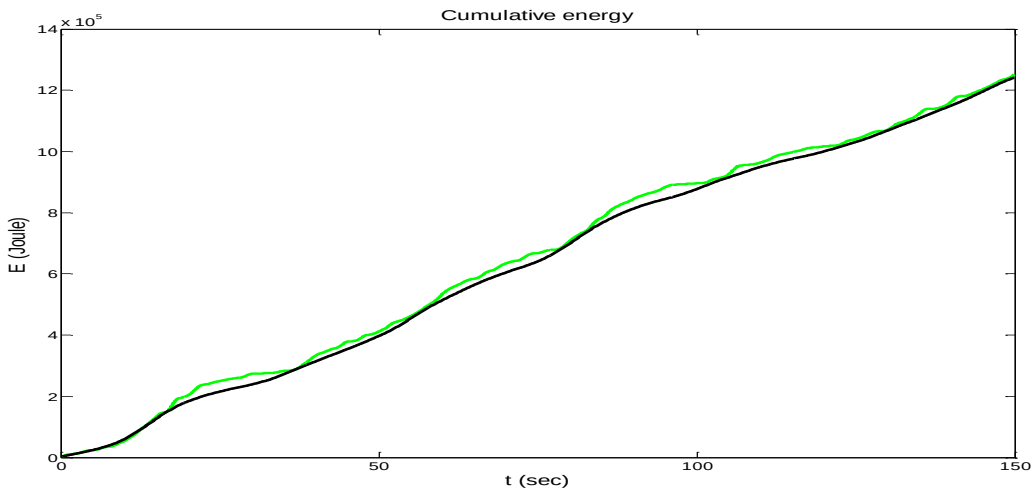

Figure 6.11 (g). Cumulative energy with the conventional control (Eqn. (1.8)) (black) and with the proposed control (green).

From the above figures it can be seen that the wind speed estimation is quite accurate, although peaks are observed, due to the absence of dynamic inflow model (a=11.25, b=7.25) in the estimation algorithm, as expected from Section 5.5 and also due to the unmodeled HILS dynamics, which cause larger excursions of the estimated aerodynamic torque, as expected from Section 4.8.1.4 (see Appendices A.13&23). The resulting speed reference is quite close to the ideal one and after it is low pass filtered, the influence of the torque peaks due to the dynamic inflow are effectively eliminated. Also, the cumulative energy stays always slightly above the one produced by the conventional control (Eqns. (1.8)), although the gain in the energy is negligible as expected for rotors with a broad peaked C_p curve (Figure 2.12).

The advantage of the method can be seen, when the sharper C_p curve of Figure 2.12 is used. It is mentioned that although the sharper C_p curve is used in the WT model, for the speed reference calculation, the original C_p curve is still used for design simplicity (Figure 5.1). In addition, the effective wind speed now includes rotational sampling effects. The following figures show the obtained results. The input wind speed has been limited to 7.5m/sec in order to limit the developed torque levels on the HILS.

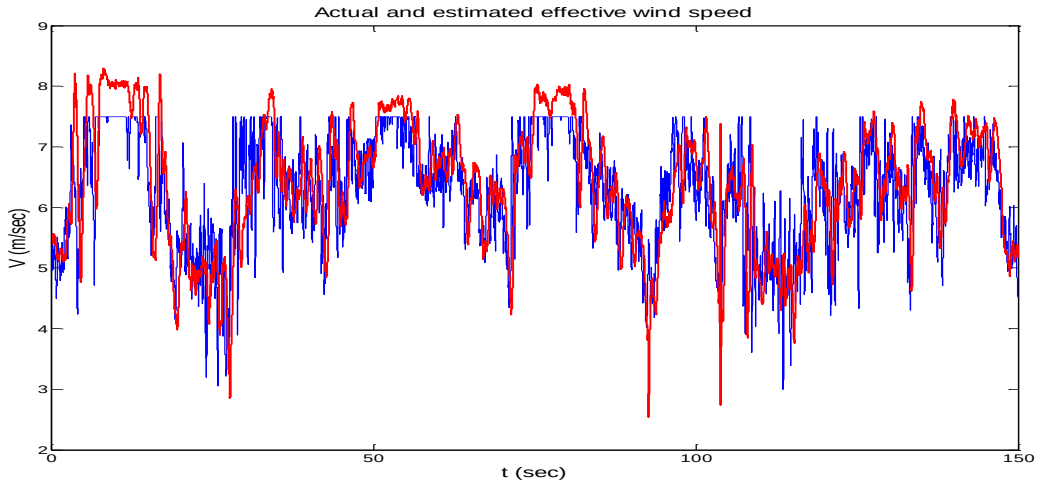

Figure 6.12 (a). Actual (blue) and estimated (red) wind speed.

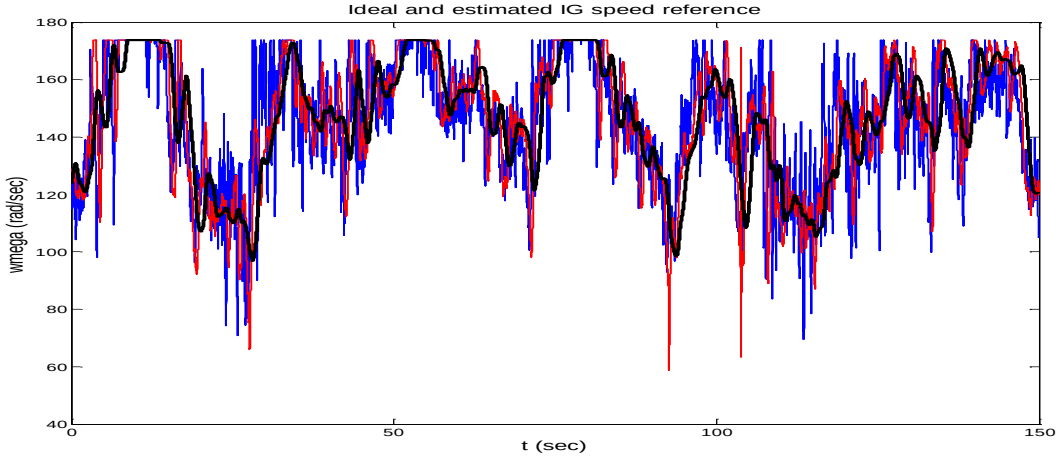

Figure 6.12 (b). Ideal (blue), estimated (red) and low pass filtered estimated IG speed reference (black).

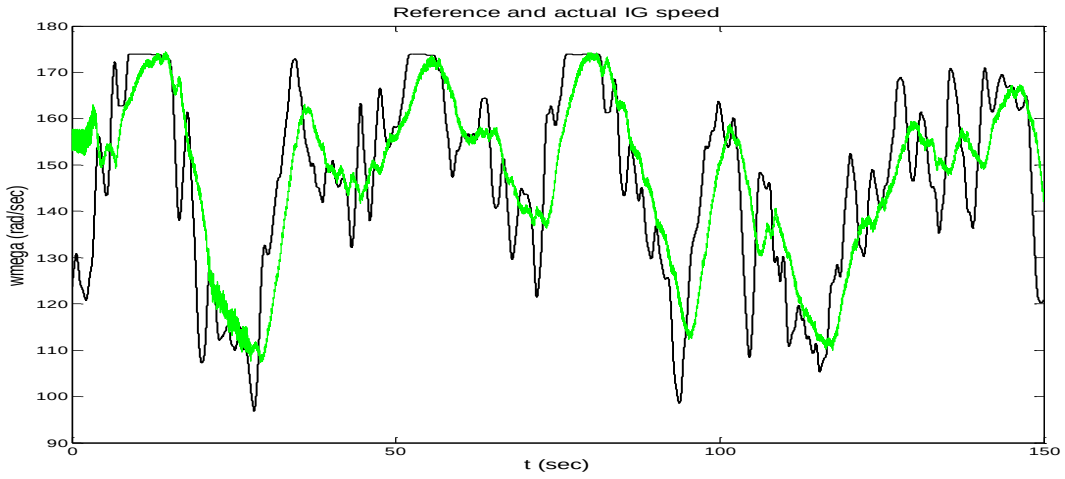

Figure 6.12 (c). Reference (LPF) (black) and actual (green) IG speed.

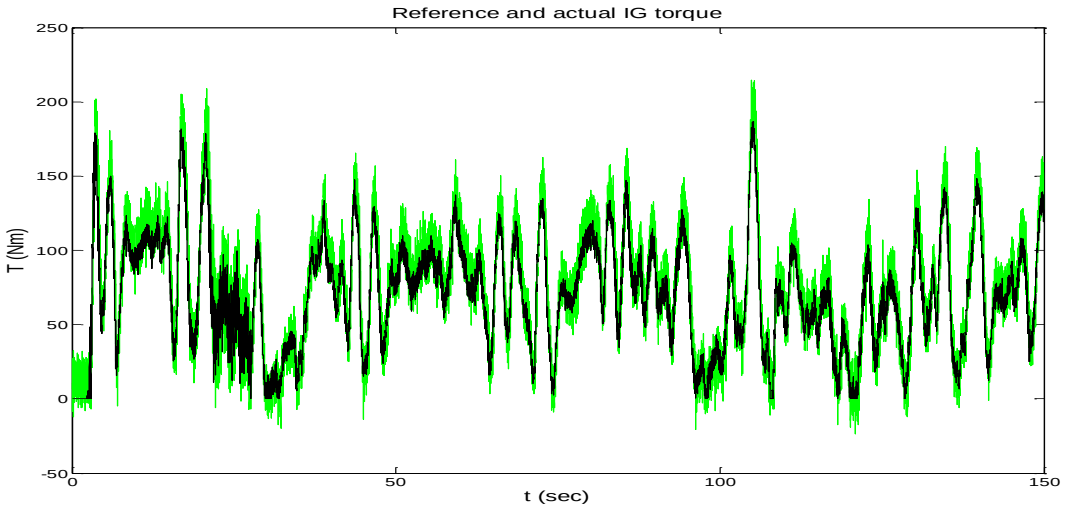

Figure 6.12 (d). Torque demand ($T_{g_{ref}}$) (black) and actual IG torque (T_g) (green).

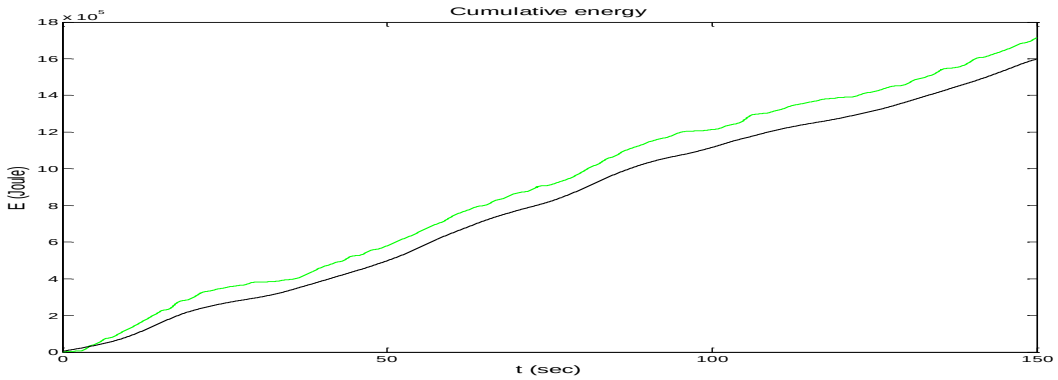

Figure 6.12 (e). Cumulative energy with the conventional control (Eqn. (1.8)) (black) and with the proposed control (green).

As can be seen from Figures 6.12(a-e) the control scheme is quite effective for below rated operation for a rotor with steeper C_p characteristic, even without readjustment of the approximation of the new C_p curve in the NR algorithm (Chapter 5). This can be seen by the considerable gain of 6.5% in the cumulative energy. Also, this gain offers a further reduction in the control torque pulsations by relaxing the controller tracking or by further filtering the speed reference without a considerable energy loss.

It is noted that the energy levels of Figure 6.12(e) are higher than of Figure 6.11(g), because the additional effective wind speed pulsations due to the rotational sampling

frequencies, contribute to smaller excursions from the peak of the C_p curve when considered in a long time horizon (see Figures 6.11(c) and 6.12(c)).

Figure 6.13 shows the extracted cumulative energy with (1) the conventional control and (2) an I-P controller of lower I-P gains of 8 and 4 Nm/rad/sec, respectively for (a) the original and (b) the steeper C_p curve (it is noted that Figure 6.13 has been obtained for lower wind speeds, so the energy levels between Figures 6.13 and 6.12(e) cannot be compared).

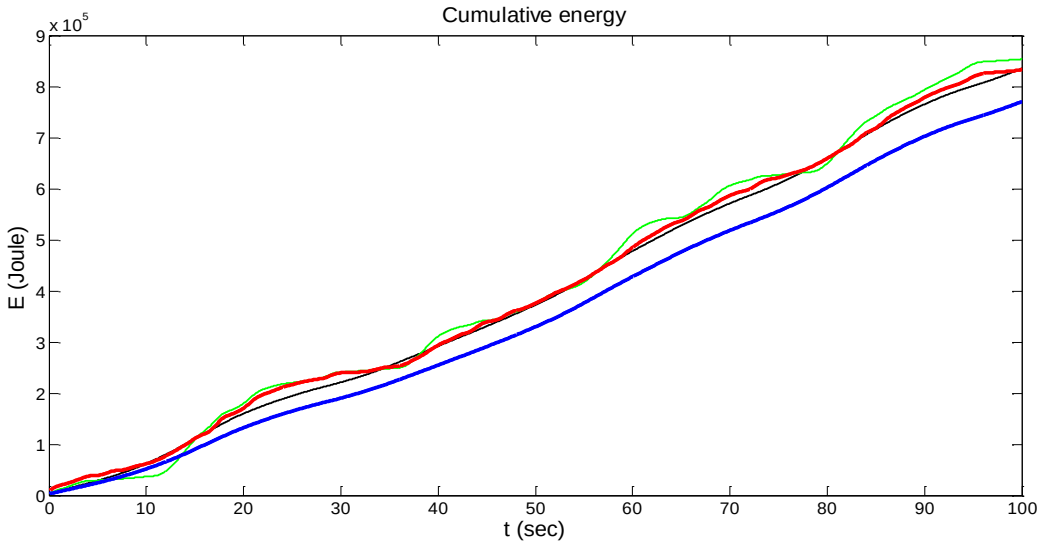

Figure 6.13. Cumulative energy with (1a) conventional (black) and (2a) I-P control (green) with the original C_p curve. (2a) conventional (blue) and (2b) I-P control (red) for steeper C_p curve.

From Figure 6.13 a considerable energy gain can be observed even with the use of a less tight speed controller.

Finally, Figure 6.14 demonstrates the tracking of the I-P controller of Figures 6.11-12 for above rated conditions, where the applied wind speed is the same as that of Figure 6.5. In Figure 6.14 the rated speed has been set ω_R=4rad/sec (ω_g= 157rad/sec), corresponding to $C_{p\,max}$ operation at $V_{\omega_R} = 6.76$m/sec.

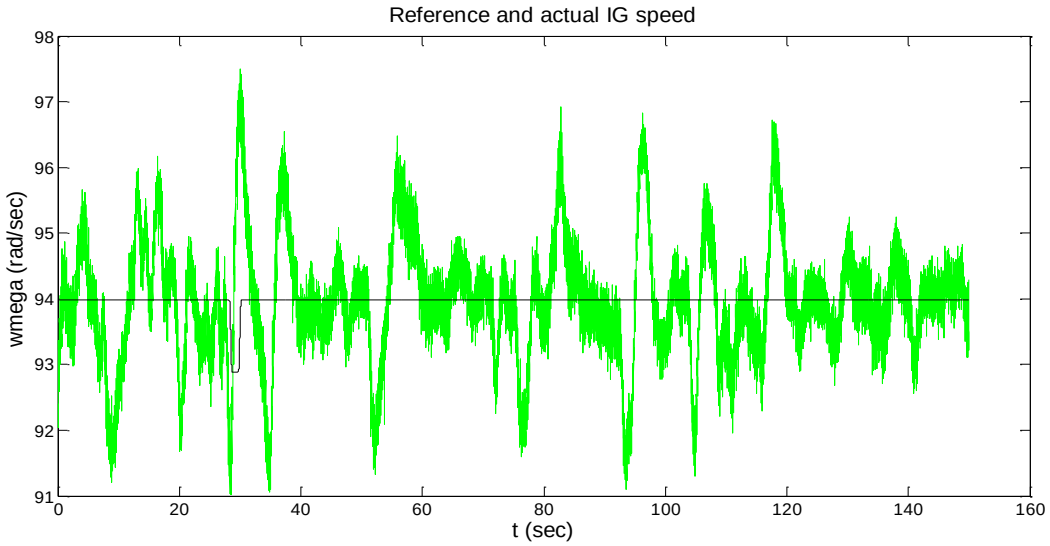

Figure 6.14. Reference (LPF) (black) and actual (green) IG speed.

Figure 6.14 shows poor reference tracking in high wind speeds, which is expected due to the low achievable bandwidth with this I-P controller. For that reason, a gain scheduled scheme with two I-P controllers is presented in the next section.

6.4.2. Gain scheduled proportional-integral controllers

6.4.2.1. Introduction

As was shown in the previous section, it is desirable to achieve tight speed control for above rated conditions, without impacting on the below rated performance of the WT. In order to achieve this, more than one controller is required. Here, an arrangement with two I-P controllers is described, one for below and one for above rated operation, scheduled according to the generator speed, ω_2. For the smooth transition between the controllers, a bumpless transfer circuit is included, based on the method described in [83]. Figure 6.15 (a) shows the whole scheme and (b) its Simulink implementation with two I-P controllers.

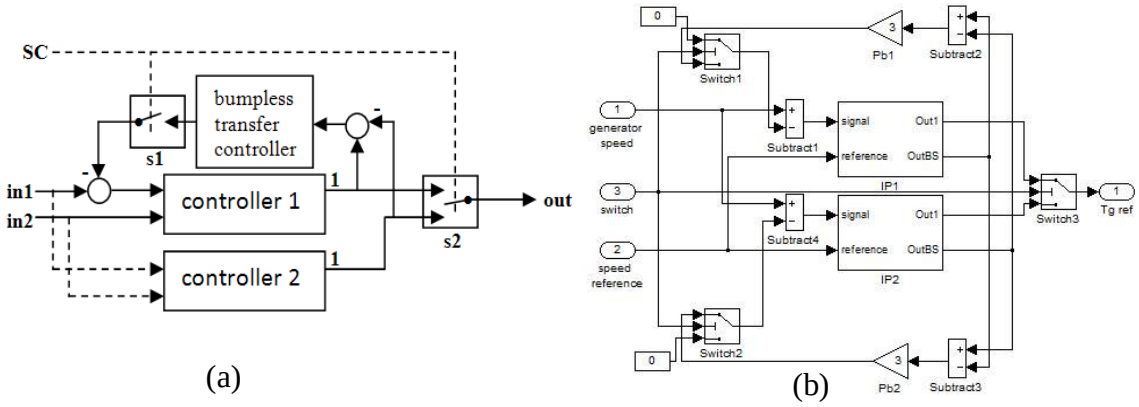

Figure 6.15. (a) Gain scheduled controller with bumpless transfer circuit and (b) Simulink implementation for two I-P controllers.

As can be seen in Figure 6.15 (a), there is a Switch Command (SC) signal that selects the control output via switch "s2". The same signal is responsible for the activation of the Bumpless Transfer Controller (BTC). Specifically, when "controller 2" is activated, the BTC for "controller 1" is activated too. The BTC receives as input the difference of the outputs of the two controllers and drives "controller 1" through one of its inputs such that this difference becomes zero. It is mentioned that the same BTC exists for "controller 2", but if the dynamic characteristics of the two controllers are not very different, a single BTC can be used for both of them. Finally, in the case that each controller has its own BTC, this can be also used as anti-windup compensator when the controller is activated, eliminating that way the anti-windup circuit of Figure 6.8. For the present application all these schemes exhibit the same performance, so they are not discussed separately.

In the Simulink implementation of Figure 6.15 (b), it can be seen that two proportional controllers (gains "Pb1" and "Pb2" respectively) are used and applied to the "signal" input of the I-P controllers. The BTCs have as inputs the difference between the "OutBS" outputs of the I-P controllers, which correspond to the outputs "2" shown in Figure 6.8. Through simulations a suitable choice for the proportional gain for the BTC

was found to be 3rad/sec/Nm. It is noted that in the literature BTCs are found to be connected to the reference inputs of the controllers. However, here these are connected to the feedback path, as otherwise the path through the proportional term of the I-P controllers is not affected.

The proposed scheme for the switching between I-P1 and I-P2 is based on the IG speed, ω_2 and the operating mode of the WT (maximum power point or stall regulation operation). Specifically, I-P2 is activated when $\omega_2 > \omega_{HIGH}$, where ω_{HIGH} is a selected upper bound for the IG speed, while I-P1 is activated when $\omega_2 < \omega_{LOW}$, where ω_{LOW} is a low bound for the IG speed. The region between ω_{LOW} and ω_{HIGH} is a deadzone, which is created in order to avoid continuous switching between IP1 and IP2 due to wind turbulence. Further, since $\omega_2 < \omega_{LOW}$ can also happen when stall regulation is in operation, a flag "fl" associated with this event is checked, before operation is returned to I-P1, since for stall regulation tighter controller is required. The scheme can be described by the flowchart of Figure 6.16.

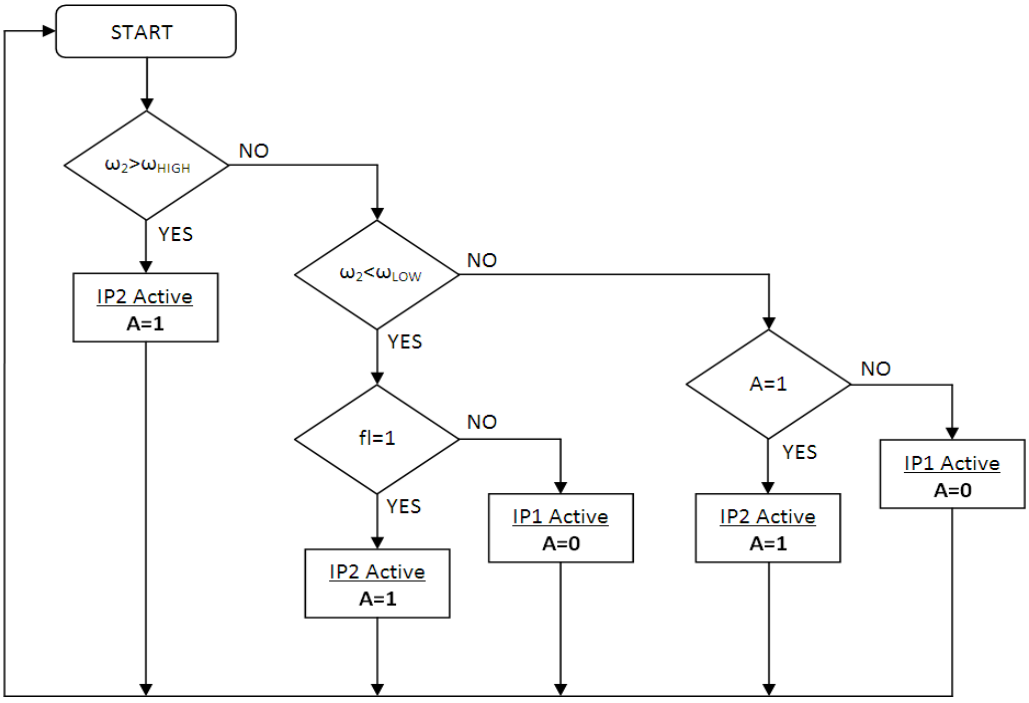

Figure 6.16. Flowchart of the switching logic between the controllers.

As can be seen, a variable A is associated with the states of the flowchart (A=1 when I-P2 is ON and A=0 when I-P1 is ON), in order to provide one state memory for the switching decision when $\omega_{LOW} < \omega_2 < \omega_{HIGH}$.

Here, the following choices for the parameters were made: ω_{HIGH}=155rad/sec, ω_{LOW}=154rad/sec.

It is mentioned that the above switching scheme is used for switching between two controllers. In practice more controllers may be required, in order to smoothly change the control over a wider bandwidth range, since a transition between a very slow and a very fast controller would cause abrupt changes in the torque. In case more than one controller are used for the stall region an additional criterion, based on the estimated λ, will be necessary.

6.4.2.2. Simulation results

A) Software modeling of controller for above rated operation

The dynamic behavior of an I-P controller (I-P2) for above rated operation, with gains K_p=30 and K_I=50 Nm/rad/sec is examined here through software modeling. Figure 6.17 shows the Bode plots of $G_{\omega_{ref}\omega_2}$ for ω_1=4rad/sec and V=30m/sec.

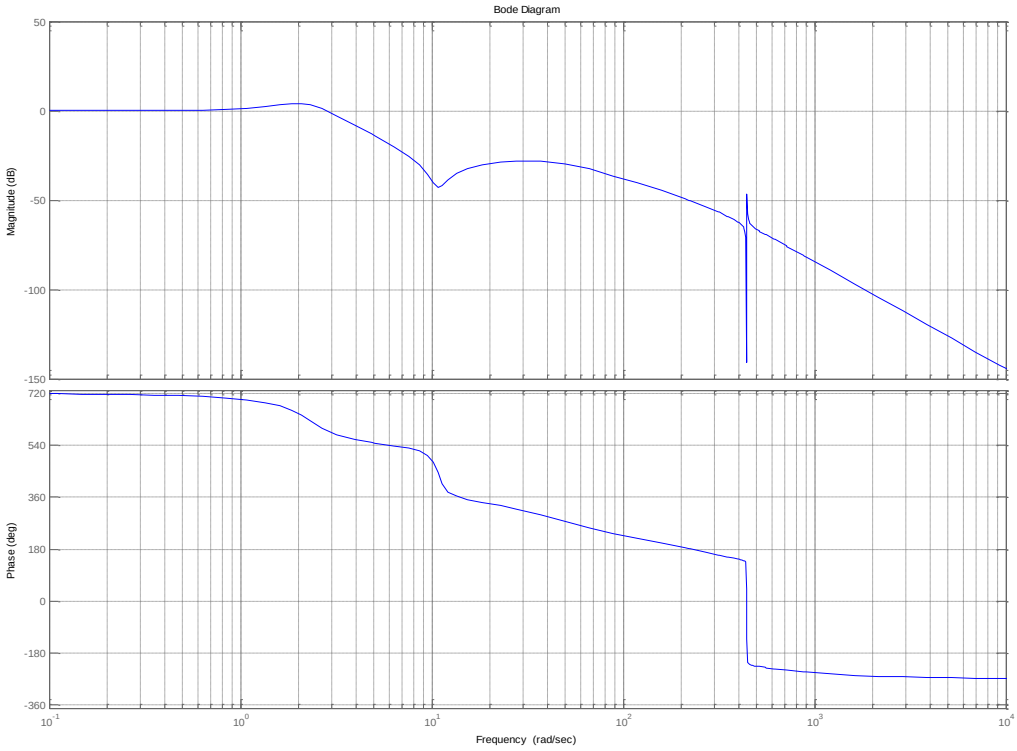

Figure 6.17. Bode plots of $G_{\omega_{ref}\omega_2}$ for ω_1=4rad/sec and V=30m/sec.

As can be seen, the bandwidth of $G_{\omega_{ref}\omega_2}$ is increased to 3.2rad/sec, while the magnitude plot exhibits a reduced peak at 2.2rad/sec (4.2dB) compared to the one of Figure 6.9 (blue) at 0.9rad/sec (5.5dB).

B) Simulation results using the hardware in the loop simulator

The following hardware simulation results were obtained after using two I-P controllers with K_{p1}=10, K_{I1}=*20* and K_{p2}=20 and K_{I2}=30Nm/rad/sec, where the lower I-P2 gains did not considerably reduce the tracking performance of I-P2, while at the same time achieving a smoother torque change during the switching between the controllers (Simulations with higher gains of K_{p2}=30 and K_{I2}=50Nm/rad/sec are shown in a later section).

Figures 6.18(a-d) demonstrate the performance in below rated operation. This time the wind speed is limited to a lower level of 6.76m/sec (corresponding to ω_R=4rad/sec for $C_{p\,max}$ operation).

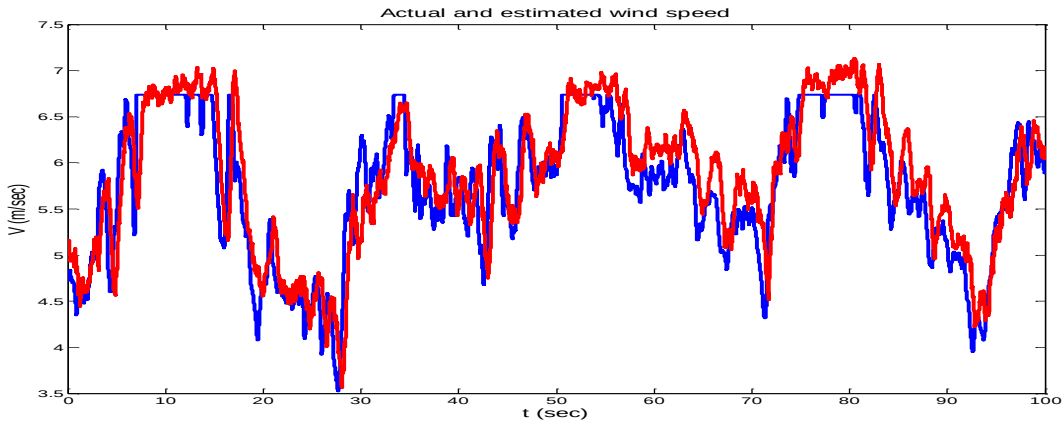

Figure 6.18 (a). Actual (blue) and estimated (red) wind speed.

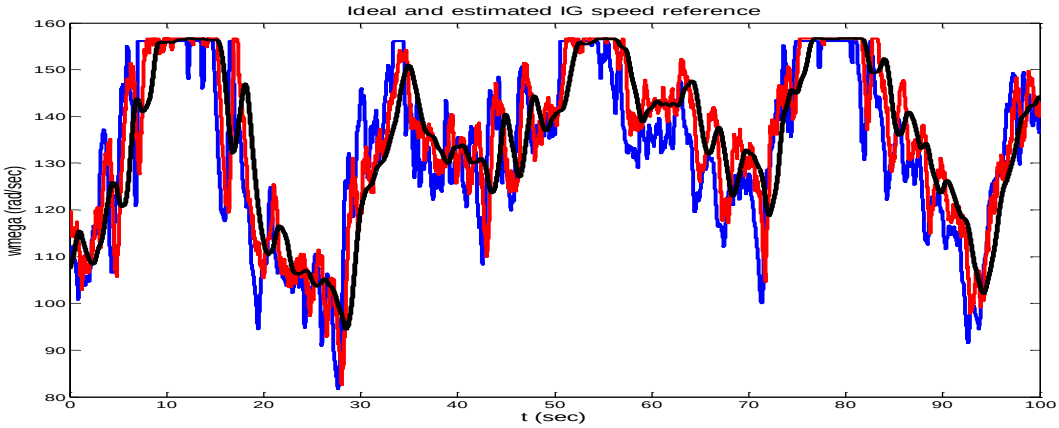

Figure 6.18 (b). Ideal (blue), estimated (red) and low pass filtered estimated IG speed reference (black).

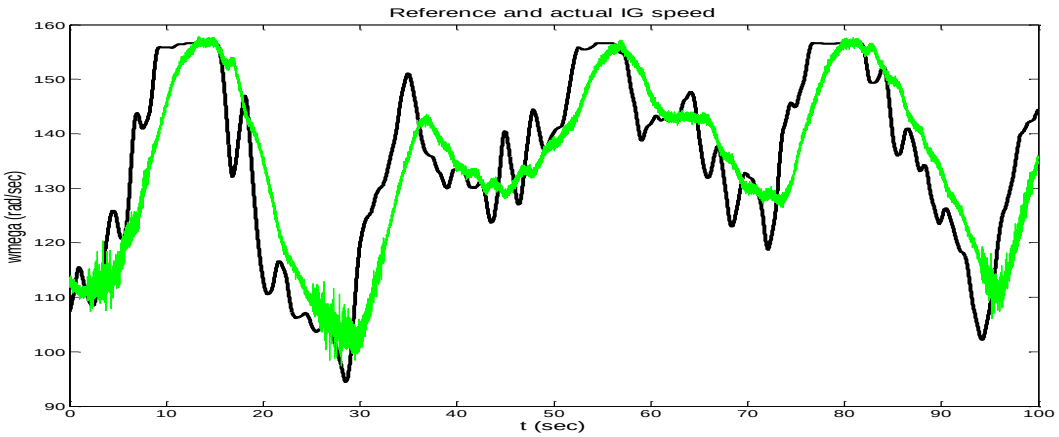

Figure 6.18 (c). Reference (LPF) (black) and actual (green) IG speed.

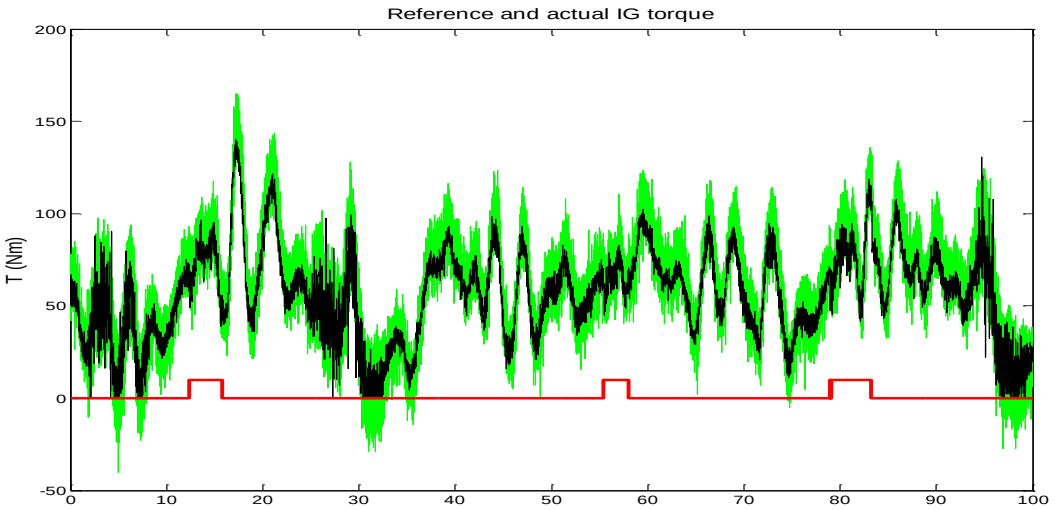

Figure 6.18 (d). Torque demand ($T_{g_{ref}}$) (black), actual IG torque (T_g) (green) and switching signal between the two controllers (red).

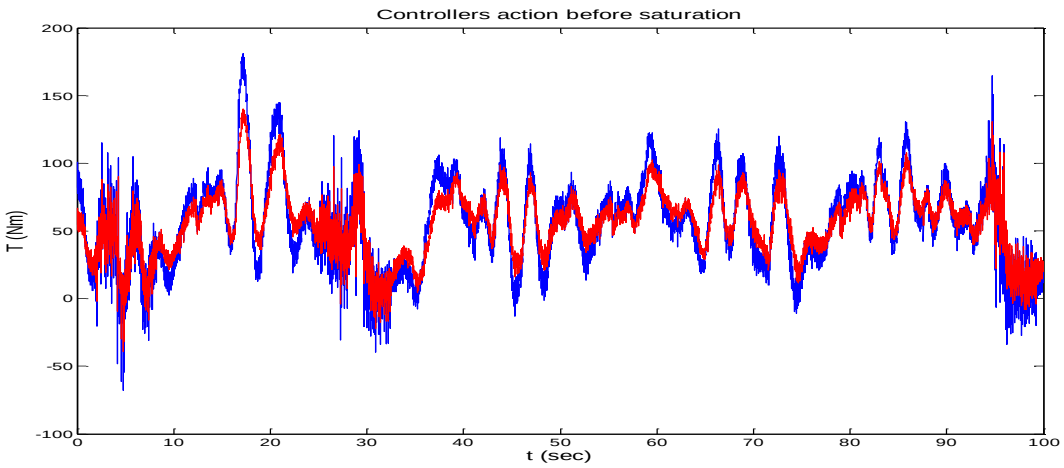

Figure 6.18 (e). Torque demand ($T_{g_{ref}}$) of controller I-P 1 (below rated) (red) and I-P 2 (above rated) (blue).

The above figures exhibit similar characteristics to Figures 6.11, while in Figure 6.18(d) a switching signal indicates the transition between I-P1 (low) and I-P2 (high). From Figures 6.18 (d&e) it can be also seen that there is no considerable transient at the transition between the controllers as a result of the successful tracking between them, shown in Figure 6.18(e). This tracking can be further improved by increasing the gains of the BTCs.

Regarding the performance using a rotor with a steeper C_p curve, a higher energy yield is achieved, similar to what was observed in with Section 6.4.1.

In Figure 6.19(a) the performance of I-P1 and I-P2 is compared for above rated wind speeds, while figure 6.19(b) shows the control torque and the IG torque by using I-P2. As can be seen, the tight controller I-P2 reduces considerably the speed excursions observed with the I-P1 and also does not result in unacceptable torque pulsations. The conclusion of this section is therefore that gain-scheduled I-P control is a suitable choice for operation during stall regulation, which will be further discussed in a later section.

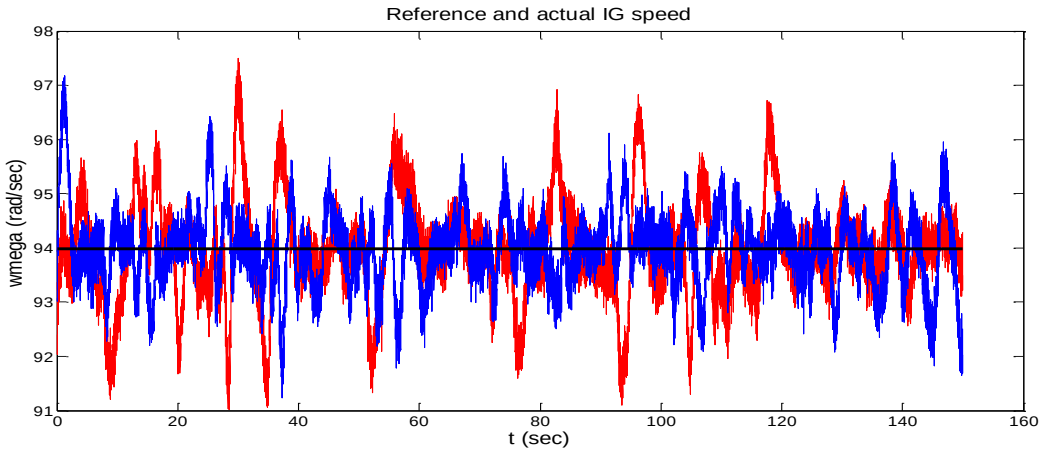

Figure 6.19(a). Reference speed (black), IG speed response with (a) controller I-P 1 (red) and (b) I-P 2 (above rated) (blue).

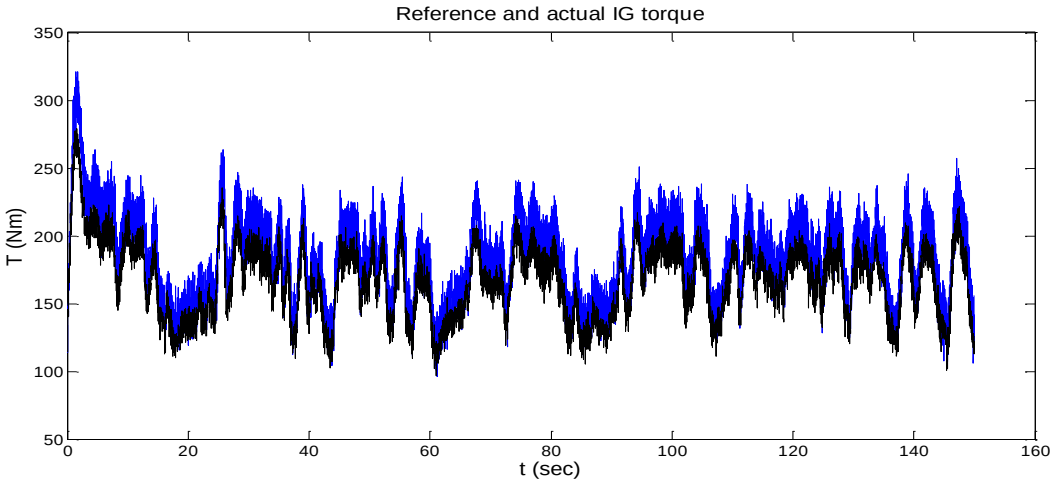

Figure 6.19(b). Reference (LPF) (black) and actual (green) IG torque.

The next section describes the design of robust controllers for the WT, through H_∞ optimization.

6.5. H-infinity control

6.5.1. Introduction

Classic control design methods based on the open loop plant characteristics comprise an easy and effective way to design PID regulators as well as dedicated lead-lag compensators for plants of higher complexity. However, it may be difficult to design an optimum or a near-optimum controller for plants of high complexity.

The advantage of control based on H_∞ optimization over the classic design methods, is that it enables the direct shaping of the closed loop transfer functions, based on simultaneous satisfaction of a number of predefined control objectives. Therefore, there is no need for the designer to explicitly compensate the plant irregularities via tailor-made lead-lag terms, which in the case of very complicated plants can become a quite demanding task.

Due to the above feature, the H_∞ control methods are quite attractive. The design and implementation of H_∞ controllers for a VS SR WT is considered worthy to investigate, since it has not been previously addressed. More details about H_∞ control can be found in [27, 84, 85].

6.5.2. Proposed scheduled H_∞ controller

6.5.2.1. General

Here, a scheduled H_∞ controller for a VS SR WT has been developed. The controller consists of two H_∞ controllers one for below and one for above rated conditions with BWs of 0.6 and 2 rad/sec respectively. These controllers have been designed in the analogue domain through S/KS optimization [27, 84, 85], using the function "hinfsyn" of the Robust Control Toolbox" of Matlab. More details about the design can be found in Appendix A.19.

After the controllers were converted in state space form, they were discretized using the function "c2d" with sampling frequency T_s=200Hz. For real time implementation the controllers were programmed using M-code inside an "Embedded Matlab function" block (B.13). The whole arrangement can be seen in Figure 6.20.

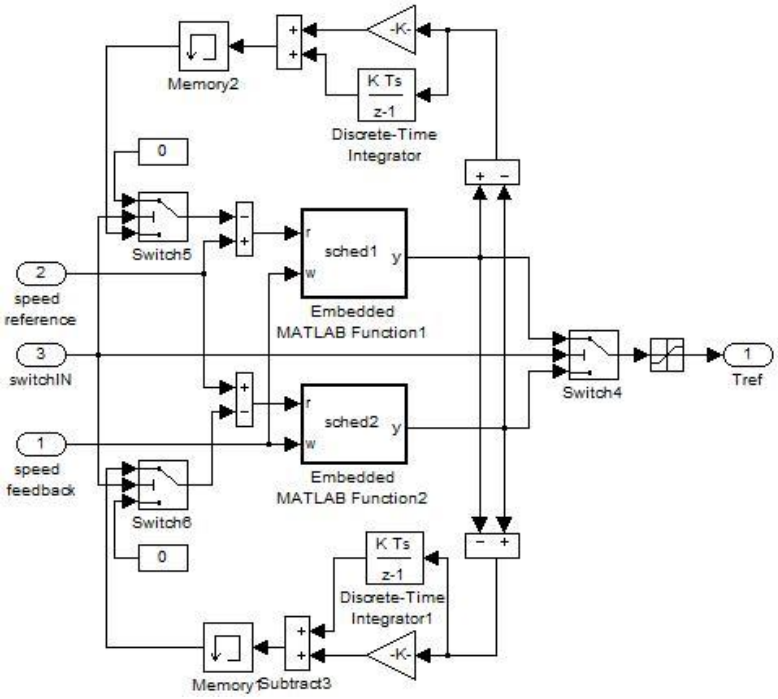

Figure 6.20. Simulink implementation of scheduled H_∞ controllers scheme with bumpless transfer circuits.

As can be seen, the arrangement is similar to the one of Figure 6.15(b). In Figure 6.22 two discrete PI BTCs can be also seen. The "memory" block is used to avoid the creation of algebraic loops.

6.5.2.2. Anti-wind up

Due to the requirement of zero motoring torque demand, saturation of the control action can be quite frequent. Also, saturation to maximum can also happen during wind speeds higher than the cut-out value. Through simulations it was seen that when the control output reached saturation, it wound up, similar to the case of an integrator. Therefore, anti-windup control is required for the H_∞ controllers, similar to the case of I-P controllers.

In the literature anti-windup methods for H_∞ controllers based on optimization using Linear Matrix Inequalities (LMI) were found [86-89]. However, these methods are of high complexity. In addition, hardware simulation results using these methods were not found.

Anti-windup methods using simpler approaches were also found, such as the one proposed in [90]. Such methods have been tried here, but without success, due to their simplistic approach.

Here, a simple and very effective novel anti-windup scheme is proposed. The proposed scheme does not require tuning and the only parameters needed by the algorithm are the saturation limits of the controller. Therefore, it can be applied to any type of controller of arbitrary order. The proposed anti-windup scheme is based on simultaneous observation of the status of the control action and the speed tracking error. Specifically,

the states of the controller are reset every time the control action saturates and the controller returns to its normal operation when the speed tracking error or the control torque level return to specified levels. Figure 6.21 shows the logic diagram of this algorithm, where x is the controller state vector, $e=\omega_{ref}-\omega_g$ the speed tracking error of the IG, u the control torque demand to the IG, st a vector storage variable, a a binary control variable and T_U the upper saturation limit for u.

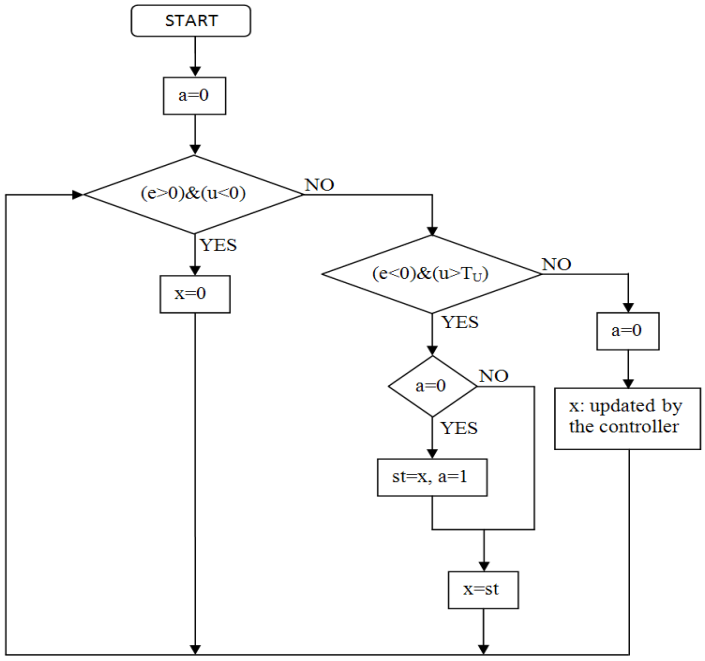

Figure 6.21. Logic diagram of the anti-windup circuit used for the H_∞ controllers.

When $e>0$ and $u<0$, $x=0$. That way, when the control output saturates to zero, the controller stops to integrate. When $u>0$, the controller returns to its normal operation. Also, when $e<0$ and $u>T_U$ for the first time, the current value of x is stored in st and this plays the role of a constant state vector of the controller, for the time while $e<0$ and $u>T_U$. Thus, the controller stops to integrate, since it acts as a proportional controller. The value of a is used as an indication of whether the controller saturated for the first

time, such that *st* is updated only when a=0. It is noted that so far the above scheme has been tested to controllers of one-dimensional output.

6.5.3. Hardware simulation results

The scheduled H_∞ controller has been tested through software (Simulink) and hardware (HILS) simulations. Here HILS simulation results are presented.

Figures 6.22 (a-e) show the most representative results for $C_{p\,max}$ operation.

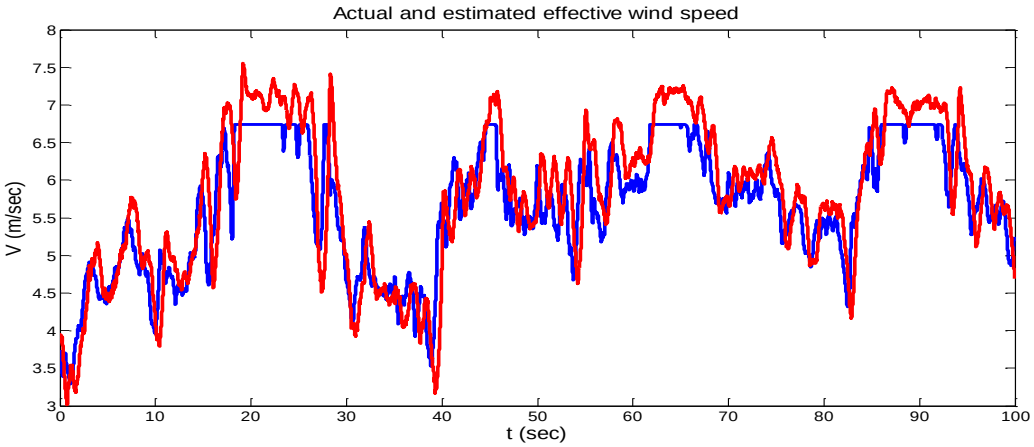

Figure 6.22(a). Actual (blue) and estimated (red) wind speed.

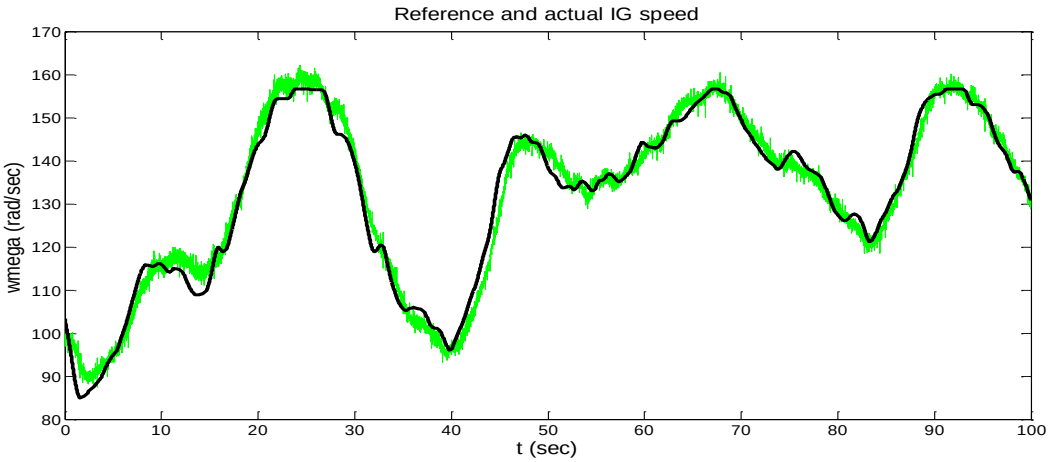

Figure 6.22(b). Reference (LPF) (black) and actual (green) IG speed.

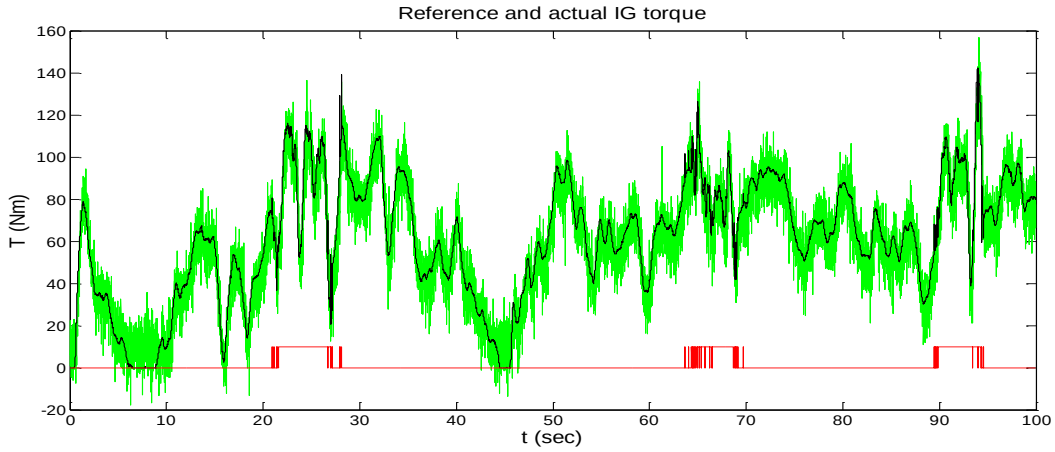

Figure 6.22(c). Torque demand ($T_{g_{ref}}$) (black), actual IG torque (T_g) (green) and switching signal between the two controllers (red).

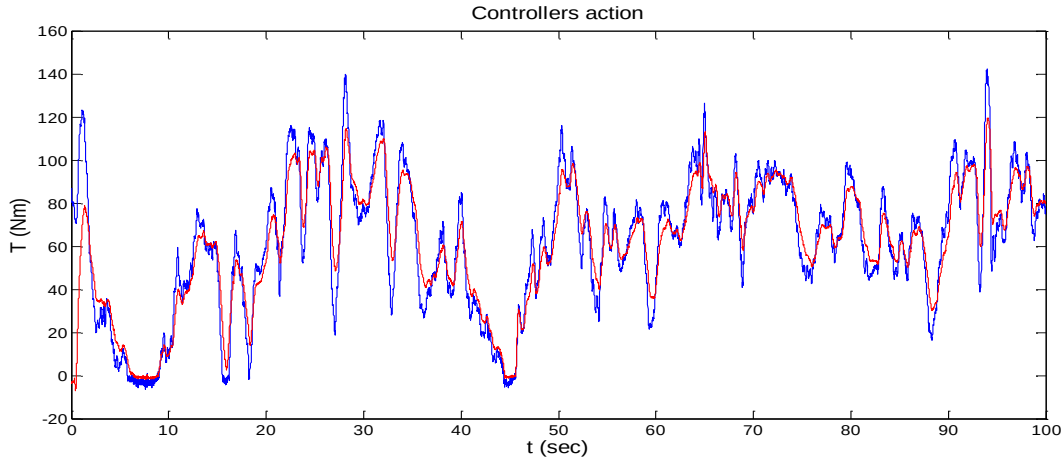

Figure 6.22(d). Torque demand ($T_{g_{ref}}$) for below rated (red) and above rated (blue) controller.

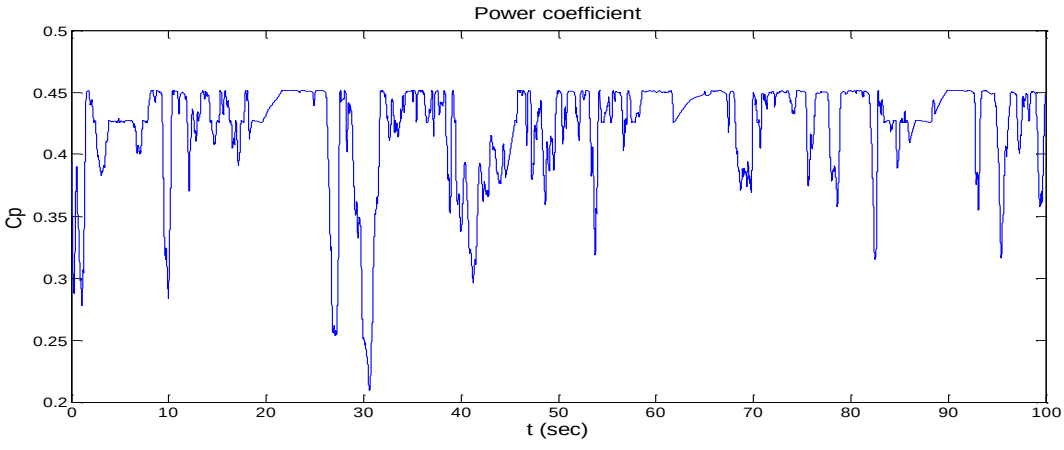

Figure 6.22(e). Power coefficient.

As can be seen from Figure 6.22(b), the control scheme exhibits perfect reference speed tracking. From Figure 6.22(c) it can be seen that the control torque demand is noise-free, which indicates more effective noise rejection of the controller compared to the I-P controller. Also, the control action does not exhibit unacceptable pulsations and stays in lower levels compared to the I-P controllers. The small bumps observed at the transitions of the controllers can be effectively eliminated by increasing the gains of the BTCs for the below rated controller in order to improve the tracking between them, as seen in Figure 6.22(d). From the same figure it can be seen that the anti-windup circuit effectively limits the control action to zero. Finally, from Figure 6.22(e) it can be seen that C_p is kept high, which results to high power production. It is mentioned that the cumulative energy is slightly higher than of the conventional quadratic control, as was observed for the I-P controllers. Similar observations hold for simulations using the steeper C_p curve.

Figures 6.23 show results for above rated conditions (constant speed).

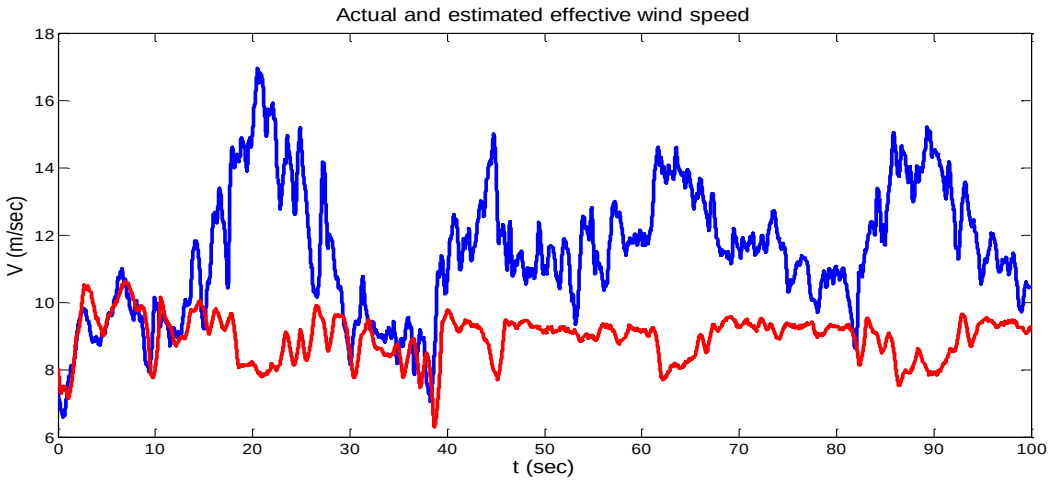

Figure 6.23(a). Actual (blue) and estimated (red) wind speed.

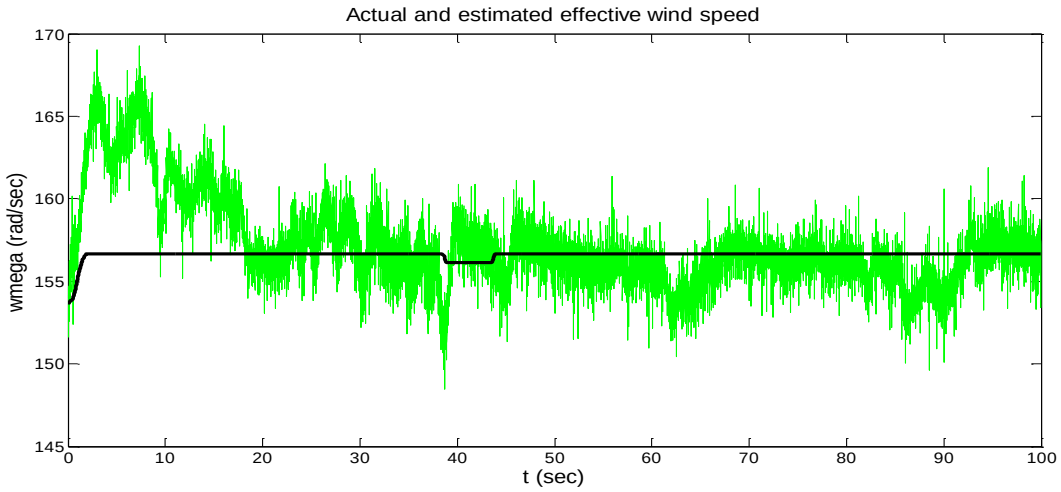

Figure 6.23(a). Reference (LPF) (black) and actual (green) IG speed.

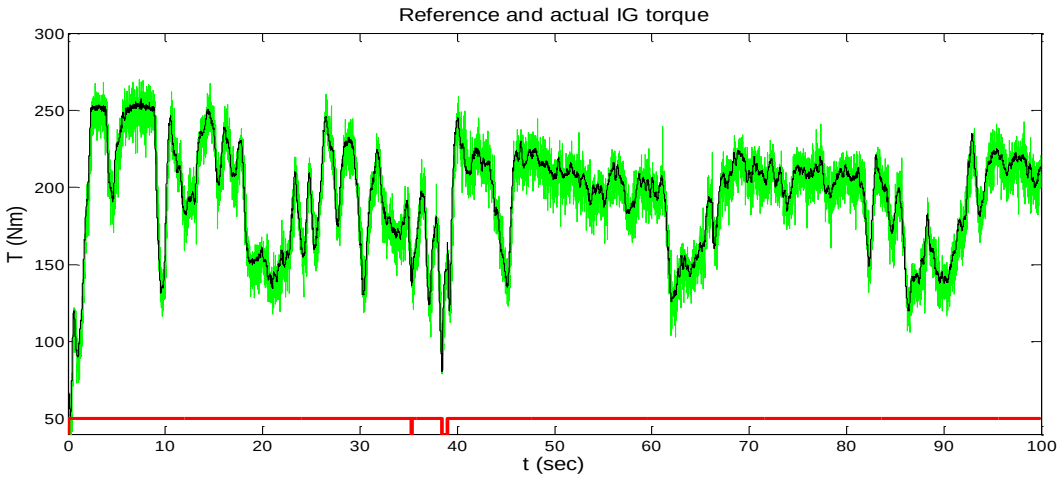

Figure 6.23(b). Reference (LPF) (black) and actual (green) IG torque.

From Figure 6.23(a) it can be seen that the speed tracking for above rated wind speeds is very good, even a control loop of relatively low BW of 2 rad/sec is used. Figure 6.23(b) shows a smooth control action as a result of successful design as well as effective control action limitation to the upper saturation limit of 250Nm as a result of the effective proposed anti-wind up algorithm.

In general, from all the previous hardware simulation results it can be concluded that with the H_∞ control method a control scheme with improved characteristics compared to I-P schemes can be obtained. Although with classic design methods similar result can

be obtain using higher order designs, the H_∞ method facilitates this procedure through optimization.

It is mentioned that in general the improved performance comes with the cost of higher computation load, since the H_∞ controllers are of equal order with the controlled plant plus the shaping weights.

6.6. Other types of robust controllers

Other types of robust controllers that have been investigated are the H_∞ LPV and the SMC.

6.6.1. Linear Parameter Varying controller

The H_∞ LPV controller for a VS SR WT has been simulated in Simulink and has also been implemented in the HILS, where it has been tested under various wind conditions (Appendix A.20).

Through software and hardware simulations it was shown that when this type of controller is saturated, it becomes unstable and in the literature effective methods for anti-windup control of LPV controllers have not yet been proposed. However, this limitation was effectively overcome by applying the anti-windup scheme described in Section 6.5.3.2.

In general, through hardware simulation results, it was shown that this controller is not quite straightforward to be applied in an actual system, since during simulations in the HILS, considerable deviations from the expected by software simulations performance, was observed.

6.6.2. Sliding mode controller

Unlike the control methods presented so far, the SMC applies a discontinuous high frequency control to the plant, in order to constrain the states of the closed loop system to move on a desired trajectory, the sliding surface, were they exhibit desirable dynamics. This control method can be quite advantageous due to its robustness in plant uncertainties and external disturbances and also due to its relatively ease of implementation [91].

Because of the above features and since in the field of wind energy this method has only been studied in theory and using simplified models [36, 92], it was considered worthwhile to investigate.

Here, continuous time and discrete time sliding mode controllers have been designed and tested in Simulink and HILS, as part of the proposed control algorithm for VS SR WTs. In Appendix A.21 details from the design and implementation of two discrete time sliding mode controllers, using combination of methods found in [91, 93, 94] are given, as well as Simulink and HILS results.

In brief, the designed controllers appear to perform very satisfactory and without chattering in the Simulink simulations. However, in HILS acceptable tracking performance in below rated winds was accompanied with a poorer tracking performance in above rated winds and in order to improve the tracking, chattering occurred in both operating regions, although methods to prevent chattering were also tried. Therefore, further work is required for the application of this type of controller in an actual system.

6.7. Hardware simulation results of stall regulation at constant power

6.7.1. Simulation results - original Windharvester rotor

In this section the performance of the algorithm for stall regulation at constant power, presented in Section 5.4.2, is assessed, using the HILS. The WT model used is that of the Windharvester WT and the results demonstrate the capability of the algorithm to achieve any desired power level through speed control of the IG. The applied wind speed contains rotational sampling effects (1st and 3rd blade passing frequency harmonics) and the used dynamic inflow model has lead lag coefficients a=11.25 and b=7.25, respectively. The speed controller that was initially used, is the one consisting of two I-P controllers with gains K_{p1}=20, K_{I1}=10, K_{p2}=30 and K_{I2}=20Nm/rad/sec. Figures 6.24 show simulation results from power regulation at 25kW.

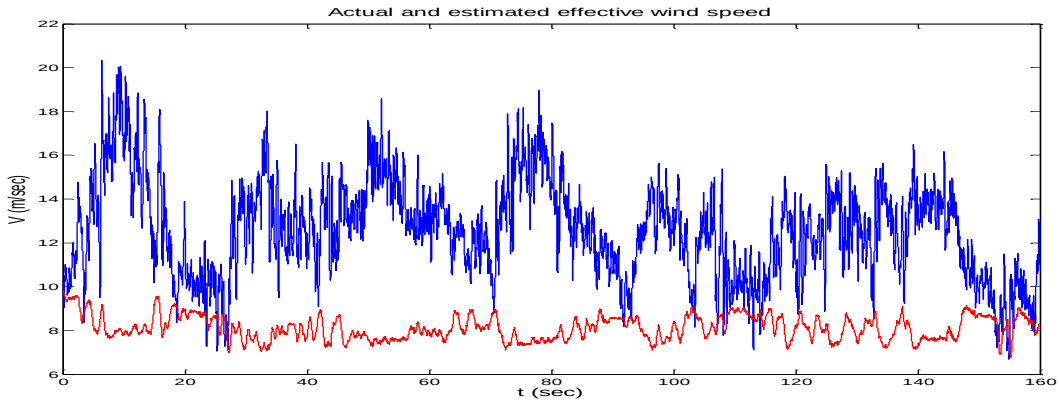

Figure 6.24(a). Actual V (blue) and estimated $\hat{V}$ (red).

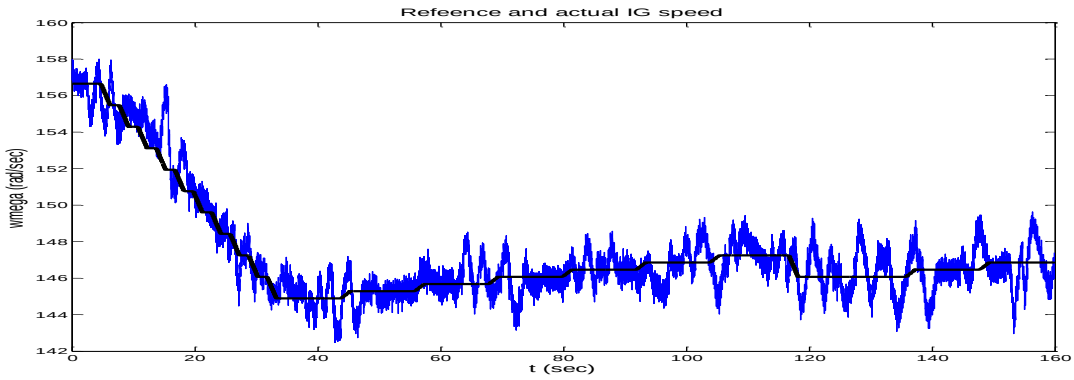

Figure 6.24(b). Reference (black) and actual (blue) IG speed.

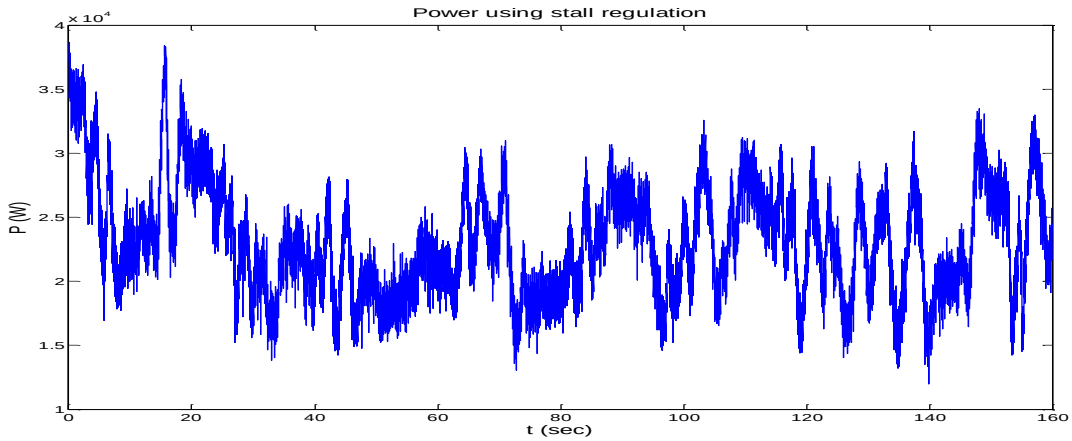

Figure 6.24(c). IG power.

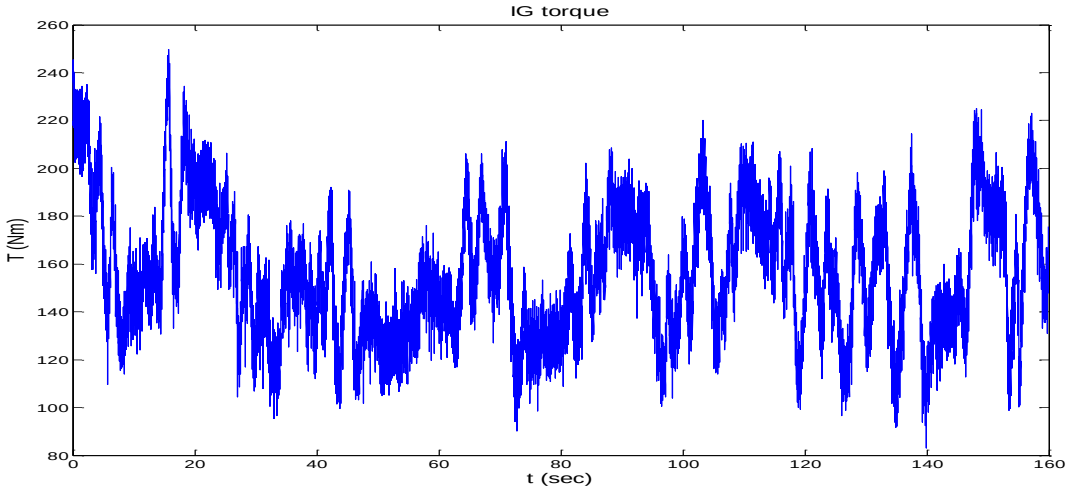

Figure 6.24(d). IG torque.

As can be seen, the wind speed is estimated from the algorithm, described in Section 5.1. Also, the obtained speed reference, according to Eqn. (5.2), is further adjusted by the stall regulation algorithm, as seen in Figure 6.24(b) in order to keep the power constant. Figure 6.24(c) shows that the power effectively stays at 25kW on average. Also, the IG torque stays at the rated value of 161Nm in average, as shown in Figure 6.24(d). Next, it is shown that by using a tighter controller for above rated operation, this performance is considerably improved.

Figures 6.25(a-d) depict results from power regulation, with a step change in the reference power from 25kW to 20kW at the 115th second of simulation. A tighter I-P2

controller is now used for above rated operation, with gains K_{p2}=50 and K_{I2}=30Nm/rad/sec (see Section 6.4.2.2. (A)).

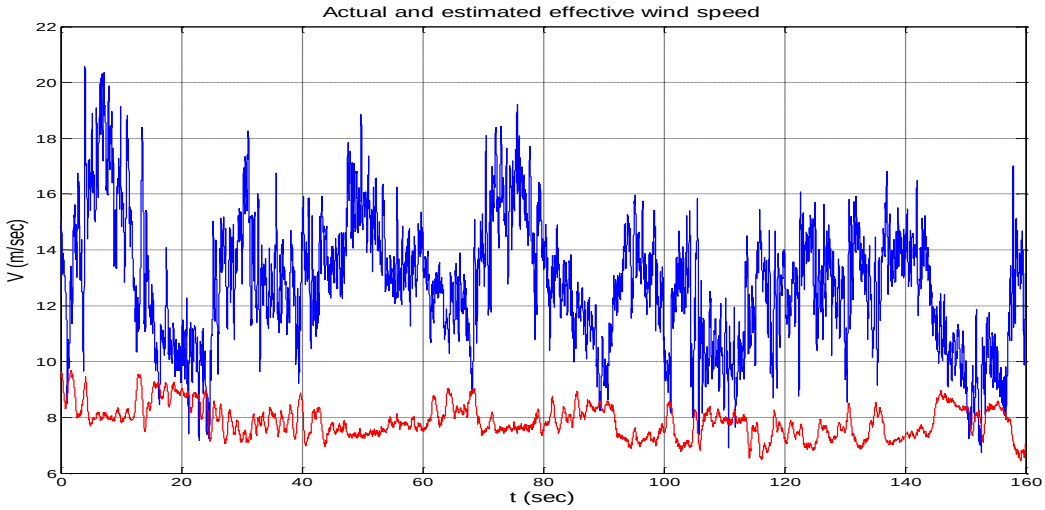

Figure 6.25(a). Actual V (blue) and estimated $\hat{V}$ (red).

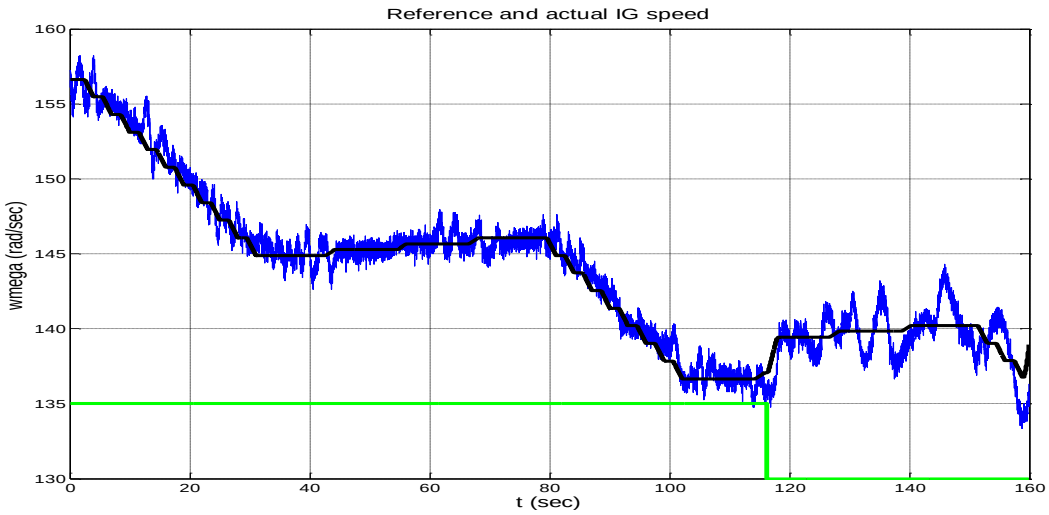

Figure 6.25(b). Reference (black), actual (blue) IG speed and control switching command (green) (High: I-P2, Low: I-P1).

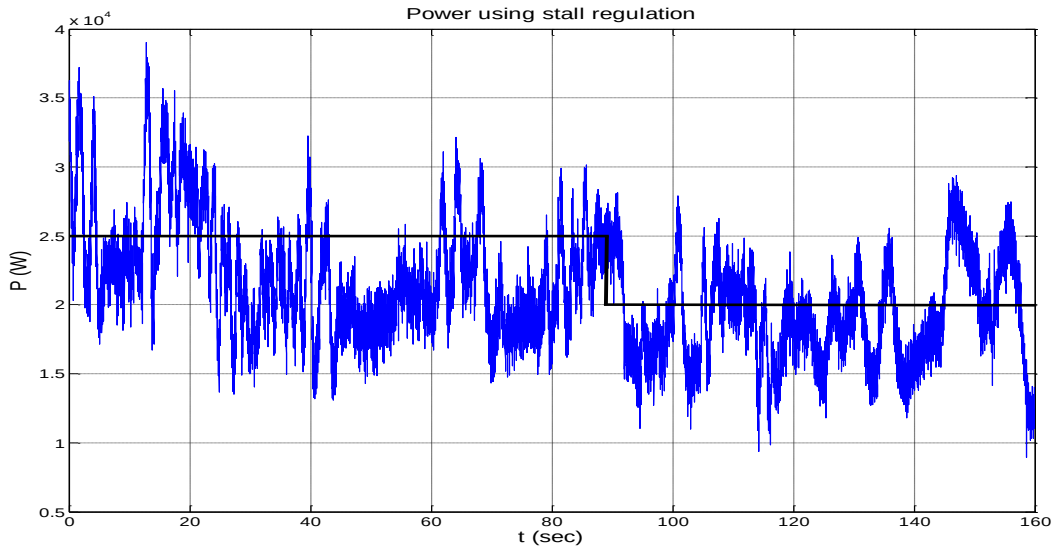

Figure 6.25(c). Reference (black) and actual (blue) IG power.

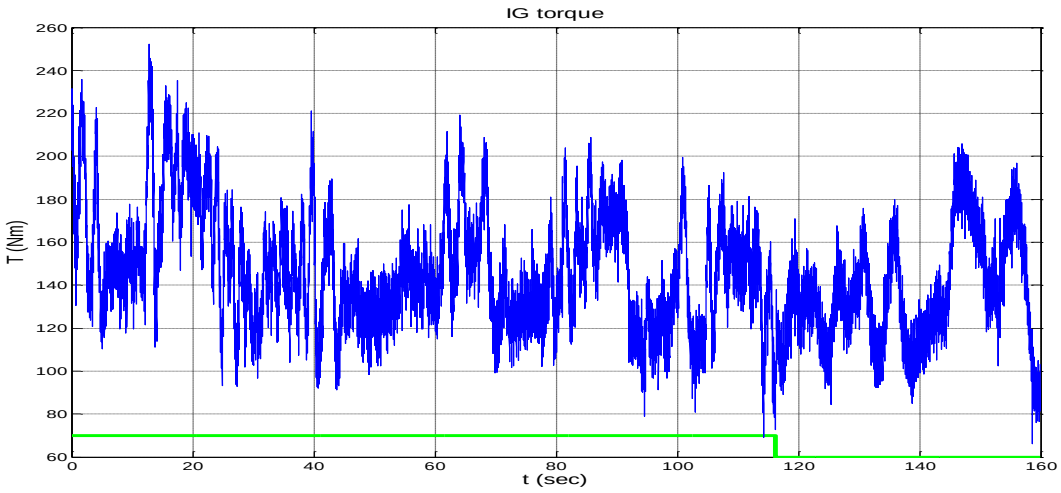

Figure 6.25(d). IG torque (blue) and control switching command (green) (High: I-P2, Low: I-P1).

As can be seen, the tighter controller achieves remarkable improvement in the reference tracking and in the power regulation.

In Figures 6.25(b) and (d) the control switching command is also seen. As can be observed, the command in general stays "High" during the stall regulation, activating that way the dedicated I-P2 controller. However, in the 116th second this signal switches back to the below rated controller I-P1, while stall regulation is still active.

This happens, because at this time, the $\hat{V}$ estimate, seen in Figure 6.25(a), takes below rated values, as a consequence of the relatively high power levels in combination with the low rotor speed (see Section 5.1 about intersection of T_a characteristics). This malfunction of the algorithm has been effectively eliminated by a simple modification of the control switching routine, as presented in a later section.

6.7.2. Simulation results - steeper power coefficient characteristic

Figures 6.26(a-c) show stall regulation simulation results of the rotor with the steeper C_p curve (Figure 2.12(c)). Also, the initial I-P2 controller gains are now used: K_{p2}=20 and K_{I2}=10Nm/rad/sec.

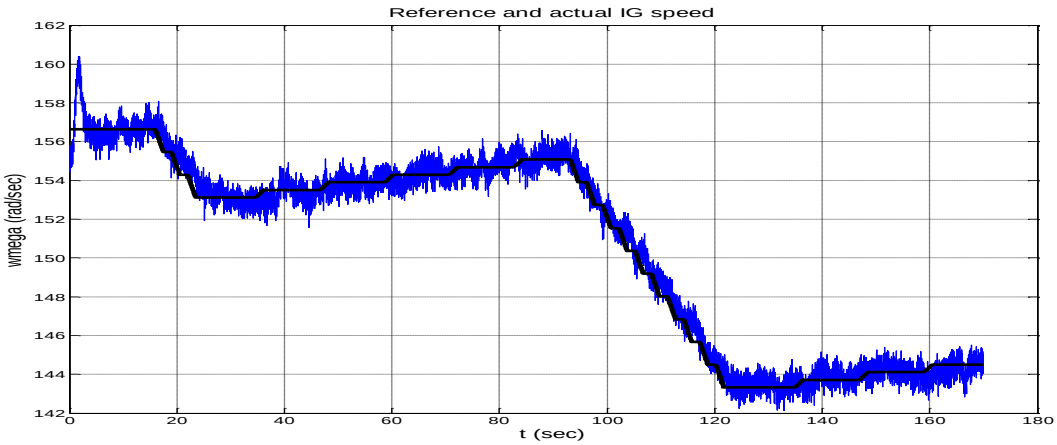

Figure 6.26(a). Reference (black) and actual (blue) IG speed.

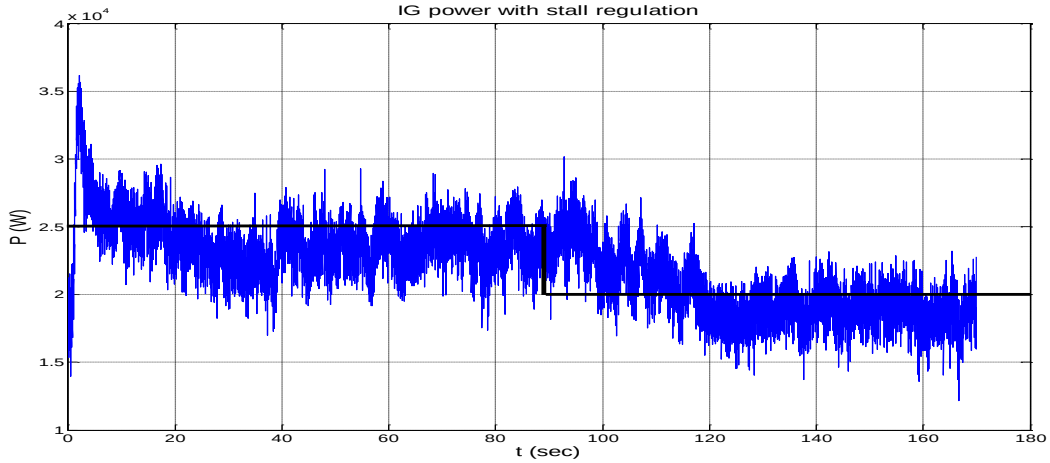

Figure 6.26(b). Reference (black) and actual (blue) IG power.

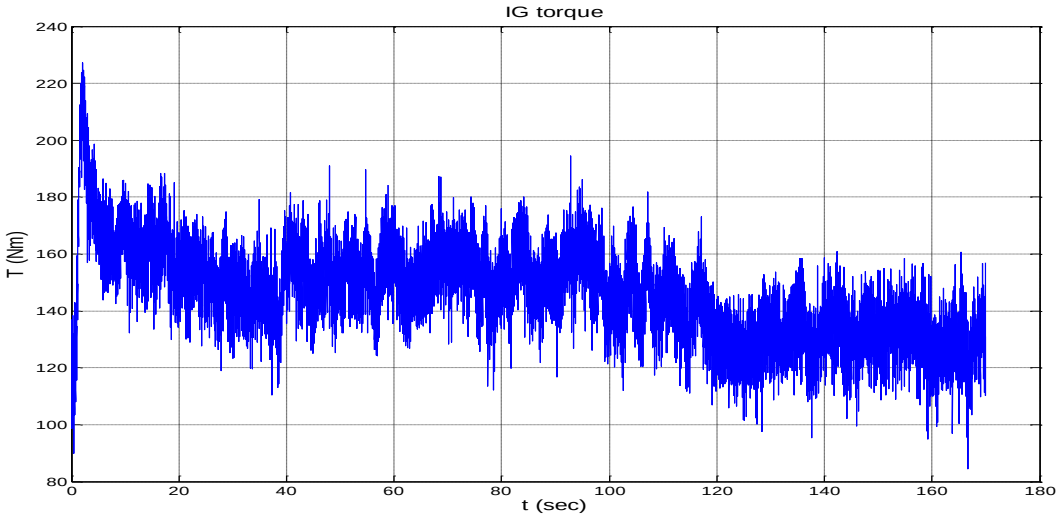

Figure 6.26(c). IG torque.

The above figures show that stall regulation at constant power can be better achieved with a less tight speed controller, using this rotor. Also, as can be observed by comparing Figures 6.25(b) and 6.26(a), less speed reduction is now required, because of the steeper C_p curve [79]. Finally, from Figure 6.26(c) it can be seen that the IG torque excursions are considerably reduced compared to Figure 6.25(d). In general, the results show that by using a slightly steeper C_p curve, remarkable improvement in the power regulation can be achieved, while the control bandwidth is not severely impacted (Appendix A.3).

6.7.3. Further improvements of the stall regulation control scheme

6.7.3.1. Controller switching

As mentioned in Section 6.7.1, incorrect controller switching can happen as a result of the imprecise $\hat{V}$ estimation during stall operation (see Section 5.1), since $\hat{V}$ is the main decision parameter for the controllers switching, according to the scheme of Figure 6.16. In order to avoid this malfunction of the system, the switching scheme of Figure

6.16 has been upgraded to the one of Figure 6.27, where the flag "fl", indicating power regulation, is now put in the same priority with $\hat{V}$.

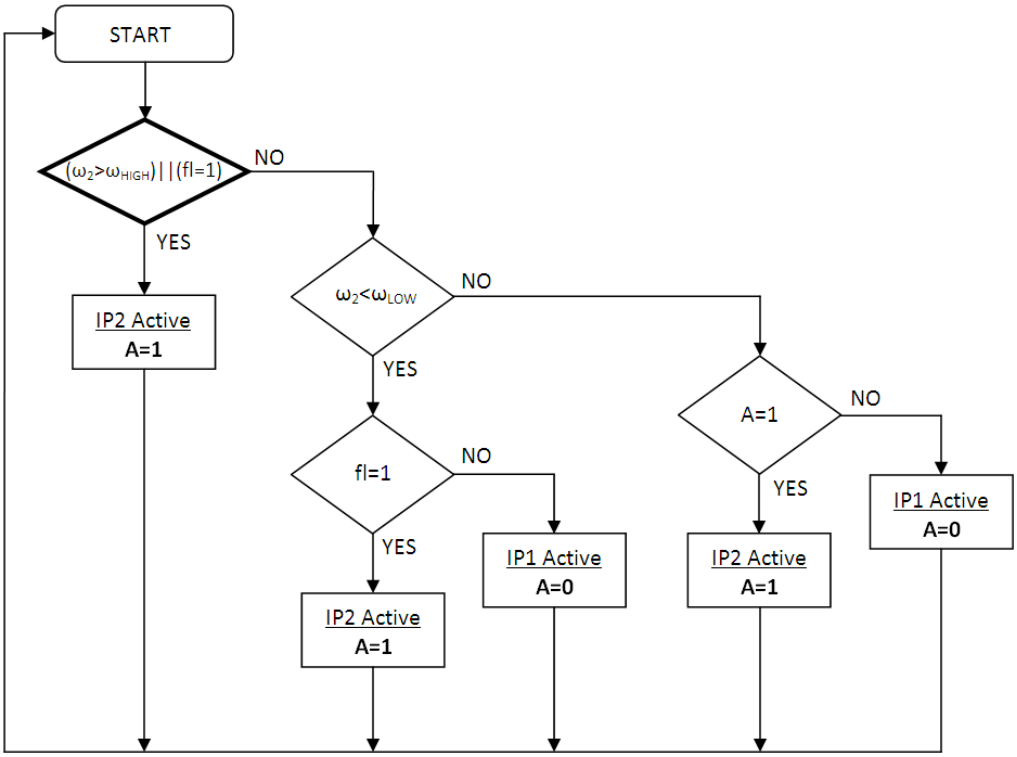

Figure 6.27. Upgraded switching scheme of Figure 5.16 (the modification is seen in bold).

6.7.3.2. Fast response to a power increase demand

In Section 5.4.2, where the stall regulation algorithm is described, it is mentioned that the rate of increase of the speed reference following a previous speed reduction, is lower, in order to achieve a hysteretic recovery of the rotor speed and to avoid speed reference swings due to wind turbulence. However, this slow rate of increase is not satisfactory when a power increase demand is applied. Therefore, the algorithm shown in Figure 5.12 has been enhanced with a mechanism that increases the speed increase rate only when a higher power demand is detected and until the new power level is effectively reached (it is mentioned that a similar mechanism can be applied when faster

response to a power reduction demand is required). Figures 6.28 (a&b) show simulation results of a power demand increase from 20 to 25kW at the 90th second of the simulation (assuming a rotor with a steep C_p curve).

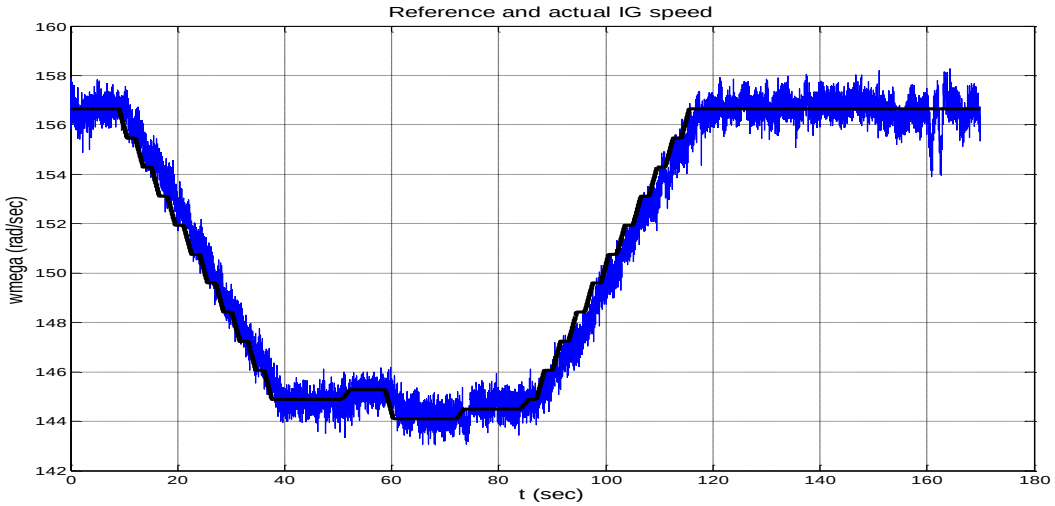

Figure 6.28(a). Reference (black) and actual (blue) IG speed.

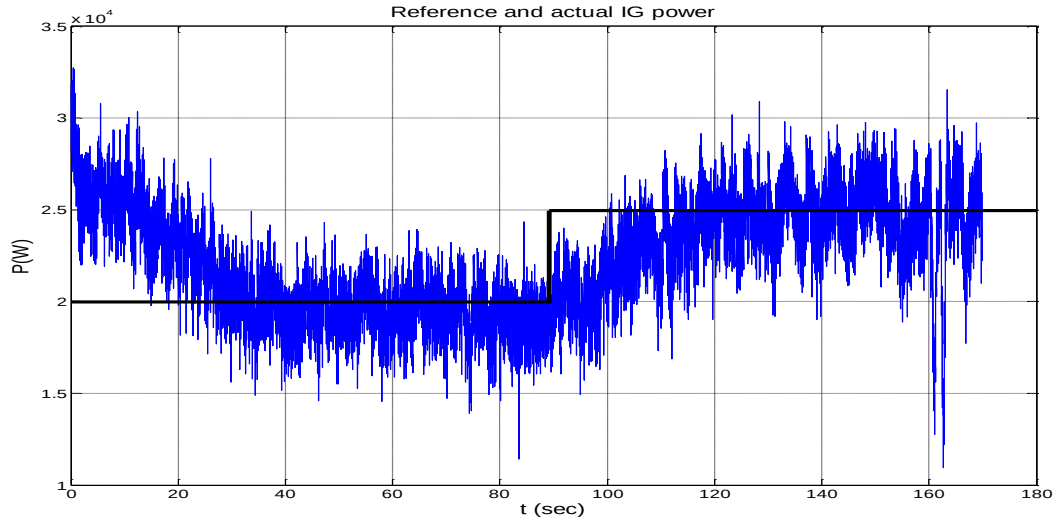

Figure 6.28(b). Reference (black) and actual (blue) IG power.

6.8. Conclusions

In this chapter the design and implementation of novel speed controllers for a VS SR WT have been presented. These controllers were obtained by combining several

designs, such as I-P or H_∞ controllers and subsystems in order to achieve dedicated implementations that will satisfy the performance specifications of a VS SR WT.

As it was shown through HILS results, the designed controllers achieved optimum operation over the entire operating region of the WT, while limitations of certain designs regarding their implementation in VS SR WTs, such as LPV and SMC controllers were for the first time pointed out.

The hardware simulation results showed that the proposed control algorithm can achieve increased aerodynamic efficiency over conventional controllers for below rated conditions and for rotors with a steep power coefficient curve. This kind of curve achieves better power regulation performance.

The proposed control algorithm also achieved very effective stall regulation at constant power for a rotor with a broader power coefficient curve. Therefore, various designs of VS SR WT can be possible.

In the next chapter general conclusions and recommendations for future work are presented.

7. Conclusions - Future Work - Original Contribution

7.1. Discussion

In this thesis the design and implementation of a complete novel feedback control system for variable speed stall regulated wind turbines was presented. This control system aims to continuously provide the appropriate speed reference for the generator of the wind turbine, in order for the last to achieve maximum power production for a wide wind speed range lower than the rated and also to efficiently limit its output power to desirable levels for wind speeds higher than the rated. The optimum speed reference for the simulated wind turbine is shown in Figure 7.1 (black).

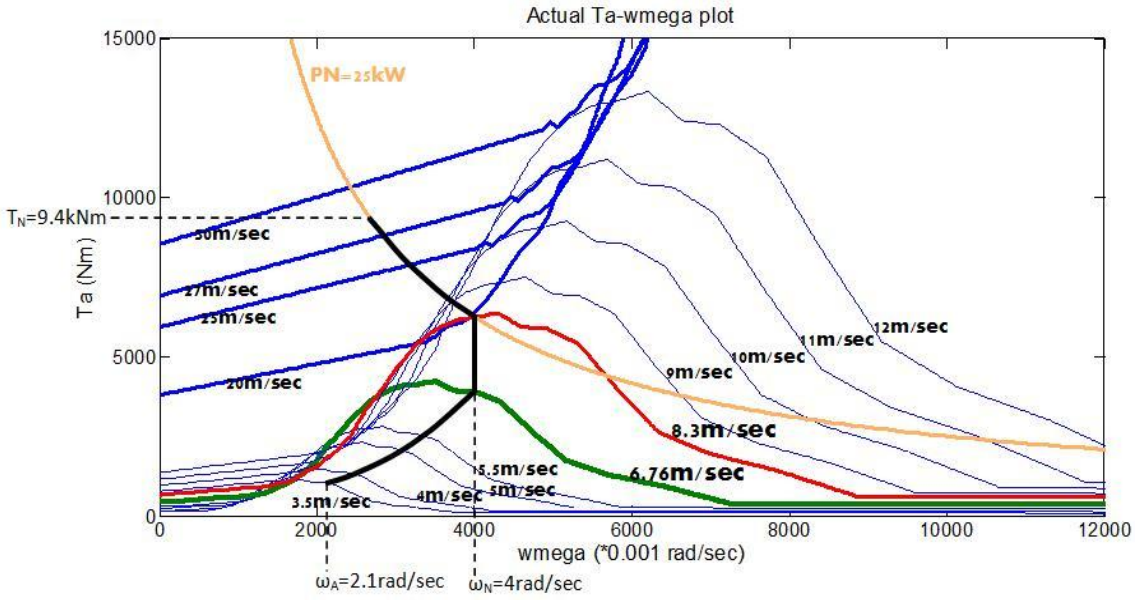

Figure 7.1. Optimum speed reference trajectory (black) for all wind conditions. Rated power curve (orange), T_a-ω characteristics (blue), rated wind speed (red).

The proposed control system consists of an aerodynamic torque estimation stage, a speed reference determination stage and a speed controller, as can be seen in Figure 7.2.

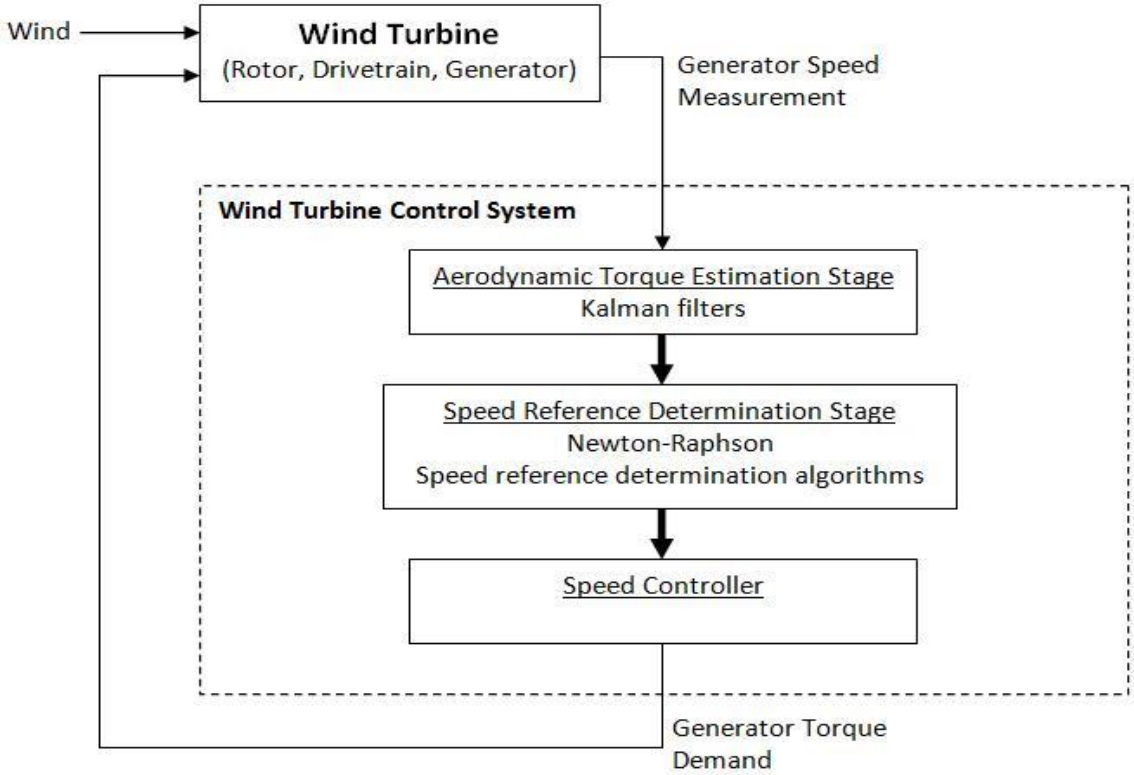

Figure 7.2. Wind turbine control system overview.

The aerodynamic torque estimation stage has been implemented using adaptive Kalman filters, which can provide torque estimates of highest possible accuracy. The high accuracy of the torque estimates is very important, because it results to more efficient operation for the wind turbine.

The speed reference determination stage is of high importance, because it provides the optimum speed reference for the wind turbine for below rated operation, based on the wind speed conditions, in order to achieve maximum energy extraction. For this reason this stage includes a wind speed estimation process, using a high performance Newton-Raphson algorithm. This algorithm continuously provides the control system with wind speed estimates and it is designed such that it has guaranteed convergence for all possible operating conditions. Furthermore, the speed determination stage has the task

to provide the appropriate speed reference in above rated wind conditions, such that the wind turbine limits its power to the specified level. This operation is implemented using novel speed reference determination algorithms, based on the estimated aerodynamic torque.

Finally, the speed controller, which continuously updates torque demands to the generator of the wind turbine, is a crucial part of the control system, because it is responsible that the generator speed closely follows its reference. In addition, the controller must eliminate high frequency torque resonances in the drivetrain, which can be caused due to the wind turbulence and can result to reduction of its lifetime.

Due to the nonlinear dynamics of the wind turbine, a gain scheduled controller has mainly been used in this study. This controller, which consists of PI or H_∞ controllers, was designed such that it satisfies the different bandwidth requirements, depending on the operating conditions.

Specifically, for below rated operation, which for the simulated wind turbine means operation for wind speeds below 6.76m/sec, a control bandwidth between 0.5 and 1 rad/sec was chosen, for maximum energy extraction. As can be seen from the Bode plot of Figure 6.9 in closed loop, the controller very effectively suppresses the first drivetrain mode, which exists at 53rad/sec (see Figure 2.15). The controller achieves a closed loop response with an attenuation of 40dBs at 50rad/sec and roll off rate of 50dB/dec. That way it eliminates any oscillations in the drivetrain due to the high frequency components of the effective wind speed, as mentioned in Section 1.6, so wear of the drivetrain is effectively avoided. In addition, the system achieves accurate reference generator speed tracking, which results to operation very close to the maximum power point without unacceptable torque excursions ($T_g<T_N$ during

operation), as can be seen by all the experimental generator speed, power coefficient and torque time series for below rated operation of Chapter 6. It is mentioned that higher values of the bandwidth were also tried for this operating region, but the improvement in the tracking was taken with the cost of unacceptable control torque pulsations. Therefore, the choice of 0.5-1rad/sec was considered the optimum for this system.

Furthermore, it was shown that for above rated and stall operation (wind speeds above 8.3m/sec for the simulated wind turbine), the lower control bandwidth requirement that guarantees stability of the system, can increase to 0.94rad/sec and higher (see Figure 6.1 and Table 6.1). In addition, at this operation region the gain of the disturbance increases considerably (see Figure 6.4). This can result to dramatic power excursions and therefore, higher disturbance attenuation is required. For these reasons, for this operating region controllers of higher gains were used, which achieved closed loop bandwidths of 2 and 3rad/sec. These controllers achieved a high suppression of the first drivetrain mode, as seen in the Bode plots of Figure 6.17 (-17dBs at 50rad/sec) and this resulted to absence of unacceptable drivetrain torque oscillations as this can be observed from the generator torque time series provided in Section 6.7. From the same section it can be also seen that the designed controllers achieved the desired speed reference tracking performance, which resulted to effective power limitation.

It is mentioned that higher control bandwidths than 3rad/sec for above rated operation can result to even better disturbance attenuation and consequently improved power regulation. However, this bandwidth must not exceed the frequency of the RHP zeros that appear at this operating region. For the simulated wind turbine these appear at 10rad/sec, while in general this can be different depending on the particular drivetrain dynamics.

To sum up, the designed control system achieved the desired performance for the simulated variable speed stall regulated wind turbine, which is for the first time achieved for this type of wind turbine. This achievement has a great value for the industrial development of this type of wind turbine, because it provides the general directions, in order to overcome the existing control challenges for any drive system. These challenges are associated with the peaky shape of the rotor aerodynamic coefficients (C_p and C_q), which render the maximum power point tracking quite difficult unless high performance wind speed estimation methods, incorporating Kalman filters, are used. Finally, regarding the control design task, it is very important that the closed loop bandwidth increases as the operation of the system moves further into the stall region, but without exceeding the maximum limit imposed by RHP zeros. In addition, in general, care must be taken, in order to avoid excitement of drivetrain oscillations due to the first drivetrain mode, which can appear in relatively low frequency, as the rotor diameter increases.

7.2. Conclusions

In the previous chapters, the design and implementation of a control scheme for variable speed stall regulated wind turbines was presented. This type of wind turbine uses a rotor with a fixed blade pitch angle, which makes the construction simpler, more robust and cheaper. However, due to existing challenges on the control of stall regulated wind turbines, as a result of the changeable dynamic response from minimum phase to nonminimum phase as the operating conditions change and also as a result of the higher sensitivity of the achieved aerodynamic efficiency to excursions of the operating point

during maximum power point operation, this type of wind turbine is not yet commercially available.

In this thesis, it was shown through simulations using a wind turbine hardware-in-loop simulator that the proposed control method can effectively overcome the above challenges using hardware existing in contemporary variable speed wind turbines and therefore gives confidence for its applicability to an actual variable speed stall regulated wind turbine.

For this study, very detailed wind turbine models, based on actual data of a wind turbine rotor, drivetrain and generator, as well as hardware consisting of an induction generator and industrial variable speed drive, similar to the ones used in actual variable speed wind turbines, were combined, in order to develop a hardware in the loop simulator that represents as close as possible the dynamics of a variable speed wind turbine. The developed wind turbine simulator effectively achieved this goal, as this was shown from experimental transfer function measurements and through numerous simulations with actual wind site data.

The proposed algorithm was implemented and run in real time on the hardware in the loop simulator and was able to effectively control the simulated wind turbine achieving maximum power production for below rated winds and also effective power regulation at different desirable levels for above rated wind speeds, without resulting in excessive torque loading of the generator. In addition, the control method was able to achieve a smooth control transition between the operating regions of the wind turbine and at the same time to eliminate speed oscillations due to wind turbulence and rotational sampling effects, without this to result in unacceptable torque and power pulsations.

The very good performance of the control algorithm under varying operating conditions was a result of the effective operation and coordination of several subsystems that the control algorithm consists from. Specifically, the aerodynamic torque of the wind turbine rotor was effectively estimated to a high level of accuracy by adaptive Kalman filters despite changeable statistics of the wind and high levels of measurement noise. This aerodynamic torque estimate was then used in to numerically compute the effective wind speed of the rotor and to continuously provide the optimum speed reference for the generator, in order to achieve maximum power production over a wide range of wind speeds. The numerical computation of the effective wind speed was performed using a Newton - Raphson routine enhanced with an algorithm that guarantees its convergence. Furthermore, the aerodynamic torque estimate was effectively used by the stall regulation algorithms, which provided the speed reference for the generator in above rated conditions to enforce stall regulation at constant power. The proposed stall regulation algorithm achieved effective power control by smoothly adjusting the speed reference for the generator. That way the power set point was effectively tracked avoiding torque and power peaks, which would otherwise happen during abrupt speed changes, in stall operation.

The speed control of the generator was performed via a gain scheduled Integral-Proportional controller, which achieved the desired tracking performance in the whole operating region of the wind turbine, without imposing intense cyclic torque loads on the drivetrain and also without exhibiting torque bumps during switching between the controllers, as a result of the successful operation of the applied scheduling algorithm and the bumpless transfer control algorithm.

In addition, other types of speed controllers, such as scheduled H-infinity, Linear Parameter Varying H-infinity and sliding mode controllers, were tested in the wind

turbine simulator and possible advantages, shortcomings or challenges on the application of these controllers to actual wind turbines, were revealed.

In particular, the H-infinity control methods can provide optimum control solutions in applications where the effectiveness of Proportional – Integral – Derivative regulators is limited by the complexity of the plant and where designing of optimum lead lag compensators using classical control methods is a quite demanding task. Here, scheduled H-infinity controllers were designed for the variable speed stall regulated wind turbine and implemented in real time in hardware-in-the-loop simulator, while challenges regarding their practical implementation such as anti-windup control and bumpless control transfer were effectively overcome. From hardware simulation results it was shown that these controllers performed very satisfactory, which indicates their effectiveness and potential for use.

Regarding the Linear Parameter Varying controller, its performance was inferior during the hardware simulations compared with that achieved through software simulations.

Finally, the sliding mode control was also tested, because it appears to be an attractive control solution due to its robustness to external disturbances and also due to its relatively easy implementation, since no considerable programming effort is required. Two types of sliding mode controller were implemented in the wind turbine simulator and tested in real time. However, although these controllers achieved quite good reference tracking, undesirable control torque chattering occurred in above rated conditions, which indicates the need of further research on the application of this type of controller in this type of wind turbine.

Through hardware simulations using a model of a rotor with a narrower power coefficient curve (which would be more preferred for a variable speed stall regulated

wind turbine) it was shown that the proposed control scheme increased considerably the achieved aerodynamic efficiency in below rated operation without intense control action, outperforming the conventional quadratic control. This was achieved even without readjustment of the control algorithm parameters to fit the characteristics of the new rotor, which shows the robustness of the scheme.

From previous research it is known that although a rotor with peaky power coefficient characteristic makes stall control easier, it poses stricter control bandwidth requirements in above rated conditions. However, here it was shown that a slightly sharper power coefficient curve of the rotor does not strongly increases the lower control bandwidth requirement, while at the same time considerable improvement in the power regulation can be achieved using the proposed control algorithm in combination with speed controllers with moderate gains.

From the above, it can be concluded that the proposed control method provides a promising solution for the control of variable speed stall regulated wind turbines. Therefore, it provides the confidence that it is possible to construct a variable speed stall regulated wind turbine, which achieve high aerodynamic efficiency and accurate power control.

7.3. Future work

Since the proposed control algorithms exhibited the desired performance in the hardware-in-loop simulator, the next step should be to apply them in an actual wind turbine. In the following paragraphs, areas that require further research towards this direction are presented.

In this research, the rotor aerodynamics were modeled using static models. Therefore a more accurate assessment of the performance of the control algorithm is required, under realistic conditions. Unless dynamic models of increased complexity of these phenomena become available, the only way to fully test the proposed control method is to implement it on a real wind turbine. Specifically, stochastic changes in the aerodynamic behaviour of the wind turbine may affect the performance of the wind speed estimation algorithm and therefore the below rated operation as well as the performance or even the stability of the whole system during stall regulation. Therefore, the first step is to investigate the statistics of these changes in the aerodynamics.

Specifically, regarding below rated operation, if the changes of the power coefficient curve during operation are characterized by short correlation on time, then no considerable impact on the control is expected, since these will act as white noise in the estimated effective wind speed, which can be filtered in order to obtain a smooth and accurate wind speed estimate. However, if these changes appear to have considerable correlation in time then reduction of the achieved aerodynamic efficiency is expected, the amount of which depends on the deviation from the theoretical curve and on the correlation time. In that case, further research is required in order to increase the robustness of the wind speed estimation algorithm to these phenomena. Possible solutions to be investigated are intelligent algorithms that could predict or adjust the power coefficient, based on its short time history may provide the solution to the above challenges.

Regarding the control in above rated operation, if the stochastic variations of the power coefficient are considerably correlated in time, deterioration of the stall regulation algorithm is expected, since the used fixed rates of change of the generator speed will

result in slow power control in case the actual power coefficient curve appears broader than expected and to less smooth power control, in case the curve appears narrower. Therefore, the statistics of the power coefficient variations need to be examined in order to optimally adjust the power regulation algorithm parameters, while alternative intelligent adaptive solutions can also be a challenging area for further research.

The variations of the power coefficient curve are reflected to variation of the positions of the right half plain poles and zeros of the system during operation in deep stall. Therefore, the optimal choice of the bandwidth of the closed loop speed control, in order to guarantee stability as well as acceptable performance, becomes quite a challenging task. This is another challenge that has to be assessed based on real data. Further work is required towards the design of robust or adaptive controllers and their assessment in an actual system.

Regarding the aerodynamic torque estimation using adaptive Kalman filtering, when the filter is applied to an actual wind turbine, considerable uncertainty in the exact wind turbine parameters is involved and therefore, the robustness of the Kalman filter estimators needs to be further examined. It is mentioned that in general, the effect of the uncertainty can be reduced by appropriately increasing the process noise covariance matrix of the Kalman filter model. However, in this case the relative weight on the speed measurement increases and therefore, the filter becomes more susceptible to the measurement noise. Therefore, the use of multiple model adaptive estimation or other adaptive methods may provide more effective solutions and therefore requires further research.

Regarding the control of the generator, further research on the application of linear parameter varying controllers and sliding mode controllers is required, since these are

likely to achieve quite effective control, with reduced complexity or less programming effort.

Furthermore, the effects of the tower for aft motion, which affect the apparent wind speed seen by the rotor, in the control of the variable speed stall regulated wind turbines is another area for future research. Specifically, the changes in the thrust forces during stall regulation may cause tower vibrations, which in turn can result to power fluctuations. Therefore, robustness of the power regulation algorithm to such phenomena needs to be experimentally assessed.

Finally, further research is required on the hardware-in-loop simulator for variable speed wind turbines (which can be considered as a valuable tool for intermediate testing of controllers performance) in order to achieve perfect simulation of the wind turbine dynamics. In general, it is expected that for larger wind turbines with slower dynamics the influence of the simulator hardware becomes more negligible. Also, an exact simulation of the actual generator characteristics, such as the rotor time constant, in case this is considerably slower than of the generator of the simulator, requires compensation terms to be included in the vector control algorithm of the induction generator drive used in the simulator.

Future work should in general be directed at hardware testing of the proposed control method in an actual wind turbine. The whole control scheme does not require additional sensors and uses the existing hardware in commercial wind turbines. The whole scheme can be implemented on a DSP board. Challenges that then need to overcome have to do with the verification of the obtained effective wind speed estimate, since this is not measurable. Therefore, further work is required in this area too.

Funded research work in conjunction with the wind turbine industry may overcome the above challenges, in order to construct a variable speed stall regulated wind turbine, which has not been feasible so far.

7.4. Original contribution of the thesis

The main original contribution of the thesis is the development and implementation of a complete control system for variable speed stall regulated wind turbines. This control system achieves high performance over the whole operating region of the wind turbine with improved efficiency compared to the conventional quadratic control for below rated operation and accurate stall regulation at constant power for above rated conditions, using existing hardware and without the use of additional measurements of the wind turbine. In addition, during the development of the control system further original contributions were made to the following areas:

1) Examination of the sensitivity of the modes of the wind turbine linearized model to system parameters and operating conditions through modal analysis using generalized participations. That way it was possible to explicitly observe the dependency of every distinct mode to the changes in the operating point.
2) Modeling of variable speed field oriented controlled drives using a proportional-integral torque controller. This way of modeling of a vector controlled drive was motivated after the observation through simulations that the dynamic response of the vector controller is basically characterized by its internal current controllers response. The estimation of the direct and quadrature axis currents in the rotating reference frame is in practice very accurate, when an encoder is used to obtain the speed of the generator, so the influence of this mechanism can be neglected. In addition, through hardware simulations it was shown that in

general the speed response of the generator was close to what was expected from software simulations, so modeling of the switching function of the converters is not considered essential, for a control design study.

3) Development of a fully dynamic hardware-in-loop simulator for constant speed and variable speed wind turbines using industrial hardware and a high performance simulation platform, which enabled the testing of complicated control systems for variable speed stall regulated wind turbines. In this work the main objectives for the design of hardware-in-loop simulators for wind turbines are identified. In addition, a dynamic analysis of simulators of different type and with more complex drive systems including a belt drive is presented. This analysis comprises also novel work in this area, since it gives the directions in order to design high performance hardware-in-loop simulators.

4) Aerodynamic torque estimation using adaptive Kalman filters. This work presents the way to design high performance aerodynamic torque estimators that effectively adapt to arbitrary wind turbulence and measurement noise conditions. Therefore the challenge of the optimum tuning of the filters is overcome. Two types of adaptive estimators have been developed and implemented:

   a) Multiple model adaptive estimator, which uses a bank of Kalman filters tuned to different parameter values and therefore can provide accurate estimates for an arbitrarily broad range of parameter variations. Further to the implementation of the algorithm in the wind turbine simulator, the operation and theoretical aspects of this algorithm are presented in a thorough and comprehensive way, in order to be understood and applied to

wind turbine applications. Furthermore, challenges that can appear during the implementation and ways to overcome are presented in detail.

b) A novel adaptive algorithm for process noise variance estimation. This algorithm enables the development of high performance innovation based adaptive estimators with less computation load than the multiple model estimators. The proposed algorithm outperformed the existing ones.

5) Complete description and ways to overcome the challenges regarding the wind speed estimation through the aerodynamic torque. An effective method to control the generator of any wind turbine using the effective wind speed is presented.

6) Development of novel algorithms for stall regulation at constant power. The proposed algorithms have been shown to achieve very good performance through hardware simulations using rotors of different power coefficient curves. This motivated further enhancements using more intelligent methods to increase robustness against uncertainties during operation. Also, other power regulation algorithms have been seen to be very promising through software simulations.

7) Design and implementation in the wind turbine simulator of several control schemes such as scheduling proportional-integral, scheduling H-infinity, linear parameter varying and sliding mode controllers and detailed examination of their performance to reveal advantages and disadvantages. The design of the above controllers, although based in existing theory, is novel, since similar implementations have not previously been described or tested through hardware simulations.

8) Development and implementation in the wind turbine simulator of a novel anti-windup scheme applicable to any type of higher order controllers as well as to

linear parameter varying controllers. The operation of the proposed anti-windup scheme does not depend on the dynamics of the controller and therefore does not require tuning; it is directly implementable in discrete time with minimum programming effort and the only information required is the values of saturation limits of the controller. Hardware simulation results have demonstrated this effectiveness.

9) A complete control solution for variable speed stall regulated wind turbines has for the first time been tested on a hardware-in-loop simulator. This includes the identification, analysis and explanation of the interactions between the wind turbine simulators and the control systems under test, in order to characterize as accurately as possible the performance of the proposed control system.

Further to the above developments, future directions have been given, in order to extend the presented methods and to increase their effectiveness in real applications.

As a conclusion of the above, the presented work comprises a considerable contribution in the future development of variable speed stall regulated wind turbines.

In addition, the research made contributions to areas such as adaptive state estimation as well as anti-windup control, which can have a broader application in engineering systems.

A. APPENDIX

Table of Contents

A.1. Linearization of dynamic models

Non-linear model: $\dot{x} = f(x,u,v)$, $y = g(x)$, perturbation $\tilde{x}, \tilde{u}, \tilde{v}$ around $\bar{x}$, $\bar{u}$, $\bar{v}$.

Linearized model: $\dot{\tilde{x}} = A\tilde{x} + B\tilde{u} + D\tilde{v}$

Jacobians: $A = \frac{\partial f(\bar{x},\bar{u},\bar{v})}{\partial x}$, $B = \frac{\partial f(\bar{x},\bar{u},\bar{v})}{\partial u}$, $D = \frac{\partial f(\bar{x},\bar{u},\bar{v})}{\partial v}$

Output vector: $\tilde{y} = C\tilde{x}$

$C = \frac{\partial g(\bar{x})}{\partial x}$

A.2. Power and torque coefficient data -Windharvester [3]

```
Tip_speed_ratio=[1.3693 1.3976 1.4270 1.4577 1.4897 1.5232 1.5582
1.5949 1.6333 1.6736 1.7160 1.7606 1.8075 1.8570 1.9094 1.9647 2.0233
2.0856 2.1518 2.2224 2.2977 2.3783 2.4648 2.5578 2.6581 2.7666 2.8843
3.0125 3.1526 3.3064 3.4760 3.6639 3.8733 4.1080 4.3730 4.6746 5.0209
5.4226 5.8941 6.4554 7.1349 7.9743 9.0376]

Power_coefficient=[0.0195 0.0203 0.0204 0.0214 0.0222 0.0234 0.0246
0.0254 0.0263 0.0276 0.0295 0.0317 0.0344 0.0373 0.0408 0.0440 0.0471
0.0516 0.0593 0.0647 0.0718 0.0829 0.0939 0.10 0.11 0.12 0.136 0.16
0.177 0.21 0.264 0.30 0.332 0.372 0.401 0.42 0.4512 0.4482 0.3667
0.2593 0.2122 0.1744 0.0832]

Torque_coefficient=[0.0142 0.0145 0.0143 0.0147 0.0149 0.0154 0.0158
0.0159 0.0161 0.0165 0.0172 0.0180 0.0190 0.0201 0.0214 0.0224 0.0233
0.0248 0.0276 0.0291 0.0312 0.0349 0.0381 0.0442 0.0505 0.0551 0.0614
0.0684 0.0747 0.0815 0.0870 0.0914 0.0944 0.0955 0.0977 0.0910 0.0899
0.0827 0.0622 0.0402 0.0297 0.0219 0.0092]
```

A.3. Pole-zero locations and power/torque coefficient curve width

Figure A.3.1. shows the original torque coefficient curve, its polynomial approximation and another narrower polynomial curve.

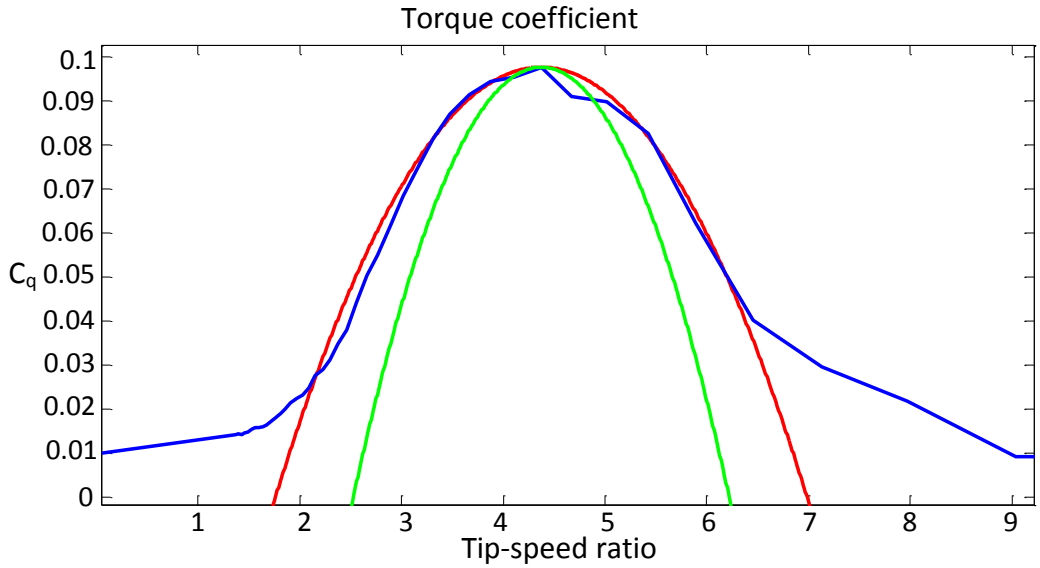

Figure A.3.1. Original (blue), approximated (Kq=0.0143) (red) and narrow (Kq=0.0143*2) (green) C_q curve.

Figure A.3.2 shows the pole-zero locations of the dynamic system of Eqns. (2.28-32) for operating conditions: ω_1=4rad/sec, V=20m/sec using the red and green C_q curve.

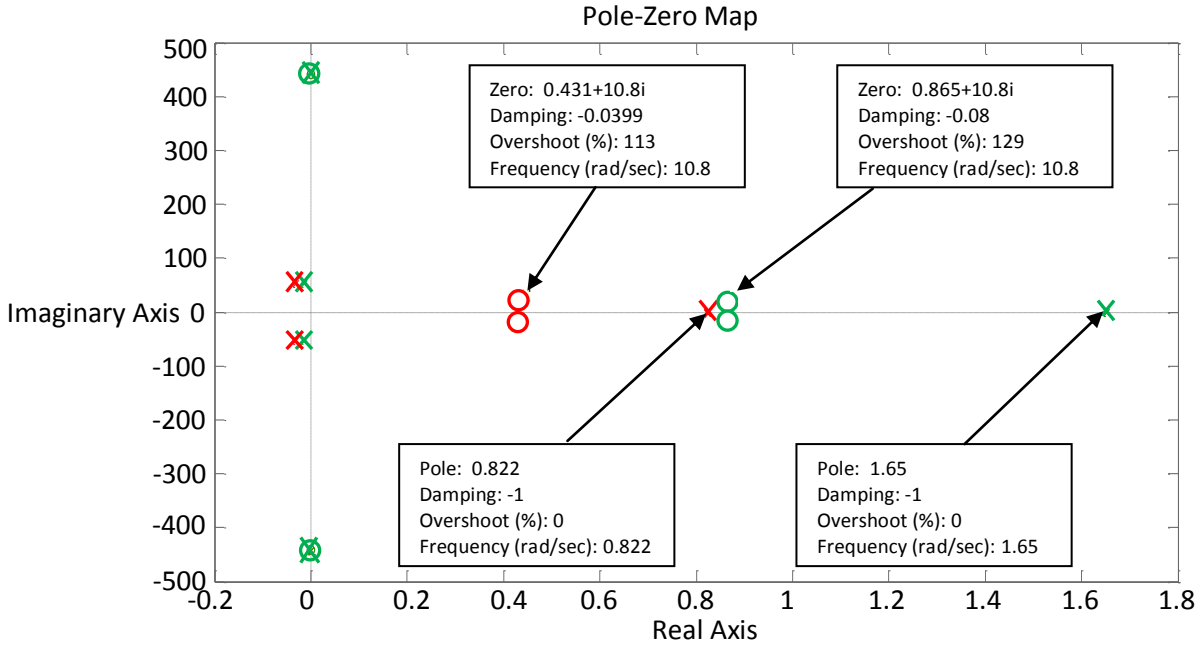

Figure A.3.2. Pole zero locations corresponding to the polynomial curves of Figure A.3.1.

As can be seen, by multiplying by 2 the factor determining the width of the curve, the frequency of the RHP pole and the damping of the RHP zeros are doubled.

A.4. Constant speed wind turbine hardware in the loop simulator

A.4.1. Description of the CS HILS

The CS HILS consists of the following parts:

a) A PC equipped with MATLAB/Simulink and a dSPACE ds1103 simulation platform. (Initially a ds1102 was used, but soon this was replaced by ds1103, due to improved performance and facilities)

b) A DC motor drive and DC motor as a prime mover.

c) A grid-connected IG as a generator.

Also, a signal analyzer was used to measure and display the currents, voltages and power of the IG. A simple diagram of the arrangement is given in Figure A.4.1.

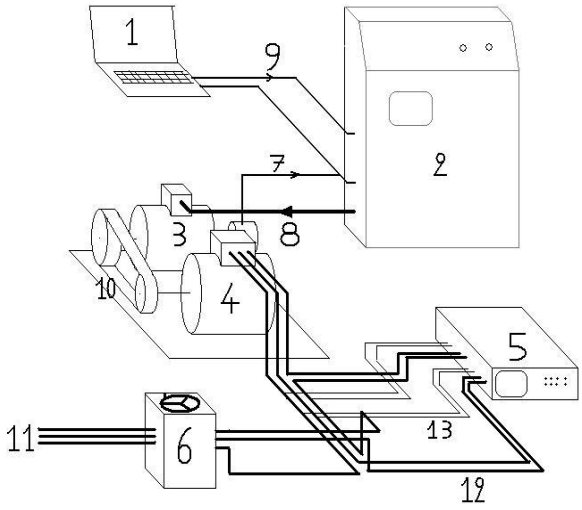

1. PC
2. Control Techniques Mentor II DC motor drive
3. DC motor
4. IG
5. Power analyzer
6. Variac
7. DC tacho-generator feedback
8. Torque current demand to the motor
9. Torque demand from PC/dSPACE
10. Belt drive system
11. Connection to the grid
12. Current measurement lines
13. Voltage measurement lines

Figure A.4.1. Schematic of the CS HILS

As can be seen from Figure A.4.1, a speed measurement is fed back to the DC drive and the PC. This speed measurement is obtained from a DC tacho-generator attached on the

shaft of the motor and it is used by the DC drive (if used as a speed controller) and by the wind turbine model to close the simulation loop.

The power of the IG is measured by a digital power analyzer using the two watt-meters method. Finally, the Variac is there to limit the current during start-up of the generator.

A.4.2. Dynamics of the CS HILS

A dynamic block diagram of the CS HILS is given in Figure A.4.2, where T_D is the torque demand that propagates from the software model through the DC drive/motor and the Belt drive to the IG. The loop is closed through ω_2, which is fed back to the model. In the diagram, the stator frequency, ω_z, for the IG, comes as an input from the electricity grid.

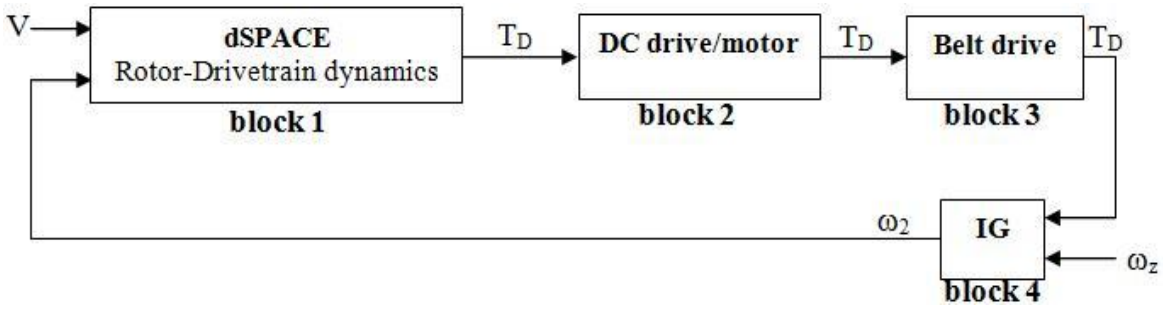

Figure A.4.2. Block diagram of the dynamics of the CS HILS.

A.4.3. Hardware compensation

The DC motor compensation proposed in [3] is shown in Figure A.4.3 (blue coloured blocks).

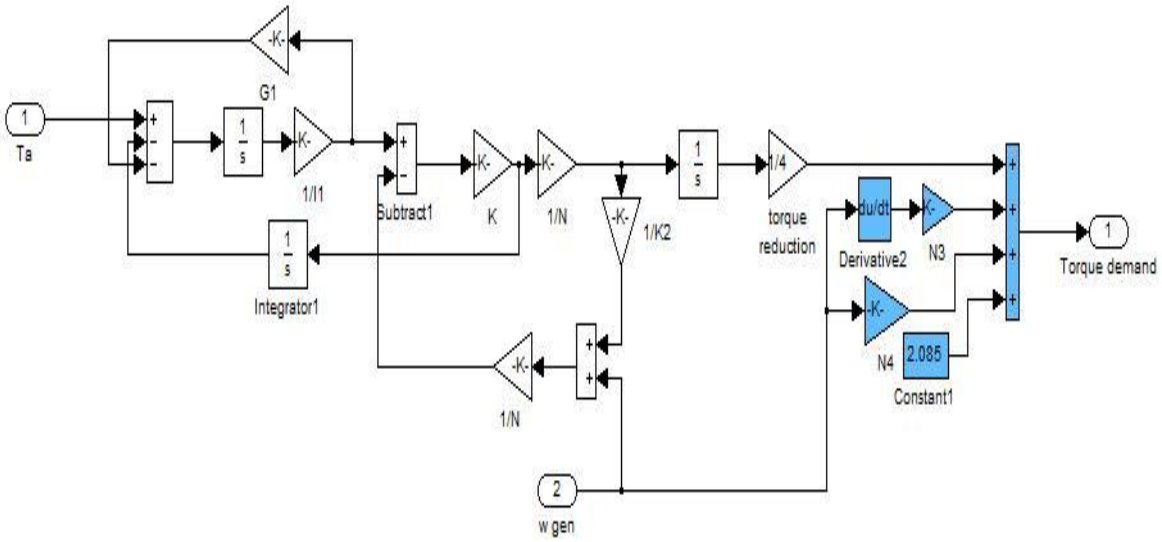

Figure A.4.3. Drivetrain Simulink model used in the CS HILS with DC motor compensation (blue) [3].

As can be seen, the DC motor compensation consists of a derivative with a gain "N3", to compensate the inertia of the DC motor (I_M=0.488kgm^2) and the large pulley (I_p=0.3kgm^2) (combined inertia I_c=0.788kgm^2), a block "N4" for friction losses compensation and a constant term for constant torque load compensation [3]. Considering that the actual WT generator has inertia 0.3897kgm^2 and the HILS hardware 0.788kgm^2, the HILS needs additional torque both during acceleration and deceleration in order to accurate simulate the actual IG. However, according to [3], the DC drive was set to work in the first quadrant only (motoring operation), which cancels negative torque demands and so, compensation during deceleration. For these reasons the compensation scheme of Figure A.4.3 is considered incomplete.

Here, hardware compensation based on a speed controller is proposed. This speed controller provides the T_D in order for ω_2 to follow a desired value coming from a reference model. The Simulink implementation of this scheme is shown in Figure A.4.4. This compensation method was inspired by [58, 59], where similar methods were used to simulate loads for IG drive testing.

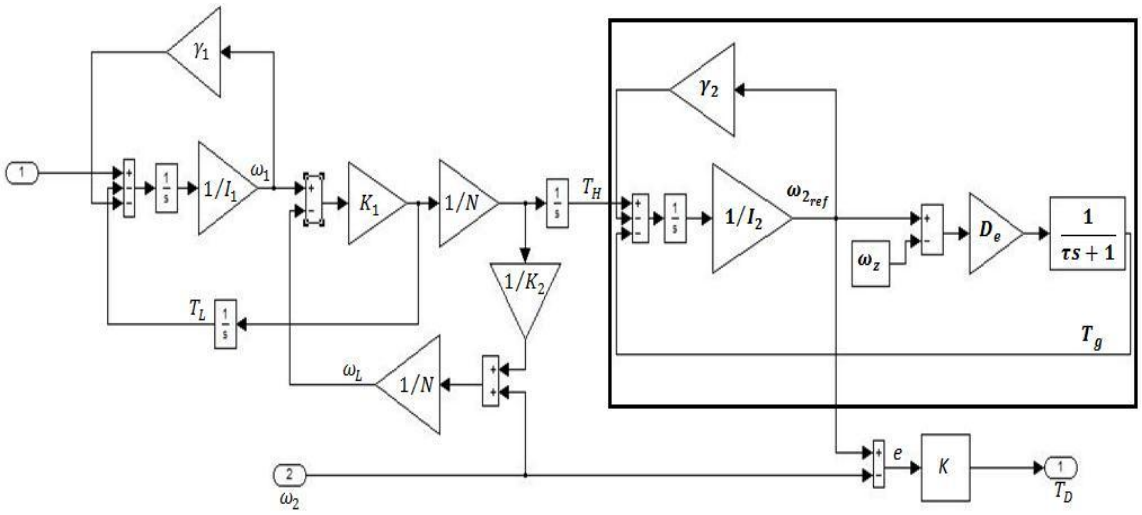

Figure A.4.4. Compensation method for CS HILS.

Demonstration of hardware compensation

Assume that "block 2" and "block 3" of Figure 3.2 are ideal, so they can be represented by a gain of unity. Then, the Bode plots of the transfer function from T_a to ω_2, $G_{T_a\omega_2}$ will be compared for the following models:

A) For the model of the actual WT with parameters given in Section 2.7.1.

B) For the model of the WT after it is simulated in HILS (belt and DC motor are neglected).

C) For the model of the WT after it is simulated in HILS with hardware compensator (PI speed controller).

The HILS IG parameters are given in Table A.4.1.

Inertia of the generator, I_2	0.075 Kgm^2
slope of the slip curve, D_e	4.5 Nm/rad/sec
Rotor time constant, τ	26.5msec
number of pole pairs, p	1
IG friction loss constant, γ_2	0.002

Table A.4.1. HILS IG parameters.

The three transfer functions for the above models are:

$$\text{A)}\ G_{T_a\omega_{2(A)}} = \frac{4.015s+151.5}{s^4+37.77s^3+3942s^2+6.195e004+4.343e005}$$

$$\text{B)}\ G_{T_a\omega_{2(B)}} = \frac{7.662s+209.9}{s^4+27.51s^3+7953s^2+7.918e004+5.925e005}$$

$$\text{C)}\ G_{T_a\omega_{2(C)}} = \frac{2609s^2+1.7e005s+2.7e006}{s^6+405.8s^5+3.074e004s^4+3.324e006s^3+1.418e008s^2+1.25e009s+8.97e009}$$

The Bode plots are shown in Figure A.4.5, where the differences between (A) and (B) can be observed due to the replacement of the actual IG with the one of the HILS.

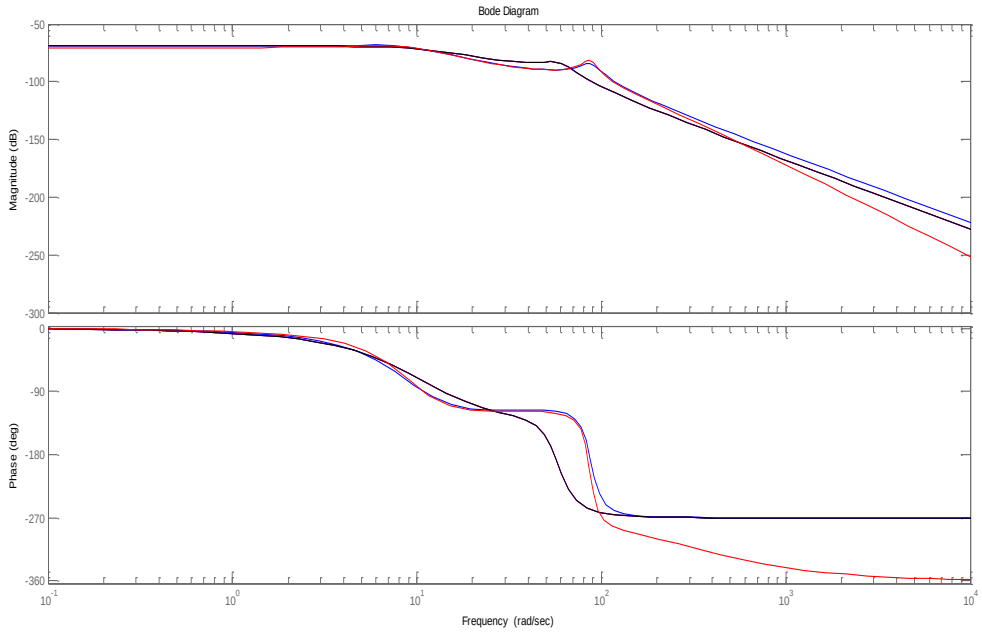

Figure A.4.5. Bode plots for cases (A), black, (B), blue and (C), red.

From Figure A.4.5 it can be seen that the compensated system (C) is quite close to the actual (B), for frequencies below 100rad/sec. (It is mentioned that the differences in the spectrums observed in [3] were in the frequency band of 20 to 100rad/sec, which absolutely agrees with the observed differences of the above Bode plots.)

A.4.4. Implementation of the CS HILS

The compensation method that has been described was implemented in HILS in the laboratory. Figure A.4.6 shows the initial Simulink file used to control the operation of the constant speed HILS, using the compensation of [3] and enhanced with a starting mechanism in order to avoid large torque transients [3].

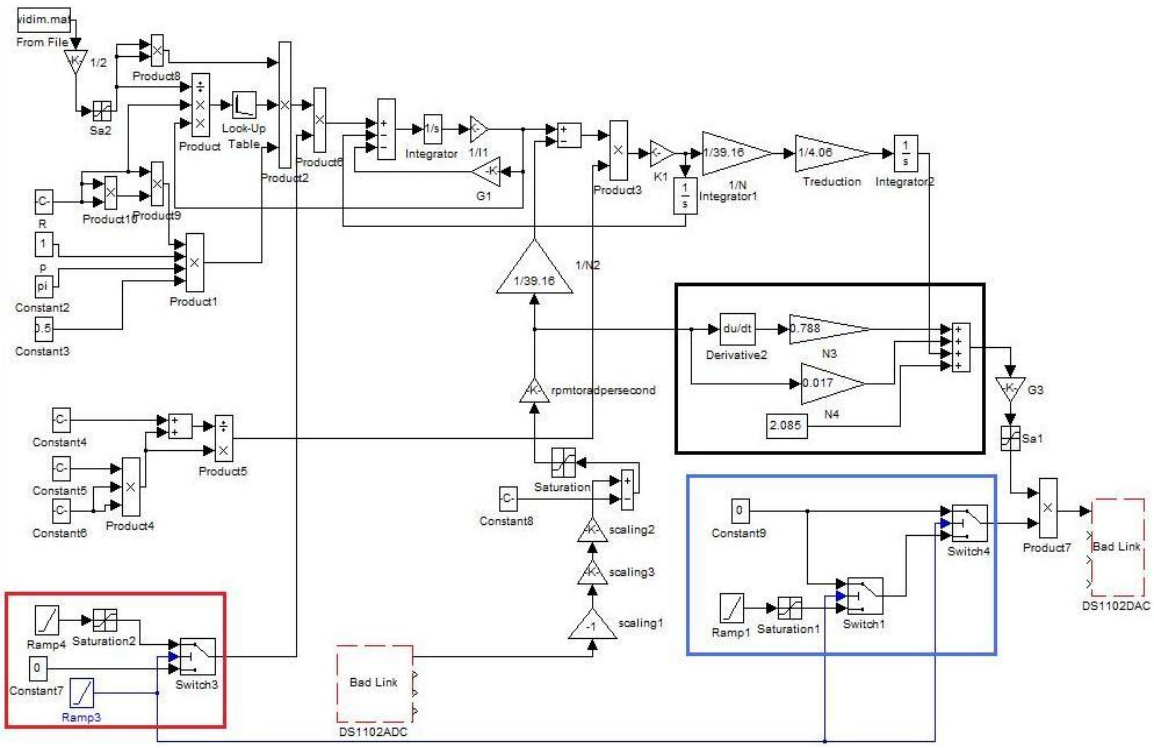

Figure A.4.6. Complete Simulink model used for the constant speed HILS.

A.4.5. Hardware simulation results

Figures A.4.7 and A.4.8 show the IG speed and the associated torque demand on the IG for operation without and with compensation respectively, for various choices of the DC speed offset (rpm), (the offset is explained in the next paragraph).

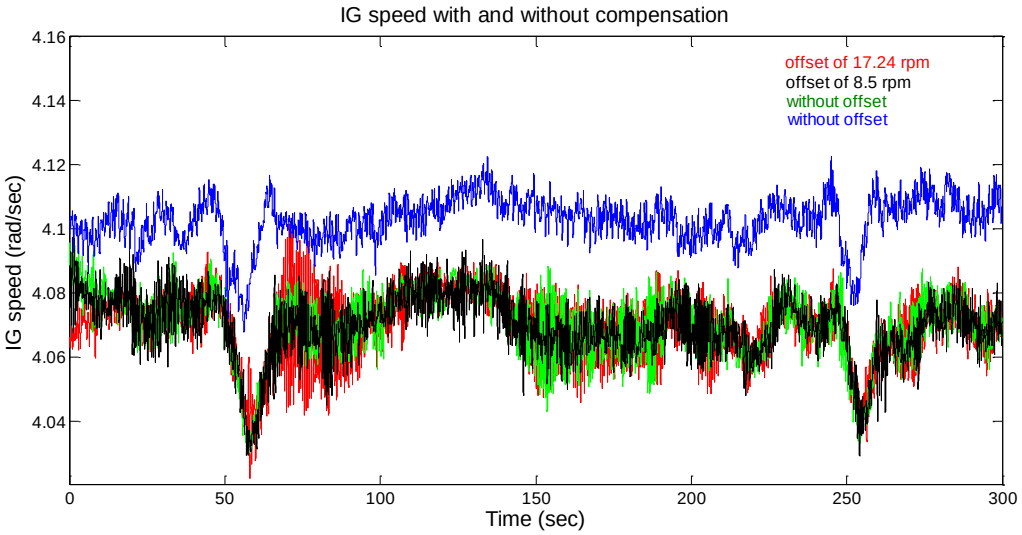

Figure A.4.7. IG speed without (blue) and with compensation (black, green, red).

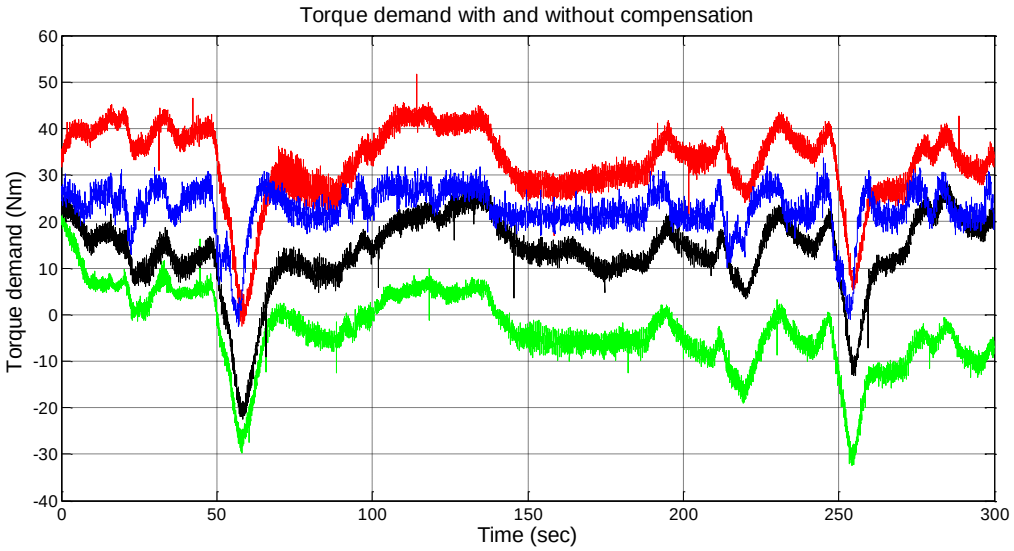

Figure A.4.8. Torque demand on the IG.

The actual WT generator has smaller rated slip than the IG of the HILS. Therefore if no compensation for this is used in HILS, the IG speed is higher relative to the speed of the actual system under simulation (blue line). By using compensation, the speed is reduced from an average value of 4.1 to 4.08 rpm, which is what is expected for the actual system. However, in order for this to be achieved, the PI compensator applies motoring demand on the IG, to reduce its speed. If this is not desired, a DC offset can be added to the IG speed feedback. This offset keeps the speed of the IG to a lower

value relative to the desired, imposed by the actual IG model in Simulink, consequently, the compensator applies generating demand in order to meet the specifications required.

A.5. Variable speed hardware in the loop simulator - test rig with belt drive connection

In order to examine the influence of the DC drive and belt drive and to the simulated WT dynamics, these are modelled using simplified models as follows:

DC drive/motor

The DC drive has been modelled as a PI speed controller and the motor as inertia, ignoring fast internal current loop dynamics. The dynamic equations are:

$$\dot{x} = \omega_2 - \omega_M \quad \text{(A.5.1)}$$

$$T_D = K_{I_{DC}} x + K_{P_{DC}}(\omega_2 - \omega_M) \quad \text{(A.5.2)}$$

$$I_M \dot{\omega}_M = T_D - 2T_B \quad \text{(A.5.3)}$$

where ω_M is the motor speed, I_M the motor inertia, $K_{P_{DC}}$ and $K_{I_{DC}}$ the PI gains of the DC drive model and $2T_B$ the reaction torque of the belt drive on the motor side.

Belt drive

The belt drive has been modelled using the equations:

$$\dot{x}_b = r_M \omega_M - r_g \omega_g \quad \text{(A.5.4)}$$

$$2T_B = r_M K_b x_b \quad \text{(A.5.5)}$$

where x_b represents the distance of the stretch of the belt due to the difference on the applied forces $r_M \omega_M$ and $r_s \omega_s$, where r_M and ω_M are the radius and the rotational speed of the motor pulley respectively. r_g and ω_g are the corresponding values for the IG pulley.

IG

The dynamics of the IG can be represented by:

$$I_g\dot{\omega}_g = T_B - T_g - \gamma\omega_g \qquad \text{(A.5.6)}$$

$$\tau\dot{T}_g + T_g = D_e(\omega_g - \omega_z) \qquad \text{(A.5.7)}$$

where I_g is the inertia of the IG and γ its friction loss coefficient. ω_z is given by the model of the IG drive (Section 2.5):

$$\dot{x}_d = T_{G_{ref}} - T_G \qquad \text{(A.5.8)}$$

$$\omega_z = K_I x_d + K_p(T_{G_{ref}} - T_G) \qquad \text{(4.5.9)}$$

where the K_P and K_I of Eqn. (A.5.9) should not be confused with the ones of Eqn. (A.5.2).

Table A.5.1, shows the parameter values of the HILS hardware.

I_M	0.788Kgm^2
I_s	0.075 Kgm^2
r_M	0.17m
D_e	4.57Nm/rad/sec
τ	0.0265sec
$K_{P_{DC}}$	10Nm/rad/sec
$K_{I_{DC}}$	48Nm/rad/sec

Table A.5.1. Parameters of the HILS hardware.

The value of the belt stiffness K_b is not known, so several values between 100 and 10000 (Nm/rad) were tried.

Figure A.5.1 shows the transfer function $G_{T_{g_{ref}}\omega_g}$ of the theoretical model of the Windharvester WT and of the model including the HILS drive system model of Figure A.5.1, for operating conditions (ω_1=4rad/sec, V=6.76m/sec). K_b has been set to several values.

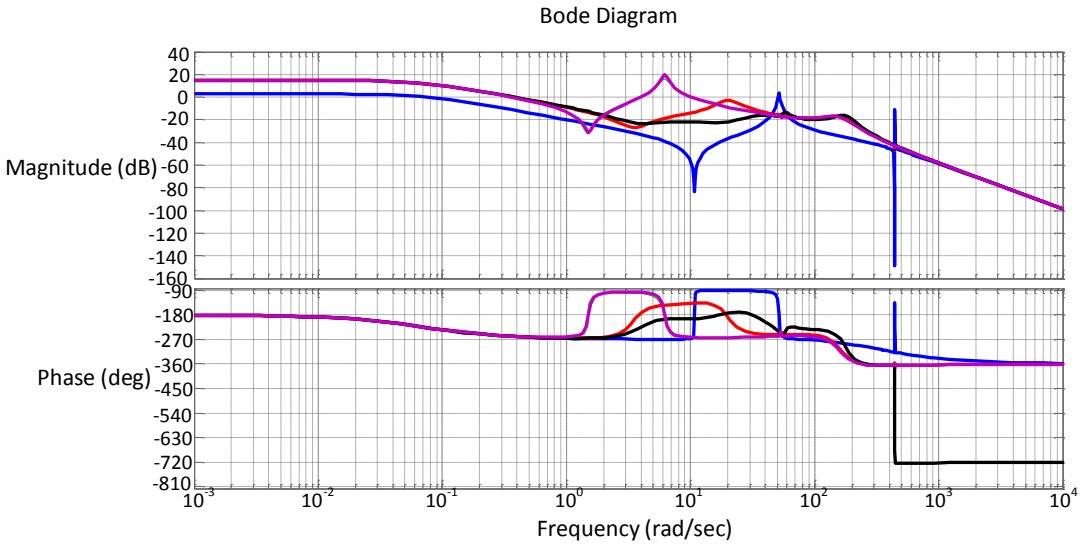

Figure A.5.1. Bode plots of $G_{T_{g_{ref}}\omega_g}$ for the theoretical WT model (blue), its simulation with HILS: K_b=200 (magenta), 2000 (red) and 10000 (black) (Nm/rad).

As can be seen, there is a considerable deviation of the HILS simulated WT dynamics from the theoretical ones for any choice of belt stiffness. It is mentioned that similar observations hold for any choice of the PI gains of the DC drive model, so further Bode plots are not appended. Figures A.5.2 (a & b) show the pole – zero map of the red and black models of Figure A.5.1, were only the most revealing poles and zeros are shown.

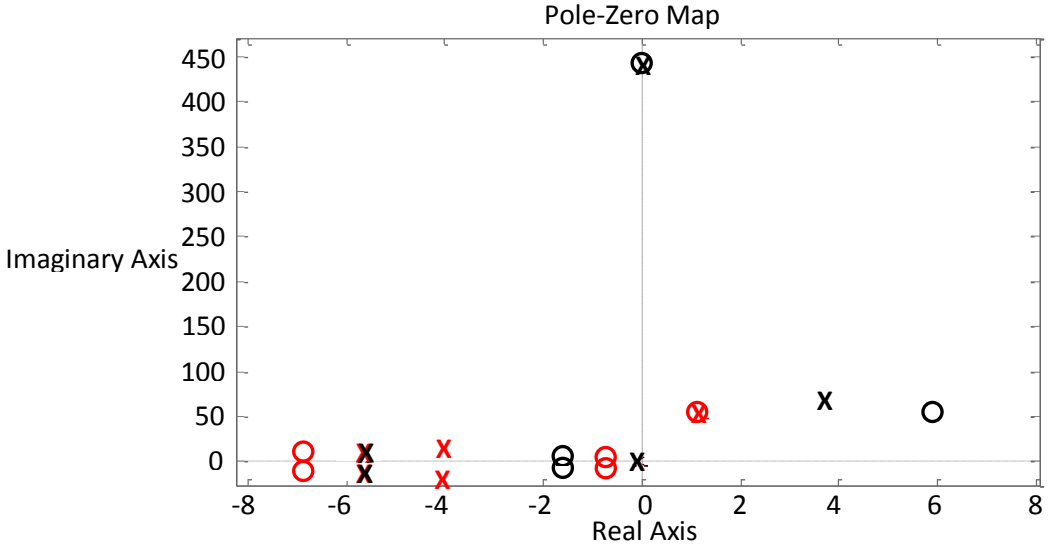

Figure A.5.2(a). Pole – zero map of $G_{T_{g_{ref}}\omega_g}$ of the red and black models of Figure A.6.1.

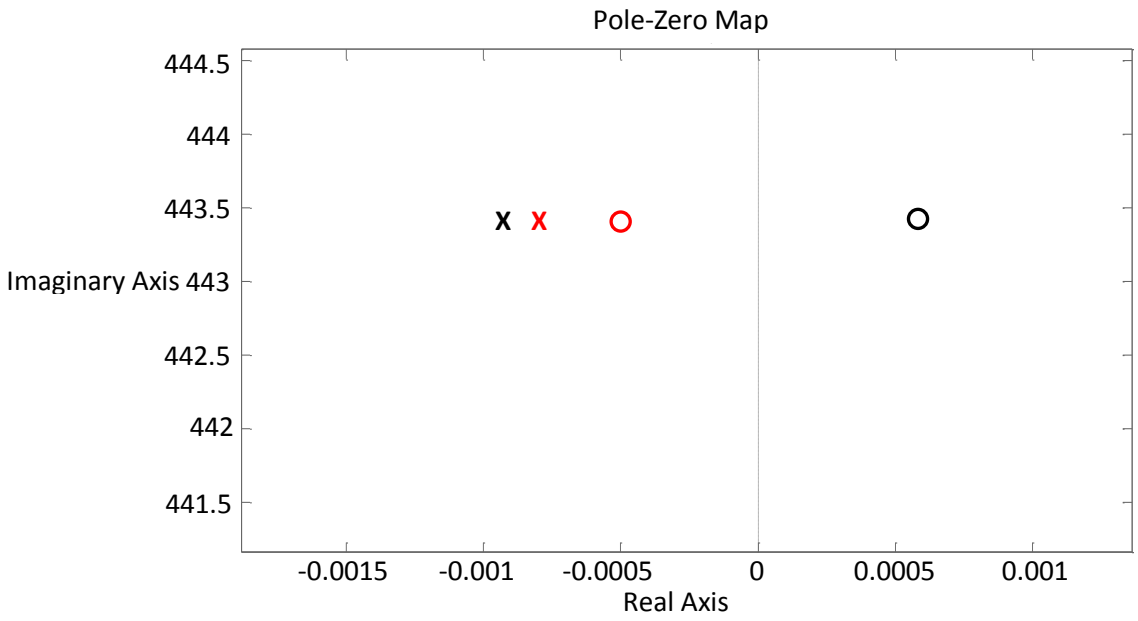

Figure A.5.2(b). Closer view.

As can be seen from Figure A.5.2(a), RHP poles and zeros are observed. For K_b=2000Nm/rad, the RHP pole pair nearly cancels the RHP zero pair. The same observation holds for any 200<K_b<2000. However, by further increasing the belt stiffness to 10000, these separate. In addition, one more zero pair migrates to the RHP, as seen in Figure A.5.2(b).

Figure A.5.3 shows Bode plots of $G_{T_{g_{ref}}\omega_g}$ for operating conditions (ω_1=4rad/sec, V=16.76m/sec) and for K_b=200Nm/rad.

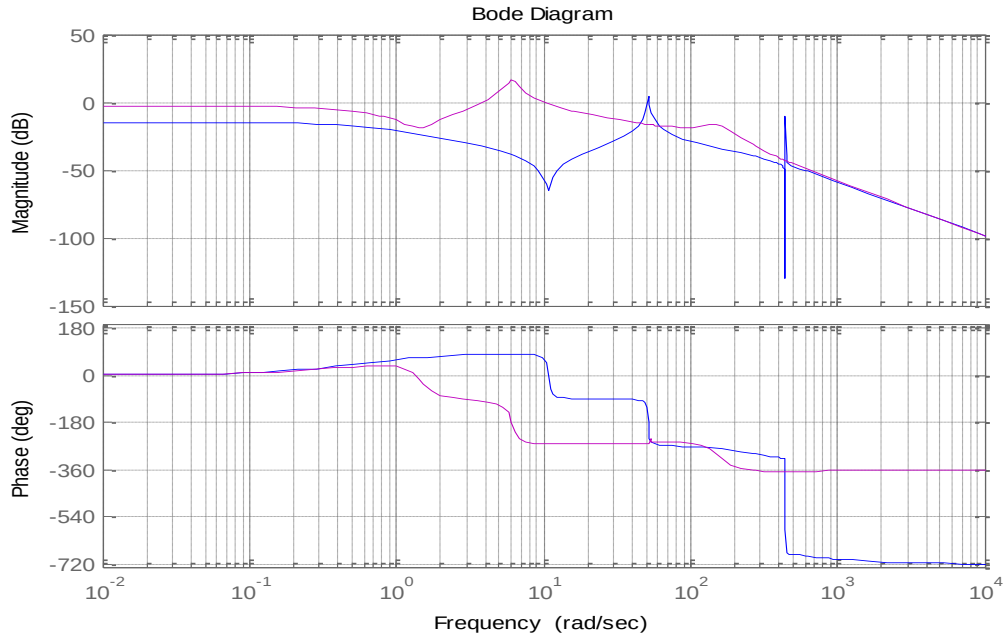

Figure A.5.3. Bode plots of $G_{T_{g_{ref}}\omega_g}$ for the theoretical WT model (blue), its simulation with HILS: K_b=200Nm/rad (magenta).

As can be seen, there is a considerable phase drop of almost 180 degrees for the HILS model at the frequency of 2rad/sec. Figure A.5.4 shows the associated pole-zero maps.

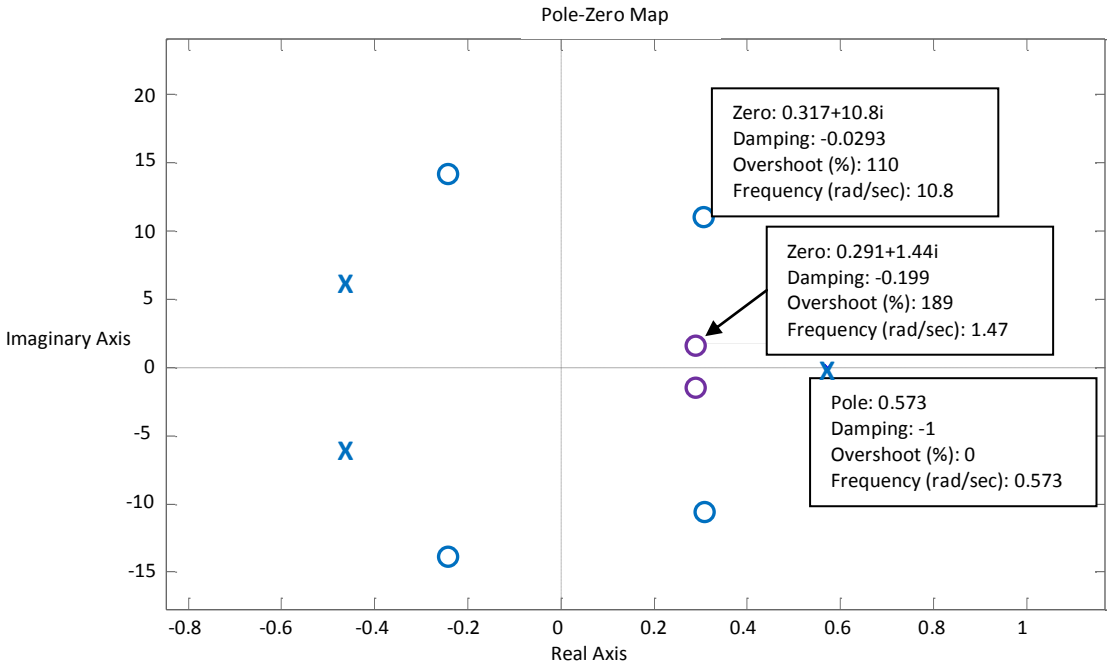

Figure A.5.4. Pole – zero map of $G_{T_{g_{ref}}\omega_g}$ seen in Figure A.6.3.

In Figure A.5.4, a RHP pole at 0.57rad/sec and a RHP zero pair at 10.8rad/sec can be observed for the theoretical model. Also the same pole can be observed for the HILS model (it is actually hidden by the blue "x"). However, the frequency of the RHP zeros has been reduced to 1.44rad/sec. This results to a dramatic decrease of the available bandwidth that is required in order to achieve speed control of the WT at this operating region.

Figure A.5.5 shows the HILS $G_{T_{g_{ref}}\omega_g}$ for K_b=200 and operating conditions (ω_1=4rad/sec, V=16.76m/sec) when compensation is used.

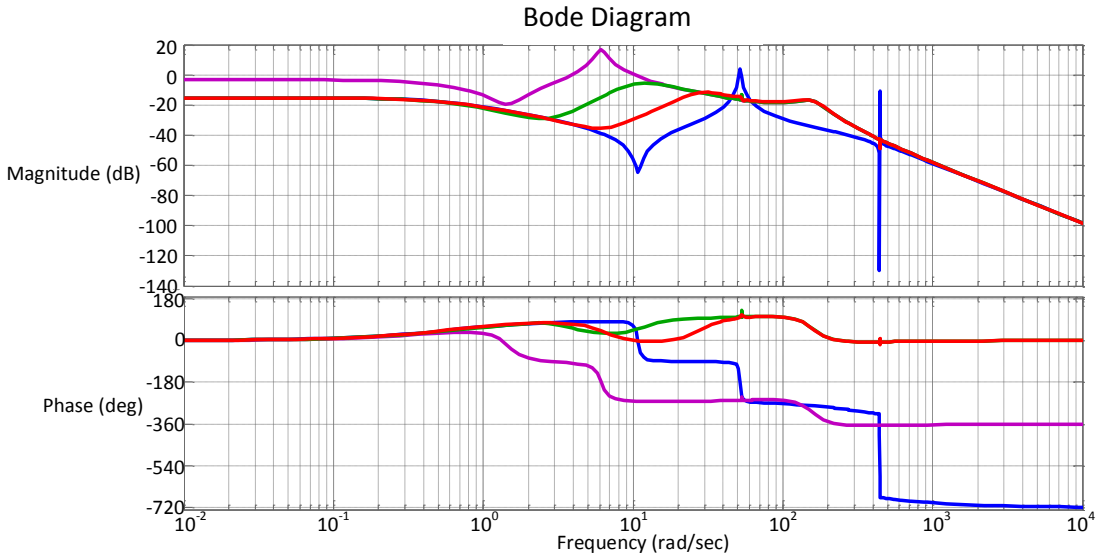

Figure A.5.5. $G_{T_{g_{ref}}\omega_g}$ of the theoretical WT model (blue), without compensation (magenta), with compensator PI gains 10 and 40 (Nm/rad/sec) (green) and with PI gains 200 and 40 (red).

As can be seen, the magnitude Bode plots gradually become similar to the theoretical. However, this is not the case for the phase plots, where considerable differences from the theoretical model are observed. The pole-zero map of Figure A.5.6 shows that the compensator moves the poles and zeros of $G_{T_{g_{ref}}\omega_g}$ to the RHP. In addition, RHP poles appear in higher frequencies than the RHP zeros, which makes the system impossible to stabilize with closed loop control.

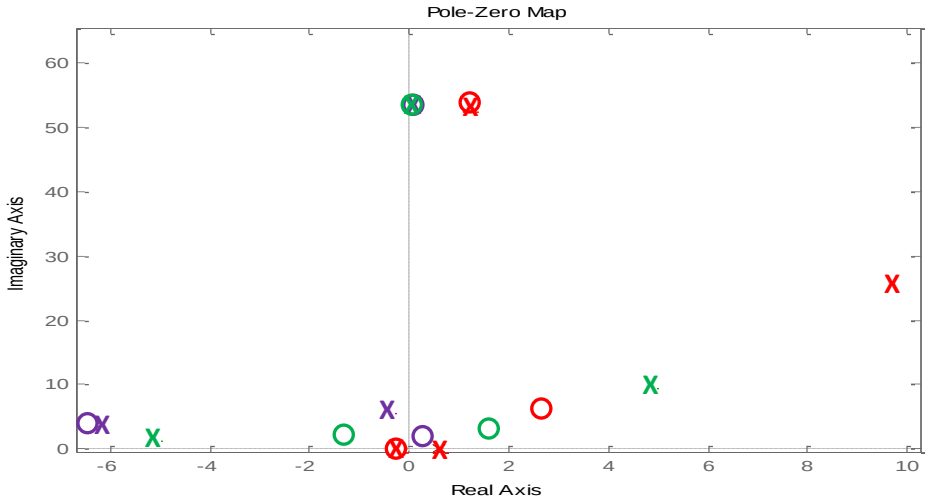

Figure A.5.6. Pole – zero map of $G_{T_{g_{ref}}\omega_g}$ without compensation (magenta), with compensator PI gains 10 and 40 (Nm/rad/sec) (green) and with PI gains 200 and 40 (red).

From the closer view of Figure A.5.7 it can be seen that by increasing the PI gains of the compensator, the RHP zeros of the WT model gradually move to a higher frequency. However, at the same time their negative damping increases to much higher than the theoretical values.

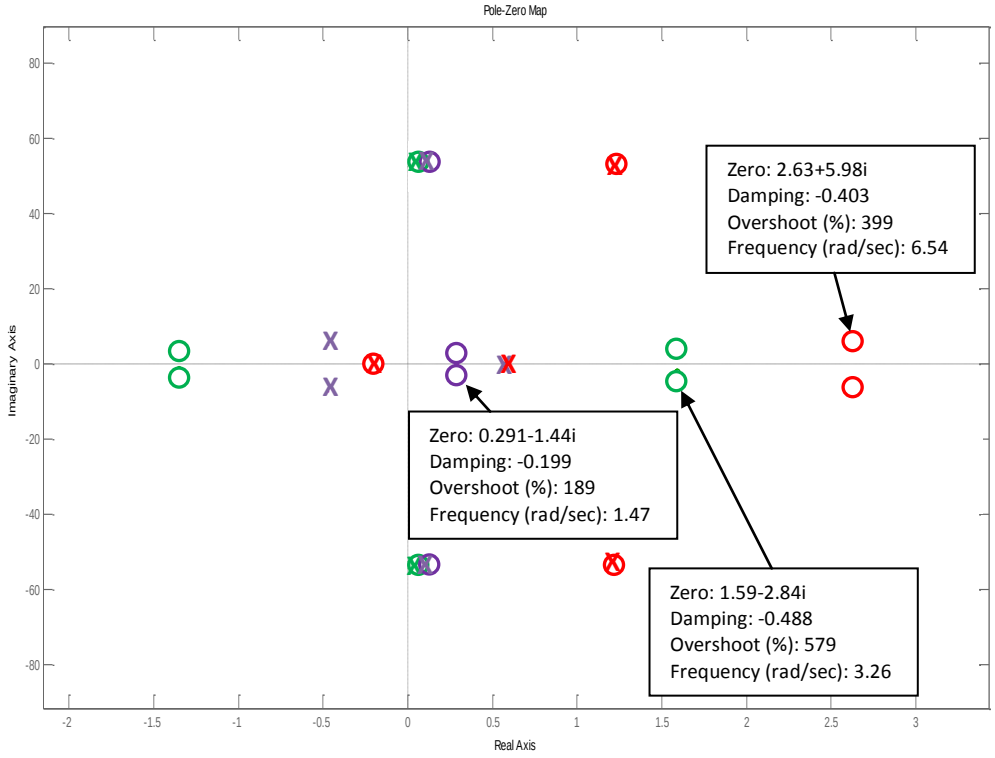

Figure A.5.7. Close up of Figure A.5.6.

As a conclusion, this method fails to effectively compensate the HILS dynamics. Possibly more complicated compensators than a PI controller can be more effective.

A.6. Power electronic converters installation diagram

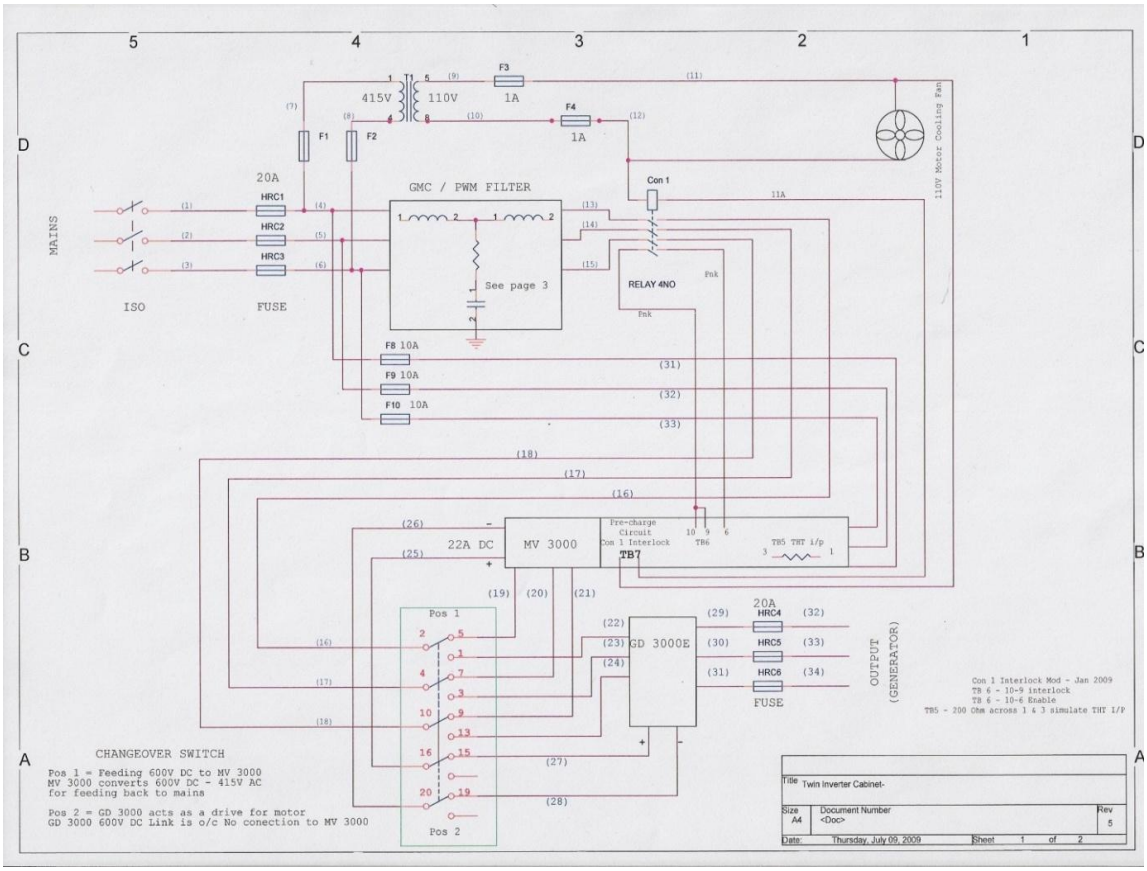

A.7. LCL filter design

A.7.1. Capacitor values

The function of the filter is to suppress harmonics due to converter's PWM switching. It consists of two inductors, one capacitor and a damping resistor per phase. The per-phase equivalent circuit is shown below:

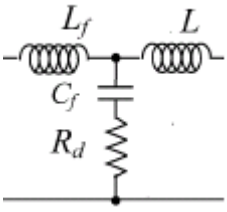

Figure. A.7.1. LCL filter.

The values of the inductors are indicated in the ALSPA MV3000 manual and are:

L_1=583μH and L_2=1749μH

In addition the switching frequency of the PWM sequence of the MV3000 is given 2.5KHz

Now, the capacitors and the damping resistors have to be chosen.

Resonance frequency (rad) of the filter:

wres=sqrt(L/C), L=(L1+L2)/(L1*L2)=1kHz

Per phase capacitor value:C=58μF (C_Δ=20μF).

For the damping resistor, its value should be equal to 1/3 of the capacitor impedance at the resonance [96], so 0.91 Ω.

I_{out}/v_{in} =(1/(L1*L2*C))*abs((1+R*C*i*w)/(i*w*(-w^2+i*w*R*C*wres^2+wres^2)))

of the LCL filter at the resonance frequency (Figure A.7.2):

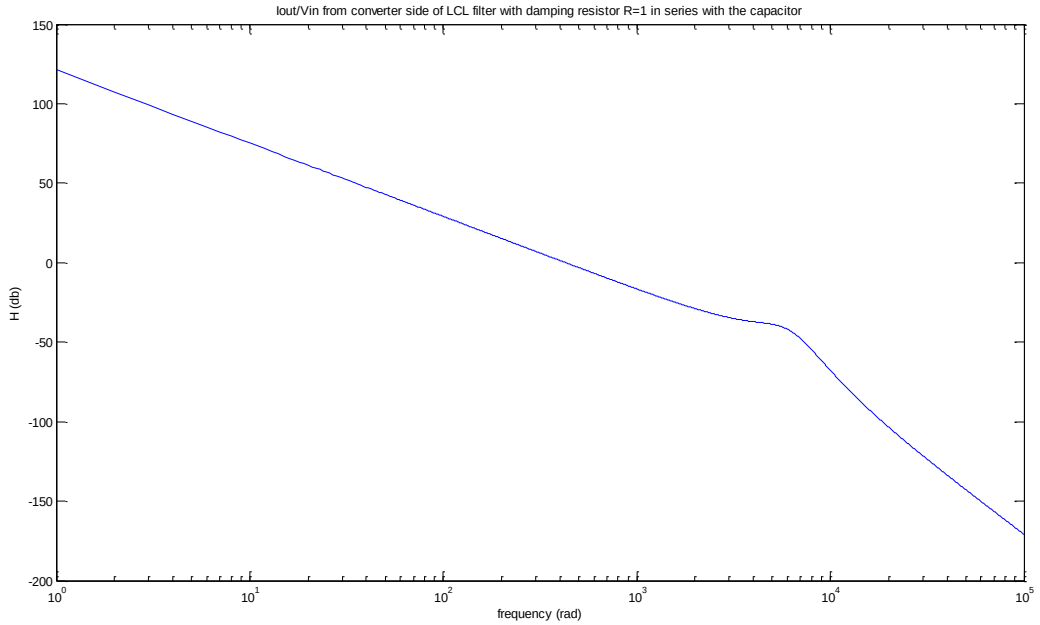

Figure A.7.2. Iout/Vin from converter side of the LCL filter (Iout=Igrid).

A resistor of 1Ω is therefore sufficient then for the application (R_Δ=3Ω).

A.7.2. Rating of the damping resistor (star connection case-R=1 Ω)

During the operation of the converter, the control loop will maintain the power coefficient close to 1. Thus, the current on the grid side of the filter should be in phase with the grid voltage. Under these conditions, the 50Hz current of the capacitor branch with R=1Ω is found: I_c=4.52<89.8° A. In addition, for the worst case, (power coefficient =0), the rms value of the current again is almost the same.

The power dissipation on the resistor is $P_{50Hz}=I^2R$=20.4Watt

The peak to peak ripple voltage at 2.5KHz at the capacitor-damping resistor branch, considering 700V DC link, is [97]:

$700*((X_C+X_R)//X_{L1}) /(X_{L2}+(X_R+X_C)//X_{L1})$=40.34 V.

The rms value of this voltage considering that it is a square wave is equal to its amplitude: 40.34/2=20.17V. This voltage in practice approximates a sinusoidal waveform due to the complex impedances on the network. The rms value then is: 20.17/√2=14.26 V.

The harmonic current 2.5KHz in the capacitor-resistor branch due to this voltage is: $I_C=14.26/(X_C+X_R)$=6.92A and the power dissipation on the resistor: $P_{2.5KHz}$=47.88Watt

Therefore the total dissipation in the damping resistor is equal to: $P= P_{50Hz}+ P_{2.5KHz}$=68.28Watt. This is the lowest rating of the damping resistor in star connection.

A.8. Transfer function measurements in HILS

The wind input of the HILS was set to 6.76m/sec by applying an appropriate constant DC voltage. The $T_{g_{ref}}$ of the WT model was produced by a HP signal analyzer and contained a DC component that lead to ω_1=4rad/sec and a component of variable frequency and small amplitude of 0.1V (corresponding to 0.2Nm (Rated torque of the

IG: 20Nm)), in order to perform the transfer function identification at the window from 250mHz to 100Hz. Figure A.8.1 shows the arrangement

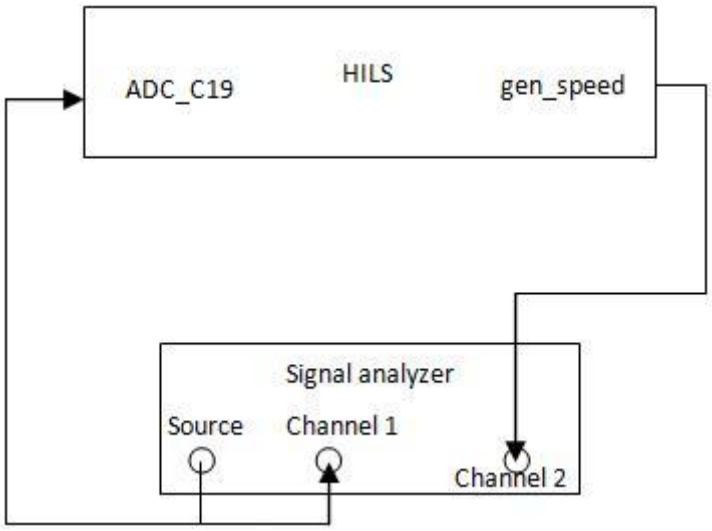

Figure A.8.1. Schematic diagram of HILS connected to the HP signal analyzer for measurement of transfer function from torque to speed of the generator.

As can be seen, the torque signal is provided by the source of the analyzer to the HILS and to Channel 1 of the analyzer. The speed measurement is fed to Channel 2 of the analyzer. The measurement was performed using a chirp signal from the source with the aforementioned DC offset, in order to achieve operation at the desired operating point.

A.9. Augmented dynamic model used in Kalman filtering

If the dynamic model of Eqns. (2.4-2.8) is expressed in the form:

$$\dot{x} = Ax + Bu \qquad \text{(A.9.1)}$$

then the state and input vactors, *x* and *u* respectively, are:

$$x = [\omega_1\ \omega_2\ \theta_1\ \theta_2\ \omega_L]^T,\ u = [T_a\ T_G]^T \qquad \text{(A.9.2)}$$

and the matrices A and B are:

$$A = \begin{bmatrix} -\frac{B_1}{I_1} & 0 & -\frac{K_1}{I_1} & 0 & 0 \\ 0 & -\frac{B_2}{I_2} & 0 & \frac{K_2}{I_2} & 0 \\ 1 & 0 & 0 & 0 & -1 \\ 0 & -1 & 0 & 0 & N \\ 0 & 0 & \frac{K_1}{I_g} & -\frac{NK_2}{I_g} & 0 \end{bmatrix}, \; B = \begin{bmatrix} \frac{1}{I_1} & 0 \\ 0 & -\frac{1}{I_2} \\ 0 & 0 \\ 0 & 0 \\ 0 & 0 \end{bmatrix}, \; C = [0\ 1\ 0\ 0\ 0] \qquad \text{(A.9.3)}$$

By including Eqn. (4.12) into Eqn. (A.9.1), the above vectors and matrices become:

$x = [\omega_1\ \omega_2\ \theta_1\ \theta_2\ \omega_L\ T_a]^T, u = [m\ T_G]^T,$

$$A = \begin{bmatrix} -\frac{B_1}{I_1} & 0 & -\frac{K_1}{I_1} & 0 & 0 & \frac{1}{I_1} \\ 0 & -\frac{B_2}{I_2} & 0 & \frac{K_2}{I_2} & 0 & 0 \\ 1 & 0 & 0 & 0 & -1 & 0 \\ 0 & -1 & 0 & 0 & N & 0 \\ 0 & 0 & \frac{K_1}{I_g} & -\frac{NK_2}{I_g} & 0 & 0 \\ 0 & 0 & 0 & 0 & 0 & 0 \end{bmatrix}, \; B = \begin{bmatrix} 0 & 0 \\ 0 & -\frac{1}{I_2} \\ 0 & 0 \\ 0 & 0 \\ 1 & 0 \end{bmatrix}, C = [0\ 1\ 0\ 0\ 0\ 0],$$

(A.9.4)

where the white noise $m \epsilon R^{1x1}$ can be excluded from the input vector, u, in order to comply with the form of Eqns. (4.1-4.2) (in continuous time):

$\dot{x} = Ax + Bu + \xi$, (A.9.5)

$y = Cx + \nu$, (A.9.6)

The vector $\xi = [0\ 0\ 0\ 0\ 0\ m]^T$ represents the process noise due to modeling uncertainty in Eqn. (A.13.5), while $\nu \epsilon R^{1x1}$ is the measurement noise vector.

The covariance matrix $\Xi \epsilon R^{6x6}$ of ξ is given by:

$$\Xi = \begin{bmatrix} 0 & \cdots & 0 \\ \vdots & \ddots & \vdots \\ 0 & \cdots & S_0 \end{bmatrix}, \qquad \text{(A.9.7)}$$

where only the element $\Xi[6,6]$ is non-zero and equal to the covariance S_0 of the white noise m of Eqn. (4.11).

After discretization, the covariance matrix Ξ becomes:

$$Q = \begin{bmatrix} 0 & \cdots & 0 \\ \vdots & \ddots & \vdots \\ 0 & \cdots & TS_0 \end{bmatrix} \qquad \text{(A.9.8)}$$

where Q_w=TS_0.

A.10. Effects of measurement noise in Kalman filter state estimates

In the following figures the effect of an increased level of the measurement noise on $\hat{T}_a$ estimate obtained by a KF can be seen. Namely, the intensity of the simulated measurement noise, is multiplied by 10 (using the "Band-limited white noise" block of Simulink), while in the KF algorithm R is not updated with the new value. Figure A.10.1 shows the effect on $\hat{T}_a$ estimate of the nonadaptive KF.

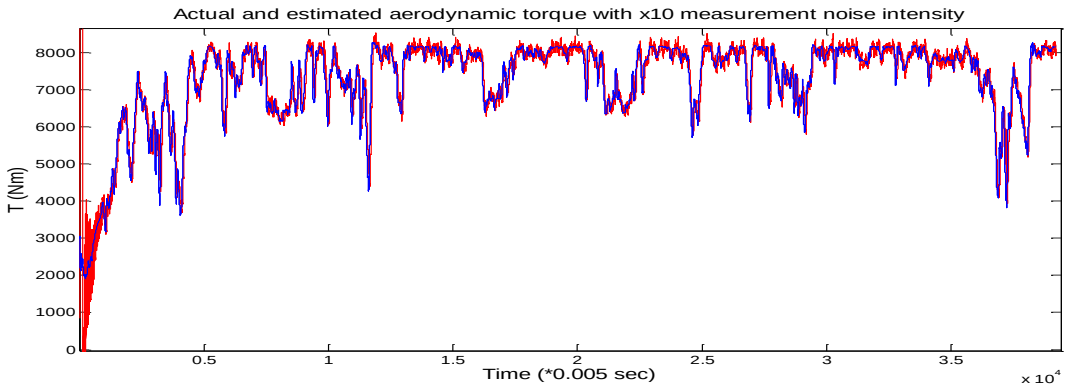

Figure A.10.1. T_a (blue) and $\hat{T}_a$ (red) of KF/UKF under increased measurement noise conditions.

As it can be seen, the estimated waveform becomes noisier. This is because the KF "trusts" the measurement more than it should, since it is not "aware" of the correct amount of uncertainty that is included in the measurement. It is noted that the same effect is observed for the UKF.

Figure A.10.2 shows the effect of an increase in the measurement noise in the AKFs – AUKFs (IAE).

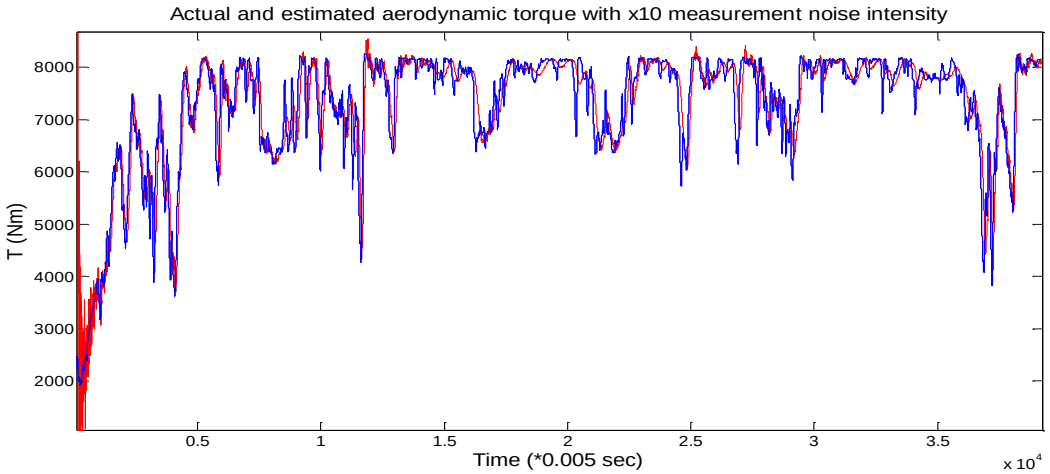

Figure A.10.2. T_a (blue) and $\hat{T}_a$ (red) of AKF/AUKF under increased measurement noise conditions.

As can be seen, the estimated waveform appears a bit distorted. This happens, because due to the high confidence that the filter is set to have in the measurement, the divergence of the innovations of the KF due to the high measurement noise is attributed to a high value of Q. Consequently, the Q-adaptation algorithm tends to underestimate Q, which results to a sluggish state estimate, as seen in Figure A.10.2.

A.11. Adaptation in changeable measurement noise variance.

The algorithm was found in [60] and it is given in Eqn. A.11.1, where it can be seen that it assigns $R=S'_k$, where S'_k is given in Eqn. (4.20).

$$\widehat{R}[k+1] = S'_k = \frac{1}{N-1}\sum_{i=k+1-N}^{k+1}(r_i - \overline{r})(r_i - \overline{r})^T \qquad \text{(A.11.1)}$$

This approach resulted to a quite accurate estimate of R, since this has the largest contribution on the value of S_k (see Eqn. (4.17)). This can be seen by Figure A.11.1, which displays S_k over time for 5 KFs designed with different Q=5*10^7, 5*10^8, 10^9,

$5*10^9$ and 10^{10} $(Nm)^2$, respectively and all employed for T_a estimation in the 3MW WT (see Table 4.2) and subjected to the same measurement noise of intensity R=0.01$(rad/sec)^2$.

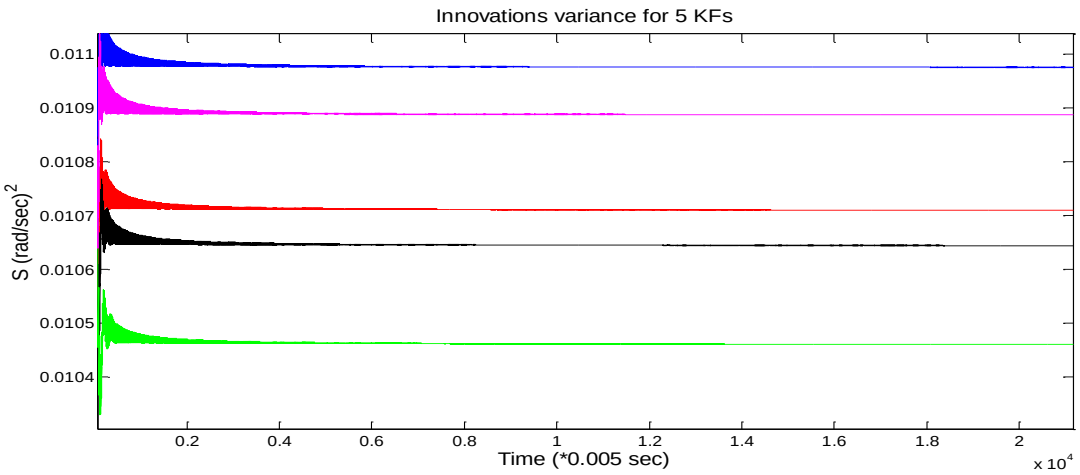

Figure A.11.1. Innovations variance, S_k for KFs (Low to high S corresponds to low to high Q).

As can be seen, the considerably large value of Q=$10^{10}$$(Nm)^2$ (Q=10^9 is sufficient for an accurate estimate) results to S_k just 10% higher than R=0.01$(rad/sec)^2$. Considering that this value for R is relatively low for a speed measurement obtained by an IG drive (from IG speed measurements in the laboratory this was estimated R=0.25$(rad/sec)^2$), the discrepancy between the real R and the estimated by Eqn. (A.11.1) is negligible. Otherwise, the quantity $CP^{-}C^T$ can be subtracted by the $\widehat{R}$ estimate of Eqn. (A.11.1). Finally, it is mentioned that Eqn. (A.11.1) asymptotically converges to R providing that infinite samples are taken into account. In practice, the bigger is the number of samples N in Eqn. (A.11.1), the better is the estimate. (However, choosing a longer moving window makes the adaptation slower.). A similar R adaptation method was found in [63, 64].

A.12. Other methods for adaptation in changeable process noise variance.

A.12.1. *Q*-adaptation 1

The presented algorithm was found in [60], is summarized in the formula:

$$\hat{Q}_{k+1} = \hat{Q}_k \exp[\Lambda(\Gamma_1 + \Gamma_2 + \cdots + \Gamma_l)\Gamma_0^{-1}], \qquad \text{(A.12.1)}$$

which is a recursive estimator of *Q*, where $\Lambda \epsilon R^{nxr}$ is a coefficient matrix and $\Gamma_l \epsilon R^{rxr}$ are the autocorrelations of the innovations of the KF given by:

$$\Gamma_{j_{k+1}} = \frac{1}{N}\sum_{i=K+1-N}^{k+1}(r_k r_{k-j}^T), \qquad \text{(A.12.2)}$$

When the filter is optimum, so that $\hat{x}[k+1|k+1]$ has minimum error variance $\widehat{P}[k+1|k+1]$, the innovation sequence is white noise, so its autocorrelations $\Gamma_j[k+1]$ for any $j \neq 0$ and any *k* are equal to zero. When the process noise covariance *Q* is not set to an appropriate value, any oscillations in the estimated value, will appear in the innovation sequence, which will be seen to be correlated for $j \neq 0$, which is an indication of suboptimum, KF operation.

The adaptive algorithm establishes a negative feedback through *Q* via the empirical equation (A.12.1), in order to correct any deviation of Γ_j from zero. The number of Γ_j used, the values of the coefficient matrix Λ and the stability of the algorithm were accessed experimentally. A brief assessment of the stability of the method can be found in [60].

It was observed that a very short window resulted to quite noisy estimate, while a very long one to bad adaptation due to the considerably bigger time-lag. In general, a length of 50 or 100 samples (sample time of 5msec) was adopted and two or three autocorrelations of time lag of 1, 2 and 3 steps.

This algorithm in general provided a very oscillatory aerodynamic torque estimate, since Eqn. (A.12.1) tends to produce intense variations in Q, due to the exponential. Although these oscillations were removed via low pass filtering, it was found that it is difficult to choose appropriate values in Λ, in order to perform satisfactory.

A.12.2. *Q*-adaptation 2

This algorithm was found in [63, 71] and is based in:

$$\hat{Q}_k = K_k \Gamma_{0_k} K_k^T \qquad \text{(A.12.3)}$$

where K_k is the Kalman gain at time k and Γ_{0_k} computed using (A.12.2).

This approach also produces a very accurate T_a estimate for various wind conditions with less computations than the previous algorithm. However, it exhibits considerably larger settling time during the initialization of the KF. In addition, when it is combined with simultaneous R adaptation, it gets unstable.

A.13. Influence of HILS in the KF estimates

When the speed controller of IG produces a highly varying torque demand, this causes transients in the IG speed, mainly due to (a) the limited speed control bandwidth of the IM drive, which is therefore unable to keep the speed unaffected by the torque variations, as a rigid WT HSS would do and (b) the instant excitement of the shaft dynamics. Therefore, the assumption of a rigid shaft connection between the HSS of the WT and the IG, as assumed in the WT model used in HILS, is violated.

Specifically, when the IG torque reduces abruptly, there is an instant overspeed until the IM drive responds. Therefore, when ω_g is fed to the KF, it tends to overestimate T_a.

Similar effect has an abrupt increase of IG torque (It causes an underestimation of T_a). These effects explain the peaks in $\hat{T}_a$ shown in Figure 4.14 (B)(i).

Based on the incomplete models used in the KFs, the MMAE correctly selects the estimate of KF_3 with the largest Q, because the largest excursions of $\hat{T}_a$ due to mismodeling are better estimated by a large Q.

As a conclusion, incomplete models in the KFs of the MMAE, result to an unfair selection between the KFs, since the only selection criterion that the MMAE has is the value of Q, while it "believes" that the rest of the parameters of the dynamic models of the KFs are absolutely accurate.

As a final remark, the effects of mismodelling in the MMAE were not so severe in the case of the 3MW WT, because the considerably slower dynamics of this WT than of the Windharvester WT, due to its considerably larger inertia as well as due to absence of shafts modeling, dominated the dynamics of the HILS IG drives. Therefore, the hypothesis testing of the MMAE algorithm was unaffected.

A.14. Estimated process noise variance

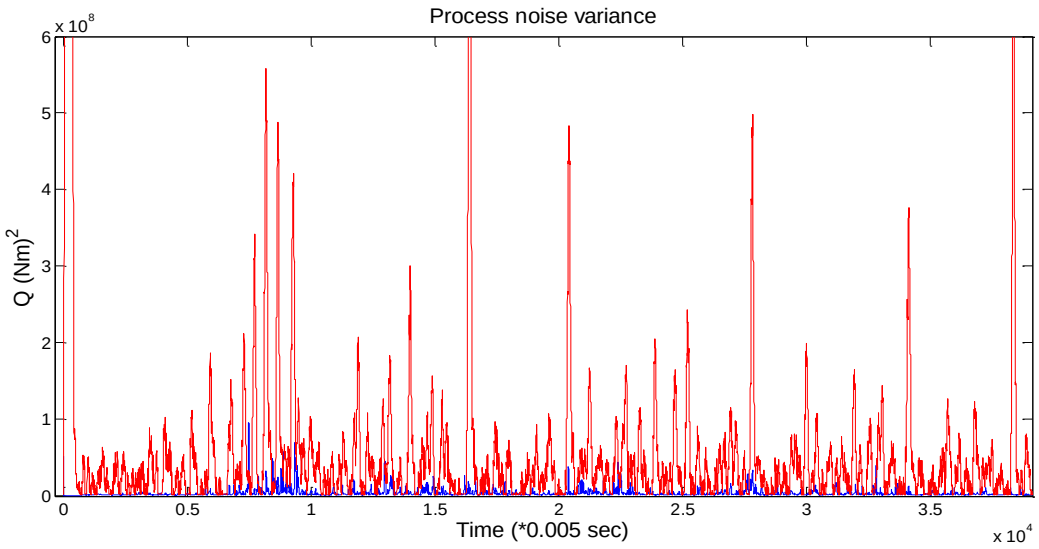

Figure A.14.1. Actual (blue) and estimated (red) process noise variance Q (Simulik) in a moving window of 100samples using the proposed IAE algorithm (Section 4.8.2).

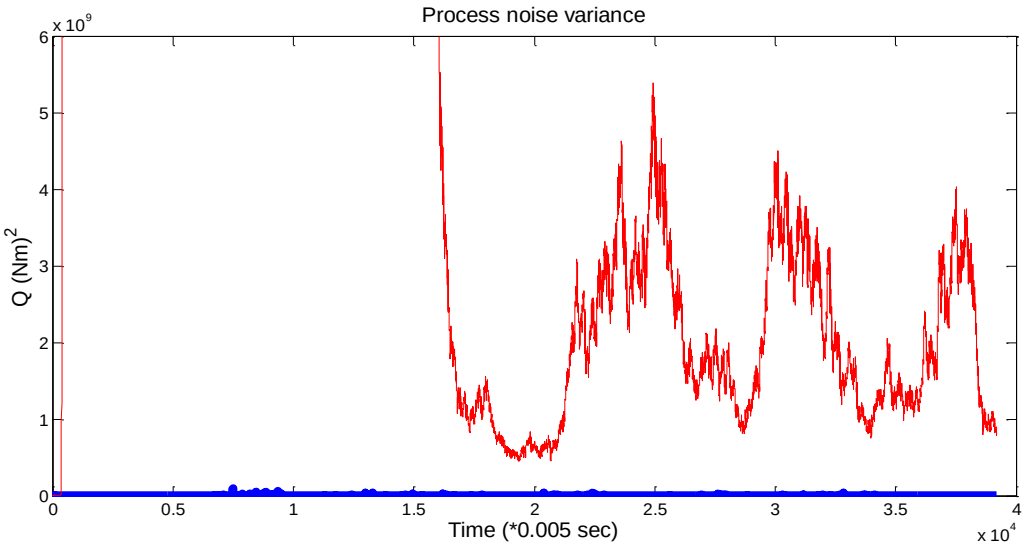

Figure A.14.2. Actual (blue) and estimated (red) process noise variance *Q* (Simulik) in a moving window of 100samples using the algorithm of Section A.12.2.

A.15. Comparison of aerodynamic torque IAE estimates

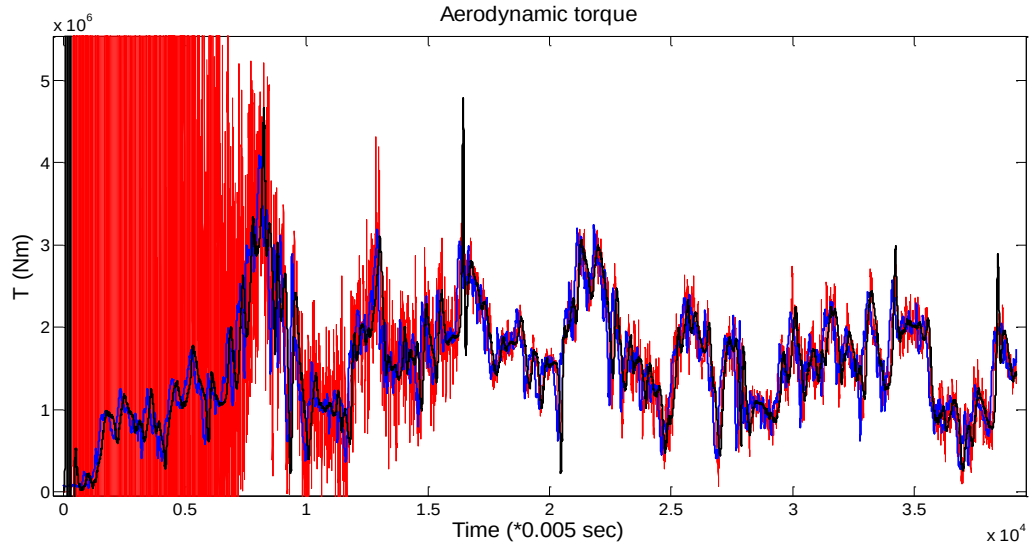

Figure A.15.1. Actual aerodynamic torque (red), estimated by IAE KF (Section 4.8.2) (black) and estimated by IAE KF (Section A.12.2) (red).

A.16 Unscented Kalman Filter

Unscented transformation

The unscented transformation is as follows [77, 78]:

For a vector $x \epsilon R^{nx1}$ transformed by a nonlinear function $y=f(x)$, $2n+1$ sigma points x_i are chosen as follows:

$$x_0 = \bar{x} \qquad \text{(A.16.1)}$$

$$x_i = \bar{x} + (\sqrt{(n+\lambda)P})_i, \quad i = 1 \dots n \qquad \text{(A.16.2)}$$

$$x_i = \bar{x} + (\sqrt{(n+\lambda)P})_{i-n}, \quad i = n+1 \dots 2n \qquad \text{(A.16.3)}$$

The following weights are also defined:

$$W_0^{(m)} = \frac{\lambda}{n+\lambda} \qquad \text{(A.16.4)}$$

$$W_0^{(c)} = \frac{\lambda}{n+\lambda} + (1 - a^2 + \beta) \qquad \text{(A.16.5)}$$

$$W_i^{(m)} = W_i^{(c)} = \frac{1}{2(n+\lambda)}, \quad i = 1 \dots 2n \qquad \text{(A.16.6)}$$

where $\lambda = \alpha^2(\nu + \kappa) - n$ is a scaling factor and $(\sqrt{(n+\lambda)P})_i$ is the ith column of the matrix square root $\sqrt{(n+\lambda)P}$, such as $(\sqrt{(n+\lambda)P})^T \sqrt{(n+\lambda)P} = (n+\lambda)P$ [76, 77, 78]. The above matrix square root is found by using the Cholesky factorization routine of MATLAB, "chol", applied to positive definite matrices. The parameter $\alpha \geq 0$, usually set to 1, adjusts the distance of the sigma points from $\bar{x}$. $\beta \geq 0$ is used to incorporate knowledge of the higher order moments of the estimated distribution. In the present application several values of β have been chosen, without visible change on the results.

In [77] β=2 is suggested as optimal for Gaussian priors as it is the case in the application of this paper. Finally, κ≥0 guarantees the positive definiteness of the covariance matrix.

The use of the unscented transformation in the KF

The prediction stage of the proposed KF is the same as of the UKF. We consider the discrete time linear dynamic system given by:

$$x[k+1] = Ax[k] + Bu[k] \quad \text{(A.16.7)}$$

$$z[k] = Cx[k] \quad \text{(A.16.8)}$$

Then, using the unscented transformation described above, the prediction stage is implemented with the following steps:

$2n$+1 sigma points $x_i[k|k], i = 0 \dots 2n$ are constructed according to Eqns. (A.16.1-3) after the substitutions: $\bar{x} = \hat{x}[k|k]$ and $P = \hat{P}[k|k]$.

The sigma points are then propagated in time using the discrete equivalent of (79), such as:

$$x_{\mathrm{i}}[\mathrm{k}+1|\mathrm{k}] = \mathrm{A}x_{\mathrm{i}}[\mathrm{k}|\mathrm{k}] + \mathrm{Bu}[\mathrm{k}] \quad \text{(A.16.9)}$$

The a-priori state estimate at time k+1 is given by:

$$\hat{x}[\mathrm{k}+1|\mathrm{k}] = \sum_{\mathrm{i}=0}^{2\mathrm{n}} W_i^{(m)}\, x_{\mathrm{i}}[\mathrm{k}+1|\mathrm{k}] \quad \text{(A.16.10)}$$

The a-priori state error covariance at time k+1 is:

$$\hat{P}[k+1|k] = \sum_{\mathrm{i}=0}^{2\mathrm{n}} W_i^{(c)} ([\mathrm{k}+1|\mathrm{k}] - \hat{x}[\mathrm{k}+1|\mathrm{k}])\, ([\mathrm{k}+1|\mathrm{k}] - \hat{x}[\mathrm{k}+1|\mathrm{k}])^{\mathrm{T}} + \mathrm{Q},$$

(A.16.11)

where Q is the process noise covariance matrix.

The measurement update step is implemented as in the linear KF and the aposteriori state estimate is given by:

$$\hat{x}[k+1|k+1] = A\hat{x}[k+1|k] + K[k+1](z[k+1] - C\hat{x}[k+1|k]) \qquad \text{(A.16.12)}$$

where

$$K[k+1] = \widehat{P}[k+1|k]C^T(C\,\widehat{P}[k+1|k]C^T + R)^{-1} \qquad \text{(A.16.13)}$$

is the Kalman gain and R the measurement noise covariance matrix.

Finally, the aposteriori error covariance is:

$$\widehat{P}[k+1|k+1] = A(I - KC)\,\widehat{P}[k+1|k] \qquad \text{(A.16.14)}$$

A.17. Power regulation based on the effective wind speed-1

In Figure A.17.1 the speed reduction required to keep the power at P_N, is shown in a V-ω plane, for three rotors with gradually broader C_p characteristic [79].

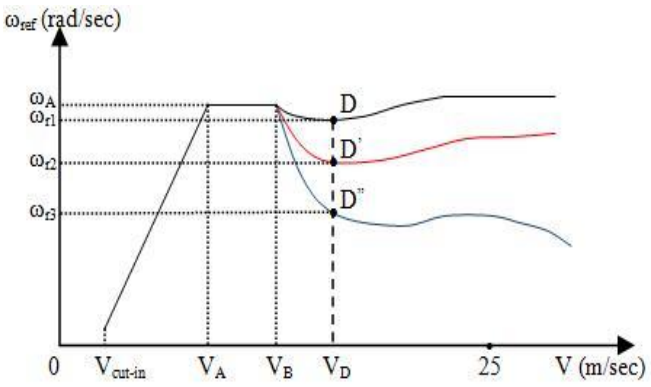

Figure A.17.1. Operating point locus in *V-ω* coordinates for three rotors with gradually broader C_p characteristic (black, red and blue, respectively).

From Figure A.17.1 it can be seen that as the C_p curve becomes broader, more speed reduction is required to keep the power constant for the same wind speed V_D.

In order for the power to be limited to P_N, ω should follow a characteristic similar to the ones displayed in Figure A.17.1 for $V>V_B$. This characteristic can be easily programmed as a look-up table. However, the inability of correct V estimation when $V=V_2$ or $V=V_3$, (Figure 5.4) poses limitations. This is seen in Figure A.17.2.

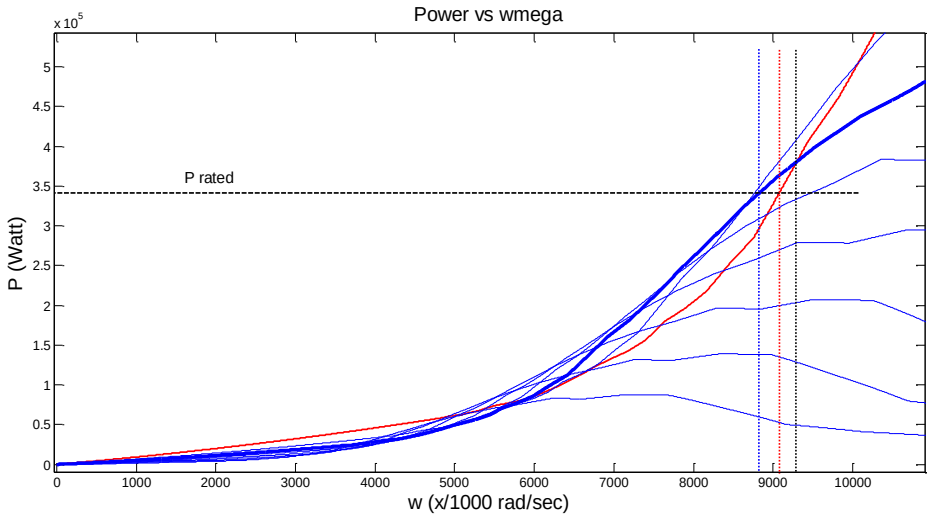

Figure A.17.2. P_a characteristics of the WT for different wind speeds.

The black vertical line represents the rated rotational speed, ω_R and the red power curve corresponds to the actual effective wind speed V_3. It can be seen that for this wind speed $P>P_N$ for $\omega=\omega_R$. Also, another power curve of a lower wind speed V_2 (bold blue curve) intersects $\omega=\omega_R$ at the same point with the power curve of V_2. This is in fact the solution returned by NR. From Figure A.17.2 it can be seen that if $V=V_2$, ω should be reduced more that it would be required if $V=V_3$, in order for the power to be reduced to P_N. Consequently, when the control is based only on the estimate of NR_1, a high speed reduction corresponding to that wind speed would cause a power deep and possibly instability in fast changeable winds, since as it can be seen in Figure A.17.2, the slope of the red power curve is much steeper than that of the blue power curve. Considering the above, a new compromising trajectory for the rotational speed is needed to be used instead of the ones shown in Figure A.17.1. This is shown in Figure A.17.3. In addition,

the estimated wind speed *V*, is first passed through a low pass MA filter in order to smooth out fast and large variations, which would lead to undesirable power drops.

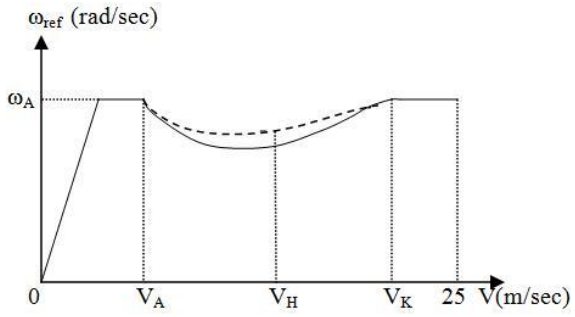

Figure A.17.3. Modified trajectory for the rotational speed in the stall region.

From Figure A.17.3 it can be seen that a shallower curve (dashed) is used for the speed regulation in the stall region. This curve is a non-optimum one and tries to compensate the lack of knowledge of the actual wind speed by compromising between the control objectives in high and very high wind speeds. The term "high" is quite relative and depends on the rated rotational speed of the WT. It actually describes wind speeds until $V=V_H$ in Figure A.17.3, where maximum speed reduction is required. "Very high" is used to describe wind speeds closer to V_K, where very little or no speed reduction is required.

If the speed reduction factor is noted as $a < 1$, such as the reference for the rotational speed is $\omega_{ref} = \omega'_{ref} a$, then for wind speeds $V_A \leq V \leq V_H$, it is $a_A \geq a \geq a_H$, as can be observed from Figure A.17.3. The power curves of these wind speeds do not intersect each other and therefore these wind speeds are effectively returned by NR_1.

For $V>V_H$, a increases with *V*, since for the particular ω_R the power curves of these wind speeds are steeper. These power curves intersect the power curves of the wind speeds $V_A \leq V \leq V_H$. The wind speeds $V>V_H$ correspond to V_2 or V_3 of Figure 5.5 and cannot be estimated. Instead, the V_1 corresponding to the intersected power curve will be returned

by NR. However, the a factor of V_1 can be quite smaller than the one corresponding to V_2 depending on their relative distance in the x axis of Figure A.17.3. Therefore, the modified curve is designed such as it assigns a higher a factor for wind speeds $V_A \leq V \leq V_H$ (In Figure A.17.3 the modified line is plotted also for $V > V_H$ for reasons of completeness). This has as a consequence to reduce the effectiveness of power limitation at wind speeds $V_A \leq V \leq V_H$ while at the same time to alleviate the power deeps that can be caused when $V > V_H$.

The trajectory of Figure A.17.3 can be implemented by multiplying ω_{ref} with the factor $a = f(V)$, where the shape of the function f, depends on the shape of the C_p curve. However, because this shape is not static during operation, a conservative choice (not very deep) for the function f may be desirable. A typical simplified function f is given in Figure A.17.4.

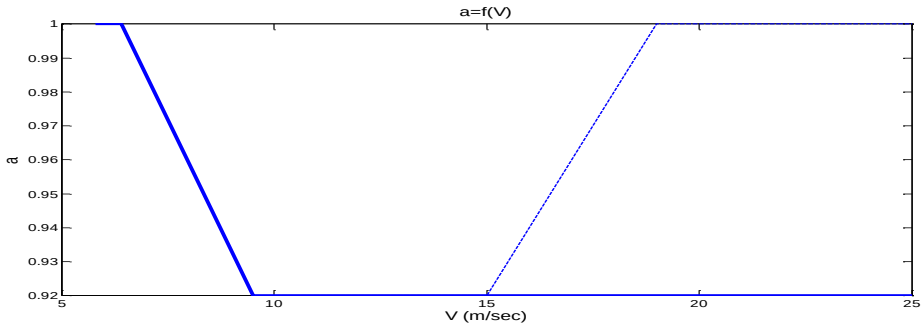

Figure A.17.4. $a = f(V)$.

Figures A.17.5 (a-c) show hardware simulation results.

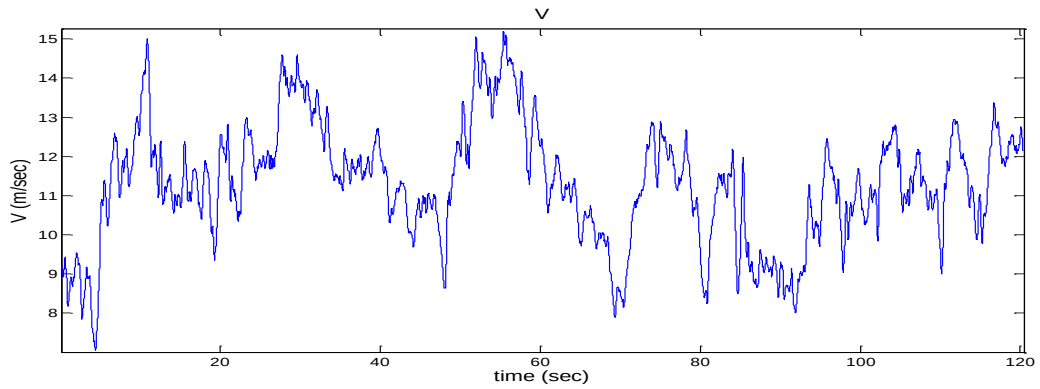

Figure A.17.4(a). Wind speed.

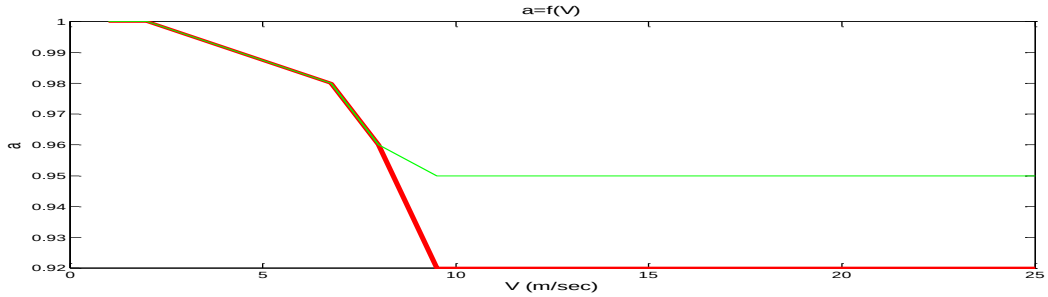

Figure A.17.4(b). $a=f_1(V)$ (red), $a=f_2(V)$ (green).

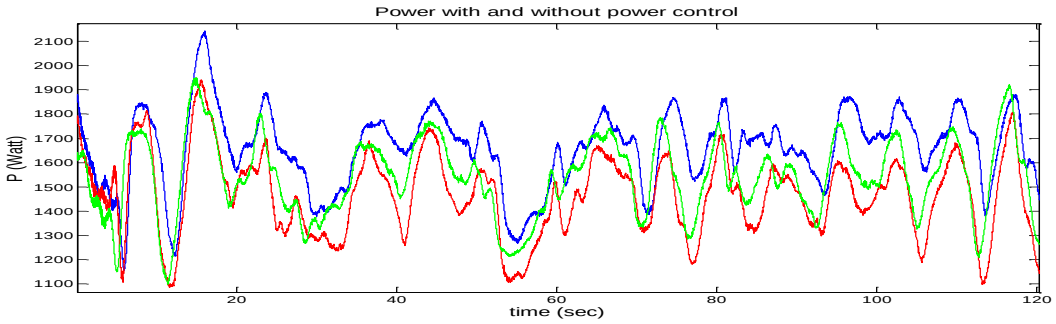

Figure A.17.4(c). Output power without (blue) and with power control (green and red).

A.18. Power regulation based on the effective wind speed-2.

This method of power regulation is based on estimation of all possible V_1, V_2, V_3 solutions, based on a look up table of the power or torque coefficient of the rotor and using the method of interpolation. Then, for each of the three V solutions, the speed reference that leads to the desirable power level is calculated and then the speed reference that requires the least speed reduction is chosen. From Figure A.18.1, it can be seen that from ω=4rad/sec, if the power should be reduced to 20kW and V=23m/sec,

then ω should become 3rad/sec. However, if V=6m/sec, this can be achieved to a higher ω. Therefore, this will be chosen as the speed reference, so uncertainty in V knowledge is overcome with conservatism is the speed reduction.

Figures A.18.2(a-c) show Simulink results from power regulation to 25kW. The routine updates the speed reference every 0.5sec.

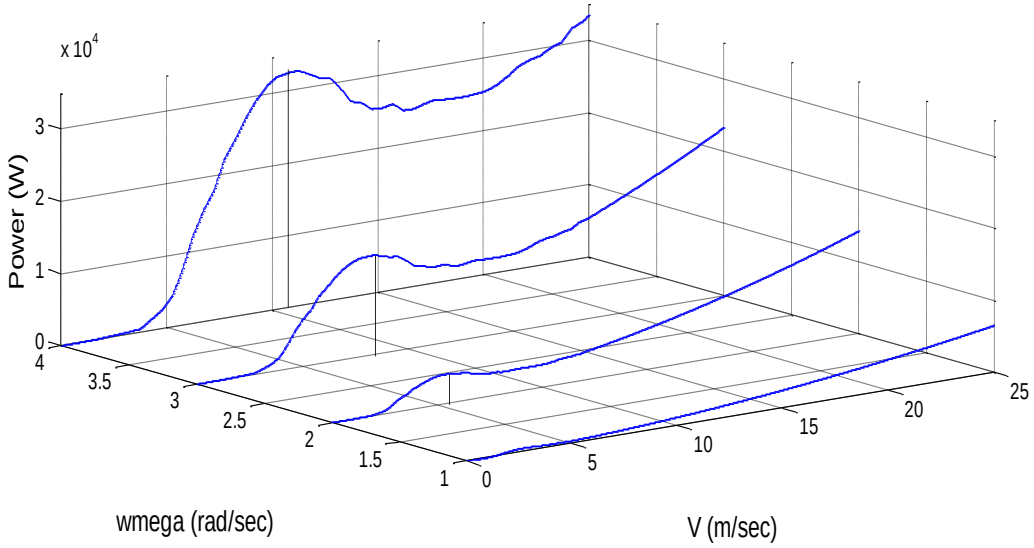

Figure A.18.1. P versus V for different ω.

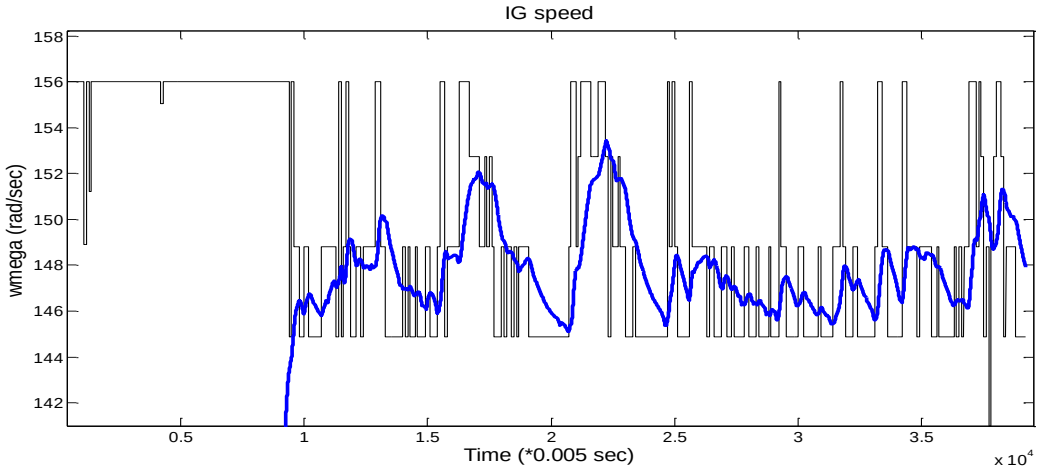

Figure A.18.2(a). Reference (black) and actual (blue) IG speed.

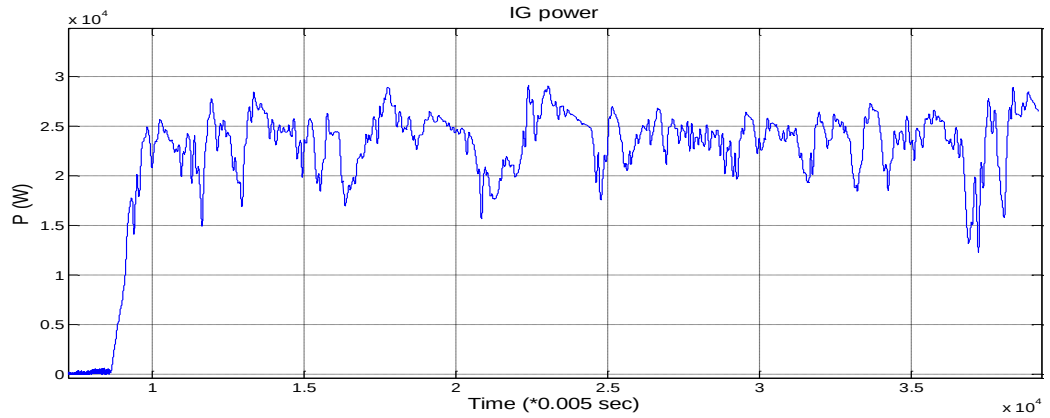

Figure A.18.2(b). IG power.

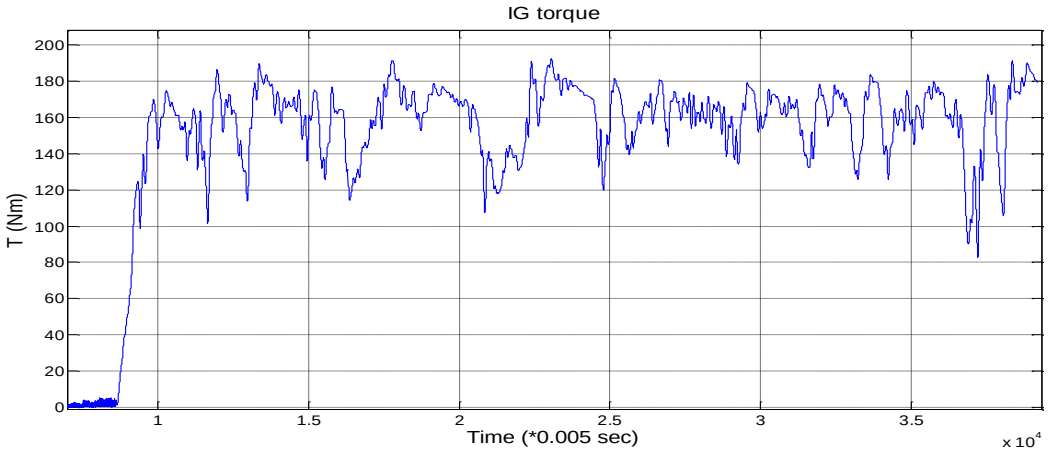

Figure A.18.2(c). IG torque.

From the above figures it can be seen that the method achieves remarkable power regulation, without considerable speed variations and torque pulsations. The same performance is achieved for several power levels.

Due to the very good results, further work on the application of the algorithm in an actual WT is important, in order to examine the robustness of the algorithm in power or torque coefficient changes.

A.19. H-infinity control theory

Assume the general control configuration of Figure A.19.1, where the plant is represented by P and the controller by K, both transfer function matrices.

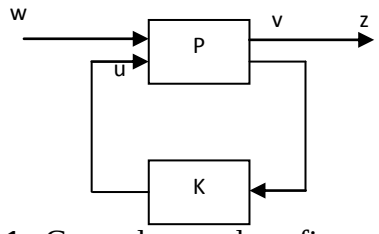

Figure A.19.1. General control configuration [27].

P can is defined by:

$$\begin{bmatrix} z(s) \\ v(s) \end{bmatrix} = \begin{bmatrix} P_{11}(s) & P_{12}(s) \\ P_{21}(s) & P_{22}(s) \end{bmatrix} \begin{bmatrix} w(s) \\ u(s) \end{bmatrix}, \qquad \text{(A.19.1)}$$

where w is a column vector representing the disturbances to the control loop (it includes external disturbances and command signals) and u a column vector of the control inputs given by:

$$u = Kv\ , \qquad \text{(A.19.2)}$$

where v is a column vector containing measurements from the plant. Finally, z is a column vector of signals to be minimized depending on the predefined control objectives.

A state space realization of the plant P is:

$$\dot{x} = Ax + B_1 w + B_2 u \qquad \text{(A.19.3)}$$

$$z = C_1 x + D_{11} w + D_{12} u \qquad \text{(A.19.4)}$$

$$v = C_2 x + D_{21} w + D_{22} u \qquad \text{(A.19.5)}$$

where x is the state vector.

The closed loop system of Figure A.19.1 can be represented by the system of Figure A.19.2.

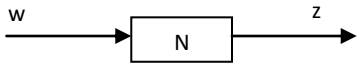

Figure A.19.2. Closed loop system.

Then, the transfer function N is given by [27]:

$$N = P_{11} + P_{12}K(I - P_{22}K)^{-1}P_{21} \triangleq F_l(P, K), \qquad \text{(A.19.6)}$$

where $F_l(P, K)$ is called lower "Linear Fractional Transformation" (LFT) of P with K as parameter [27]. Therefore:

$$z = F_l(P, K)w \qquad \text{(A.19.7)}$$

The H_∞ norm of $F_l(P, K)$ is defined as

$$||F_l(P, K)||_\infty = \max_\omega \bar{\sigma}(F_l(P, K)(j\omega)), \qquad \text{(A.19.8)}$$

which is the maximum of the maximum singular value of $F_l(P, K)$ over infinite frequencies.

H_∞ optimization aims to find a controller, K that minimizes the H_∞ norm of $F_l(P, K)$, which is equivalent to the minimization of the effects of the disturbance signals w to the signals z over infinite frequencies.

Often, it is impossible to satisfy these effects at the same time and in the same frequency band, therefore appropriate frequency weighting is applied to the elements of $F_l(P, K)$ in order for the optimization routine to converge to a control solution, K.

Figure A.19.3 shows the WT model with the frequency weights, structured such that it agrees with the usual control design configuration found in [27]. As can be seen,

through the transfer function $G_{T_{g_{ref}}\omega_2}$ closed loop speed control is established. The transfer function $G_{V\omega_2}$ acts as a disturbance to the control loop via its output signal d (rad/sec). It is mentioned that these transfer functions have been evaluated for a particular operating point of the WT, using the linearized model of Section 2.5.2. The resulting disturbed speed output $y = \omega_2 + d$, is then used as input to the controller, K, which is not available yet. The outputs z_1 and z_2 result after the weights W_u and W_v are applied to the control input, $u=T_{g_{ref}}$ and the tracking error $v = \omega_{ref} - y$ respectively.

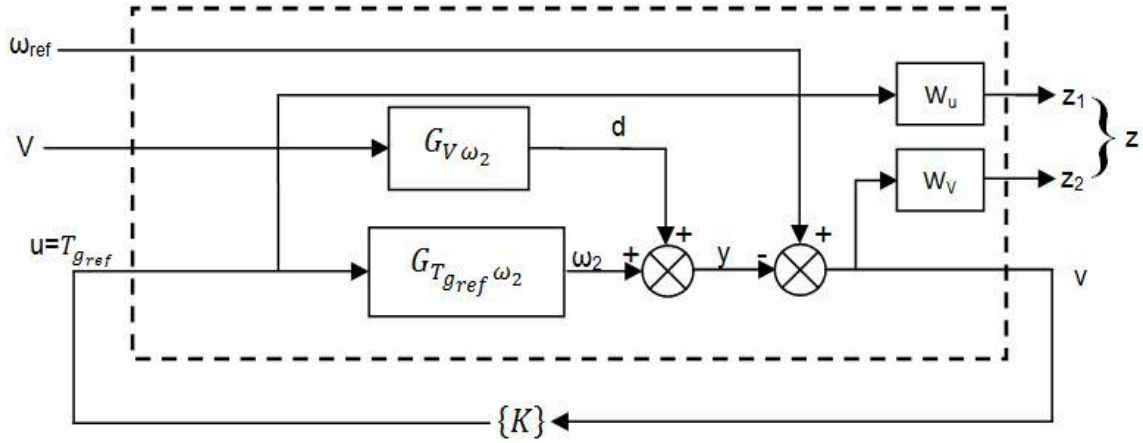

Figure A.19.3. WT speed control loop for H_∞ controller design.

Based on the configuration of Figure A.19.3, a state space description of the model inside the dashed frame, where the input disturbance signals ω_{ref} and V form a vector w, is used by the H_∞ optimization algorithm, which seeks a controller K that minimizes the effect of the inputs w to the outputs z. Such a procedure can be performed by certain functions of the Robust Control Toolbox of Matlab, such as the "hinfsyn".

Regarding W_u and W_v, these are stable transfer functions. In several applications W_u is usually chosen as a high pass filter, in order to minimize the gain of the transfer functions from w to u at the high frequencies. Also, hardware and software simulations showed that very good performance can be achieved even if W_u is selected as a constant value. That way the order of the controller and the computational load are kept lower.

W_v is usually chosen as a low pass filter, in order to reduce the energy of the tracking error at the lower frequencies.

The plant seen inside the dashed frame of Figure A.19.3 can be expressed by the input-output relation:

$$\begin{bmatrix} z_1 \\ z_2 \\ \hline v \end{bmatrix} = \left[\begin{array}{cc|c} 0 & 0 & W_u \\ -W_v G_{V\omega} & W_v & -W_v G \\ \hline -G_{V\omega} & 1 & -G \end{array}\right] \begin{bmatrix} V \\ \omega_{ref} \\ \hline u \end{bmatrix} \qquad \text{(A.19.9)}$$

where G stands for $G_{T_{g_{ref}}\omega_2}$ and $G_{V\omega}$ for $G_{V\omega_2}$.

Using Eqn. (A.22.6) with P_{11}, P_{12}, P_{21}, P_{22} obtained from Eqn. (A.19.9), N is expressed by:

$$N = \begin{bmatrix} \frac{-W_u G_{V\omega} K}{1+GK} & \frac{W_u K}{1+GK} \\ \frac{-W_v G_{V\omega}}{1+GK} & \frac{W_v}{1+GK} \end{bmatrix} = \begin{bmatrix} -W_u G_{V\omega} KS & W_u KS \\ W_v G_{V\omega} S & W_v S \end{bmatrix} \qquad \text{(A.19.10)}$$

and its H_∞ norm is:

$$\|N\|_\infty = \left\| \begin{bmatrix} -W_u G_{V\omega} KS & W_u KS \\ W_v G_{V\omega} S & W_v S \end{bmatrix} \right\|_\infty \qquad \text{(A.19.11)}$$

Therefore, minimization of Eqn. (A.19.11) needs to be performed. This approach is called S/KS mixed sensitivity minimization, because as can be seen from Eqn. (A.19.10), the transfer functions S and KS are involved. It is noted that a different selection of minimization variables results to a different minimization method, such as S/T and S/KS/T [27].

From the above analysis it is obvious that control objectives, such as reference tracking and disturbance rejection are explicitly expressed in terms of the shape of the closed loop transfer functions of the system (*S*, *KS*, *T*) in the complex frequency domain and

these control objectives are formulated via the shape of the performance weights, W over infinite frequencies.

For an optimum controller, the following requirement holds:

$$\left\| \begin{bmatrix} -W_u G_{V\omega} KS & W_u KS \\ W_v G_{V\omega} S & W_v S \end{bmatrix} \right\|_\infty < 1, \qquad \text{(A.19.12)}$$

which if considered for a particular element of Eqn. (A.19.12), for example $W_v S$, it can be expressed as:

$$\|W_v S\|_\infty < 1 \leftrightarrow \|S\|_\infty < 1/\|W_v\|_\infty, \qquad \text{(A.19.13)}$$

where W_v is assumed to have no zeros at zero frequency.

From Eqn. (A.19.13) it can be seen that the weight W_v comprises a maximum bound for S for infinite frequencies. The selection of this maximum bound has a direct impact on the performance and robustness of the closed loop system, since the peaks of the closed loop transfer functions are closely related with the stability margins (phase and gain margin) of the open loop transfer function $L = GK$ [27].

The weight that is often used for the sensitivity is the following [27]:

$$W_1(s) = \frac{\frac{s}{M_1} + \omega_b}{s + \omega_b A_1}, \qquad \text{(A.19.14)}$$

where $M_1 \geq 1$ and $A_1 \leq 1$. The Bode plot of $1/W_1(s)$ is shown in Figure A.19.3, for M_1=2, ω_b=2 rad/sec and A_1=10^{-4}.

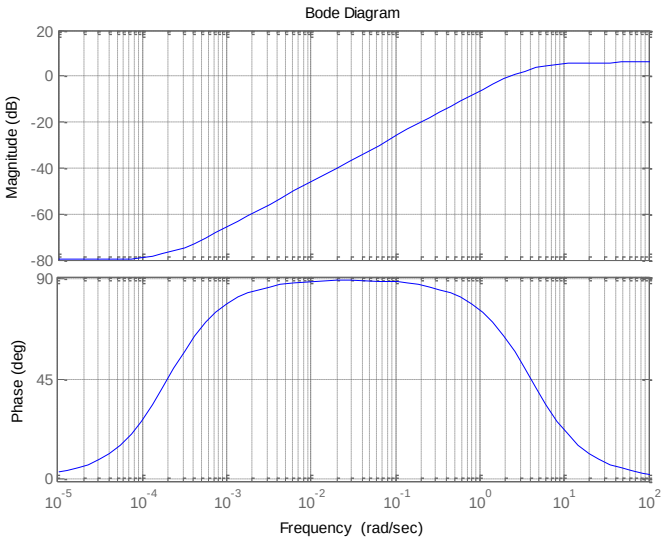

Figure A.19.3. Bode plot of $1/W_1(s)$.

The frequency ω_b is almost equal to the desired bandwidth and it actually provides a lower bound for this, while an upper bound for the bandwidth can be specified through other constraints (weighting of T or KS). The parameter *M* adjusts the allowed maximum height for the peak value of *S*, while the parameter *A* defines the amount of attenuation at the low frequencies.

For the complementary sensitivity function, *T*, an appropriate weight is [27]:

$$W_2(s) = \frac{s+\frac{\omega_a}{M_2}}{A_2 s+\omega_a} \qquad \text{(A.19.15)}$$

The parameters of Eqn. (A.19.15) have a similar function as the ones of Eqn. (A.19.14). The Bode plot of $1/W_2(s)$ for M_2=2, ω_a=1rad/sec and A_2=10^{-4} is shown in Figure A.19.4.

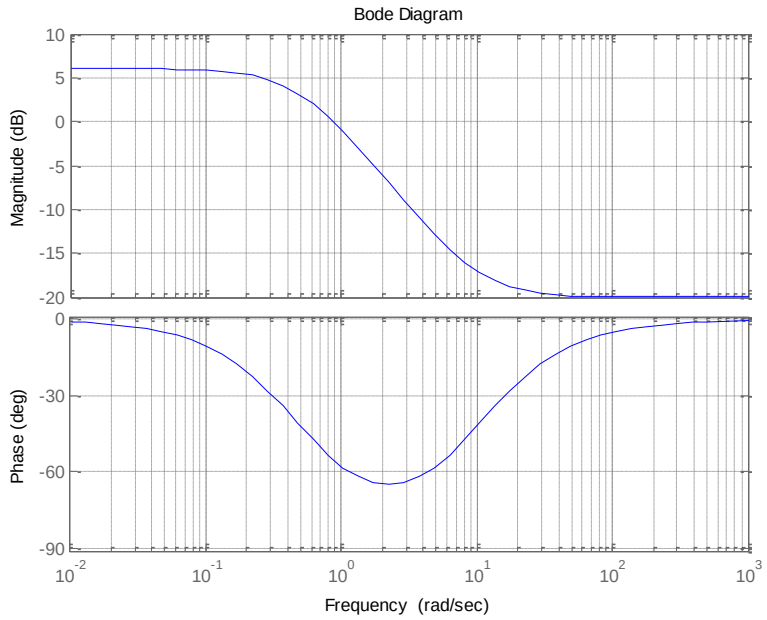

Figure A.19.4. Bode plot of $1/W_2(s)$.

Usually, it may be impossible or require considerable design effort to find an optimum solution for the controller, which satisfies (A.19.12). Therefore, in practise suboptimal solutions can be acceptable. Specifically, Eqn. (A.19.12) can be rather expressed as:

$$\left\| \begin{bmatrix} -W_u G_{V\omega} KS & W_u KS \\ W_v G_{V\omega} S & W_v S \end{bmatrix} \right\|_\infty < \gamma, \qquad \text{(A.19.16)}$$

where γ is the performance index that indicates how close is the obtained solution to the optimum, given by Eqn. (A.19.12).

Matlab provides functions for expressing mixed sensitivity criteria in terms of Eqn. (A.19.11) and routines for solving the H_∞ optimization problem of Eqn. (A.19.16) using Linear Matrix Inequalities (LMI) [27]. One of these routines, used for the design here is the "hinfsyn" of the Robust Control Toolbox of Matlab.

Regarding the design parameters of the shaping filters, these were chosen as: M_1=2, which guarantees sufficient stability margins [27] and A_1=10^{-10}, which ensures very high disturbance attenuation. Also, ω_b=1 and 2rad/sec resulted to a good performance

in below and above rated operation respectively. Finally, it was shown that a constant weight for KS, $W_2 = 1/250$ or 1/300, which defines an upper bound for the control torque of 250 and 300Nm respectively for all frequencies, achieved similar performance as by using the weight of Eqn. (A.19.15), so the constant weight was preferred, since it results to controller of reduced order.

A.20. Linear parameter varying controller

A.20.1. Introduction

The LPV controllers can self adapt to the changeable dynamics of the WT by been continuously updated with the scheduling parameters that define the operating point of the system (rotor speed, ω_1 and effective wind speed, V, see Chapter 2) [1].

[1] describes the design and application of an LPV controller in VS SR WTs from a theoretical point of view, where simplified drivetrain and electrical system models of the WT are used. In addition, windup of the controller and anti-windup control is not addressed, as it is in general the case in the literature for this type of controllers.

Here, software and hardware simulation results from an LPV controller for a VS SR WT are presented. This controller is updated in real time with the rotor speed, ω_1 and the effective wind speed V as these are estimated by the KF and NR algorithms (Chapter 5). It is noted that although at high wind speeds, the $\hat{V}$ estimate is not realistic, this did not affect the performance of eh controller as was seen through simulations in Simulink. Also, oscillations or instability caused by the fact that ω_1 is also a state of the WT model, as this is expected according to [98], were not observed, since ω_1 varies very slow relative to the controller response as a result of the slow rotor dynamics [1].

In the next section Simulink and HILS results from an S/KS based design are shown. (S/T and S/KS/T designs were also performed, but not preferred for the same reasons as mentioned in 6.5.3.)

A.20.2. Design

After the augmented plant P is created, based on the method described in [1] and the polytope Θ is defined [1], the LPV controller can be obtained by specialized software that solves the optimization problem. Such facility is provided in MATLAB, through the function "hinfgs" of the robust control toolbox. The function "hinfgs" returns N LTI controllers, K_{θ_i}, $i = 1, \dots, N$, each one for each vertex of the polytope Θ. The LTI controllers are returned in state space form packed inside a "system matrix", which is a format that MATLAB uses for compact state space data representation.

Then, the LPV controller is obtained in real time through the following procedure:

1) The parameter vector $\theta(t)$ is measured in real time at every time-step k and the parameters $c_1(t_k), \dots, c_N(t_k)$ of the convex decomposition are computed.

   $\theta(t_k) = c_1(t_k)\theta_{v_1} + \cdots + c_N(t_k)\theta_{v_N}, \quad c_i \geq 0, \quad \sum_{i=1}^{N} c_i = 1$ (A.20.1)

2) The controller $K(\theta(t_k))$ is given by:

   $K\big(\theta(t_k)\big) = \sum_{i=1}^{N} c_i K_{\theta_i}$ (A.20.2)

The design and real time implementation of the controller is based on [99].

A.20.3. Simulation results

A.20.3.1. Simulink results

Figure A.20.1(a) shows the applied wind speed (b) the speed response of the WT at low and high wind speeds and Figure (c) the control torque to the IG.

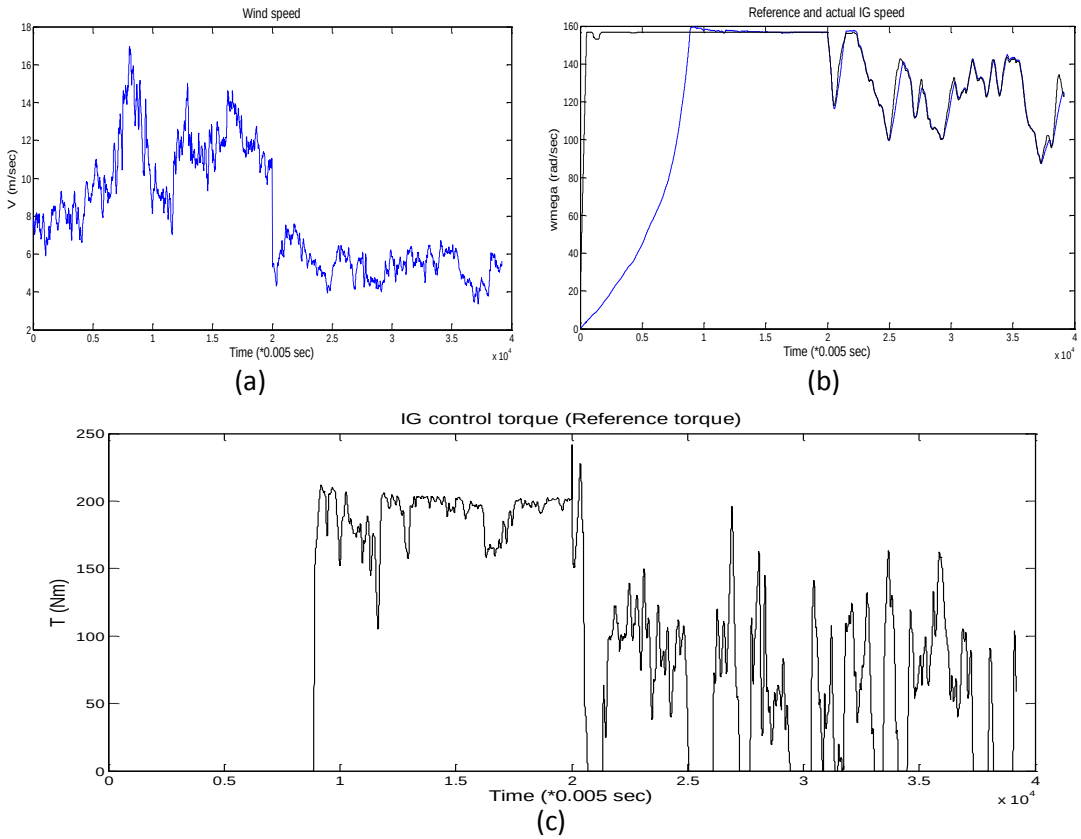

Figure A.20.1. (a) Effective wind speed, (b) Reference (black) and actual (blue) IG speed and (c) IG torque reference.

As can be seen, the controller achieves perfect tracking for both above rated and below rated wind speeds and the control torque is effectively saturates without winding up effects.

A.20.3.2. Results using the Hardware In the Loop simulator

The results shown in Figures A.20.2(a-b) have been obtained for $C_{p\ max}$ operation.

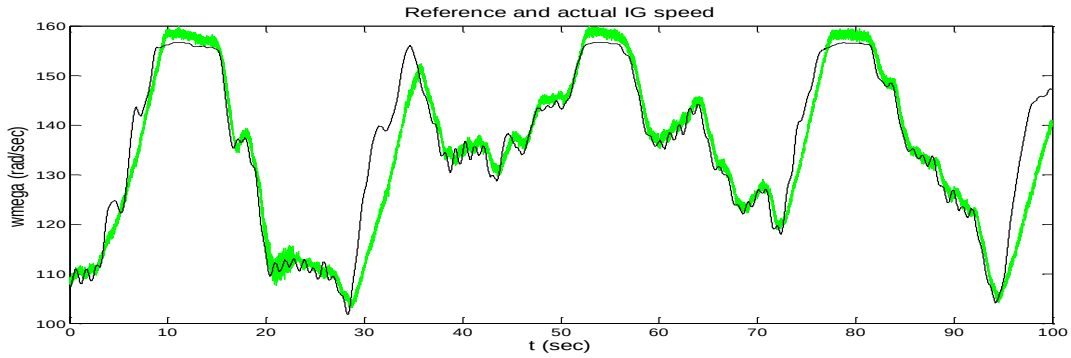

Figure A.20.2(a). Reference (LPF) (black) and actual (green) IG speed.

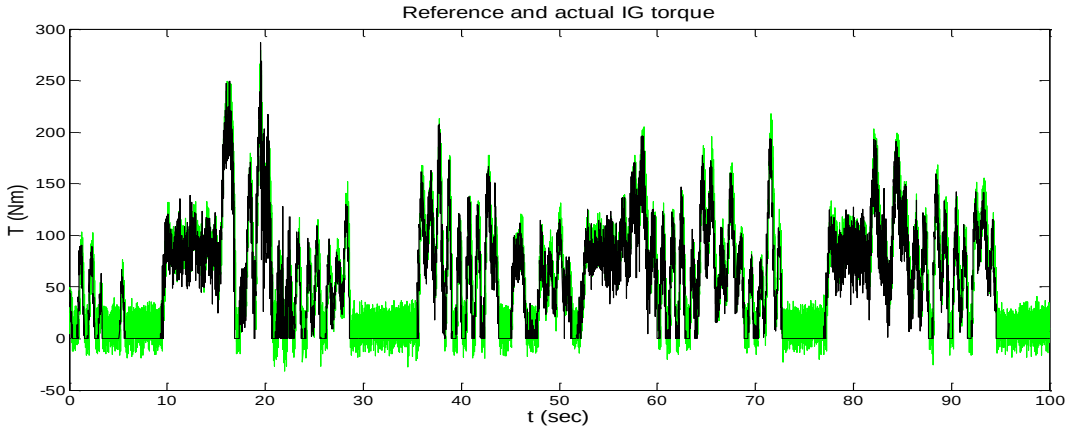

Figure A.20.2(b). Reference (LPF) (black) and actual (green) IG torque.

Figures A.20.3(a-b) show results for above rated operation.

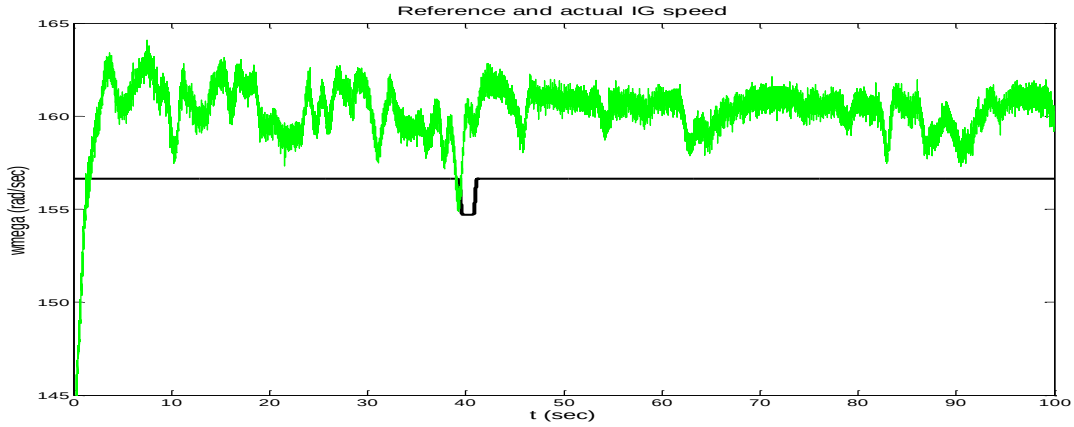

Figure A.20.3(a). Reference (LPF) (black) and actual (green) IG speed.

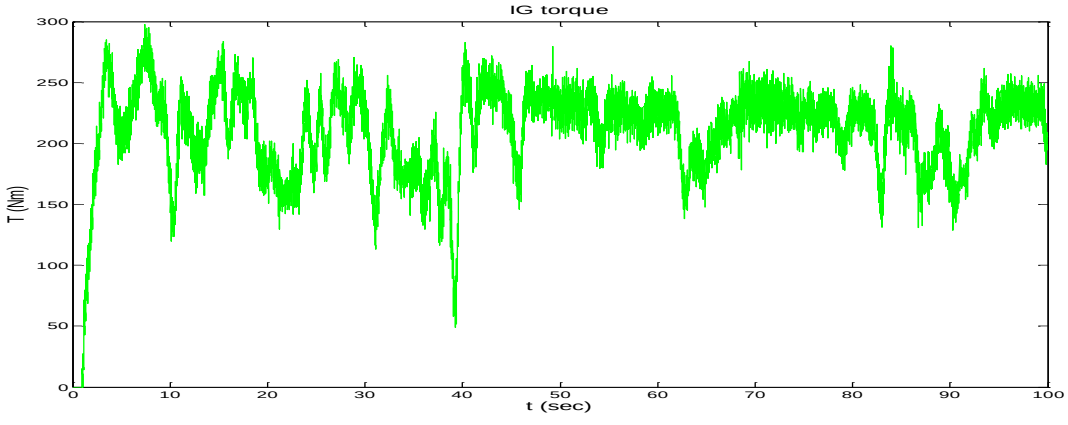

Figure A.20.3(b). IG torque.

As can be seen from the above results, for below rated operation, the reference tracking is quite good, although the control action is seen to be more intense compared to the theoretical response of Figure A.20.1(c), for similar wind conditions.

For above rated operation, the IG speed stays always above its reference and the torque of the IG is quite high compared to the software simulations.

In general, further work is required in order for the LPV controller to achieve the desired tracking performance in an actual system, due to the uncertainty involved in the used state space model during the design.

A.21. Sliding mode controller

A.21.1. Discrete time sliding mode controller-1

The design of the Discrete-Time Sliding Mode Controller (DTSMC) is based on the approach found in [93].

Consider the following discrete-time dynamic system:

$$x(k+1) = Ax(k) + Bu(k) \qquad \text{(A.21.1)}$$

Then, according to [93] the state response of this system when a DTSMC is applied via *u(k)*, can be separated in a reaching, sliding and steady-state mode (RM, SM and SSM respectively). The meaning of these modes is revealed in Figure A.21.1, where a two dimensional state space with a sliding line is shown. As can be seen, the state vector moves towards the sliding line and once it reaches it, it oscillates around it as a result of the switching frequency of the discrete-time hardware and moves towards the zero point (equilibrium point). When the state vector reaches the zero point, it oscillates around it. The motion of the state vector after reaching the sliding surface is called Quasi-Sliding Mode (QSM) and it can be described as a zig-zag motion, with the state vector crossing

the sliding surface between any sampling period, *T*. For a stable system, the step size of the zig-zag should not increase and also the motion should be constrained within a specified band around the surface. In [93], a reaching law that satisfies the reaching condition and QSM has been derived.

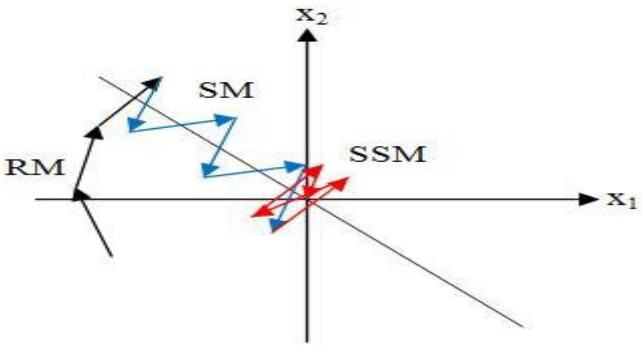

Figure A.21.1. State vector motion under DT SMC.

Consider the sliding surface s(k):

$$s(k) = c^T x(k). \qquad \text{(A.21.2)}$$

Then, the reaching law is given by:

$$s(k+1) - s(k) = -qTs(k) - \varepsilon T \operatorname{sgn}(s(k)), \qquad \text{(A.21.3)}$$

where T is the sampling period and q and ε are parameters to adjust the width of the switching band (SB) [93]. Eqn. (A.21.2) defines the dynamics on the switching surface *s(k)*.

After substituting (A.21.2) into (A.21.3) and using (A.21.1), the control law for *u(k)* is derived as:

$$u(k) = -(c^T B)^{-1}[c^T Ax(k) - c^T x(k) + qTc^T x(k) + \varepsilon T \operatorname{sgn}(c^T x(k))] \qquad \text{(A.21.4)}$$

where it is assumed that c^T is selected such as $(c^T B)^{-1}$ exists.

Equation (A.21.4) gives the control law when no disturbance to the plant is considered. When a disturbance term $B_d d(k)$ is considered, (A.21.4) becomes:

$$u(k) = -(c^T B)^{-1}[c^T Ax(k) - c^T x(k) + qTc^T x(k) + \varepsilon T \operatorname{sgn}(c^T x(k)) + c^T B_d d(k)] \quad \text{(A.21.5)}$$

(A.25.2) can be expressed by means of the error between the state vector and its reference:

$$s(k) = c^T e(k) = c^T (x(k) - x_{ref}(k)) \quad \text{(A.21.6)}$$

with:

$c^T = [0\ 1\ 0\ 0\ 0]$, (A.21.7)

while more choices including additional state feedbacks, as these were obtained by the KF/AKF did not result to any visible difference in the tracking performance of the control loop.

The control $u(k)$ is:

$$u(k) = -(c^T B)^{-1}[c^T (A - I)e(k) + c^T B_d d(k) + C(Ax_{ref}(k) - x_{ref}(k+1)) + qTc^T e(k) + \varepsilon T \operatorname{sgn}(c^T e(k))] \quad \text{(A.21.8)}$$

where $d(k) = T_a(k)$ and the matrices A, B, B_d are discretized.

As can be seen from (A.21.8), disturbance terms containing $T_a(k)$ and also $x_{ref}(k+1)$ appear. In [93], in order to overcome the uncertainty in the knowledge of disturbance a method based on replacement of them with conservatively large enough values is proposed. However, in the WT application considered here, this approach resulted in a quite aggressive control action for low values of the disturbance, $T_a(k)$ in below rated operation, as was found experimentally in hardware simulations. Therefore, the

estimated $\hat{T}_a(k)$ obtained by the KF is used. Regarding x_{ref}(k+1) this was set x_{ref}(k+1)= x_{ref}(k).

A.21.2. Discrete time sliding mode controller-2

A second sliding mode controller has been designed using the model reference approach found in [94]. This is called the Model Reference DT SMC (MR DT SMC).

The derivation of the method, according to [94], is as follows:

Dynamic system:

$$x_{k+1} = \Phi x_k + \Gamma u_k + B_d d_k \qquad \text{(A.21.9)}$$

$$y_k = C x_k \qquad \text{(A.21.10)}$$

Reference model for the states x_k of Eqn. (A.21.11):

$$x_{k+1}^d = \Phi x_k^d + \Gamma u_k^d \qquad \text{(A.21.12)}$$

$$u_k^d = -L_f x_k^d + \rho r_k \qquad \text{(A.21.13)}$$

Control:

$$u_k = -(\Lambda\Gamma)^{-1}\left((\Lambda\Phi - I)e_k + \Lambda B_d d_k + qTs_k + \varepsilon Tsgn(s_k)\right) + u_k^d$$

(A.21.14)

A.21.3. Chattering reduction

In order to reduce the chattering, the *sgn* function has been replaced with the logistic function, as similar techniques are proposed in [91]:

$$f = 2(-0.5 + \frac{1}{1+\exp(-Gs_k)}) \qquad \text{(A.21.14)}$$

A.21.4. Simulation results

A) Simulink results

Figures A.21.2(a-b) show the speed tracking response and the generator torque of a MR DT SMC applied to the full model of the WT in Simulink. At the middle of the simulation (90sec) the wind speed is halved in order to simulate both above and below rated operation. The matrix L_f has been designed using pole placement and also using the "dlgr" function of MATLAB for LQR controllers, were then (A.21.13) was expressed as $u_k^d = -L_{f_{lgr}}(x_k^d - r_k)$. Both approaches produced the same result, since both achieved perfect reference tracking.

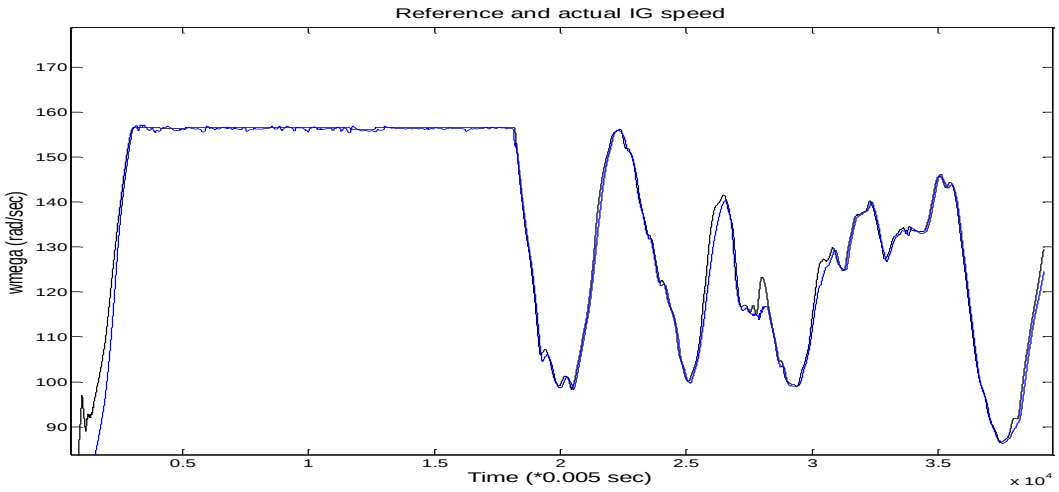

A.21.2(a) Reference (black) and actual (blue) IG speed.

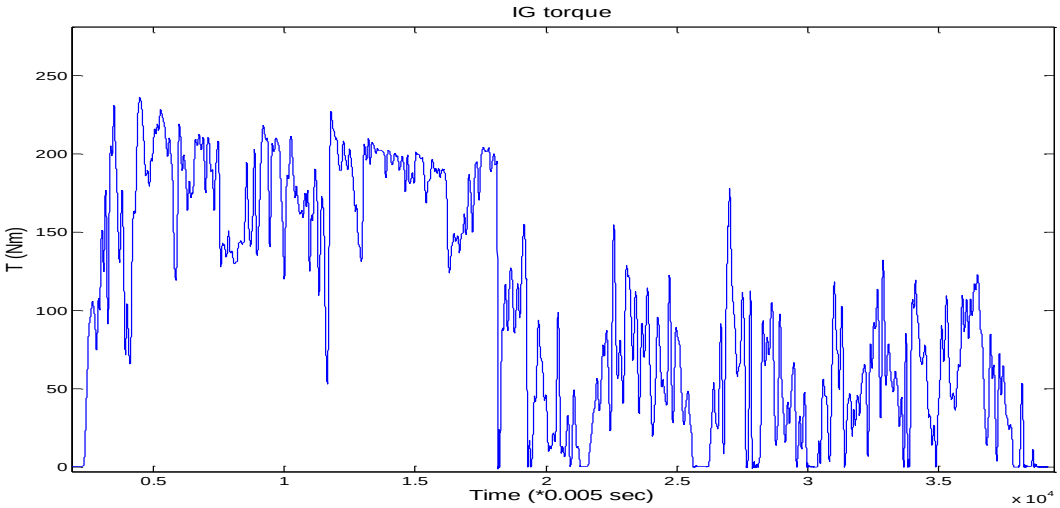

A.21.2(b) IG torque.

As can be seen, the controller exhibits perfect reference tracking without chattering for both high and low wind speeds ($t<1.7*10^4$ and $t>1.7*10^4$ samples, respectively).

B) Hardware simulation results.

Here results of MR DT SMC using the HILS are shown.

Below rated:

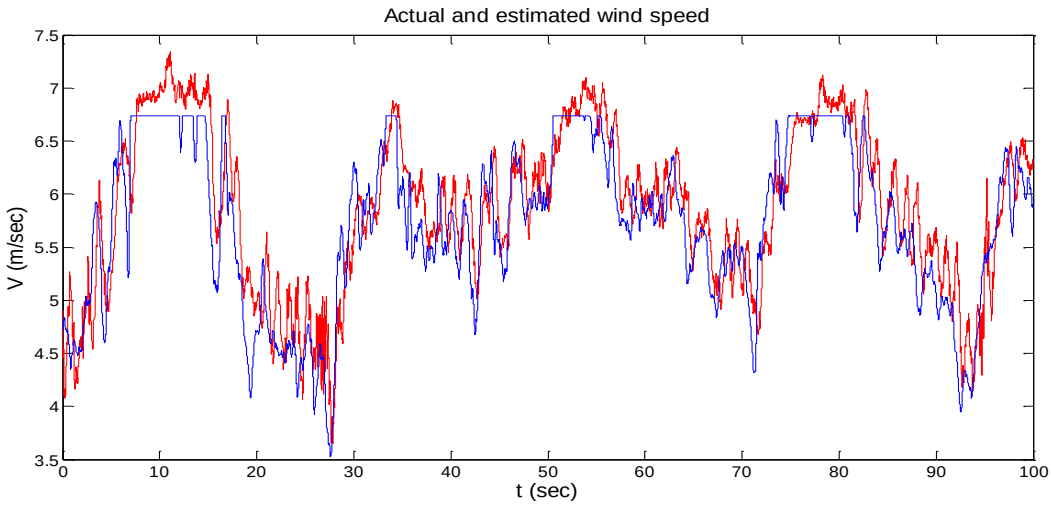

A.21.3(a). Actual (blue) and estimated (red) *V*.

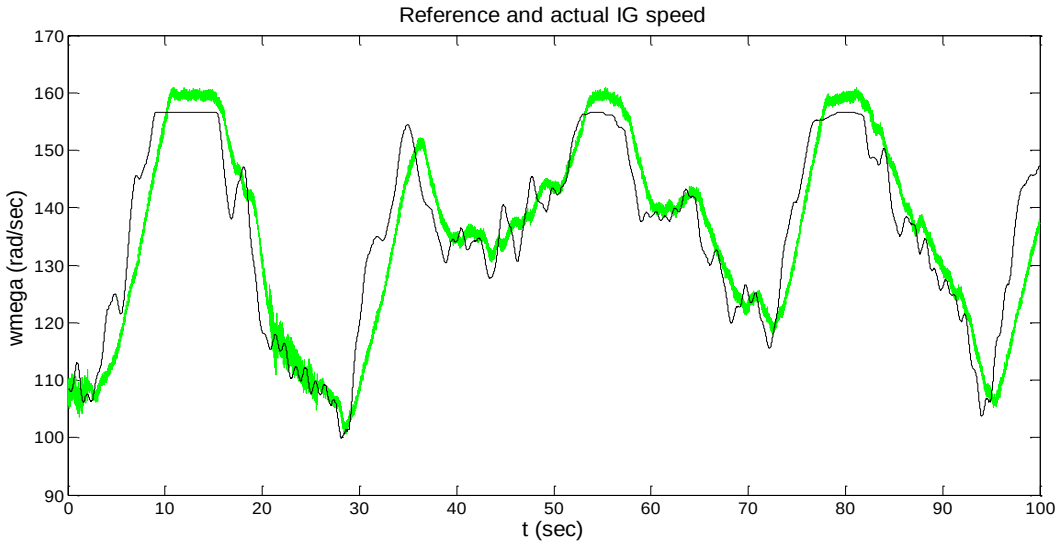

A.21.3(b). Reference (black) and actual (green) IG speed.

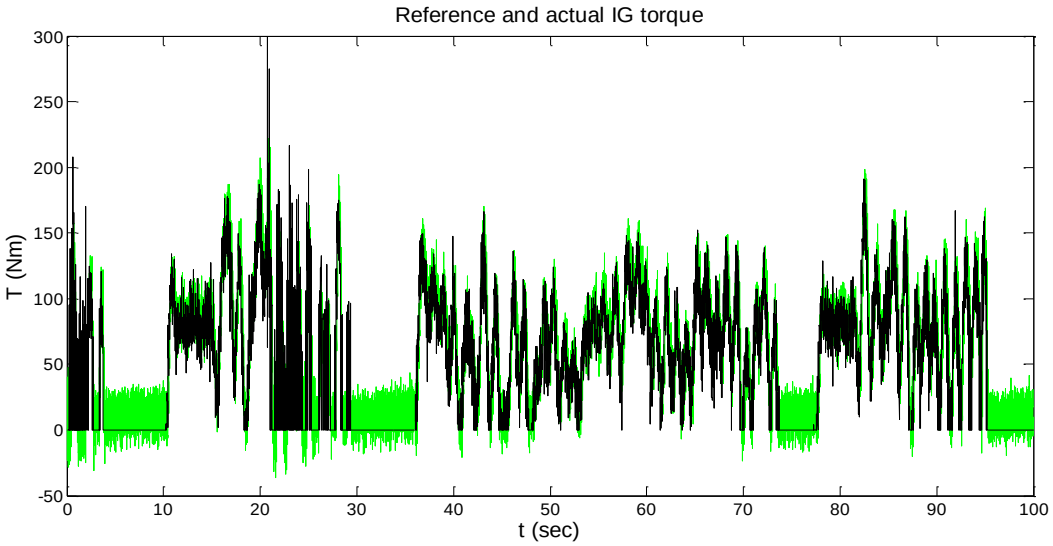

A.21.3(c). Reference (black) and actual (green) IG torque.

From the above it can be seen, that the controller performs similar to Figures A.21.2 for below rated conditions, although the torque is slightly more pulsating.

In above rated wind speeds, the controller resulted to poorer performance, with a constant speed error above the speed reference of 2rad/sec on average. By altering the parameters ε and q, this speed error was eliminated. However, chattering occurred then, for both below and above rated wind speeds. In order to reduce the chattering, Eqn. (A.21.18) was used. Below and above rated results are following.

<u>Below rated:</u>

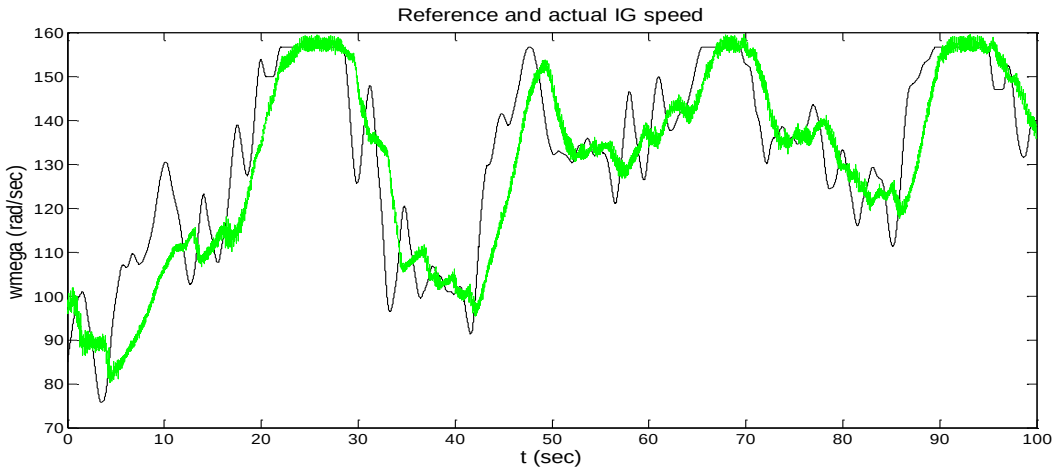

A.21.4(a). Reference (black) and actual (green) IG speed.

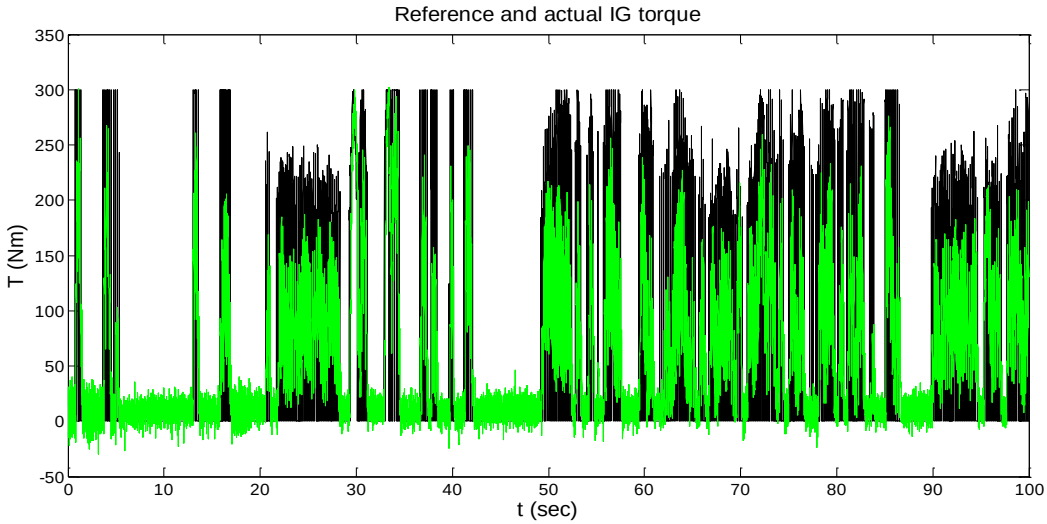

A.21.4(b). Reference (black) and actual (green) IG torque.

Above rated:

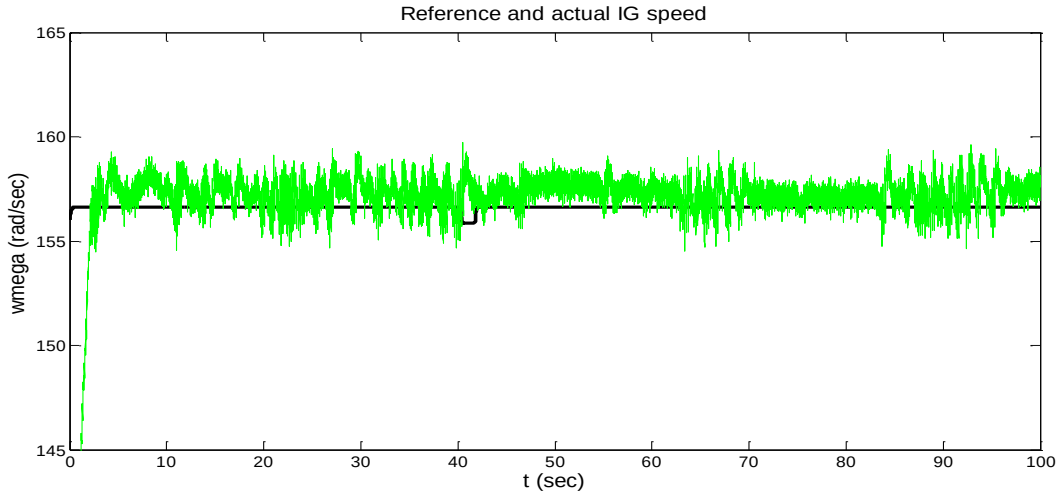

A.21.5(a). Reference (black) and actual (green) IG speed.

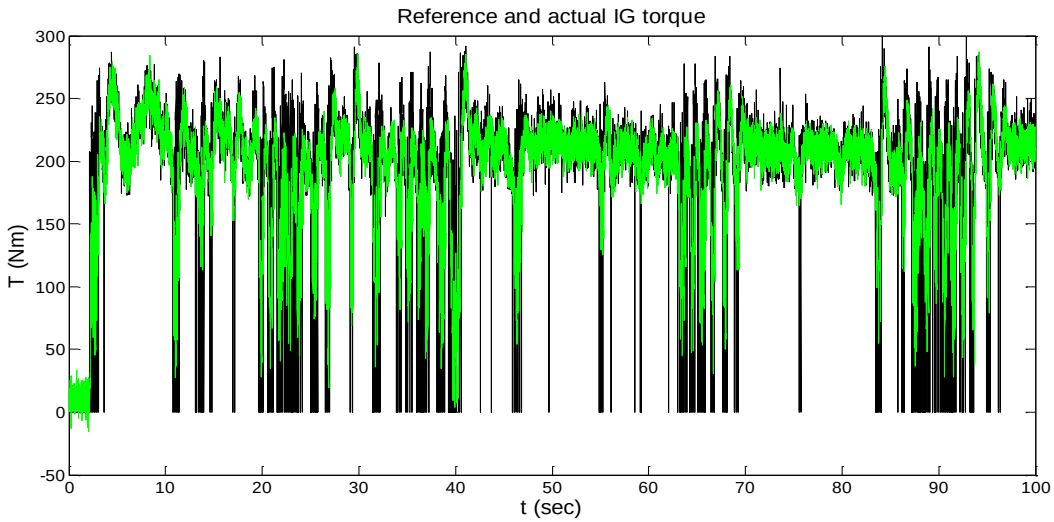

A.21.5(b). Reference (black) and actual (green) IG torque.

From the above results it can be seen that controller exhibits perfect tracking, but unacceptable chattering in below rated conditions. Furthermore, the tracking in above rated conditions is quite good, while the chattering is kept in more acceptable levels.

A.21.5. Conclusion

In this section, the design of novel discrete sliding mode controllers for a variable speed stall regulated wind turbine was presented. The controllers were tested in Simulink and also in HILS using detailed WT modelling and using the proposed control algorithm with the proposed process and measurement noise IAE AKF.

The presented hardware simulations of the SMCs, in general comprise novel work in the area of wind energy and reveal important information regarding the applicability of SMC in WTs. Specifically, the controllers exhibited quite degraded performance and chattering in the HILS, which is the cause of absence of modelling of the uncertainty involved in the dynamic models, due to the HILS hardware. Therefore, further work is required in order to eliminate the chattering, while at the same time to achieve acceptable tracking performance.

A.22. Measurement noise estimation results

In nonadaptive Kalman filter

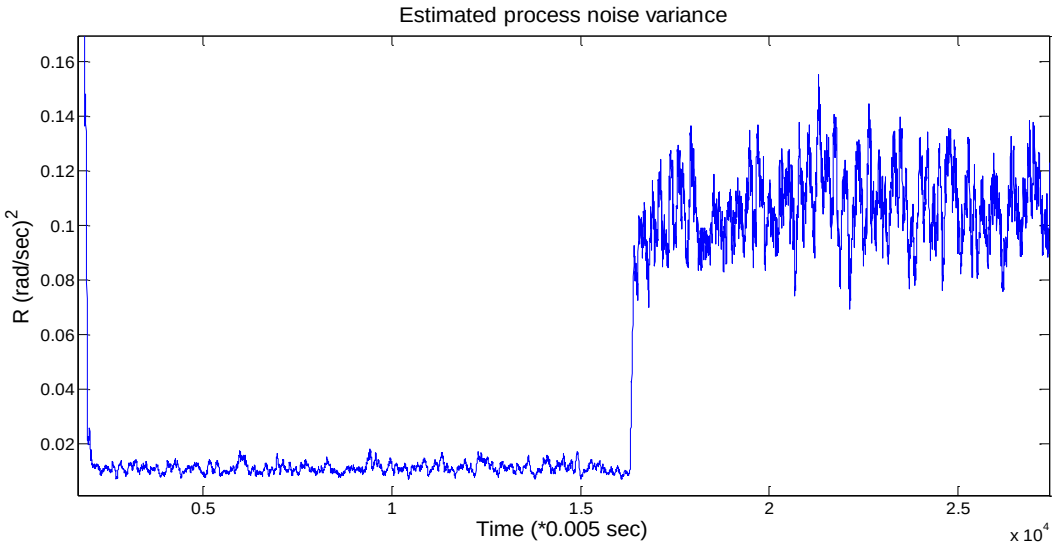

Figure A.22.1(a). $\hat{R}$ estimate during a step in measurement noise variance from 0.01 to 0.1 (rad/sec).

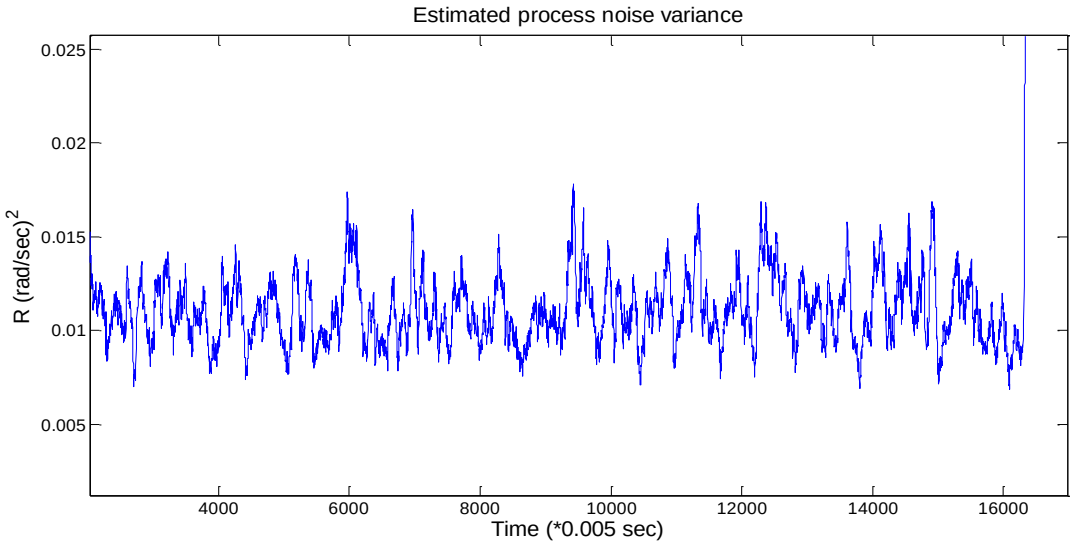

Figure A.22.1(b). Closer view.

In the proposed adaptive Kalman filter

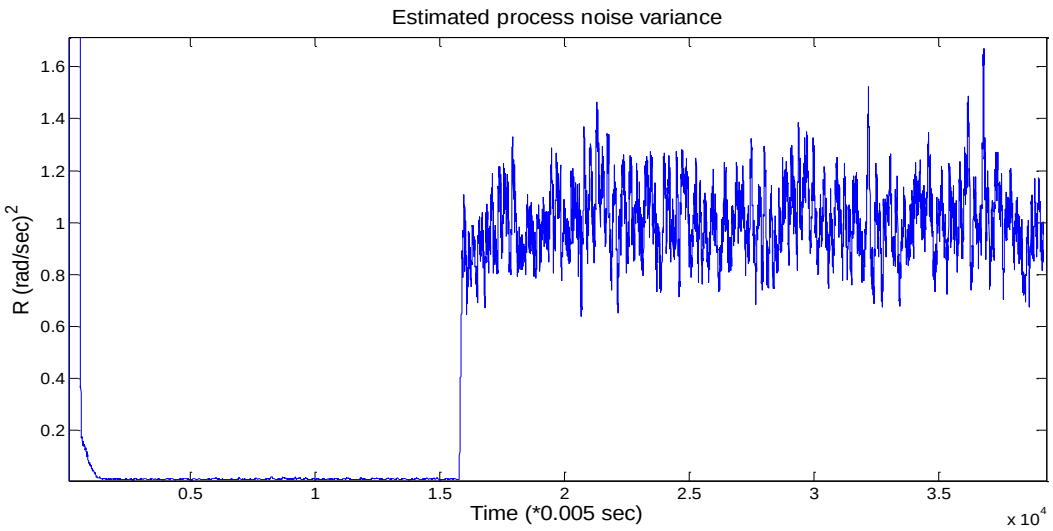

Figure A.22.2(a). $\hat{R}$ estimate during a step in measurement noise variance from 0.01 to 1 (rad/sec).

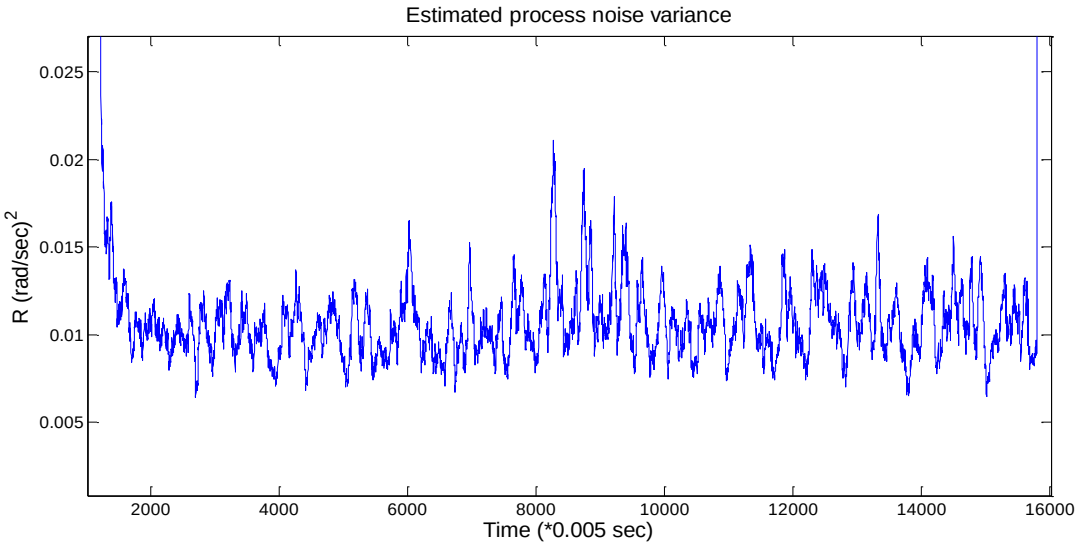

Figure A.22.2(b). Closer view.

Comment

Slightly higher peaks can be observed in the $\hat{R}$ estimate of the AKF than of the KF, due to the interaction between R and Q adaptation. In general, if the PI gains of the adaptive algorithm are set higher, higher peaks of the $\hat{R}$ estimate are observed, during fast changes of T_a. However, these do not impact the performance of the filter in general, as they happen instantly and not continuously.

From Figure A.22.2(c) that follows it can be seen that the estimated T_a is not affected by the dramatic change in the measurement noise level, as a result of the effective R adaptation.

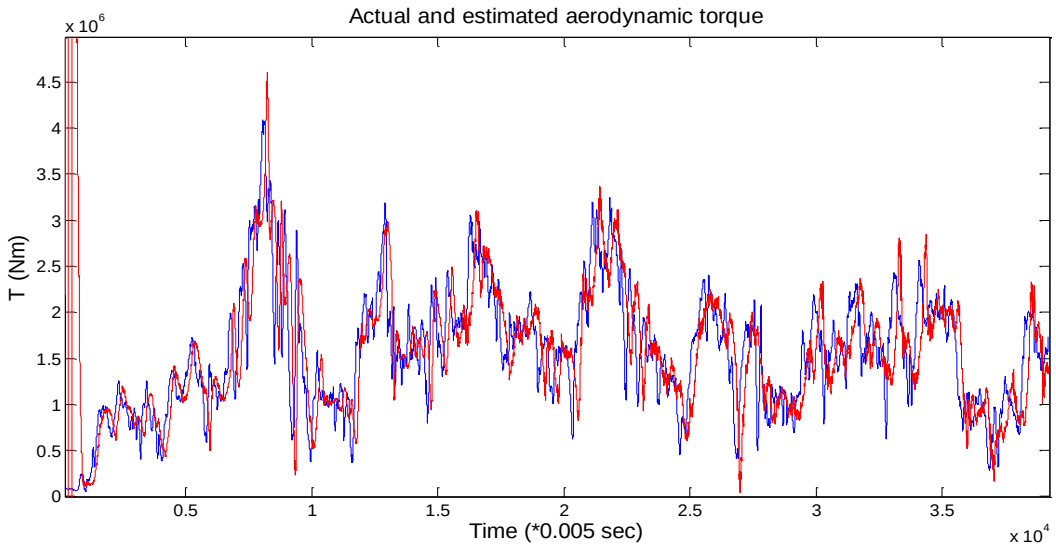

Figure A.22.2(c). Actual (blue) and estimated (red) T_a.

A.23. Larger speed controller gains of the induction machine

In order to verify the above observations (A.13, Chapter 4, Chapter 6), regarding the influence of the HILS IM drive bandwidth in the simulations, the gains of the IM drive were increased. Below the old and new values (bold) of the PI gains are shown:

P gain: 0.67 Nm/rad/sec, **2.01 Nm/rad/sec**

I gain: 13.5Nm/rad/sec, **40.5 Nm/rad/sec**

A simulation of below rated operation was performed (V is cut to 6.74m/sec) using a gain scheduled I-P speed controller for the IG (IP1: 20 and 10 Nm/rad/sec, IP2: 50 and 30 Nm/rad/sec).

Figure A.23.1 shows the actual and estimated wind speed.

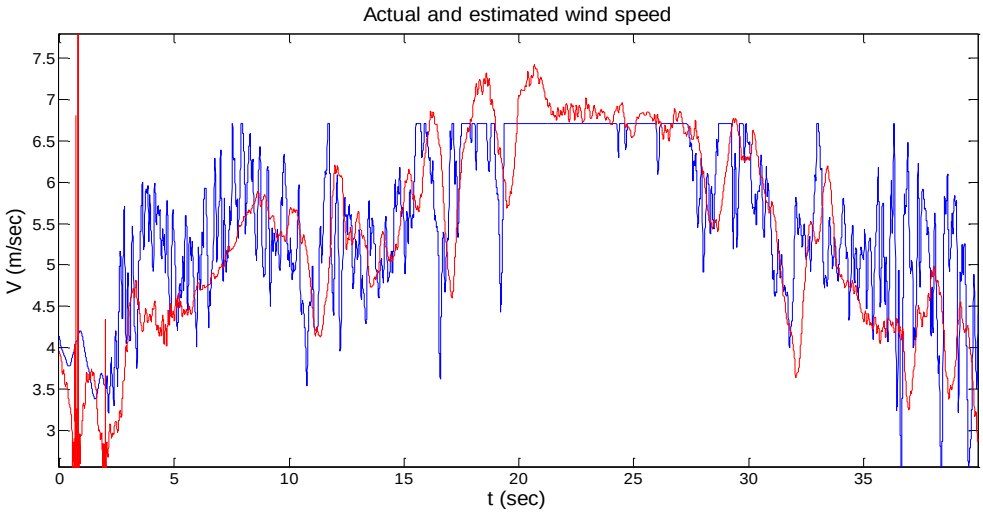

Figure A.23.1. Actual (blue) and estimated (red) wind speed.

As can be seen, the estimated wind speed does not exhibit large excursions as it is the case in the Figures of Chapter 6, which indicates that the consideration of the influence of the IM drive is correct. However, the applied settings of the IM speed controller eventually caused instability to the speed demand. It was actually difficult to find other PI gains that could achieve stable operation of the HILS. Therefore, the default gains were set, in order to produce the simulation results of Chapter 6, since as it was shown the proposed control scheme was effectively simulated.

REFERENCES

[1] Fernando D. Biachi, Hernan De Battista, Ricardo L. Mantz, "Wind turbine control systems. Principles, Modeling and Gain Scheduling Design. Advances in Industrial Control," Springer, 2007.

[2] Manwell, James, "Wind energy explained: theory, design and application," Willey, 2002.

[3] David Anthony Parker,"The design and development of a fully dynamic simulator for renewable energy converters, Phd Thesis, University of Leicester, 2000.

[4] Kathryn E. Johnson, et al, "Control Of Variable-Speed Wind Turbines. Standard And Adaptive Techniques For Maximizing Energy Capture," IEEE Control Systems Magazine, Vol. 26, No. 3, June 2006, pp. 70-81.

[5] W.E. Leithead, et al, "Design of a controller for a test-rig for a variable speed wind turbine," Proceedings of the Third IEEE Conference on Control Applications, Glasgow, UK, 24-26 Aug 1994, pp. 239-244.

[6] W.E. Leithead, et al, "Wind turbine modelling and control," University of Strathclyde, UK.

[7] Ferhat Kurtulmus, Ali Vardar, Nazmi Izli, "Aerodynamic Analyses of Different Wind Blade Profiles," Journal of Applied Sciences, 2007, pp. 663-670.

[8] D. Goodfellow, G.A. Smith, G. Gardner, "Control strategies for variable-speed wind energy recovery," Proceedings of the BWECS conference, 1988.

[9] B. Connor, W.E. Leithead, "Control strategies for variable speed stall regulated wind turbines," Proceedings of the 5th European Wind Energy Association Conference and Exhibition, Thessaloniki, Greece, 10-14 Oct 1994, Vol. 1, pp. 420-424.

[10] W.E. Leithead, B. Connor, "Control of Variable Speed Wind Turbines: Design Task," International Journal of Control, Vol. 73, No. 13, 2000, pp. 1189-1212.

[11] W.E. Leithead, "Dependence of performance of variable speed wind turbines on the turbulence, dynamics and control," IEE Proceedings, Vol. 137, No. 6, November 1990.

[12] E.A. Bossanyi, "Wind Turbine Control for Load Reduction," Wind Energy, Vol. 6, No. 3, 3 Jun 2003, pp. 229-244.

[13] H. Munz, B. Connor, W.E. Leithead, "Sensitivity of stall regulated variable speed HAWTs to rotor inertia," Proceedings of the 17th BWEA Wind Energy Conference, 1995, pp. 261-266.

[14] P. Ridanpää, H. Vihriälä, L. Söderlund, "Reducing cost of wind energy by self-tuning controller," Proceedings of the European Wind Energy Conference, Nice, France, 1-5 March 1999, pp. 873-876.

[15] H. Vihriälä, P. Ridanpää, L. Söderlund, "Control of variable speed, stall regulated wind turbine: Comparison between adaptive and fuzzy controller," Proceedings of the European Wind Energy Conference, Dublin Castle, Ireland, Oct 1997, pp. 559-563.

[16] B. Connor, W.E. Leithead, "Performance assessment of variable speed wind turbines," Proceedings of the International Conference on Opportunities and Advances in International Electric Power Generation, Durham, UK, 18-20 Mar 1996, pp. 65-68.

[17] R. Cardenas, G.M. Asher, G. Asher, "Torque Observer for the Control of Variable Speed Wind Turbines Operating Below Rated Wind Speed," Wind Engineering, Vol. 20, No. 4, 1996, 259-284.

[18] A.S. Mercer, E.A. Bossanyi, "The use of variable speed drives for active stall regulation," Garrad Hassan and Partners Ltd.

[19] F.D. Biachi, R.J. Mantz, C.F. Christiansen, "Gain Scheduling Control of Variable-Speed Wind Energy Conversion Systems Using Quasi-LPV Models," Control Engineering Practice, Vol. 13, No. 2, Feb 2005, pp. 247-255.

[20] Fabien Lescher, Jing-Yun Zhao, Pierre Borne, "Switching LPV Controllers for a Variable Speed Pitch Regulated Wind Turbine," International Journal of Computers, Communications & Control, Vol. 1, No. 4, 2006, pp. 73-84.

[21] Iulian Munteanu, et al, "Optimization of Variable Speed Wind Power Systems Based on a LQG Approach," Control Engineering Practice, Vol. 13, No. 7, July 2005, pp. 903-912.

[22] K.Z. Østergaard, P. Brath and J. Stoustrup, "Estimation of Effective Wind Speed," Journal of Physics: Conference Series, Vol. 75, No. 1, 2007, pp. 1-9.

[23] P. Novak, et al, "Modelling and Control of Variable-Speed Wind-Turbine Drive-System Dynamics," IEEE Control Systems Magazine, Vol. 15, No. 4, Aug 1995, pp. 28-38.

[24] H. Vihriälä, et al, "Control of a variable speed wind turbine with feedforward of aerodynamic torque," Proceedings of the European Wind Energy Conference, Nice, France, 1-5 Mar 1999, pp. 881-884.

[25] Endusa Billy Muhando, et al, "Augmented LQG Controller for Enhancement of Online Dynamic Performance for WTG System," Renewable Energy, Vol. 33, No. 8, Aug 2008, pp. 1942-52.

[26] Endusa Billy Muhando, et al, "Gain Scheduling Control of Variable Speed WTG Under Widely Varying Turbulence Loading," Renewable Energy, Vol. 32, No. 14, Nov 2007, pp. 2407-2423.

[27] Sigurd Skogestad, Ian Postlethwaite, "Multivariable Feedback Control. Analysis and Design,", 2nd Ed, Wiley, Feb 2007.

[28] Hui Li, K.L. Shi, P.G.McLaren, "Neural-Network-Based Sensorless Maximum Wind Energy Capture With Compensated Power Coefficient," IEEE Transactions on Industy Applications, Vol. 41, No. 6, Nov 2005, pp. 1548-1556.

[29] Wei Qiao, et al, "Wind Speed Estimation Based Sensorless Output Maximization Control for a Wind Turbine Driving a DFIG," IEEE Transactions on Power Electronics, Vol. 23, No. 3, May 2008, pp. 1156-1169.

[30] C.L. Bottasso, A. Croce, B. Savini, "Performance Comparison of Control Schemes for Variable-Speed Wind Turbines," Journal of Physics: Conference Series, Vol. 75, No. 1, 2007, pp. 1-9.

[31] M. Sedighizadeh, A. Rezazadeh, "Adaptive PID Control of Wind Energy Conversion Systems Using RASP1 Mother Wavelet Basis Function Networks," Proceedings of World Academy of Science, Engineering and Technology, Vol. 27, Feb 2008, pp. 269-273.

[32] U. Ozbay, E. Zergeroglu, S. Sivrioglu, "Adaptive Backstepping Control of Variable Speed Wind Turbines," International Journal of Control, Vol. 81, No. 6, June 2008, pp. 910-919.

[33] Ronilson Rocha, "Control of Stall Regulated Wind Turbine Through H_∞ Loop Shaping Method," Proceedings of the IEEE International Conference on Control Applications, Mexico City, Mexico, 5-7 September 2001, pp. 925-929.

[34] B. Boukhezzar, H. Siguerdidjane, "Robust Multiobjective Control of a Variable Speed Wind Turbine," Proceedings of the European Wind Energy Conference, London, UK, 22-25 November 2004, pp. 1-8.

[35] B. Boukhezzar, H. Siguerdidjane, "Nonlinear control of variable speed wind turbines without wind speed measurement," Proceedings of the 44th IEEE Conference on Decision and Control, and the European Control Conference 2005, Seville, Spain, December 12-15, 2005, pp. 3456-3461.

[36] B. Beltran, T. Ahmed-Ali, M.E.H. Benbouzid, "Sliding mode power control of variable speed wind energy conversion systems," IEEE International Electrical Maxhines & Drives Conference, Antalya, 3-5 May 2007, pp. 943-948.

[37] I. Munteanu, A.I. Bratcu, E. Geanqa, "Wind Turbulence Used As Searching Signal For MPPT in Variable-Speed Wind Energy Conversion Systems," Renewable Energy, Vol. 34, No. 1, Jan. 2009, pp. 322-7.

[38] B. Connor, W.E. Leithead, S.S. Robertson, "A robust two-level control design approach to variable speed stall regulated wind turbines," Proceedings of the European Wind Energy Conference, Dublin Castle, Ireland, Oct 1997, pp. 551-554.

[39] P. Mutschler, B. Hagenkort, S. Jöckel, "Control method for variable speed stall controlled wind turbines," Proceedings of the European Wind Energy Conference, Dublin Castle, Ireland, Oct 1997, pp. 542-545.

[40] Thommy Ekelund, "Speed control of wind turbines in the stall region," Proceedings of the 3rd IEEE Conference on Control Applications, Glasgow, Scotland, 24-26 Aug. 1994, pp. 227-232.

[41] C. Nichita, et al, "Large Band Simulation of the Wind Speed for Real Time Wind Turbine Simulators," IEEE Transactions on Energy Conversion, Vol. 17, No. 4, 6 Jan 2003, pp. 523-529.

[42] Tomas Petru, Torbjörn Thiringer, "Modeling of Wind Turbines for Power System Studies," IEEE Transactions on Power Systems, Vol. 17, No. 4, Nov 2002, pp. 1132-1139.

[43] T.G. van Engelen, E.L. van der Hooft, "Dynamic Inflow Compensation for Pitch Controlled Wind Turbines," Energy Centre of the Netherlands (ECN), Wind Energy.

[44] D. Bourlis, J.A.M. Bleijs, "A wind estimation method using adaptive Kalman filtering for a variable speed stall regulated wind turbine," Proceedings of the 11th IEEE International Conference on Probabilistic Methods Applied to Power Systems, Singapore, 14-17 July, pp. 89-94.

[45] D. Bourlis, J.A.M. Bleijs, "Control of stall regulated variable speed wind turbine based on wind speed estimation using an adaptive Kalman filter," Proceedings of the European Wind Energy Conference, Warsaw, Poland, 20-23 April 2010, pp. 242-246.

[46] W.E. Leithead, M.C. Rogers, "Improving damping by a simple modification to the drivetrain," University of Strathclyde, UK.

[47] Peter Vas, "Vector Control of AC Machines," Oxford University Press, Oxford, 1990.

[48] W.E. Leithead, B. Connor, "Control of Variable Speed Wind Turbines: Dynamic Models," International Journal of Control, Vol. 73, No. 13, 2000, pp. 1173-1188.

[49] Helge Aagaard Madsen, et al, "The phenomenon of double stall," Proceedings of the European Wind Energy Conference, Dublin Castle, Ireland, Oct 1997, pp. 453-457.

[50] Prabha Kundur, "Power System Stability and Control," The EPRI Power System Engineering Series. McGraw-Hill, Inc., 1993.

[51] F. Luis Pagola, Ignatio J. Perez-Arriaga, George C. Varghese, "On Sensitivities, Residues and Participations: Applications to Oscillatory Stability Analysis and Control," IEEE Transactions on Power Systems, Vol. 4, No. 1, Feb 1989, pp. 278-285.

[52] R. Cardeans, et al, "Experimental emulation of wind turbines and flywheels for wind energy applications," Proceedings of the 9th European Conference on Power Electronics and Applications, Graz, 2001, pp. 1-9.

[53] H.M. Kojabadi, L. Chang, T. Boutot, "Development of a Novel Wind Turbine Simulator for Wind Energy Conversion Systems Using an Inverter-Controlled Induction Motor," IEEE Transactions on Energy Conversion, Vol. 19, No. 3, Sept 2004, pp. 547-552.

[54] M. Molinas, et al, "Control of wind turbines with induction generators interfaced to the grid with power electronics converters," Norwegian University of Science and Technology, Trondheim, Norway.

[55] B. Neammanee, S. Sirisumrannukul, S. Chatratana, "Development of a wind turbine simulator for wind generator testing," International Energy Journal, Vol. 8, 2007, pp. 21-28.

[56] Md. Arifujjaman, M.T. Iqbal, J.E. Quaicoe, "Emulation of a Small Wind Turbine System with a Separately-Excited DC Machine," Journal of Electrical & Electronics Engineering, Vol. 8, No. 1, 2008, pp. 569-579.

[57] Md. Arifujjaman, M.T. Iqbal, J.E. Quaicoe, "An isolated small wind turbine emulator," Proceedings of the Canadian Conference on Electrical and Computer Engineering, 2007, pp. 1854-1857.

[58] Z.H. Akpolat, G.M. Asher, J.C. Clare, "Dynamic Emulation of Mechanical Loads Using a Vector-Controlled Induction Motor-Generator Set," IEEE Transactions on Industrial Electronics, Vol. 46, No. 2, April 1999, pp. 370-379.

[59] Z.H. Akpolat, G.M. Asher, J.C. Clare, "Experimental Dynamometer Emulation of Nonlinear Mechanical Loads," IEEE Transactions on Industry Applications, Vol. 35, No. 6, Nov 1999, pp. 1367-1373.

[60] C.K. Chui, G. Chen, "Kalman filtering. With real time applications," 3rd ed. Springer, 1999.

[61] B.D.O. Anderson, J.B. Moore, "Optimal Filtering," Prentice-Hall Information and System Sciences Series, Englewood Cliffs, N.J., 1979.

[62] Written by the Technical Staff, The Analytic Sciences Corporation, "Applied Optimal Estimation," Edited by Arthur Gebl, The MIT Press, Cambridge, Massachusetts, USA, 1974.

[63] “Stochastic Modelling Strategies in GPS/INS Data Fusion Process,” International Global Navigation satellite Systems Society, IGNN Symposium, Holiday Inn Surfers Paradise, Australia, 17-21 July, 2006, No. 35.

[64] W. Ding, J. Wang, C. Rizos, “Improving covariance based adaptive estimation for GPS/INS integration,” School of Surveying and Spatial Information Systems, University of New South Wales, Sydney, Australia.

[65] D. Loebis, et al, “Adaptive Tuning of a Kalman Filter via Fuzzy Logic for an Intelligent AUV Navigation System,” Control Engineering Practice, Vol. 12, No. 12, Dec 2004, pp. 1531-9.

[66] Joon-Young Park, et al, “Design of simulator for 3MW wind turbine and its condition monitoring system,” Proceedings of the International MultiConference of Engineers and Computer Scientists, Hong Kong, 17-19 March 2010, Vol. 2.

[67] S. Fekri, M. Athans, A. Pascoal, “Robust Multiple Model Adaptive Control (RMMAC): A Case Study,” International Journal of Adaptive Control and Signal Processing, Vol. 21, No. 1, Feb 2007, pp. 1-30.

[68] S. Fekri, M. Athans, A. Pascoal, “Issues, Progress and New Results in Robust Adaptive Control,” International Journal of Adaptive Control and Signal Processing, Vol. 20, No. 10, Dec 2006, pp. 519-79.

[69] S.F. Asl, M. Athans, A. Pascoal, “Identification of mass-spring-dashpot systems using multiple-model adaptive estimation (MMAE) algorithms,” Proceedings of the 11th Mediterranean Conference on Control and Automation, 2003.

[70] P.D. Hanlon, P.S. Maybeck, “Characterization of Kalman filter residuals in the presence of mismodeling,” IEEE Transactions on Aerospace and Electronic Systems, Vol. 36, No. 1, Jan 2000, pp. 114-131.

[71] A.H. Mohamed, K.P. Schwarz, “Adaptive Kalman Filtering for INS/GPS,” Journal of Geodesy, Vol. 73, No. 4, May 1999, pp. 193-203.

[72] P.S. Maybeck, P.D. Hanlon, “Performance Enhancement of a Multiple Model Adaptive Estimator,” IEEE Transactions on Aerospace and Electronic Systems, Vol. 31, No. 4, Oct 1995, pp. 1240-1254.

[73] P.D. Hanlon, P.S. Maybeck, “Multiple-Model Adaptive Estimation Using a Residual Correlation Kalman Filter Bank,” IEEE Transactions on Aerospace and Electronic Systems, Vol. 36, No. 2, April 2000, pp. 393-406.

[74] S. Fekri, M. Athans, A. Pascoal, “RMMAC: A Novel Robust Adaptive Control Scheme – Part I: Architecture,” Proceedings of the 43rd IEEE Conference on Decision and Control, Atlantis, Paradise Island, Bahamas, 14-17 Dec 2004. pp. 1134-1139.

[75] P.D. Hanlon, "Practical Implementation of Multiple Model Adaptive Estimation using Neyman-Pearson based hypothesis yesting and spectral estimation tools," PhD Thesis, Air Force Institute of Technology, Air University, Sept 1996.

[76] Dan Simon, "Optimal State Estimation," 1st ed., John Wiley & Sons, Hoboken, New Jersey, USA, 2006.

[77] E.A. Wan, R. Van Der Merwe, "The unscented Kalman filter for nonlinear estimation," Proceedings of the IEEE Adaptive Systems for Signal Processing, Communications and Control Symposium, 2000, pp. 153-8.

[78] G.A. Terejanu, "Unscented Kalman filter tutorial," Department of Computer Science and Engineering, University at Buffalo, Buffalo, NY.

[79] A.S. Mercer, E.A. Bossanyi, "Stall regulation of variable speed HAWTS," Proceedings of the European Wind Energy Conference, Göteborg, Sweden, 20-24 May 1996, pp. 825-828.

[80] M.A. Johnson, M.H. Moradi, "PID Control. New Identification and Design Methods," Springer, 2005.

[81] J. Wilkie, M.A. Johnson, R. Katebi, "Control Engineering. An introductory course," Palgrave, 2002.

[82] P.N. Paraskevopoulos, "Digital Control Systems," Prentice Hall, 1996.

[83] S.F. Graebe, A. Ahlen, "Dynamic transfer among alternative controllers," Proceedings of the 12th IFAC World Congress, Sydney, Astralia, 18-23 July 1993.

[84] U. Mackenroth, "Robust control systems: Theory and case studies," Springer, 2004.

[85] H. Kwakernaak, "Robust control and H_∞ optimization-Tutorial paper," Automatica, Vol. 29. No. 2, 1993, pp. 255-273.

[86] C. Edwards, I. Postlethwaite, "Anti-windup and bumpless transfer schemes," Proceedings of the IEE UKACC International Conference on Control, 2-5 September 1996, No. 427, pp. 394-399.

[87] M.V. Kothare, "A Unified Framework for the Study of Anti-windup Designs," Automatica, Vol. 30, No. 12, Dec 1994, pp. 1869-83.

[88] M.L. Kerr, M.C. Turner, "Practical approaches to low-order anti-windup compensator design: A flight control comparison," Proceedings of the 17th World Congress. The International Federation of Automatic Control, Seoul, Korea, 6-11 July 2008, pp. 14162-14167.

[89] F. Suzuki, Y. Hori, "Anti-windup control using saturated state observer," Transactions of the Institute of Electrical Engineers of Japan, Part D, Vol. 120-D, No. 1, Jan 2000, pp. 120-5.

[90] K. Ohishi, T. Mashimo, "Digital robust speed servo system with complete avoidance of output saturation effect," Proceedings of the Power Conversion Conference, Nagaoka, 1997, Vol. 1, pp. 501-6.

[91] V. Utkin, J. Guldner, J. Shi, "Sliding mode control in electromechanical systems," Taylor & Francis, 1999.

[92] I. Munteanu, et al, "Optimal Control of Wind Energy Systems: Towards a Global Approach (Advances in Industrial Control)," Springer, 2008.

[93] W.Gao, Y. Wang, A. Homaifa, "Discrete-Time Variable Structure Control Systems," IEEE Transactions on Industrial Electronics, Vol. 42, No. 2, April 1995, pp. 117-122.

[94] Yu-Feng Li, Jan Wikander, "Model reference discrete-time sliding mode control of linear motor precision servo systems," Mechatronics, Vol. 14, No. 7, Sept 2004, pp. 835-851.

[95] J. Wilkie, W.E. Leithead, C. Anderson, "Modelling of Wind Turbines by Simple Models," Wind Engineering, Vol. 14, No. 4, 1990, pp. 247-267.

[96] M. Liserre, F. Blaabjerg, S. Hansen, "Design and Control of an LCL-Filter-Based Three-Phase Active Rectifier," IEEE Transactions on Industry applications, Vol. 41, No. 5, Sept 2005, pp. 1281-1291.

[97] ALSPA GD4000 (9 January 1996). GD4000 in its Environment. An application guide. CEGELEC Industrial Control Limited. Kidsgrove, England.

[98] D.J. Leith, W.E. Leithead, "Counter-Example to a common LPV gain scheduling design approach," Proceedings of the UKACC International Conference on Control, 2000.

[99] P. Gahinet, et al, "LMI Control Toolbox. For Use with MATLAB," User's Guide, Version 1, The Mathworks.

[100] "Quick Start Quide to Cegelec Alspa GD3000E. The universal drive," Publication No. T1690, Issue 1, June 1998.

[101] "ALSPA GD3000E Technical Manual. Firmware Specific Addendum for models GD30005E to GD32262E. Firmware version 4.120," ALSTOM, Publication No. T1675, Issue 5, Aug 1998.

[102] "ASPA GD3000E Technical Manual for models GD30005E to GD32262E," ALSTOM, Publication No. T1660, Issue 3, Sept 1998.

[103] Peter Vas, “Electrical Machines and Drives. A space Vector Theory Approach,” Oxford Science Publications, 1992.